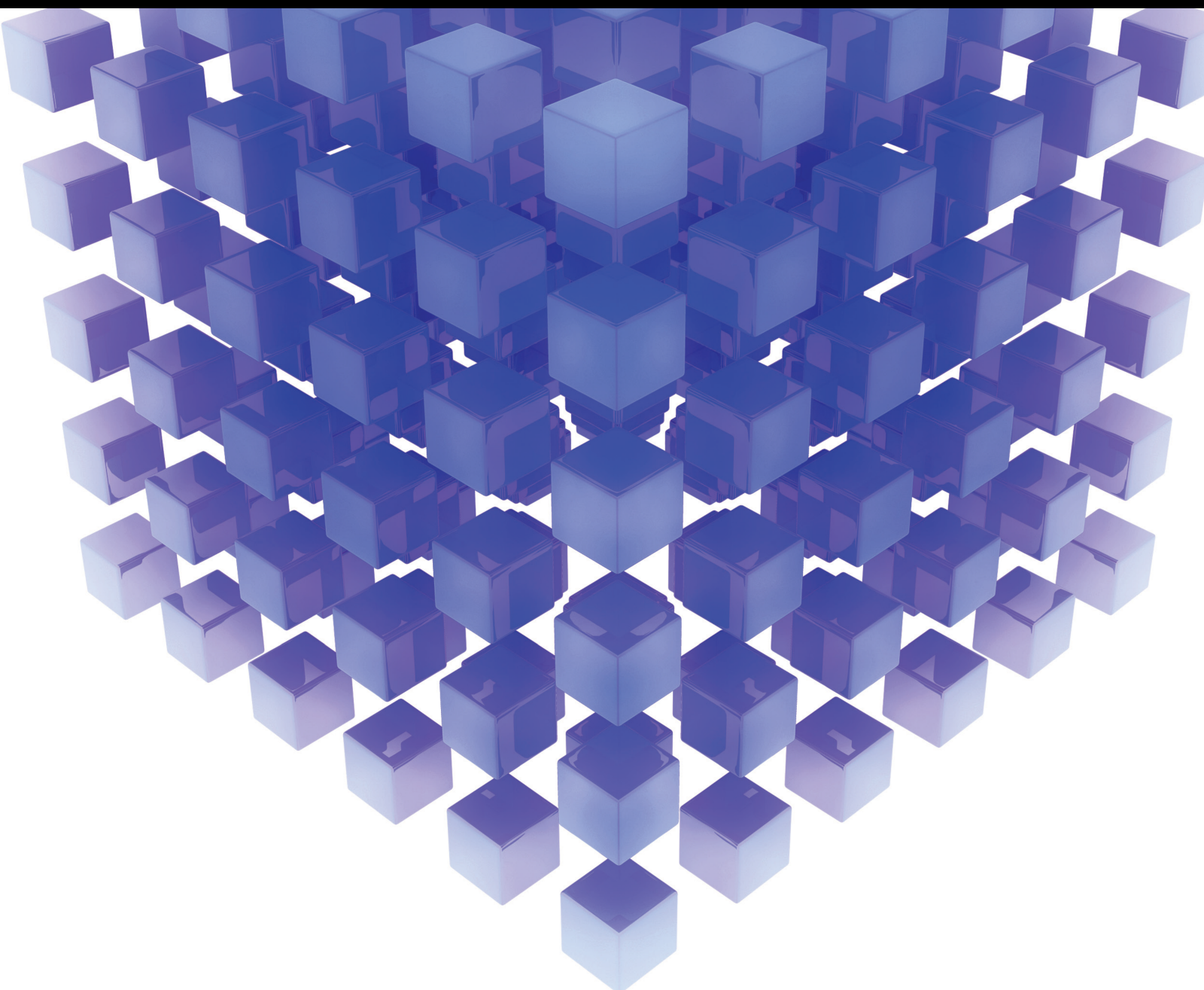


Numerical Study of Fluid Forces Reduction

Lead Guest Editor: Shams Ul-Islam

Guest Editors: Chaoying Zhou, Hamid Rahman, Waqas Abbasi, and Suvash Chandra Saha





Numerical Study of Fluid Forces Reduction

Mathematical Problems in Engineering

Numerical Study of Fluid Forces Reduction

Lead Guest Editor: Shams Ul-Islam


Guest Editors: Chaoying Zhou, Hamid Rahman,
Waqas Abbasi, and Suvash Chandra Saha



Copyright © 2022 Hindawi Limited. All rights reserved.

This is a special issue published in “Mathematical Problems in Engineering.” All articles are open access articles distributed under the Creative Commons Attribution License, which permits unrestricted use, distribution, and reproduction in any medium, provided the original work is properly cited.

Chief Editor

Guangming Xie , China

Academic Editors

Kumaravel A , India
Waqas Abbasi, Pakistan
Mohamed Abd El Aziz , Egypt
Mahmoud Abdel-Aty , Egypt
Mohammed S. Abdo, Yemen
Mohammad Yaghoub Abdollahzadeh
Jamalabadi , Republic of Korea
Rahib Abiyev , Turkey
Leonardo Acho , Spain
Daniela Addessi , Italy
Arooj Adeel , Pakistan
Waleed Adel , Egypt
Ramesh Agarwal , USA
Francesco Aggogeri , Italy
Ricardo Aguilar-Lopez , Mexico
Afaq Ahmad , Pakistan
Naveed Ahmed , Pakistan
Elias Aifantis , USA
Akif Akgul , Turkey
Tareq Al-shami , Yemen
Guido Ala, Italy
Andrea Alaimo , Italy
Reza Alam, USA
Osamah Albahri , Malaysia
Nicholas Alexander , United Kingdom
Salvatore Alfonzetti, Italy
Ghous Ali , Pakistan
Nouman Ali , Pakistan
Mohammad D. Aliyu , Canada
Juan A. Almendral , Spain
A.K. Alomari, Jordan
José Domingo Álvarez , Spain
Cláudio Alves , Portugal
Juan P. Amezcua-Sanchez, Mexico
Mukherjee Amitava, India
Lionel Amodeo, France
Sebastian Anita, Romania
Costanza Arico , Italy
Sabri Arik, Turkey
Fausto Arpino , Italy
Rashad Asharabi , Saudi Arabia
Farhad Aslani , Australia
Mohsen Asle Zaem , USA

Andrea Avanzini , Italy
Richard I. Avery , USA
Viktor Avrutin , Germany
Mohammed A. Awadallah , Malaysia
Francesco Aymerich , Italy
Sajad Azizi , Belgium
Michele Bacciocchi , Italy
Seungik Baek , USA
Khaled Bahlali, France
M.V.A Raju Bahubalendruni, India
Pedro Balaguer , Spain
P. Balasubramaniam, India
Stefan Balint , Romania
Ines Tejado Balsera , Spain
Alfonso Banos , Spain
Jerzy Baranowski , Poland
Tudor Barbu , Romania
Andrzej Bartoszewicz , Poland
Sergio Baselga , Spain
S. Caglar Baslamisli , Turkey
David Bassir , France
Chiara Bedon , Italy
Azeddine Beghdadi, France
Andriette Bekker , South Africa
Francisco Beltran-Carbajal , Mexico
Abdellatif Ben Makhlof , Saudi Arabia
Denis Benasciutti , Italy
Ivano Benedetti , Italy
Rosa M. Benito , Spain
Elena Benvenuti , Italy
Giovanni Berselli, Italy
Michele Betti , Italy
Pietro Bia , Italy
Carlo Bianca , France
Simone Bianco , Italy
Vincenzo Bianco, Italy
Vittorio Bianco, Italy
David Bigaud , France
Sardar Muhammad Bilal , Pakistan
Antonio Bilotta , Italy
Sylvio R. Bistafa, Brazil
Chiara Boccaletti , Italy
Rodolfo Bontempo , Italy
Alberto Borboni , Italy
Marco Bortolini, Italy

Paolo Boscariol, Italy
Daniela Boso , Italy
Guillermo Botella-Juan, Spain
Abdesselem Boulkroune , Algeria
Boulaïd Boulkroune, Belgium
Fabio Bovenga , Italy
Francesco Braghin , Italy
Ricardo Branco, Portugal
Julien Bruchon , France
Matteo Bruggi , Italy
Michele Brun , Italy
Maria Elena Bruni, Italy
Maria Angela Butturi , Italy
Bartłomiej Błachowski , Poland
Dhanamjayulu C , India
Raquel Caballero-Águila , Spain
Filippo Cacace , Italy
Salvatore Caddemi , Italy
Zuowei Cai , China
Roberto Caldelli , Italy
Francesco Cannizzaro , Italy
Maosen Cao , China
Ana Carpio, Spain
Rodrigo Carvajal , Chile
Caterina Casavola, Italy
Sara Casciati, Italy
Federica Caselli , Italy
Carmen Castillo , Spain
Inmaculada T. Castro , Spain
Miguel Castro , Portugal
Giuseppe Catalanotti , United Kingdom
Alberto Cavallo , Italy
Gabriele Cazzulani , Italy
Fatih Vehbi Celebi, Turkey
Miguel Cerrolaza , Venezuela
Gregory Chagnon , France
Ching-Ter Chang , Taiwan
Kuei-Lun Chang , Taiwan
Qing Chang , USA
Xiaoheng Chang , China
Prasenjit Chatterjee , Lithuania
Kacem Chehdi, France
Peter N. Cheimets, USA
Chih-Chiang Chen , Taiwan
He Chen , China

























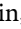

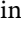
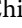
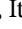

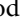

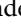

Kebing Chen , China
Mengxin Chen , China
Shyi-Ming Chen , Taiwan
Xizhong Chen , Ireland
Xue-Bo Chen , China
Zhiwen Chen , China
Qiang Cheng, USA
Zeyang Cheng, China
Luca Chiapponi , Italy
Francisco Chicano , Spain
Tirivanhu Chinyoka , South Africa
Adrian Chmielewski , Poland
Seongim Choi , USA
Gautam Choubey , India
Hung-Yuan Chung , Taiwan
Yusheng Ci, China
Simone Cinquemani , Italy
Roberto G. Citarella , Italy
Joaquim Ciurana , Spain
John D. Clayton , USA
Piero Colajanni , Italy
Giuseppina Colicchio, Italy
Vassilios Constantoudis , Greece
Enrico Conte, Italy
Alessandro Contento , USA
Mario Cools , Belgium
Gino Cortellessa, Italy
Carlo Cosentino , Italy
Paolo Crippa , Italy
Erik Cuevas , Mexico
Guozeng Cui , China
Mehmet Cunkas , Turkey
Giuseppe D'Aniello , Italy
Peter Dabnichki, Australia
Weizhong Dai , USA
Zhifeng Dai , China
Purushothaman Damodaran , USA
Sergey Dashkovskiy, Germany
Adiel T. De Almeida-Filho , Brazil
Fabio De Angelis , Italy
Samuele De Bartolo , Italy
Stefano De Miranda , Italy
Filippo De Monte , Italy

José António Fonseca De Oliveira
Correia , Portugal
Jose Renato De Sousa , Brazil
Michael Defoort, France
Alessandro Della Corte, Italy
Laurent Dewasme , Belgium
Sanku Dey , India
Gianpaolo Di Bona , Italy
Roberta Di Pace , Italy
Francesca Di Puccio , Italy
Ramón I. Diego , Spain
Yannis Dimakopoulos , Greece
Hasan Dinçer , Turkey
José M. Domínguez , Spain
Georgios Dounias, Greece
Bo Du , China
Emil Dumic, Croatia
Madalina Dumitriu , United Kingdom
Premraj Durairaj , India
Saeed Eftekhari Azam, USA
Said El Kafhali , Morocco
Antonio Elipse , Spain
R. Emre Erkmen, Canada
John Escobar , Colombia
Leandro F. F. Miguel , Brazil
FRANCESCO FOTI , Italy
Andrea L. Facci , Italy
Shahla Faisal , Pakistan
Giovanni Falsone , Italy
Hua Fan, China
Jianguang Fang, Australia
Nicholas Fantuzzi , Italy
Muhammad Shahid Farid , Pakistan
Hamed Faruqi, Iran
Yann Favennec, France
Fiorenzo A. Fazzolari , United Kingdom
Giuseppe Fedele , Italy
Roberto Fedele , Italy
Baowei Feng , China
Mohammad Ferdows , Bangladesh
Arturo J. Fernández , Spain
Jesus M. Fernandez Oro, Spain
Francesco Ferrise, Italy
Eric Feulvarch , France
Thierry Floquet, France

Eric Florentin , France
Gerardo Flores, Mexico
Antonio Forcina , Italy
Alessandro Formisano, Italy
Francesco Franco , Italy
Elisa Francomano , Italy
Juan Frausto-Solis, Mexico
Shujun Fu , China
Juan C. G. Prada , Spain
HECTOR GOMEZ , Chile
Matteo Gaeta , Italy
Mauro Gaggero , Italy
Zoran Gajic , USA
Jaime Gallardo-Alvarado , Mexico
Mosè Gallo , Italy
Akemi Gálvez , Spain
Maria L. Gandarias , Spain
Hao Gao , Hong Kong
Xingbao Gao , China
Yan Gao , China
Zhiwei Gao , United Kingdom
Giovanni Garcea , Italy
José García , Chile
Harish Garg , India
Alessandro Gasparetto , Italy
Stylianos Georgantzinou, Greece
Fotios Georgiades , India
Parviz Ghadimi , Iran
Ştefan Cristian Gherghina , Romania
Georgios I. Giannopoulos , Greece
Agathoklis Giaralis , United Kingdom
Anna M. Gil-Lafuente , Spain
Ivan Giorgio , Italy
Gaetano Giunta , Luxembourg
Jefferson L.M.A. Gomes , United Kingdom
Emilio Gómez-Déniz , Spain
Antonio M. Gonçalves de Lima , Brazil
Qunxi Gong , China
Chris Goodrich, USA
Rama S. R. Gorla, USA
Veena Goswami , India
Xunjie Gou , Spain
Jakub Grabski , Poland

Antoine Grall , France
George A. Gravvanis , Greece
Fabrizio Greco , Italy
David Greiner , Spain
Jason Gu , Canada
Federico Guarracino , Italy
Michele Guida , Italy
Muhammet Gul , Turkey
Dong-Sheng Guo , China
Hu Guo , China
Zhaoxia Guo, China
Yusuf Gurefe, Turkey
Salim HEDDAM , Algeria
ABID HUSSANAN, China
Quang Phuc Ha, Australia
Li Haitao , China
Petr Hájek , Czech Republic
Mohamed Hamdy , Egypt
Muhammad Hamid , United Kingdom
Renke Han , United Kingdom
Weimin Han , USA
Xingsi Han, China
Zhen-Lai Han , China
Thomas Hanne , Switzerland
Xinan Hao , China
Mohammad A. Hariri-Ardebili , USA
Khalid Hattaf , Morocco
Defeng He , China
Xiao-Qiao He, China
Yanchao He, China
Yu-Ling He , China
Ramdane Hedjar , Saudi Arabia
Jude Hemanth , India
Reza Hemmati, Iran
Nicolae Herisanu , Romania
Alfredo G. Hernández-Díaz , Spain
M.I. Herreros , Spain
Eckhard Hitzer , Japan
Paul Honeine , France
Jaromir Horacek , Czech Republic
Lei Hou , China
Yingkun Hou , China
Yu-Chen Hu , Taiwan
Yunfeng Hu, China
Can Huang , China
Gordon Huang , Canada
Linsheng Huo , China
Sajid Hussain, Canada
Asier Ibeas , Spain
Orest V. Iftime , The Netherlands
Przemyslaw Ignaciuk , Poland
Giacomo Innocenti , Italy
Emilio Insfran Pelozo , Spain
Azeem Irshad, Pakistan
Alessio Ishizaka, France
Benjamin Ivorra , Spain
Breno Jacob , Brazil
Reema Jain , India
Tushar Jain , India
Amin Jajarmi , Iran
Chiranjibe Jana , India
Łukasz Jankowski , Poland
Samuel N. Jator , USA
Juan Carlos Jáuregui-Correa , Mexico
Kandasamy Jayakrishna, India
Reza Jazar, Australia
Khalide Jbilou, France
Isabel S. Jesus , Portugal
Chao Ji , China
Qing-Chao Jiang , China
Peng-fei Jiao , China
Ricardo Fabricio Escobar Jiménez , Mexico
Emilio Jiménez Macías , Spain
Maolin Jin, Republic of Korea
Zhuo Jin, Australia
Ramash Kumar K , India
BHABEN KALITA , USA
MOHAMMAD REZA KHEDMATI , Iran
Viacheslav Kalashnikov , Mexico
Mathiyalagan Kalidass , India
Tamas Kalmar-Nagy , Hungary
Rajesh Kaluri , India
Jyotheeswara Reddy Kalvakurthi, India
Zhao Kang , China
Ramani Kannan , Malaysia
Tomasz Kapitaniak , Poland
Julius Kaplunov, United Kingdom
Konstantinos Karamanos, Belgium
Michal Kawulok, Poland

Irfan Kaymaz , Turkey
Vahid Kayvanfar , Qatar
Krzysztof Kecik , Poland
Mohamed Khader , Egypt
Chaudry M. Khalique , South Africa
Mukhtaj Khan , Pakistan
Shahid Khan , Pakistan
Nam-Il Kim, Republic of Korea
Philipp V. Kiryukhantsev-Korneev ,
Russia
P.V.V Kishore , India
Jan Koci , Czech Republic
Ioannis Kostavelis , Greece
Sotiris B. Kotsiantis , Greece
Frederic Kratz , France
Vamsi Krishna , India
Edyta Kucharska, Poland
Krzysztof S. Kulpa , Poland
Kamal Kumar, India
Prof. Ashwani Kumar , India
Michal Kunicki , Poland
Cedrick A. K. Kwuimy , USA
Kyandoghere Kyamakya, Austria
Ivan Kyrchei , Ukraine
Márcio J. Lacerda , Brazil
Eduardo Lalla , The Netherlands
Giovanni Lancioni , Italy
Jaroslaw Latalski , Poland
Hervé Laurent , France
Agostino Lauria , Italy
Aimé Lay-Ekuakille , Italy
Nicolas J. Leconte , France
Kun-Chou Lee , Taiwan
Dimitri Lefebvre , France
Eric Lefevre , France
Marek Lefik, Poland
Yaguo Lei , China
Kauko Leiviskä , Finland
Ervin Lenzi , Brazil
ChenFeng Li , China
Jian Li , USA
Jun Li , China
Yueyang Li , China
Zhao Li , China































Zhen Li , China
En-Qiang Lin, USA
Jian Lin , China
Qibin Lin, China
Yao-Jin Lin, China
Zhiyun Lin , China
Bin Liu , China
Bo Liu , China
Heng Liu , China
Jianxu Liu , Thailand
Lei Liu , China
Sixin Liu , China
Wanquan Liu , China
Yu Liu , China
Yuanchang Liu , United Kingdom
Bonifacio Llamazares , Spain
Alessandro Lo Schiavo , Italy
Jean Jacques Loiseau , France
Francesco Lolli , Italy
Paolo Lonetti , Italy
António M. Lopes , Portugal
Sebastian López, Spain
Luis M. López-Ochoa , Spain
Vassilios C. Loukopoulos, Greece
Gabriele Maria Lozito , Italy
Zhiguo Luo , China
Gabriel Luque , Spain
Valentin Lychagin, Norway
YUE MEI, China
Junwei Ma , China
Xuanlong Ma , China
Antonio Madeo , Italy
Alessandro Magnani , Belgium
Toqeer Mahmood , Pakistan
Fazal M. Mahomed , South Africa
Arunava Majumder , India
Sarfranz Nawaz Malik, Pakistan
Paolo Manfredi , Italy
Adnan Maqsood , Pakistan
Muazzam Maqsood, Pakistan
Giuseppe Carlo Marano , Italy
Damijan Markovic, France
Filipe J. Marques , Portugal
Luca Martinelli , Italy
Denizar Cruz Martins, Brazil

Francisco J. Martos , Spain
Elio Masciari , Italy
Paolo Massioni , France
Alessandro Mauro , Italy
Jonathan Mayo-Maldonado , Mexico
Pier Luigi Mazzeo , Italy
Laura Mazzola, Italy
Driss Mehdi , France
Zahid Mehmood , Pakistan
Roderick Melnik , Canada
Xiangyu Meng , USA
Jose Merodio , Spain
Alessio Merola , Italy
Mahmoud Mesbah , Iran
Luciano Mescia , Italy
Laurent Mevel , France
Constantine Michailides , Cyprus
Mariusz Michta , Poland
Prankul Middha, Norway
Aki Mikkola , Finland
Giovanni Minafò , Italy
Edmondo Minisci , United Kingdom
Hiroyuki Mino , Japan
Dimitrios Mitsotakis , New Zealand
Ardashir Mohammadzadeh , Iran
Francisco J. Montáns , Spain
Francesco Montefusco , Italy
Gisele Mophou , France
Rafael Morales , Spain
Marco Morandini , Italy
Javier Moreno-Valenzuela , Mexico
Simone Morganti , Italy
Caroline Mota , Brazil
Aziz Moukrim , France
Shen Mouquan , China
Dimitris Mourtzis , Greece
Emiliano Mucchi , Italy
Taseer Muhammad, Saudi Arabia
Ghulam Muhiuddin, Saudi Arabia
Amitava Mukherjee , India
Josefa Mula , Spain
Jose J. Muñoz , Spain
Giuseppe Muscolino, Italy
Marco Mussetta , Italy

Hariharan Muthusamy, India
Alessandro Naddeo , Italy
Raj Nandkeolyar, India
Keivan Navaie , United Kingdom
Soumya Nayak, India
Adrian Neagu , USA
Erivelton Geraldo Nepomuceno , Brazil
AMA Neves, Portugal
Ha Quang Thinh Ngo , Vietnam
Nhon Nguyen-Thanh, Singapore
Papakostas Nikolaos , Ireland
Jelena Nikolic , Serbia
Tatsushi Nishi, Japan
Shanzhou Niu , China
Ben T. Nohara , Japan
Mohammed Nouari , France
Mustapha Nourelfath, Canada
Kazem Nouri , Iran
Ciro Núñez-Gutiérrez , Mexico
Włodzimierz Ogryczak, Poland
Roger Ohayon, France
Krzysztof Okarma , Poland
Mitsuhiro Okayasu, Japan
Murat Olgun , Turkey
Diego Oliva, Mexico
Alberto Olivares , Spain
Enrique Onieva , Spain
Calogero Orlando , Italy
Susana Ortega-Cisneros , Mexico
Sergio Ortobelli, Italy
Naohisa Otsuka , Japan
Sid Ahmed Ould Ahmed Mahmoud , Saudi Arabia
Taoreed Owolabi , Nigeria
EUGENIA PETROPOULOU , Greece
Arturo Pagano, Italy
Madhumangal Pal, India
Pasquale Palumbo , Italy
Dragan Pamučar, Serbia
Weifeng Pan , China
Chandan Pandey, India
Rui Pang, United Kingdom
Jürgen Pannek , Germany
Elena Panteley, France
Achille Paolone, Italy

George A. Papakostas , Greece
Xosé M. Pardo , Spain
You-Jin Park, Taiwan
Manuel Pastor, Spain
Pubudu N. Pathirana , Australia
Surajit Kumar Paul , India
Luis Payá , Spain
Igor Pažanin , Croatia
Libor Pekař , Czech Republic
Francesco Pellicano , Italy
Marcello Pellicciari , Italy
Jian Peng , China
Mingshu Peng, China
Xiang Peng , China
Xindong Peng, China
Yuxing Peng, China
Marzio Pennisi , Italy
Maria Patrizia Pera , Italy
Matjaz Perc , Slovenia
A. M. Bastos Pereira , Portugal
Wesley Peres, Brazil
F. Javier Pérez-Pinal , Mexico
Michele Perrella, Italy
Francesco Pesavento , Italy
Francesco Petrini , Italy
Hoang Vu Phan, Republic of Korea
Lukasz Pieczonka , Poland
Dario Piga , Switzerland
Marco Pizzarelli , Italy
Javier Plaza , Spain
Goutam Pohit , India
Dragan Poljak , Croatia
Jorge Pomares , Spain
Hiram Ponce , Mexico
Sébastien Poncet , Canada
Volodymyr Ponomaryov , Mexico
Jean-Christophe Ponsart , France
Mauro Pontani , Italy
Sivakumar Poruran, India
Francesc Pozo , Spain
Aditya Rio Prabowo , Indonesia
Anchasa Pramuanjaroenkij , Thailand
Leonardo Primavera , Italy
B Rajanarayan Prusty, India

Krzysztof Puszynski , Poland
Chuan Qin , China
Dongdong Qin, China
Jianlong Qiu , China
Giuseppe Quaranta , Italy
DR. RITU RAJ , India
Vitomir Racic , Italy
Carlo Rainieri , Italy
Kumbakonam Ramamani Rajagopal, USA
Ali Ramazani , USA
Angel Manuel Ramos , Spain
Higinio Ramos , Spain
Muhammad Afzal Rana , Pakistan
Muhammad Rashid, Saudi Arabia
Manoj Rastogi, India
Alessandro Rasulo , Italy
S.S. Ravindran , USA
Abdolrahman Razani , Iran
Alessandro Reali , Italy
Jose A. Reinoso , Spain
Oscar Reinoso , Spain
Haijun Ren , China
Carlo Renno , Italy
Fabrizio Renno , Italy
Shahram Rezapour , Iran
Ricardo Rianza , Spain
Francesco Riganti-Fulginei , Italy
Gerasimos Rigatos , Greece
Francesco Ripamonti , Italy
Jorge Rivera , Mexico
Eugenio Roanes-Lozano , Spain
Ana Maria A. C. Rocha , Portugal
Luigi Rodino , Italy
Francisco Rodríguez , Spain
Rosana Rodríguez López, Spain
Francisco Rossomando , Argentina
Jose de Jesus Rubio , Mexico
Weiguo Rui , China
Rubén Ruiz , Spain
Ivan D. Rukhlenko , Australia
Dr. Eswaramoorthi S. , India
Weichao SHI , United Kingdom
Chaman Lal Sabharwal , USA
Andrés Sáez , Spain

Bekir Sahin, Turkey
Laxminarayan Sahoo , India
John S. Sakellariou , Greece
Michael Sakellariou , Greece
Salvatore Salamone, USA
Jose Vicente Salcedo , Spain
Alejandro Salcido , Mexico
Alejandro Salcido, Mexico
Nunzio Salerno , Italy
Rohit Salgotra , India
Miguel A. Salido , Spain
Sinan Salih , Iraq
Alessandro Salvini , Italy
Abdus Samad , India
Sovan Samanta, India
Nikolaos Samaras , Greece
Ramon Sancibrian , Spain
Giuseppe Sanfilippo , Italy
Omar-Jacobo Santos, Mexico
J Santos-Reyes , Mexico
José A. Sanz-Herrera , Spain
Musavarah Sarwar, Pakistan
Shahzad Sarwar, Saudi Arabia
Marcelo A. Savi , Brazil
Andrey V. Savkin, Australia
Tadeusz Sawik , Poland
Roberta Sburlati, Italy
Gustavo Scaglia , Argentina
Thomas Schuster , Germany
Hamid M. Sedighi , Iran
Mijanur Rahaman Seikh, India
Tapan Senapati , China
Lotfi Senhadji , France
Junwon Seo, USA
Michele Serpilli, Italy
Silvestar Šesnić , Croatia
Gerardo Severino, Italy
Ruben Sevilla , United Kingdom
Stefano Sfarra , Italy
Dr. Ismail Shah , Pakistan
Leonid Shaikhet , Israel
Vimal Shanmuganathan , India
Prayas Sharma, India
Bo Shen , Germany
Hang Shen, China

Xin Pu Shen, China
Dimitri O. Shepelsky, Ukraine
Jian Shi , China
Amin Shokrollahi, Australia
Suzanne M. Shontz , USA
Babak Shotorban , USA
Zhan Shu , Canada
Angelo Sifaleras , Greece
Nuno Simões , Portugal
Mehakpreet Singh , Ireland
Piyush Pratap Singh , India
Rajiv Singh, India
Seralathan Sivamani , India
S. Sivasankaran , Malaysia
Christos H. Skiadas, Greece
Konstantina Skouri , Greece
Neale R. Smith , Mexico
Bogdan Smolka, Poland
Delfim Soares Jr. , Brazil
Alba Sofi , Italy
Francesco Soldovieri , Italy
Raffaele Solimene , Italy
Yang Song , Norway
Jussi Sopanen , Finland
Marco Spadini , Italy
Paolo Spagnolo , Italy
Ruben Specogna , Italy
Vasilios Spitas , Greece
Ivanka Stamova , USA
Rafał Stanisławski , Poland
Miladin Stefanović , Serbia
Salvatore Strano , Italy
Yakov Strelniker, Israel
Kangkang Sun , China
Qiuqin Sun , China
Shuaishuai Sun, Australia
Yanchao Sun , China
Zong-Yao Sun , China
Kumarasamy Suresh , India
Sergey A. Suslov , Australia
D.L. Suthar, Ethiopia
D.L. Suthar , Ethiopia
Andrzej Swierniak, Poland
Andras Szekrenyes , Hungary
Kumar K. Tamma, USA






Yong (Aaron) Tan, United Kingdom
Marco Antonio Taneco-Hernández , Mexico
Lu Tang , China
Tianyou Tao, China
Hafez Tari , USA
Alessandro Tasora , Italy
Sergio Teggi , Italy
Adriana del Carmen Téllez-Anguiano , Mexico
Ana C. Teodoro , Portugal
Efstathios E. Theotokoglou , Greece
Jing-Feng Tian, China
Alexander Timokha , Norway
Stefania Tomasiello , Italy
Gisella Tomasini , Italy
Isabella Torricollo , Italy
Francesco Tornabene , Italy
Mariano Torrisi , Italy
Thang nguyen Trung, Vietnam
George Tsiatas , Greece
Le Anh Tuan , Vietnam
Nerio Tullini , Italy
Emilio Turco , Italy
Ilhan Tuzcu , USA
Efstratios Tzirtzilakis , Greece
FRANCISCO UREÑA , Spain
Filippo Ubertini , Italy
Mohammad Uddin , Australia
Mohammad Safi Ullah , Bangladesh
Serdar Ulubeyli , Turkey
Mati Ur Rahman , Pakistan
Panayiotis Vafeas , Greece
Giuseppe Vairo , Italy
Jesus Valdez-Resendiz , Mexico
Eusebio Valero, Spain
Stefano Valvano , Italy
Carlos-Renato Vázquez , Mexico
Martin Velasco Villa , Mexico
Franck J. Vernerey, USA
Georgios Veronis , USA
Vincenzo Vespri , Italy
Renato Vidoni , Italy
Venkatesh Vijayaraghavan, Australia

Anna Vila, Spain
Francisco R. Villatoro , Spain
Francesca Vipiana , Italy
Stanislav Vitek , Czech Republic
Jan Vorel , Czech Republic
Michael Vynnycky , Sweden
Mohammad W. Alomari, Jordan
Roman Wan-Wendner , Austria
Bingchang Wang, China
C. H. Wang , Taiwan
Dagang Wang, China
Guoqiang Wang , China
Huaiyu Wang, China
Hui Wang , China
J.G. Wang, China
Ji Wang , China
Kang-Jia Wang , China
Lei Wang , China
Qiang Wang, China
Qingling Wang , China
Weiwei Wang , China
Xinyu Wang , China
Yong Wang , China
Yung-Chung Wang , Taiwan
Zhenbo Wang , USA
Zhibo Wang, China
Waldemar T. Wójcik, Poland
Chi Wu , Australia
Qihong Wu, China
Yuqiang Wu, China
Zhibin Wu , China
Zhizheng Wu , China
Michalis Xenos , Greece
Hao Xiao , China
Xiao Ping Xie , China
Qingzheng Xu , China
Binghan Xue , China
Yi Xue , China
Joseph J. Yame , France
Chuanliang Yan , China
Xinggang Yan , United Kingdom
Hongtai Yang , China
Jixiang Yang , China
Mijia Yang, USA
Ray-Yeng Yang, Taiwan







Zaoli Yang , China
Jun Ye , China
Min Ye , China
Luis J. Yebra , Spain
Peng-Yeng Yin , Taiwan
Muhammad Haroon Yousaf , Pakistan
Yuan Yuan, United Kingdom
Qin Yuming, China
Elena Zaitseva , Slovakia
Arkadiusz Zak , Poland
Mohammad Zakwan , India
Ernesto Zambrano-Serrano , Mexico
Francesco Zammori , Italy
Jessica Zangari , Italy
Rafal Zdunek , Poland
Ibrahim Zeid, USA
Nianyin Zeng , China
Junyong Zhai , China
Hao Zhang , China
Haopeng Zhang , USA
Jian Zhang , China
Kai Zhang, China
Lingfan Zhang , China
Mingjie Zhang , Norway
Qian Zhang , China
Tianwei Zhang , China
Tongqian Zhang , China
Wenyu Zhang , China
Xianming Zhang , Australia
Xuping Zhang , Denmark
Yinyan Zhang, China
Yifan Zhao , United Kingdom
Debao Zhou, USA
Heng Zhou , China
Jian G. Zhou , United Kingdom
Junyong Zhou , China
Xueqian Zhou , United Kingdom
Zhe Zhou , China
Wu-Le Zhu, China
Gaetano Zizzo , Italy
Mingcheng Zuo, China

Contents

Magnetohydrodynamic Thin Film Flow through a Porous Stretching Sheet with the Impact of Thermal Radiation and Viscous Dissipation

Ziad Khan , Muhammad Jawad , Ebenezer Bonyah , Naveed Khan , and Rashid Jan 
Research Article (10 pages), Article ID 1086847, Volume 2022 (2022)

Inverse Family of Numerical Methods for Approximating All Simple and Roots with Multiplicity of Nonlinear Polynomial Equations with Engineering Applications

Mudassir Shams , Naila Rafiq , Nasreen Kausar , Shams Forruque Ahmed , Nazir Ahmad Mir ,
and Suvash Chandra Saha 
Research Article (9 pages), Article ID 3124615, Volume 2021 (2021)


T-Shaped Control Plate Effect on Flow past a Square Cylinder at Low Reynolds Numbers

Maryam Shahab, Shams Ul-Islam , and Ghazala Nazeer
Research Article (19 pages), Article ID 7562460, Volume 2021 (2021)



Numerical Computation of MHD Thermal Flow of Cross Model over an Elliptic Cylinder: Reduction of Forces via Thickness Ratio

Afraz Hussain Majeed , Rashid Mahmood , Waqas Sarwar Abbasi, and K. Usman
Research Article (13 pages), Article ID 2550440, Volume 2021 (2021)

Flow Characteristics and Fluid Forces Reduction of Flow Past Two Tandem Cylinders in Presence of Attached Splitter Plate

Ali Ahmed , Abdul Wahid, Raheela Manzoor, Noreen Nadeem, Naqib Ullah, and Shazia Kalsoom
Research Article (16 pages), Article ID 4305731, Volume 2021 (2021)

Topological Characteristics of Obstacles and Nonlinear Rheological Fluid Flow in Presence of Insulated Fins: A Fluid Force Reduction Study

Afraz Hussain Majeed , Fahd Jarad , Rashid Mahmood , and Imran Saddique
Research Article (15 pages), Article ID 9199512, Volume 2021 (2021)

Numerical Investigation of Fluid Flow past Four Cylinders at Low Reynolds Numbers

Shafee Ahmad and Shams Ul-Islam 
Research Article (24 pages), Article ID 1127324, Volume 2021 (2021)

Research Article

Magnetohydrodynamic Thin Film Flow through a Porous Stretching Sheet with the Impact of Thermal Radiation and Viscous Dissipation

Ziad Khan ¹, Muhammad Jawad ¹, Ebenezer Bonyah ², Naveed Khan ¹,
and Rashid Jan ¹

¹Department of Mathematics, University of Swabi, Swabi 23561, Khyber Pakhtunkhwa, Pakistan

²Department of Mathematics Education, Akenen Appiah Menka University of Skills Training and Entrepreneurial Development, Kumasi, Ghana

Correspondence should be addressed to Ebenezer Bonyah; ebbonyah@gmail.com

Received 16 September 2021; Revised 27 December 2021; Accepted 31 December 2021; Published 19 January 2022

Academic Editor: Shams -ul-Islam

Copyright © 2022 Ziad Khan et al. This is an open access article distributed under the Creative Commons Attribution License, which permits unrestricted use, distribution, and reproduction in any medium, provided the original work is properly cited.

In this paper, the Darcy–Forchheimer laminar thin film flow with MHD and heat transfer on an unsteady horizontal stretched surface is investigated. The impact of thermal radiation and viscous dissipation is also considered for thin film flow. The analysis of heat source with thermal radiation in a boundary layer flow can play a great role in manufacturing engineering procedures such as the production of electric power, solar energy modernization, and astrophysical flow. By using similarity transformation, the system of PDEs is converted to ODEs. Then HAM is applied for the solution of the problem. Moreover, the velocity and temperature profile for various embedded variables are discussed through graphs while the numerical solution of concerned physical quantities such as skin friction and Nusselt number are discussed through tables. The analysis shows that velocity profile is reducing function of M , K_1 , S , and F_1 . The temperature profile is an increasing function S and Ec while a reducing function of Pr and R . The overall behavior of the proposed system is highlighted analytically.

1. Introduction

Heat source, fluid flow within liquid film due to an unsteady stretching sheet, plays a very crucial role in many utilization engineering processes and technologies; for example, polymer extrusion, continuous casting, manufacturing plastic film, tinning of copper wires, crystal growth, a polymer sheet, artificial fiber, and wire and fiber coating. In addition to these, many production processes involve heat transmission in various forms such as cooling of a machine tool, pasteurization of food, heat treatment of a part in industrial furnaces, or the temperature control for initiating a chemical reaction. Heat transfer is accomplished in most of these applications using heat transfer instruments such as heat swaps, desiccation, condensers, boilers, and heat sinks. Mathematics plays an important role in different areas of research and has effective outcomes [1–4]. The importance

of mathematical tools in the investigation of fluid flow cannot be ignored. Mathematical tools help the researchers to visualize the dynamical behavior of a system and to conceptualize the importance of the input factors of a system. Numerous researchers workout to understand the flow of fluid with different assumptions and in different circumstances. The nanofluid flow over a stretching surface has been originally considered by Wang [5]; they also reduce unstable Navier–Stokes equations using similarity transformation in nonlinear ODEs, which are then calculated by multiple shooting methods. The solutions based on the analysis of a liquid thin film are obtained by Wang [6], who also validated the correctness of the homotopy analysis technique. Sufian et al [7] study the impact of heat source and fluid flow over a stretch cylinder as a function of time. Zhang et al. [8] demonstrated mass diffusion and solutal Marangoni impact on heat transmission and fluid flow in a

film toward a stretched sheet. Kalyani et al. [9] investigated the effects of Lorentz force, heat generation, and mass transfer of a Casson incompressible fluid flowing on a surface. They also discussed the impact of thermal radiation on the mass and heat transfer property of flow in a Casson liquid film [10]. The unstable mixed convection flow of the stretch sheet is considered by Devi et al. [11]. Jhankal et al. [12] studied heat source, the forced convective flow of an incompressible fluid past plate inserted in a Darcy–Forchheimer porous medium of the two-dimensional boundary layer MHD flow. The effects of thermal radiation in an upper-convective Maxwell thin film, unsteady stretched sheet inserted in a porous medium are conceptualized by Waheed [13]. Ahmad et al. [14] illustrated a solution for the heat source, MHD flow toward an exponentially stretched surface in the absence of radiation impacts and Darcy’s resistance. On the basis of boundary layer hypothesis and similarity transformation, Sparrow and Gregg [15] were the first to examine the Laminar-film condensing difficulty on a vertical plate. Dandapat and Ray explored the flow of a thin boundary layer across a spinning horizontal disc [16, 17]. Nath and Kumari [18] investigated the time-dependent MHD problem of a fluid dispersed by a spinning incompressible disc. Magnetohydrodynamic and heat flow toward a stretch sheet has been studied by Mohd Nasir et al. [19] in which we consider both the stretching and shrinking cases. Zaidi et al. [20] studied the impacts of thermal radiation, heat creation, and induced magnetic field on hydromagnetic free convection flow of pair stress fluid in an isoflux-isothermal vertical channel. Kishore et al. [21] studied the influence of thermal radiation and viscous dissipation on MHD mass, heat transfer flow past an oscillating vertical plate inserted in a porous medium with unknown surface situations. Elbashbeshy et al. [22] studied the influence of thermal radiation and heat transmission on an unstable extended sheet inserted in a porous medium in the existence of a heat sink. Thermal radioactivity and heat transfer of Sisko fluid on an uneven stretched sheet with a constant magnetic field were investigated by Khan et al. [23]. The authors of [24] discussed mass transfer and unstable boundary layer MHD flow of a UCM fluid in the absence of higher-level chemical reaction. The authors of [25] considered heat transfer, MHD flow in a liquid film over an unsteady stretched sheet. Numerical solution of MHD boundary layer flow of a nanofluid over a moving sheet in the absence of thermal radiation has been carried out by Shateyi and Prakash [26]. The MHD laminar boundary layer flow with heat and mass transport of an electrically conducting water-based nanofluid across a nonlinear stretching sheet with viscous dissipation is studied by Mabood and Khan in [27]. It has been noticed that further investigation is needed to conceptualize the impact of heat transfer, thermal radiation in a fluid film of

an unsteady stretching surface inserted in a porous medium in the absence of viscous dissipation and magnetic field impact. Therefore, in the current work, we opt to investigate the impact of heat transfer, thermal radiation in a fluid film of an unsteady stretching surface inserted in a porous medium in the absence of viscous dissipation and magnetic field impact.

The aim of the present work is to study Darcy–Forchheimer’s laminar thin film flow on an unsteady horizontal stretched surface. The laminar thin-film flow is investigated with the impact of MHD, thermal radiation, and viscous dissipation. The HAM is used to obtain analytic approximations for the solution of nonlinear ODEs. The comparison of HAM and numerical solutions are displayed. The results have been illustrated in graphical or tabular forms followed by a brief discussion and physical interpretations.

2. Mathematical Expressions of the Problem

2.1. Basic Equations and Boundary Constraints. Assume a thin liquid film extending on a stretched surface with a laminar unsteady flow which arises from a narrow slit where x -coordinates are parallel to the slit and y -coordinates are perpendicular to the sheet as exhibited in Figure 1. Along x -axis, the stretching sheet is stretched by two equal and opposite forces. Further, the latent heat effect is neglected due to evaporation by assuming the liquid to be nonvolatile. Moreover, due to a relatively thin film, the buoyancy force is also neglected.

The continuous sheet velocity is given by $U(x, t) = cx/(1 - \gamma t)$ [25], where c and γ are constants having per-time dimension. The term $cx^2/(\nu(1 - \gamma t))$ is localized Reynolds number on the sheet velocity U , and the stretched rate $c/(1 - \gamma t)$ reduces with time as $0 \leq \gamma < 1$. The nomenclature of this research work has been presented.

The stretched sheet’s surface temperature T_s is determined as [25]

$$T_s(x, t) = T_0 - T_{ref} \left[\frac{cx^2}{2\nu} \right] (1 - \gamma t)^{-3/2}, \quad (1)$$

where T_0 is the slit temperature and T_{ref} is the temperature with reference, which might be a constant temperature with a reference or a constant temperature difference. In this work, T_{ref} will be interpreted as $0 \leq T_{ref} \leq T_0$. Normally, a transverse magnetic field is applied to the extended surface, which is believed to be changeable in nature and chosen as

$$B(x, t) = B_0 (1 - \gamma t)^{-1/2}. \quad (2)$$

The temperature and velocity influence of a thin film obeys the following governing time-dependent equations with the boundary conditions [25].

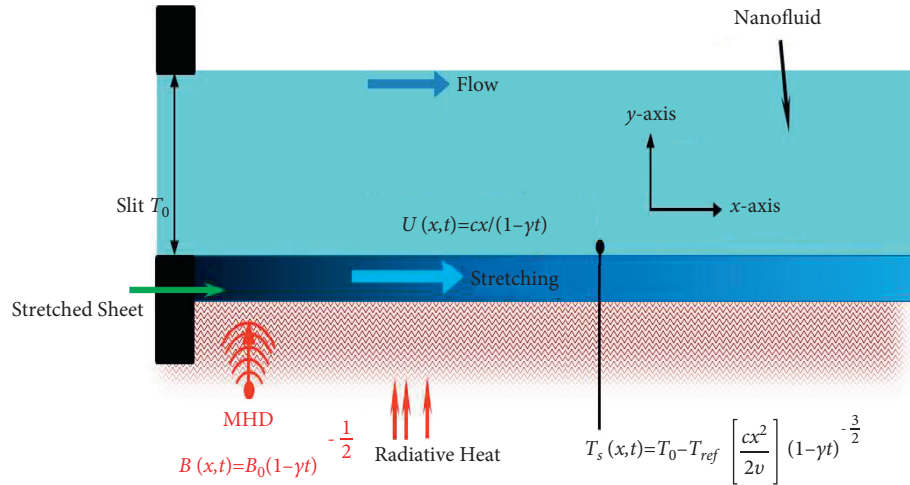


FIGURE 1: Geometric representation of thin film to illustrate its structure.

$$\frac{\partial u}{\partial x} + \frac{\partial v}{\partial y} = 0, \quad (3)$$

$$\frac{\partial u}{\partial t} + u \frac{\partial u}{\partial x} + v \frac{\partial u}{\partial y} = \nu \frac{\partial^2 u}{\partial y^2} - \frac{\sigma B_0^2}{\rho} u - \frac{\nu \varepsilon^2}{k} u - F u^2, \quad (4)$$

$$\frac{\partial T}{\partial t} + u \frac{\partial T}{\partial x} + v \frac{\partial T}{\partial y} = \frac{k}{\rho C_p} \frac{\partial^2 T}{\partial y^2} + \frac{\mu}{\rho C_p} \left(\frac{\partial u}{\partial y} \right)^2 + \frac{1}{\rho C_p} \frac{\partial q_r}{\partial y}, \quad (5)$$

$$\text{when } y = 0: \quad u = U, \quad v = 0, \quad T = T_s \quad \text{and} \quad \text{when } y = h: \quad \frac{\partial u}{\partial y} = \frac{\partial T}{\partial y} = 0, \quad v = \frac{dh}{dt}, \quad (6)$$

where u and v denote the velocity terms in the directions of x -axis and y -axis, respectively, μ is the dynamic viscosity, B_0 is the magnetic field, ρ is the density, T is the temperature, k is the thermal diffusivity, ν is the kinematic viscosity, t is the time, σ is the electrical conductivity, and h is the uniform thickness of the film sheet. In the x - and y -directions, the two terms of equation (3) reflect the net outflow (outflow minus inflow) of mass, for an unsteady flow the sum of these terms must be zero. The net rate at which x -momentum leaves due to fluid motion across its limits is signified by the 2nd and 3rd components on the left side of equation (4) while the net force owing to viscous shear stresses is shown off by the 1st component on the right side. The net rate at which thermal energy escapes due to fluid motion is represented by the 2nd and 3rd terms on the left side of equation (5). The 1st component on the right side of equation (5) shows the net input of thermal energy owing to y -direction, while the 2nd term represents the viscous dissipation that remains.

In this case, when the influence of surface tension is insignificant at a distance of $y = h$ from the surface, shear stresses operating in planes parallel to the fluid velocity are defined as

$$\tau = \mu \left(\frac{\partial u}{\partial y} \right), \quad (7)$$

where μ is a fluid property and is known as the dynamic viscosity and $\partial u / \partial y$ is the rate of shear stress.

The flow of heat at $y = h$ is defined by

$$q = -k \left(\frac{\partial T}{\partial y} \right). \quad (8)$$

In the above equation, the constant k is called thermal conductivity. Equation (8) tells us that if temperature decreases with y then q will be positive and it will flow in the y -direction, if temperature increases with y then q will be negative and it will flow opposite in the y -direction.

2.2. Similarity Transformations. Here, we use the stream function $\psi(x, y, t)$ to specify the velocity terms:

$$u = \frac{\partial \psi}{\partial y} = \left(\frac{bx}{1-\gamma t} \right) f'(\eta), \quad (9)$$

$$v = -\frac{\partial \psi}{\partial x} = -\left(\frac{\nu b}{1-\gamma t} \right)^{\frac{1}{2}} f(\eta), \quad (10)$$

satisfying continuity equation (3). New dependent and independent variables, f , θ , and η are, respectively, introduced as

$$f(\eta) = \frac{\psi(x, y, t)}{(\nu b/1 - \gamma t)^{1/2} x}, \quad \theta(\eta) = \frac{T_0 - T(x, y, t)}{T_{\text{ref}}(bx^2/2\nu(1 - \gamma t)^{-3/2})}, \quad \eta = \left(\frac{b}{\nu(1 - \gamma t)}\right)^{1/2} y. \quad (11)$$

Substitute the similarity transformation equations (9)–(11) into equations (4) and (5) to obtain a set of non-linear ODEs in the form of

$$f''' - (M + K_1)f' + f f'' - S\left(f' + \frac{\eta}{2}f''\right) - (1 + F)_1 f'^2 = 0, \quad (12)$$

$$\left(1 + \frac{4}{3}R\right)\theta'' + EcPr f''^2 - Pr\left[\frac{S}{2}(3\theta - \eta\theta') + 2\theta f' - \theta' f\right] = 0. \quad (13)$$

Following are the corresponding boundary constraints of the differential equations:

$$f(0) = 0, f'(0) = 1, \theta(0) = 1, f(\beta) = \frac{S\beta}{2}, \theta'(\beta) = 0, f''(\beta) = 0, \quad (14)$$

where the prime denotes derivative in terms of η , $S = \gamma/c$ is the unsteadiness parameter, $M = \sigma B^2/\rho c(1 - \gamma t)$ is the magnetic parameter, $K_1 = \nu \varepsilon^2/kc(1 - \gamma t)$ is the porosity parameter, $Ec = U^2/C_p(T_s - T_0)$ is the Eckert number, $Pr = \mu C_p/k$ is the Prandtl number, and R is thermal radiation. Despite the fact that the dimensionless film thickness β is constant and only relies on S , the current film thickness h is only depending on time t . So the free surface β denotes the value of similarity variable by η such that

$$\beta = \left(\frac{c}{\nu(1 - \gamma t)}\right)^{1/2} h. \quad (15)$$

By differentiating with respect to t , we have

$$\frac{dh}{dt} = -\frac{\gamma\beta}{2} \left(\frac{c}{\nu}\right)^{-1/2} (1 - \gamma t)^{-1/2}. \quad (16)$$

2.3. Physical Interest of the Problem. In this subsection, we calculated the skin friction coefficient C_f and local Nusselt number Nu_x as

$$C_f = \frac{-2\tau_s}{\rho U^2}. \quad (17)$$

And

$$Nu_x = \frac{x}{kT_{\text{ref}}} (q_s - q_r). \quad (18)$$

From equations (7) and (8), at the surface $y=0$, the surface shear stress and surface heat flux are defined as

$$\tau_s = \mu \left(\frac{\partial u}{\partial y}\right)_{y=0}, \quad (19)$$

$$q_s = -k \left(\frac{\partial T}{\partial y}\right)_{y=0}. \quad (20)$$

And the Rosseland estimation q_r is given by [23]

$$q_r = -\frac{16\sigma^* T_0^3}{3k^*} \left(\frac{\partial T}{\partial y}\right)_{y=0}, \quad (21)$$

where σ^* is the Stefan–Boltzman constant and has the numerical value

$$\sigma^* = 5.670 \times 10^{-8} \text{ Wm}^{-2} \text{ K}^4. \quad (22)$$

Inserting equations (19)–(21) into equations (17) and (18) to obtain C_f and Nu_x in terms of Re_x ,

$$C_f = -2Re_x^{-1/2} f''(0), Nu_x = \left(1 + \frac{4}{3}R\right) \frac{Re_x^{3/2}}{2} (1 - \gamma t)^{-1/2} \theta'(0), \quad (23)$$

where $Re_x = cx^2/\nu(1 - \gamma t)$ is the local Reynolds number and $R = 4\sigma^* T_0^3/kk^*$ is the radiation parameter.

3. Solution by HAM

HAM is applied for the solutions of equations (12) and (13) with boundary constraints (12). Mathematica is used for this purpose. The modeled equations are solved by HAM, the basic derivation is identified as

$$L_{\hat{\theta}}(\hat{\theta}) = \hat{\theta}'' - \hat{\theta}, L_{\hat{f}}(\hat{f}) = \hat{f}''' - \hat{f}'. \quad (24) \quad L_{\hat{f}}(\gamma_1 + \gamma_2 e^{-\eta} + \gamma_3 e^{\eta}) = 0, L_{\hat{\theta}}(\gamma_4 e^{-\eta} + \gamma_5 e^{\eta}) = 0. \quad (25)$$

Linear operators $L_{\hat{f}}$, and $L_{\hat{\theta}}$ are specified by

The nonlinear operators $N_{\hat{f}}$ and $N_{\hat{\theta}}$ are defined as follows:

$$N_{\hat{f}}[\hat{f}(\eta; \zeta)] = \hat{f}_{\eta\eta\eta} - S\left(\frac{1}{2}\eta\hat{f}_{\eta\eta} + \hat{f}_{\eta}\right) - (M + K_1)\hat{f}_{\eta} - (1F_1)\hat{f}_{\eta}^2 + \hat{f}\hat{f}_{\eta\eta}$$

$$N_{\hat{\theta}}[\hat{\theta}(\eta; \zeta), \hat{f}(\eta; \zeta)] = \left(1 + \frac{4}{3}R\right)\hat{\theta}_{\eta\eta} + EcPr\hat{f}_{\eta}^2 + Pr\left[\frac{S}{2}(\eta\hat{\theta}_{\eta} + 3\hat{\theta}) + 2\hat{\theta}\hat{f}_{\eta} - \hat{f}\hat{\theta}_{\eta}\right]. \quad (26)$$

The 0th order system for equations (12) and (13) is presented as

while BCs are as follows

$$(1 - \zeta)L_{\hat{f}}[\hat{f}(\eta; \zeta) - \hat{f}_0(\eta)] = p\hat{h}_{\hat{f}}N_{\hat{f}}[\hat{f}(\eta; \zeta)], \quad (27)$$

$$(1 - \zeta)L_{\hat{\theta}}[\hat{\theta}(\eta; \zeta) - \hat{\theta}_0(\eta)] = p\hat{h}_{\hat{\theta}}N_{\hat{\theta}}[\hat{\theta}(\eta; \zeta), \hat{f}(\eta; \zeta)],$$

$$\hat{f}(\eta; \zeta)|_{\eta=0} = 0, \frac{\partial \hat{f}(\eta; \zeta)}{\partial \eta}|_{\eta=0} = 1, \frac{\partial^2 \hat{f}(\eta; \zeta)}{\partial \eta^2}|_{\eta=\beta} = 0, \frac{\partial \hat{\theta}(\eta; \zeta)}{\partial \eta}|_{\eta=\beta} = 0$$

$$\hat{f}(\eta; \zeta)|_{\eta=\beta} = \frac{S\beta}{2}, \hat{\theta}(\eta; \zeta)|_{\eta=0} = 1. \quad (28)$$

$\hat{h}_{\hat{f}}$ and $\hat{h}_{\hat{\theta}}$ are utilized to standard for the solution confluence whereas the embedding constraint is $\zeta \in [0, 1]$; when $\zeta = 0$ and $\zeta = 1$, we get the following:

$$\hat{\theta}(\eta; 1) = \hat{\theta}(\eta), \hat{f}(\eta; 1) = \hat{f}(\eta). \quad (29)$$

Through Taylor's series, $\hat{f}(\eta; \zeta)$ and $\hat{\theta}(\eta; \zeta)$ are expanded for $\zeta = 0$:

$$\hat{\theta}(\eta; \zeta) = \hat{\theta}_0(\eta) + \sum_{n=1}^{\infty} \hat{\theta}_n(\eta)\zeta^n, \hat{f}(\eta; \zeta) = \hat{f}_0(\eta) + \sum_{n=1}^{\infty} \hat{f}_n(\eta)\zeta^n \hat{f}_n(\eta) = \frac{1}{n!} \frac{\partial \hat{f}(\eta; \zeta)}{\partial \eta}|_{p=0}, \hat{\theta}_n(\eta) = \frac{1}{n!} \frac{\partial \hat{\theta}(\eta; \zeta)}{\partial \eta}|_{p=0}, \quad (30)$$

while BCs are

Now

$$\hat{f}'(0) = 1, \hat{f}(0) = 0, \hat{\theta}(0) = 1, \hat{f}''(\beta) = 0, \hat{\theta}(\beta) = 0, \hat{f}(\beta) = \frac{S\beta}{2}. \quad (31)$$

$$\mathfrak{R}_n^{\hat{f}}(\eta) = \hat{f}_{n-1}'' - S\left(\hat{f}'_{n-1} + \frac{1}{2}\eta\hat{f}_{n-1}'\right) - (M + K_1)\hat{f}'_{n-1} - (1 - F_1)\hat{f}_{n-1}^2 + \sum_{j=0}^{w-1} \hat{f}_{w-1-j}\hat{f}_j'$$

$$\mathfrak{R}_n^{\hat{\theta}}(\eta) = \left(1 + \frac{4}{3}R\right)(\hat{\theta}_{n-1}'') + PrEc\hat{f}_{n-1}''^2 + \left[\frac{S}{2}(\eta\hat{\theta}'_{n-1} + 3\hat{\theta}_{n-1}) - 2\sum_{j=0}^{w-1} \hat{\theta}_{w-1-j}\hat{f}_j' - \sum_{j=0}^{w-1} \hat{\theta}'_{w-1-j}\hat{f}_j\right], \quad (32)$$

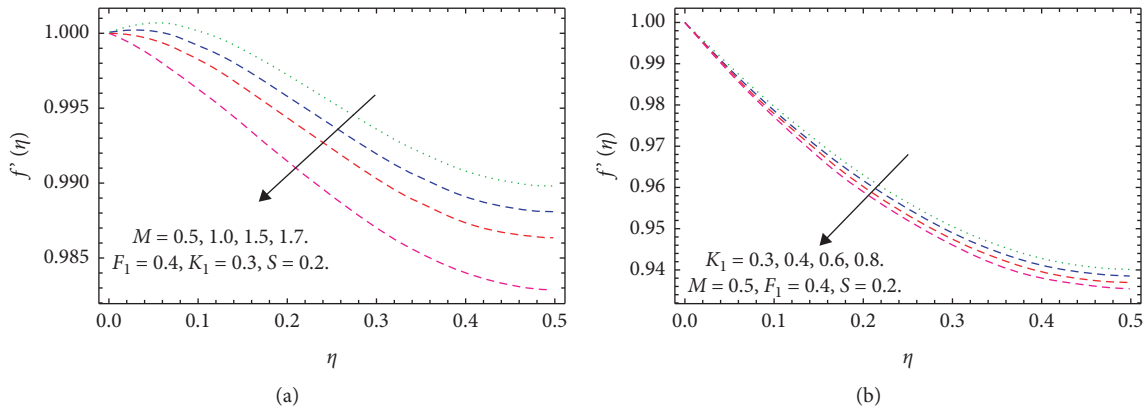


FIGURE 2: (a) Influence of M on $f'(\eta)$. (b) Influence of K_1 on $f'(\eta)$.

while

$$\chi_n = \begin{cases} 0, & \text{if } n \leq 1 \\ 1, & \text{if } n > 1 \end{cases} \quad (33)$$

4. Result and Discussion

The present work analyzes the Darcy–Forchheimer laminar thin film flow with MHD and heat transfer on an unsteady horizontal stretched surface in the absence of viscous dissipation, thermal radiation, and magnetic field of impact. The numerical, as well as analytical solutions, is given. Using similarity transformations, the governing partial differential equations of heat transfer flow are transformed into a nonlinear ordinary differential equation. Geometric representations of the problem are plotted in Figure 1 and the impact of physical parametric quantity on $f'(\eta)$ and $\theta(\eta)$ curves are depicted in Figures 2–5. Figures 2 and 3 show the impact of M , K_1 , S , and F_1 on $f'(\eta)$. The velocity profile reduces when (M) increases, as shown in Figure 2(a). This is due to the reducing nature of the Lorentz forces which reduces the motion of thin-film fluid in the boundary layer and raises its temperature. Figures 2(b) and 3(b) convey that the fluid velocity drop by rising values of (K_1) and (F_1). This is because the increasing hydromagnetic boundary layer increases the strength of porosity. Figure 3(a) illustrates the distribution of velocity gradient in the film decreases by rising values of unsteadiness parameter. As the value of (S) in the system rises, the thickness of the boundary layer declines, preventing the establishment of a transition from laminar to turbulent flow. The effect of embedded parameters Pr , R , S , and Ec on temperature profiles is exhibited in Figures 4 and 5. Figure 4(a) displays the variation of temperature reduces, as the Prandtl number increases. Being the ratio of molecular diffusivity of momentum to the molecular diffusivity of heat, it demonstrates the relative thickness of the momentum boundary layer to the thermal boundary layer. The rise in Prandtl number (Pr) decreases the temperature of the fluid. Increasing the Prandtl number, the thermal conductivity of the fluid decreases and the rate of heat transfer through stretch surface reduces; consequently, the temperature and

thermal boundary layer reduce. Figure 4(b) demonstrates the temperature gradient for different values of (R). As the values of (R) upsurge, the temperature of thin film declines. Physically, when the radiation parameter increases, the Rosseland radiative absorption coefficient k^* declines as defined by the expression for $R = 4\sigma^*T_0^3/kk^*$. Therefore, the heat flux diminishes. That is why the thin film temperature reduces. Figure 5(a) discusses the impact of unsteadiness parameter (S) on temperature profiles. As the values of (S) rise, the thermal boundary layer grows as a result, and the temperature field becomes increment for the nanofluid. Figure 5(b) demonstrates that increases in the value of (Ec) produce more temperature in the thin film. Eckert number is the ratio among kinetic energy and enthalpy, which is detected in the dissipation function of the energy equation, also known as the dissipation parameter. $Ec = 0$ means there is no viscous dissipation. Figure 5(b) displays that the behavior of (Ec) is directly proportional to the temperature, as (Ec) upsurge viscous dissipation rises, i.e., kinetic energy transformed into heat energy which in turn raises the temperature.

The physical significance of embedded parameters are displayed in Table 1 and the numerical values of skin friction and local Nusselt number are displayed in Tables 2 and 3. Table 2 demonstrates that the skin friction coefficient increases by rising various parameters, namely, S , F_1 , M , and K_1 . As these parameters increase, the unsteady parameter, the skin friction enhances due to the exertion of a drag force in the fluid thin film. The Lorentz force is a rising magnetic field that increases the resistive force on fluid movement. That is why more values of (M) enhance C_f . Table 3 lists the numerical values of Nu_x for a few physical variables, that is, Ec , S , Pr , and R . The Eckert number is normally made up of the nanofluid thermal conductivity components, which is used to raise the temperature field, which has the reverse effect on cooling operations, and hence the Nusselt number reduced for high values of (Ec). With an increase in (S), the boundary layer temperature of fluid raises, increasing the heat source of the thin film fluid; as a result, Nu_x boosts. In this table, we may observe that the Nusselt number upsurges as (R) grows, but Nu_x drops as (Pr) grows. Table 4 displays excellent agreement between the HAM and ND solve solution through computer-based package Mathematica 11.1.0.

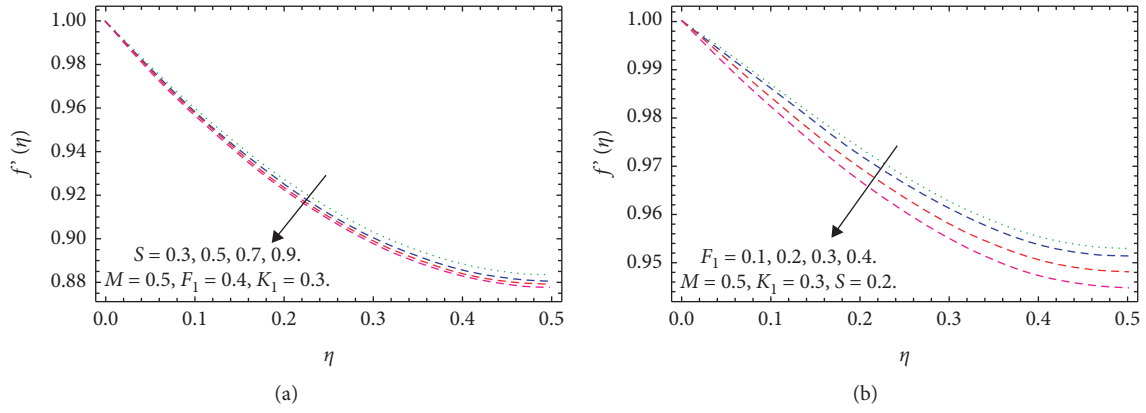


FIGURE 3: (a) Impact of S on $f'(\eta)$. (b) Impact of F_1 on $f'(\eta)$.

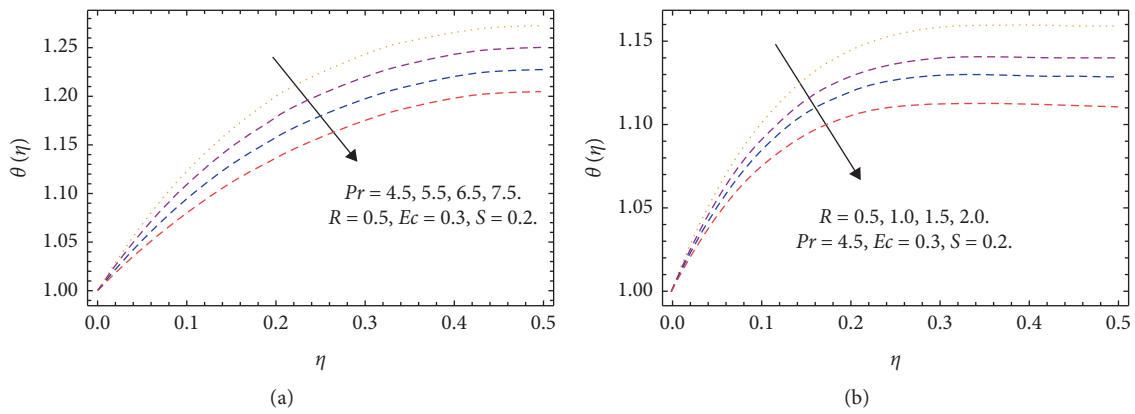


FIGURE 4: (a) Influence of Pr on $\theta(\eta)$. (b) Influence of R on $\theta(\eta)$.

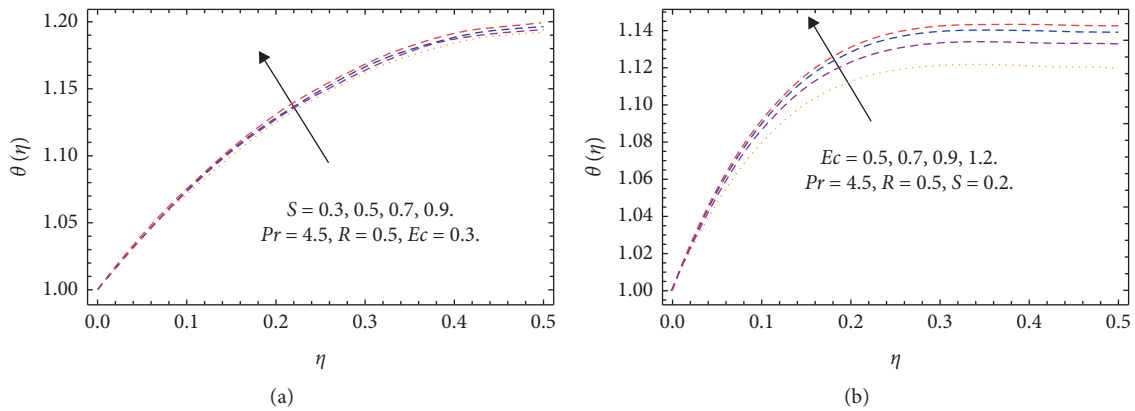


FIGURE 5: (a) Influence of S on $\theta(\eta)$. (b) Influence of Ec on $\theta(\eta)$.

TABLE 1: Dimensionless groups.

Group	Symbol	Definition	Physical interpretation
Local Nusselt number	Nu_x	$(1 + 4/3R)Re_x^{3/2}/2(1 - \gamma t)^{-1/2}\theta'(0)$	Basic dimensionless convective heat transfer coefficient (ratio of convective heat transfer to conduction in a fluid slab of thickness h)
Local Reynolds number	Re_x	$\rho U x / \mu$	The ratio of inertia to viscous forces
Eckert number	Ec	$U^2 / C_p (T_s - T_0)$	The kinetic energy of the flow relative to the boundary layer's enthalpy difference
Prandtl number	Pr	$\mu C_p / k$	The ratio of kinematic viscosity (ν) to thermal conductivity (k)
Skin friction	C_f	$-2\tau_s / \rho U^2$	Dimensionless surface shear stress

TABLE 2: Impact of different physical parameters on $C_f = -2[Re_x]^{-1/2} f''(0)$.

S	F_1	M	K_1	$-2[Re_x]^{-1/2} f''(0)$		
0.3	0.3	0.4	0.3	2.861 450 12		
0.5				2.714 365 43		
0.7				2.015 367 98		
				0.2	1.835 540 23	
				0.3	1.735 701 41	
				0.4	1.491 365 23	
					0.4	1.074 130 36
					0.9	0.786 521 51
					1.0	0.540 378 13
						0.3
			0.4	0.472 765 31		
			0.6	0.190 438 16		

TABLE 3: Influence of various physical parameters over $Nu_x = \delta y / \delta x [(1 + 4/3R)Re_x^{3/2}/2(1 - \gamma t)^{-1/2} \theta'(0)]$.

Ec	S	Pr	R	$[(1 + 4/3R)Re_x^{3/2}/2(1 - \gamma t)^{-1/2} \theta'(0)]$		
0.3	0.2	4.5	0.1	1.142 021 63		
0.5				1.075 243 01		
0.7				0.853 456 25		
				0.2	1.431 804 29	
				0.3	1.674 597 36	
				0.7	1.851 286 25	
					4.5	0.562 621 07
					5.5	0.351 293 28
					6.5	0.168 435 68
						0.1
			0.5	1.637 920 81		
			1.5	2.024 412 56		

TABLE 4: Comparison of HAM and ND solve solution. $S = 0.25, K_1 = 0.5, \beta = 0.2, Pr = 6.4, M = 0.5, Re_x = 3.5, Ec = 0.8$.

η	$f(\eta)$		$f'(\eta)$		$\theta(\eta)$	
	HAM	ND solve	HAM	ND solve	HAM	ND solve
0	0	0	0.045 721 9	0.045 718 8	0.74	0.74
0.5	0.052 695 87	0.052 596 44	0.064 868 65	0.064 868 47	0.606 868 86	0.606 867 99
1.0	0.071 730 28	0.071 729 84	0.134 258 92	0.134 257 89	0.686 235 35	0.686 235 12
1.5	0.162 572 45	0.162 571 96	0.134 575 43	0.134 554 84	0.742 782 08	0.742 781 93
2.0	0.337 234 52	0.337 134 07	0.132 731 74	0.132 721 72	0.776 867 07	0.776 856 89
2.5	0.278 375 42	0.278 374 78	0.126 932 25	0.126 932 18	1.035 200 89	1.035 200 56
3.0	0.351 556 17	0.351 454 08	0.118 621 51	0.118 621 37	1.044 847 06	1.044 846 82
3.5	0.360 926 14	0.360 723 02	0.054 304 93	0.054 304 66	1.051 488 79	1.051 478 65
4.0	0.517 202 49	0.517 062 34	0.055 871 03	0.055 870 94	1.058 526 06	1.058 525 88
4.5	0.524 530 42	0.524 432 05	0.057 471 84	0.057 471 72	1.061 174 99	1.061 174 58
5.0	0.534 362 76	0.534 260 34	0.063 165 89	0.063 165 81	1.062 544 47	1.062 544 56
5.5	0.548 134 33	0.548 035 12	0.061 417 89	0.061 417 49	1.046 048 42	1.045 066 83
6.0	0.512 423 52	0.512 424 09	0.059 671 22	0.059 680 99	1.006 788 69	1.006 487 92
6.5	0.543 545 75	0.543 545 14	0.056 754 23	0.056 754 01	0.958 425 87	0.958 424 84
7.0	0.555 015 96	0.555 014 85	0.052 641 63	0.052 641 45	0.962 045 72	0.962 045 66
7.5	0.551 920 46	0.551 920 13	0.051 719 47	0.051 718 24	0.927 408 13	0.927 407 99

5. Concluding Remarks

The boundary layer two-dimensional Darcy–Forchheimer laminar thin film flow over a horizontal stretched sheet with the impact of thermal radiation and viscous dissipation are considered. The cause of heat source and thermal radiation over an unsteady stretched surface inserted in a porous medium in the absence of a magnetic field has been solved by HAM. The important key findings of this research work are given below:

- (i) Velocity profile reduces for raise in values of M and K_1
- (ii) When the values of S and F_1 increase, the velocity profile reduces
- (iii) Temperature field increases with an increase in the values of S and Ec
- (iv) With increasing values of Pr and R , the temperature field reduces
- (v) Skin friction coefficient rises as upsurges the values of physical parameters that is S , F_1 , M , and K_1
- (vi) By increasing the values of S and R , the local Nusselt number upsurge while it declines for more values of Ec and Pr

Nomenclature

Symbols:	Description
u :	Horizontal velocity component (ms^{-1})
v :	Vertical velocity component (ms^{-1})
x :	Horizontal coordinate (m)
y :	Vertical coordinate (m)
c :	Stretching rate (s^{-1})
U :	Sheet velocity (ms^{-1})
T :	Temperature (K)
h :	Film thickness (m)
f :	Dimensionless stream function, equation (9)
C_f :	Skin friction coefficient, shown in Table 1
t :	Time (s)
S :	Unsteadiness parameter, γ/c
C_p :	Specific heat ($\text{JKg}^{-1}\text{K}^{-1}$)
q :	Heat flux, $-k(\partial T/\partial y)(\text{Js}^{-1}\text{m}^{-1})$
M :	Magnetic parameter, $\sigma B^2/\rho c(1 - \gamma t)$
K_1 :	Porosity parameter, $\nu \varepsilon^2/kc(1 - \gamma t)$
Re_x :	Local Reynolds number, shown in Table 1
Pr :	Prandtl number, shown in Table 1
Nu_x :	Local Nusselt number, shown in Table 1
Ec :	Eckert number, shown in Table 1

Greek Symbols:	Descriptions:
β :	Dimensionless film thickness, $(c\nu(1 - \gamma t))^{1/2}h$
θ :	Dimensionless temperature, equation (9)
γ :	Constant (s^{-1})
k :	Thermal conductivity (m^2s^{-1})
ν :	Kinematic viscosity (m^2s^{-1})

μ :	Dynamic viscosity ($\text{Kgm}^{-1}\text{s}^{-1}$)
η :	Similarity variable, equation (9)
τ :	Shear stress, $\mu(\partial u/\partial y)(\text{Kgm}^{-1}\text{s}^{-2})$
ψ :	Stream function (m^2s^{-1})
ρ :	Density (Kgm^{-3})

Subscripts:	Descriptions:
o :	Origin
Ref:	Reference value
s :	Sheet
x :	Localized value

Superscripts:	Descriptions:
I :	1nd derivative
II :	2nd derivative
III :	3rd derivative

Data Availability

No data are available regarding this manuscript.

Conflicts of Interest

The authors declare that they have no conflicts of interest.

References

- [1] R. Jan, H. Khan, P. Kumam, F. Tchier, R. Shah, and H. Bin Jebreen, “The Investigation of the Fractional-View Dynamics of Helmholtz Equations Within Caputo Operator,” *Computers, Materials & Continua*, vol. 68, no. 3, pp. 3185–3201, 2021.
- [2] S. Khattak, I. Hussain, J. F. Gomez-Aguilar, and R. Jan, “Analysis of PD-type iterative learning control for discrete-time singular system,” *Mathematical Methods in the Applied Sciences*, pp. 1–14, 2021.
- [3] H. M. Srivastava, R. Jan, A. Jan, W. Deebani, and M. Shutaywi, “Fractional-calculus analysis of the transmission dynamics of the dengue infection,” *Chaos: An Interdisciplinary Journal of Nonlinear Science*, vol. 31, no. 5, Article ID 053130, 2021.
- [4] F. M. Alharbi, M. Naeem, M. Zubair, M. Jawad, W. U. Jan, and R. Jan, “Bioconvection Due to Gyrotactic Microorganisms in Couple Stress Hybrid Nanofluid Laminar Mixed Convection Incompressible Flow with Magnetic Nanoparticles and Chemical Reaction as Carrier for Targeted Drug Delivery through Porous Stretching Sheet,” *Molecules*, vol. 26, no. 13, p. 3954, 2021.
- [5] C. Y. Wang, “Liquid film on an unsteady stretching surface,” *Quarterly of Applied Mathematics*, vol. 48, no. 4, pp. 601–610, 1990.
- [6] C. Wang, “Analytic solutions for a liquid film on an unsteady stretching surface,” *Heat and Mass Transfer*, vol. 42, no. 8, pp. 759–766, 2006.
- [7] M. Sufian, A. Mehmood, and A. Ali, “Time-dependent flow and heat transfer over a stretching cylinder,” *Chinese Journal of physics*, vol. 50, no. 5, pp. 828–848, 2012.
- [8] Y. Zhang, M. Zhang, and S. Qi, “Heat and Mass Transfer in a thin liquid film over an unsteable stretched sheet in the absence of variable magnetic field and thermosolutal capillarity,” *Mathematical Problems in Engineering*, vol. 2016, Article ID 8521580, 2016.

- [9] K. Kalyani, K. Sreelakshmi, and G. Sarojamma, "The three-dimensional flow of a non-Newtonian fluid over a stretching flat surface through a porous medium with surface convective conditions," *Global Journal of Pure and Applied Mathematics*, vol. 13, no. 6, pp. 2193–2211, 2017.
- [10] K. Kalyani, K. Sreelakshmi, and G. Sarojamma, "Effect of thermal radiation on the Casson thin liquid film flow over a stretching sheet," *Global Journal of Pure and Applied Mathematics*, vol. 13, no. 6, pp. 1575–1592, 2017.
- [11] C. D. S. Devi, H. S. Takhar, and G. Nath, "Unsteady mixed convection flow in stagnation region adjacent to a vertical surface," *Wärme-Und Stoffübertragung*, vol. 26, no. 2, pp. 71–79, 1991.
- [12] A. K. Jhankal, R. N. Jat, and D. Kumar, "Magnetohydrodynamics (MHD) Forced Convective Flow and Heat Transfer Over a Porous Plate in a Darcy-Forchheimer Porous Medium in Presence of Radiation," *International Journal of Current Research*, vol. 9, no. 11, pp. 1663–1674, 2017.
- [13] S. E. Waheed, "Flow and heat transfer in a Maxwell liquid film over an unsteady stretching sheet in a porous medium with radiation," *SpringerPlus*, vol. 5, no. 1, pp. 1061–14, 2016.
- [14] I. Ahmad, M. Sajid, W. Awan et al., "MHD flow of a viscous fluid over an exponentially stretched surface in a porous medium," *Journal of Applied Mathematics*, vol. 2014, Article ID 256761, 2014.
- [15] E. M. Sparrow and J. L. Gregg, "A boundary-layer treatment of laminar-film condensation," *Journal of Heat Transfer*, vol. 81, no. 1, pp. 13–18, 1959.
- [16] B. S. Dandapat and P. C. Ray, "Film cooling on a rotating disk," *International journal of non-linear mechanics*, vol. 25, no. 5, pp. 569–582, 1990.
- [17] B. S. Dandapat and P. C. Ray, "The effect of thermocapillarity on the flow of a thin liquid film on a rotating disc," *Journal of Physics D: Applied Physics*, vol. 27, no. 10, pp. 2041–2045, 1994.
- [18] M. Kumari and G. Nath, "Unsteady MHD film flow over a rotating infinite disk," *International journal of engineering science*, vol. 42, no. 11-12, pp. 1099–1117, 2004.
- [19] N. A. A. Mohd Nasir, N. A. Azeany, A. Ishak, and I. Pop, "Magnetohydrodynamic Flow and Heat Transfer Induced by a Shrinking Sheet," *Mathematics*, vol. 8, no. 7, p. 1175, 2020.
- [20] H. N. Zaidi, M. Yousif, and S. Nazia Nasreen, "Effects of Thermal Radiation, Heat Generation, and Induced Magnetic Field on Hydromagnetic Free Convection Flow of Couple Stress Fluid in an Isoflux-Isothermal Vertical Channel," *Journal of Applied Mathematics*, vol. 2020, pp. 1–12, 2020.
- [21] P. M. Kishore, V. Rajesh, and V. Verma, "The effects of thermal radiation and viscous dissipation on MHD heat and mass diffusion flow past an oscillating vertical plate embedded in a porous medium with variable surface conditions," *Theoretical and Applied Mechanics*, vol. 39, no. 2, pp. 99–125, 2012.
- [22] E. Elbashbeshy and T. G. Emam, "Effects of thermal radiation and heat transfer over an unsteady stretching surface embedded in a porous medium in the presence of heat source or sink," *Thermal science*, vol. 15, no. 2, pp. 477–485, 2011.
- [23] A. S. Khan, Y. Nie, and Z. Shah, "Impact of thermal radiation on magnetohydrodynamic unsteady thin film flow of Sisko fluid over a stretching surface," *Processes*, vol. 7, no. 6, p. 369, 2019.
- [24] S. Palani, B. R. Kumar, and P. K. Kameswaran, "Unsteady MHD flow of an UCM fluid over a stretching surface with higher order chemical reaction," *Ain Shams Engineering Journal*, vol. 7, no. 1, pp. 399–408, 2016.
- [25] M. S. Abel, N. Mahesha, and J. Tawade, "Heat transfer in a liquid film over an unsteady stretching surface with viscous dissipation in presence of external magnetic field," *Applied Mathematical Modelling*, vol. 33, no. 8, pp. 3430–3441, 2009.
- [26] S. Shateyi and J. Prakash, "A new numerical approach for MHD laminar boundary layer flow and heat transfer of nanofluids over a moving surface in the presence of thermal radiation," *Boundary value problems*, vol. 2014, no. 1, pp. 1–12, 2014.
- [27] F. Mabood, W. A. Khan, and A. I. M. Ismail, "MHD boundary layer flow and heat transfer of nanofluids over a nonlinear stretching sheet: a numerical study," *Journal of Magnetism and Magnetic Materials*, vol. 374, pp. 569–576, 2015.

Research Article

Inverse Family of Numerical Methods for Approximating All Simple and Roots with Multiplicity of Nonlinear Polynomial Equations with Engineering Applications

Mudassir Shams ¹, Naila Rafiq ², Nasreen Kausar ³, Shams Forruque Ahmed ⁴,
Nazir Ahmad Mir ² and Suvash Chandra Saha ⁵

¹Department of Mathematics and Statistics, Riphah International University I-14, Islamabad 44 000, Pakistan

²Department of Mathematics, National University of Modern Languages, Islamabad, Pakistan

³Department of Mathematics, Yildiz Technical University, Faculty of Arts and Science, Esenler 34 210, Istanbul, Turkey

⁴Science and Math Program, Asian University for Women, Chattogram 4000, Bangladesh

⁵School of Mechanical and Mechatronic Engineering University of Technology Sydney (UTS), Sydney, Australia

Correspondence should be addressed to Suvash Chandra Saha; suvash.saha@gmail.com

Received 21 September 2021; Revised 11 November 2021; Accepted 18 November 2021; Published 24 December 2021

Academic Editor: Adnan Maqsood

Copyright © 2021 Mudassir Shams et al. This is an open access article distributed under the Creative Commons Attribution License, which permits unrestricted use, distribution, and reproduction in any medium, provided the original work is properly cited.

A new inverse family of the iterative method is interrogated in the present article for simultaneously estimating all distinct and multiple roots of nonlinear polynomial equations. Convergence analysis proves that the order of convergence of the newly constructed family of methods is two. The computer algebra systems CAS-Mathematica is used to determine the lower bound of convergence order, which justifies the local convergence of the newly developed method. Some nonlinear models from physics, chemistry, and engineering sciences are considered to demonstrate the performance and efficiency of the newly constructed family of inverse simultaneous methods in comparison to classical methods in the literature. The computational time in seconds and residual error graph of the inverse simultaneous methods are also presented to elaborate their convergence behavior.

1. Introduction

Considering nonlinear polynomial equation of degree n ,

$$\begin{aligned} f(r) &= r^n + a_{n-1}r^{n-1} + \dots + a_0 = \prod_{j=1}^n (r - \zeta_j) \\ &= (r - \zeta_i) * \prod_{\substack{j=1 \\ j \neq i}}^n (r - \zeta_j), \end{aligned} \quad (1)$$

with arbitrary real or complex coefficient a_{n-1}, \dots, a_0 . Let $\zeta_1 \dots \zeta_n$ denote all the simple or complex roots of (1) with multiplicity $\sigma_1 \dots \sigma_n$. Newton's method [11] is one of the most basic and ancient methods that is used to estimate single roots of (1) at a time as below:

$$s^{(t)} = r^{(t)} - \frac{f(r^{(t)})}{f'(r^{(t)})}, \quad (t = 0, 1, \dots). \quad (2)$$

Iterative method (2) has local quadratic convergence. Nedzhibov et al. [13] presented corresponding inverse numerical technique of the same convergence order as

$$s^{(t)} = \frac{(r^{(t)})^2 f'(r^{(t)})}{r^{(t)} f'(r^{(t)}) + f(r^{(t)})}. \quad (3)$$

Here, we propose the following family of the optimal second-order convergence method for finding simple roots of (1) as

$$s^{(t)} = r^{(t)} - \frac{f(r^{(t)})}{f'(r^{(t)})} \frac{1}{(1 - \alpha f(r^{(t)})/1 + f(r^{(t)}))}, \quad (4)$$

where $\alpha \in \mathbb{R}$. Method (4) is optimal and the convergence order of (4) is 2 if ζ is a simple root of (1) and $\epsilon = r - \zeta$. The error equation of (4) is obtained using Maple-18:

$$\frac{s^{(t)} - \zeta}{(r^{(t)} - \zeta)^2} \longrightarrow (-\alpha + C_2); C_k(r) = \frac{f^{(k)}(x)}{k!f'(x)}, \quad (5)$$

or

$$s^{(t)} - \zeta = O(\epsilon^2). \quad (6)$$

Corresponding inverse methods of (4) is constructed as

$$g(r) = \frac{(r^{(t)})^2 * (f'(r^{(t)}))}{r^{(t)} f'(r^{(t)}) + f(r^{(t)}) (1/(1 - \alpha f(r^{(t)})) / 1 + f(r^{(t)}))}, g(\zeta) = \zeta \text{ (fixed point)}, \quad (8)$$

$$g'(\zeta) = 0. \quad (9)$$

Inverse iterative schemes (7) are second-order convergence as it is easy to prove $g''(\zeta) \neq 0$.

Besides simple root finding methods [3–5, 13, 15, 16, 18–20] in literature, there exists another class of numerical methods which estimate all real and complex roots of (1) at a time, known as simultaneous methods. Simultaneous numerical iterative schemes are very prevalent due to their global convergence properties and its parallel execution on computers [1, 6, 8–10, 12, 14].

The most prominent method among simultaneous derivative-free iterative technique is the Weierstrass–Dochive [17] method (abbreviated as MWM1), which is defined as

$$s_i^{(t)} = r_i^{(t)} - w(r_i^{(t)}), \quad (10)$$

where

$$\frac{f(r_i^{(t)})}{f'(r_i^{(t)})} = w(r_i^{(t)}) = \frac{f(r_i^{(t)})}{\prod_{\substack{j=1 \\ j \neq i}}^n (r_i^{(t)} - r_j^{(t)})}, \quad (i, j = 1, 2, 3, \dots, n), \quad (11)$$

is Weierstrass' correction. Method (10) has local quadratic convergence. For finding all multiple roots of (1), we use the following correction [17]:

$$w_*(r_i^{(t)}) = \frac{f(r_i^{(t)})}{\prod_{\substack{j=1 \\ j \neq i}}^n (r_i^{(t)} - r_j^{(t)})^{\sigma_j}}, \quad (i, j = 1, 2, 3, \dots, n), \quad (12)$$

where σ is the multiplicity of the roots.

2. Construction of the Inverse Simultaneous Method

Using Weierstrass correction $w(r_i^{(t)}) = f(r_i^{(t)}) / \prod_{j=1, j \neq i}^n (r_i^{(t)} - r_j^{(t)})$ in (7), we get a new family of inverse modified Weierstrass method (abbreviated as MWM2):

$$s^{(t)} = \frac{(r^{(t)})^2 * f'(r^{(t)})}{r^{(t)} f'(r^{(t)}) + f(r^{(t)}) (1/(1 - \alpha f(r^{(t)})) / 1 + f(r^{(t)}))}. \quad (7)$$

If ζ is an exact root of (1), $f(\zeta) = 0$, and the following is obtained:

$$s_i^{(t)} = \frac{(r_i^{(t)})^2 (1 + (1 - \alpha) f(r_i^{(t)}))}{r_i^{(t)} (1 + (1 - \alpha) f(r_i^{(t)})) + w(r_i^{(t)}) (1 + f(r_i^{(t)}))}. \quad (13)$$

Inverse simultaneous iterative method (13) can also be written as

$$s_i^{(t)} = r_i^{(t)} - \frac{r_i^{(t)} w(r_i^{(t)}) (1 + f(r_i^{(t)}))}{r_i^{(t)} (1 + (1 - \alpha) f(r_i^{(t)})) + w(r_i^{(t)}) (1 + f(r_i^{(t)}))}. \quad (14)$$

Thus, we construct a new derivative-free family of inverse iterative simultaneous scheme (13), abbreviated as MWM2, for estimating all distinct roots of (1). To estimate all multiple roots of (1), we use correction (12) instead of (11) in (7).

2.1. Convergence Framework. In this section, we demonstrate convergence theorem of inverse iterative scheme MWM2.

Theorem 1. Let ζ_1, \dots, ζ_n be single zero of (1) and for necessarily close primary distinct guess $r_1^{(0)}, \dots, r_n^{(0)}$ of the zero, respectively; then, MWM2 has local 2nd-order convergence.

Proof. Let $\epsilon_i = r_i^{(t)} - \zeta_i$ and $\epsilon'_i = s_i^{(t)} - \zeta_i$ be the errors in r_i and s_i respectively. For the simplicity of the calculation, we omit the iteration index. Then,

$$s_i = \frac{(r_i)^2 (1 + (1 - \alpha) f(r_i))}{r_i (1 + (1 - \alpha) f(r_i)) + w(r_i) (1 + f(r_i))}, \quad (15)$$

or

$$s_i = r_i - \frac{r_i w(r_i) (1 + f(r_i))}{r_i (1 + (1 - \alpha) f(r_i)) + w(r_i) (1 + f(r_i))}. \quad (16)$$

Using $f(r_i) / \prod_{j=1, j \neq i}^n (r_i - r_j) = w(r_i)$ in (15), we have

$$s_i = r_i - \frac{w(r_i) (1 + f(r_i))}{(1 + (1 - \alpha) f(r_i)) + w(r_i) / r_i (1 + f(r_i))}. \quad (17)$$

Thus, we obtain

$$s_i - \zeta_i = r_i - \zeta_i - \frac{w(r_i)(1 + f(r_i))}{(1 + (1 - \alpha)f(r_i)) + w(r_i)/r_i(1 + f(r_i))}, \quad (18)$$

$$\varepsilon'_i = \varepsilon_i \left[1 - \frac{\prod_{j \neq i}^n (r_i - \zeta_j)/(r_i - r_j) \left(1 + \varepsilon_i \prod_{j \neq i}^n (r_i - \zeta_j) \right)}{\left((1 + (1 - \alpha))\varepsilon_i \prod_{j \neq i}^n (r_i - \zeta_j) \right) + \left(\prod_{j \neq i}^n (r_i - \zeta_j)/(r_i - r_j) \right) \left(1 + \varepsilon_i \prod_{j \neq i}^n (r_i - \zeta_j) \right)} \right], \quad (19)$$

$$= \varepsilon_i \left[\frac{\left((1 + 1 - \alpha)\varepsilon_i \prod_{j \neq i}^n (r_i - \zeta_j) \right)}{\left((1 + (1 - \alpha))\varepsilon_i \prod_{j \neq i}^n (r_i - \zeta_j) \right) + \left(\prod_{j \neq i}^n (r_i - \zeta_j)/(r_i - r_j) \right) \left(1 + \varepsilon_i \prod_{j \neq i}^n (r_i - \zeta_j) \right)} \right]. \quad (20)$$

Using the expression $\prod_{j \neq i}^n (r_i - \zeta_j)/(r_i - r_j) - 1 = \sum_{k \neq i}^n \varepsilon_k/r_i - r_k \varepsilon \prod_{j \neq i}^{k-1} (r_i - \zeta_k)/(r_i - r_j)$ [9] in (20), we have

$$\left\{ \varepsilon'_i = \varepsilon_i \left[\frac{\left((1 + 1 - \alpha)\varepsilon_i \prod_{j \neq i}^n (r_i - \zeta_j) \right)}{\left((1 + 1 - \alpha)\varepsilon_i \prod_{j \neq i}^n (r_i - \zeta_j) \right) + \left(\sum_{k \neq i}^n \varepsilon_k/r_i - r_k \prod_{j \neq i}^{k-1} (r_i - \zeta_k)/(r_i - r_j) + 1 \right) \left(1 + \varepsilon_i \prod_{j \neq i}^n (r_i - \zeta_j) \right)} \right] \right\}. \quad (21)$$

If all the errors are assumed of the same order, i.e., $|\varepsilon_i| = |\varepsilon_k| = O(|\varepsilon|)$, then

$$\varepsilon'_i = |\varepsilon| \left[\frac{\left((1 + (1 - \alpha))\varepsilon_i \prod_{j \neq i}^n (r_i - \zeta_j) \right)}{\left((1 + (1 - \alpha))\varepsilon_i \prod_{j \neq i}^n (r_i - \zeta_j) \right) + \left(\sum_{k \neq i}^n \varepsilon_k/r_i - r_k \prod_{j \neq i}^{k-1} (r_i - \zeta_k)/(r_i - r_j) + 1 \right) \left(1 + \varepsilon_i \prod_{j \neq i}^n (r_i - \zeta_j) \right)} \right], \quad (22)$$

$$= O(|\varepsilon|^2).$$

Hence, it is proved. □

3. Lower Bound of Convergence of MWM1 and MWM2

Computer algebra system, Mathematica, has been used to find the lower bound of convergence of MWM1 and MWM2.

Consider

$$f(r) = (r - \varrho_1)(r - \varrho_2)(r - \varrho_3), \quad (23)$$

where ϱ_1, ϱ_2 , and ϱ_3 are exact zeros of (23). The first component of $\aleph_1(\mathbf{r})$ (where $\mathbf{r} = [r_1, r_2, r_3]$) of numerical iterative methods is for finding zeros of (23), $r^{(t+1)} = \aleph(r^{(t)})$,

simultaneously. We have to express the derivatives of $\aleph(r)$, i.e., the partial derivatives of $\aleph(r)$ with respect to \mathbf{r} are as follows:

$$\begin{aligned} & \frac{\partial \aleph_1(\mathbf{r})}{\partial r_1} \quad \frac{\partial \aleph_1(\mathbf{r})}{\partial r_2} \quad \frac{\partial \aleph_1(\mathbf{r})}{\partial r_3}, \\ & \frac{\partial_1^2 \aleph(\mathbf{r})}{\partial r_1^2} \quad \frac{\partial_1^2 \aleph(\mathbf{r})}{\partial r_1 \partial r_2} \quad \frac{\partial_1^2 \aleph(\mathbf{r})}{\partial r_2^2} \quad \frac{\partial^2 \Gamma_1(\mathbf{r})}{\partial r_2 \partial r_3}, \\ & \frac{\partial_1^3 \aleph(\mathbf{r})}{\partial r_1^3} \quad \frac{\partial_1^3 \aleph(\mathbf{r})}{\partial r_1^2 \partial r_2} \quad \frac{\partial_1^3 \aleph(\mathbf{r})}{\partial r_1 \partial r_2^2} \quad \frac{\partial_1^3 \aleph(\mathbf{r})}{\partial r_2^3} \quad \frac{\partial_1^3 \aleph(\mathbf{r})}{\partial r_2^2 \partial r_3}, \end{aligned} \quad (24)$$

and so on.

We obtain the lower bound of convergence order till the first nonzero element of row is found. The Mathematica

notebook codes are used for the following MWM1 and MWM2:

Weierstrass–Dochive method, MWM1:

$$\aleph_1(r_1, r_2, r_3) = r_1 - \frac{f(r_1)}{(r_1 - r_2) * (r_1 - r_3)}, \quad (25)$$

$$\text{In}[1] := \frac{D[\aleph_1[r_1, r_2, r_3], r_1]}{\{r_1 \rightarrow \varrho_1, r_2 \rightarrow \varrho_2, r_3 \rightarrow \varrho_3\}},$$

$$\text{Out}[1] = 0,$$

$$\text{In}[2] := D \frac{[\aleph_1[r_1, r_2, r_3], r_2]}{\{r_1 \rightarrow \varrho_1, r_2 \rightarrow \varrho_2, r_3 \rightarrow \varrho_3\}},$$

$$\text{Out}[2] = 0,$$

$$\text{In}[3] := D \frac{[\aleph_1[r_1, r_2, r_3], r_3]}{\{r_1 \rightarrow \varrho_1, r_2 \rightarrow \varrho_2, r_3 \rightarrow \varrho_3\}},$$

$$\text{Out}[3] = 0,$$

$$\text{In}[4] := \text{Simplify} \frac{D[\aleph_1[r_1, r_2, r_3], r_1, r_2]}{\{r_1 \rightarrow \varrho_1, r_2 \rightarrow \varrho_2, r_3 \rightarrow \varrho_3\}},$$

$$\text{Out}[4] = 0,$$

$$\text{In}[6] := \text{Simplify} \frac{[D[\aleph_1[r_1, r_2, r_3], r_1, r_2]]}{\{r_1 \rightarrow \varrho_1, r_2 \rightarrow \varrho_2, r_3 \rightarrow \varrho_3\}},$$

$$\text{Out}[6] = \frac{1}{(\varrho_1 - \varrho_2)}.$$

Modified inverse family of iterative schemes, MWM2:

$$\aleph_1(r_1, r_2, r_3) = \frac{(r_1)^2 (1 + (1 - \alpha)f(r_1))}{r_1 (1 + (1 - \alpha)f(r_1)) + (r_1 - r_2)(r_1 - r_3)(1 + f(r_1))}, \quad (27)$$

$$\text{In}[1] := D[\aleph_1[r_1, r_2, r_3], r_2] / \{r_1 \rightarrow \varrho_1, r_2 \rightarrow \varrho_2, r_3 \rightarrow \varrho_3\},$$

$$\text{Out}[1] = 0,$$

$$\text{In}[2] := D[\aleph_1[r_1, r_2, r_3], r_3] / \{r_1 \rightarrow \varrho_1, r_2 \rightarrow \varrho_2, r_3 \rightarrow \varrho_3\},$$

$$\text{Out}[2] = 0,$$

$$\text{In}[3] := D[\aleph_1[r_1, r_2, r_3], r_1] / \{r_1 \rightarrow \varrho_1, r_2 \rightarrow \varrho_2, r_3 \rightarrow \varrho_3\}, \quad (28)$$

$$\text{Out}[3] = 0,$$

$$\text{In}[4] := \text{Simplify}[D[\aleph_1[r_1, r_2, r_3], r_1, r_1]] \cdot \{r_1 \rightarrow \varrho_1, r_2 \rightarrow \varrho_2, r_3 \rightarrow \varrho_3\},$$

$$\text{Out}[4] = \frac{4 + 8 * \alpha * \varrho_1}{\varrho_3^3}.$$

4. Numerical Results

Some engineering problems are considered to demonstrate the performance and effectiveness of the simultaneous method, MWM2 and MWM1. For computer calculations,

we use CAS-Maple-18, and the following stopping criteria for termination of computer are programmed:

$$e_i^{(t)} = |r_i^{(t+1)} - r_i^{(t)}| < \epsilon = 10^{-30}, \quad (29)$$

where $e_i^{(t)}$ signifies the absolute error. In Tables 1–5, C-Time represents computational time in second.

4.1. Engineering Applications. Some engineering applications are deliberated in this section in order to show the feasibility of the present work.

Example 1. (see [2]). Considering a physical problem of beam positioning results in the following nonlinear polynomial equation:

$$f(r) = r^4 + 4r^3 - 24r^2 + 16r + 1, \quad (30)$$

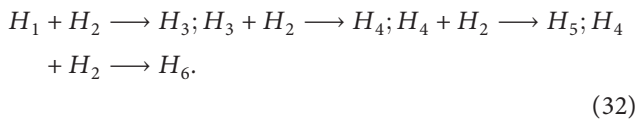
$$= (r - 2)^2(r^2 + 8r + 4).$$

The exact root of (30), $\zeta_{1,2}$, is 2 with multiplicity 2 and the remaining other two roots are simple, i.e., $\zeta_3 = -4 - 2\sqrt{3}$ and $\zeta_4 = -4 + 2\sqrt{3}$. We take the following initial estimates:

$$\begin{aligned} r_1^{(0)} &= 1.17, \\ r_2^{(0)} &= 1.17, \\ r_3^{(0)} &= -7.4641, \\ r_4^{(0)} &= -0.5354. \end{aligned} \quad (31)$$

Table 1 clearly demonstrates the superiority of MWM2 over MWM1 in terms of predicted absolute error and CPU time for guesstimating all real roots of (30) on the same number of iterations $n = 3$.

Example 2. (see [16]). In this engineering application, we consider a reactor of stirred tank. Items H_1 and H_2 are fed to the reactor at rates of β and $q\beta$, respectively. Composite reaction improves in the apparatus as below:



Douglas et al. [7] first examined this complex control system and obtained the following nonlinear polynomial equation:

$$\frac{2.98 * (r + 2.25)}{(r + 1.45) * (r + 2.85)^2 * (r + 4.35)} = \frac{1}{T_c}, \quad (33)$$

where T_c is the gain of the proportional controller. By taking $T_c = 0$, we have

$$f(r) = r^4 + 11.50r^3 + 47.49r^2 + 83.06325r + 51.23266875 = 0. \quad (34)$$

The exact distinct roots of (34) are calculated as $\zeta_1 = -1.45, \zeta_2 = -2.85, \zeta_3 = -2.85$, and $\zeta_4 = -4.45$, and we take the following initial guessed values:

$$r_1^{(0)} = -1.0, r_2^{(0)} = -1.1, r_3^{(0)} = -1.8, r_4^{(0)} = -3.9. \quad (35)$$

Table 2 evidently illustrates the supremacy behavior of MWM2 over MWM1 in terms of the estimated absolute

TABLE 1: Residual error for finding all distinct roots.

Method	C-Time	$e_1^{(3)}$	$e_2^{(3)}$	$e_3^{(3)}$	$e_4^{(3)}$	$\sigma^{(2)}$
MWM1	1.103	Div	Div	$1.3e - 27$	0.0	2.101
MWM2	0.048	0.0	0.0	0.0	0.0	2.307
<i>Residual error for finding all multiple roots</i>						
MWM2	0.312	0.0	0.0	0.0	0.0	2.735

TABLE 2: Residual error for finding all distinct roots.

Method	C-Time	$e_1^{(7)}$	$e_2^{(7)}$	$e_3^{(7)}$	$e_4^{(7)}$	$\sigma^{(6)}$
MWM1	2.119	0.07	0.02	0.1	0.1	2.125
MWM2	0.115	$3.5e - 324$	$2.0e - 319$	0.005	0.005	2.968

TABLE 3: Residual error for finding all distinct roots.

Method	C-Time	$e_1^{(8)}$	$e_2^{(8)}$	$e_3^{(8)}$	$e_4^{(8)}$	$\sigma^{(7)}$
MWM1	1.739	$1.1e - 9$	Div	$3.6e - 13$	Div	1.341
MWM2	0.032	$2.0e - 317$	$4.0e - 289$	$1.6e - 139$	$4.0e - 289$	3.167

TABLE 4: Residual error for finding all distinct roots.

Method	C-Time	$e_1^{(5)}$	$e_2^{(5)}$	$e_3^{(5)}$	$e_4^{(5)}$	$\sigma^{(4)}$
MWM1	0.125	$4.7e - 26$	$1.2e - 28$	$9.1e - 28$	$0.2e - 26$	2.314
MWM2	0.046	$1.3e - 27$	$3.1e - 30$	0.0	0.0	2.753
<i>Residual error for finding all multiple roots at $n = 1$</i>						
MWM2	0.103	0.0	0.0	0.0	0.0	

TABLE 5: Residual error for finding all distinct roots.

Method	C-Time	$e_1^{(8)}$	$e_2^{(8)}$	$e_3^{(8)}$	$\sigma^{(7)}$
MWM1	0.067	0.0	$6.4e - 27$	$6.4e - 27$	2.101
MWM2	0.043	0.0	0.0	0.0	2.231

error and in CPU time on the same number of iterations $n = 7$ for guesstimating all real roots of (34).

Example 3. (see [4]). Consider the function

$$\frac{8(4 - r)^2 r^2}{(6 - 3r)^2 (2 - r)} - 0.186 = 0, \quad (36)$$

$$f(r) = 8r^4 - 62.326r^3 + 117.956r^2 + 20.088r - 13.392. \quad (37)$$

The problem describes the fractional alteration of nitrogen-hydrogen (NH) feed into ammonia at 250 atm pressure and 500° C temperature. Since the (37) is of order four, it has four roots:

$$\begin{aligned}
\zeta_1 &= 0.2777, \\
\zeta_2 &= 3.9485 + 0.3161i, \\
\zeta_3 &= -0.3840, \\
\zeta_4 &= 3.9485 - 0.3161i.
\end{aligned} \tag{38}$$

The initial approximated value for (27) is taken as

$$r_1^{(0)} = 0.4, r_2^{(0)} = 3.7 + 0.5i, r_3^{(0)} = -0.4, r_4^{(0)} = 3.7 - 0.5i. \tag{39}$$

Table 3 evidently shows the supremacy behavior of MWM2 over MWM1 in terms of estimated absolute error and in CPU time on the same number of iterations $n = 8$ for guesstimating all real and complex roots of (37). Minuscule alteration of nitrogen-hydrogen (NH) feed into ammonia lies between (0,1); therefore, our desire root is ζ_1 up to 1900 decimal places:

$$\zeta_1 = 1.12956568412579833521973452e - 1912. \tag{40}$$

Remaining other approximating roots are $\zeta_2 = -1.283404526e - 1457 - 8.93219631521e - 1457i$, $\zeta_3 = -8.21745235223462e - 1091 + 0i$, and $\zeta_4 = -1.2834045268801e - 1457 + 8.99321963152e - 1457i$.

Example 4. (see [8]). Consider

$$\begin{aligned}
f(r) &= (r - 0.3 - 0.6i)^{100} (r - 0.1 - 0.7i)^{200} (r - 0.7 - 0.5i)^{300} \\
&\quad (r - 0.3 - 0.4i)^{400},
\end{aligned} \tag{41}$$

with multiple exact roots:

$$\zeta_1 = 0.3 + 0.6i, \zeta_2 = 0.1 + 0.7i, \zeta_3 = 0.7 + 0.5i, \zeta_4 = 0.3 + 0.4i, \tag{42}$$

The initial estimations have been taken as

$$\begin{aligned}
r_1^{(0)} &= 0.301 + 0.601i, r_2^{(0)} = 0.100 + 0.702i, r_3^{(0)} \\
&= 0.702 + 0.489i, r_4^{(0)} = 0.289 - 0.400i,
\end{aligned} \tag{43}$$

For distinct roots,

$$\begin{aligned}
f_*(r) &= (r - 0.3 - 0.6i)(r - 0.1 - 0.7i)(r - 0.7 - 0.5i) \\
&\quad (r - 0.3 - 0.4i),
\end{aligned} \tag{44}$$

Table 4 evidently shows the supremacy behavior of MWM2 over MWM1 in terms of estimated absolute error and in CPU time on the same number of iterations $n = 5$ for guesstimating all real and complex roots of (41).

Example 5. (see [5]). The sourness of a soaked solution of magnesium-hydroxide (MgOH) in hydroelectric acid (HCl) is given by

$$\frac{3.64 \times 10^{-11}}{[H_3O^+]} = [H_3O^+] + 3.6 \times 10^{-4}, \tag{45}$$

TABLE 6: Residual error for finding all distinct roots.

Method	C-Time	$e_1^{(4)}$	$e_2^{(4)}$	$e_3^{(4)}$	$e_4^{(4)}$	$\sigma^{(3)}$
MWM1	0.203	$4.1e-25$	$3.6e-30$	$7.1e-21$	$5.6e-23$	2.131
MWM2	0.115	$5.0e-38$	$4.8e-37$	$8.4e-32$	$7.9e-32$	2.707

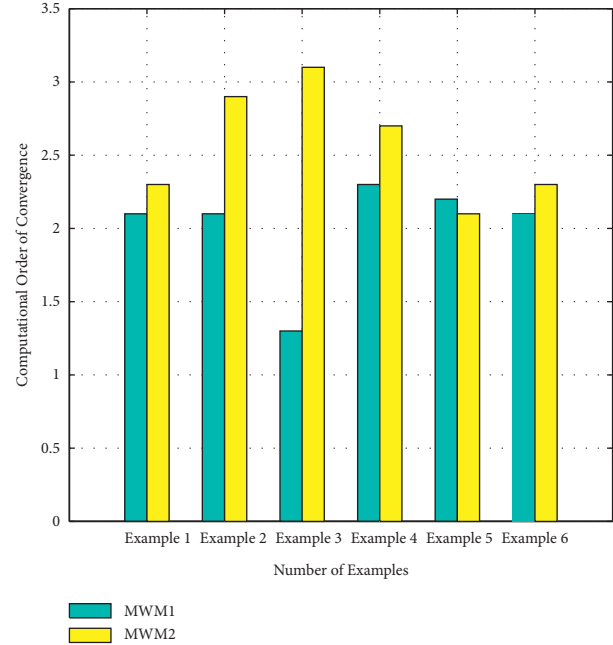


FIGURE 1: Computational order of convergence [22] of simultaneous methods, MWM1 and MWM2.

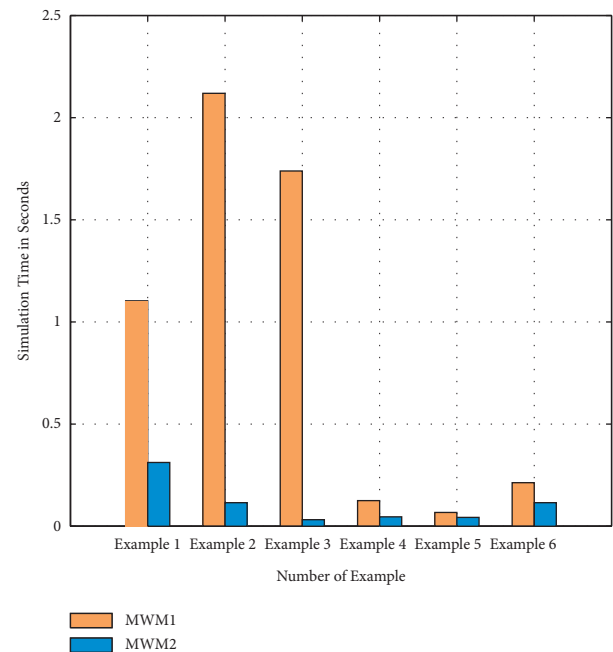


FIGURE 2: Simulation time in second of simultaneous methods, MWM1 and MWM2, for approximating all roots of polynomial equations used in Examples 1-6.

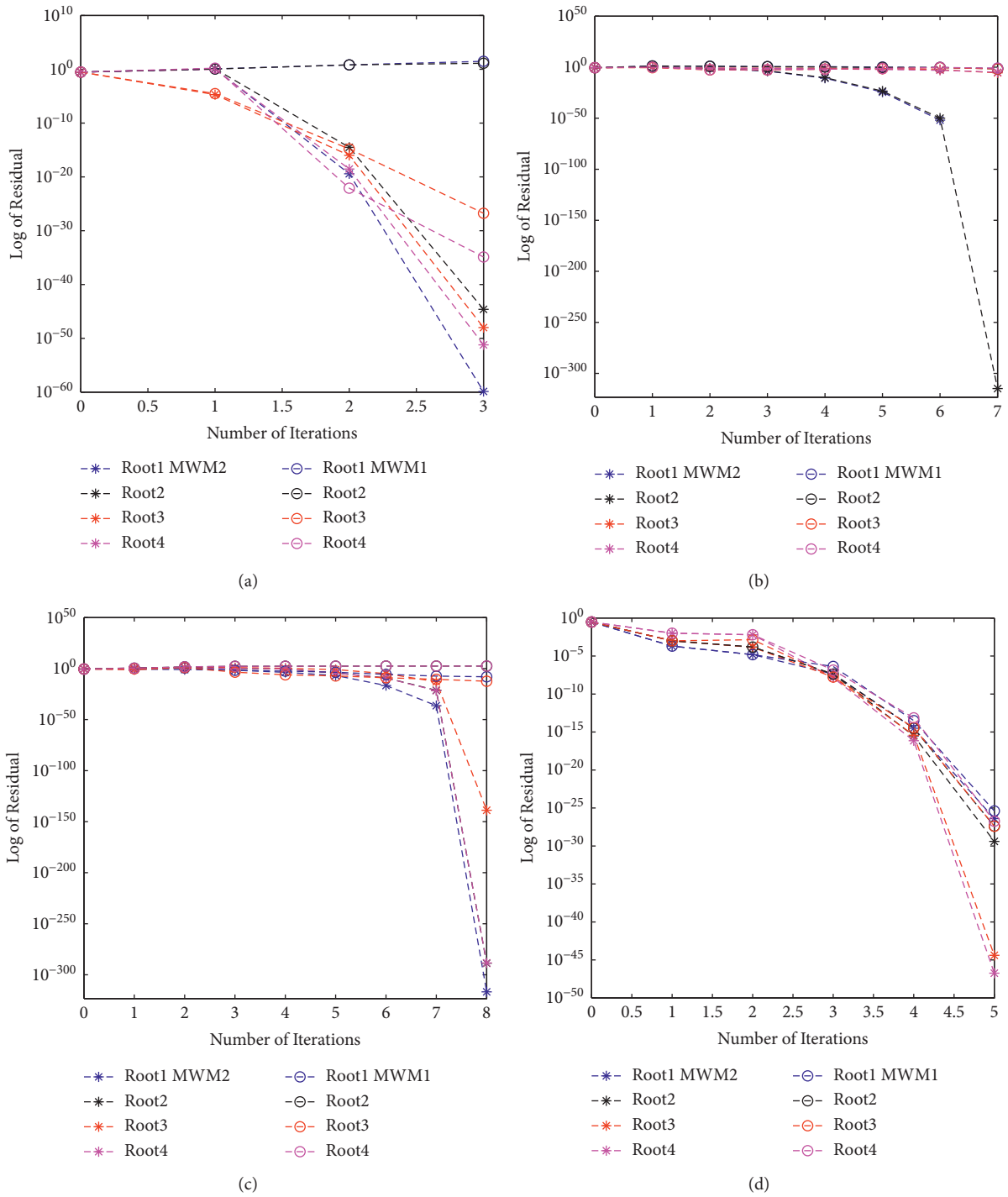


FIGURE 3: Continued.

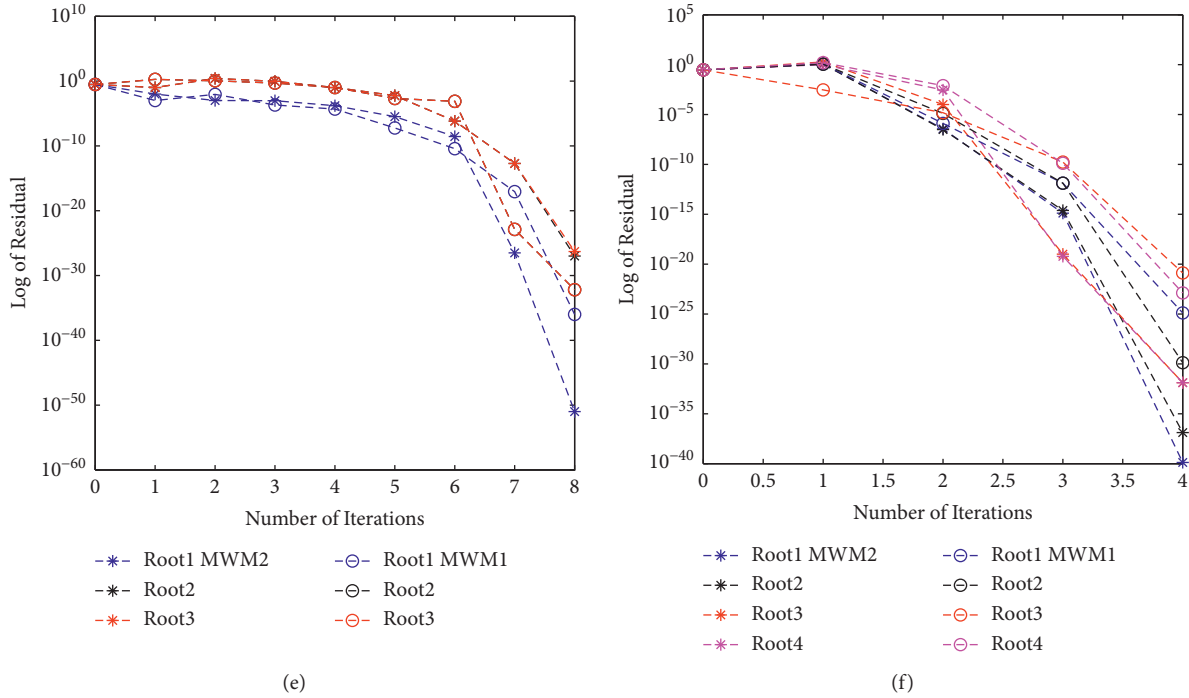


FIGURE 3: (a-f) Error graph of MWM1 and MWM2 for nonlinear polynomial equations (30), (34), (37), (41), (46) and (49), respectively. (a) Residual error graph for Example 1. (b) Residual error graph for Example 2. (c) Residual error graph for Example 3. (d) Residual error graph for Example 4. (e) Residual error graph for Example 5. (f) Residual error graph for Example 6.

for the cranium ion concentration $[H_3O^+]$. If we set $r = 10^4 [H_3O^+]$, we obtain the following polynomial:

$$f(r) = r^3 + 3.6r^2 - 36.4, \quad (46)$$

with exact roots of (46), $\zeta_1 = 2.4$ and $\zeta_{2,3} = -3.0 \pm 2.3i$ up to one decimal places. The initial estimates have been taken as

$$\begin{aligned} {}^{(0)}r_1 &= 2.45, {}^{(0)}r_2 = -3.0261 + 2.3834i, {}^{(0)}r_3 \\ &= -3.0261 - 2.3834i. \end{aligned} \quad (47)$$

Table 5 evidently illustrates the supremacy behavior of MWM2 over MWM1 in terms of estimated absolute error and in CPU time on the same number of iterations $n = 8$ for guesstimating all real and complex roots of (46).

Example 6. (see [21]). In general, mechanical engineering, as well as the majority of other scientists, uses thermodynamics extensively in their research work. The following polynomial is used to relate the zero-pressure specific heat of dry air, C_p , to temperature:

$$\begin{aligned} C_p &= 1.9520 \times 10^{-14} r^4 - 9.5838 \times 10^{-11} r^3 + 9.7215 \\ &\times 10^{-8} r^2 + 1.671 \times 10^{-4} r + 0.99403. \end{aligned} \quad (48)$$

The temperature that corresponds to specific heat of $1.2(kJ/kgK)$ needs to be determined. Putting $C_p = 1.2$ in (48), we have

$$\begin{aligned} f(r) &= 1.9520 \times 10^{-14} r^4 - 9.5838 \times 10^{-11} r^3 \\ &+ 9.7215 \times 10^{-8} r^2 + 1.671 \times 10^{-4} r + 0.99403. \end{aligned} \quad (49)$$

with exact roots $\zeta_1 = 1126.009751$, $\zeta_2 = 2536.837119 + 910.5010371i$, and $\zeta_3 = -1289.950382, 2536.837119 - 910.5010371i$. The initial estimations of (49) have been taken as

$${}^{(0)}r_1 = 1126, {}^{(0)}r_2 = 2536 + 910i, {}^{(0)}r_3 = -1289, {}^{(0)}r_4 = 2536 - 910i. \quad (50)$$

Table 6 clearly illustrates the supremacy behavior of MWM1 over MWM2 in estimated absolute error and in CPU time on the same number of iterations $n = 4$ for guesstimating all real and complex roots of (49).

5. Conclusion

A new derivative-free family of inverse numerical methods of convergence order 2 for simultaneous estimations of all distinct and multiple roots of (1) was introduced and discussed in this paper. Tables 1–5 and Figure 1 clearly show that computational order of convergence of the proposed and existing methods are agreed with the theoretical results. Simulation time, from Figure 2, clearly indicates the supremacy of our newly proposed method MWM2 over

existing Weierstrass method MWM1. The results of numerical test cases from Tables 1–5, CPU time, and residual error graph from Figure 3 demonstrated the effectiveness and rapid convergence of our proposed iterative method MWM2 as compared to MWM1.

Data Availability

No data were used to support this study.

Disclosure

The statements made and views expressed are solely the responsibility of the authors.

Conflicts of Interest

The authors declare that they have no conflicts of interest.

Authors' Contributions

All authors contributed equally and significantly in writing this article. All authors read and approved the final manuscript.

References

- [1] M. Shams, N. Rafiq, and N. Kausar, "On highly efficient derivative-free family of numerical methods for solving polynomial equation simultaneously," *Advances in Difference Equations*, vol. 2021, p. 465, 2021.
- [2] F. I. Chicharro, A. Cordero, and J. R. Garrido N & Torregrosa, "Stability and applicability of iterative methods with memory," *Journal of Mathematical Chemistry*, vol. 2, 2018.
- [3] F. I. Chicharro, A. Cordero, and J. R. Garrido N & Torregrosa, "Generating root-finder iterative methods of second order convergence and stability, axioms," 2019.
- [4] A. Cordero, H. Ramos, and J. R. Torregrosa, "Some variants of Halley's method with memory and their applications for solving several chemical problems," *Journal of Mathematical Chemistry*, vol. 58, no. 4, pp. 751–774, 2020.
- [5] Y. M. Chu, N. Rafiq, M. Shams, S. Akram, N. A. Mir, and H. Kalsoom, "Computer methodologies for the comparison of some efficient derivative free simultaneous iterative methods for finding roots of non-linear equations," vol. 16, *Computers, Materials & Continua*, 2020.
- [6] S. I. Cholakov, "Local and semilocal convergence of Wang-Zheng's method for simultaneous finding polynomial zeros," *Symmetry*, vol. 736, p. 15, 2019.
- [7] J. M. Douglas, *Process Dynamics and Control*, Prentice-Hall, Englewood Cliffs, NJ, USA, 1972.
- [8] M. R. Farmer, *Computing the zeros of polynomials using the divide and conquer approach*, Ph.D Thesis, Department of Computer Science and Information Systems, Birkbeck, University of London, London, UK, 2014.
- [9] S. Kanno and T. Yamamoto, "On some methods for the simultaneous determination of polynomial zeros," *Japan Journal of Applied Mathematics*, vol. 13, pp. 267–288, 1995.
- [10] N. A. Mir, R. Muneer, and I. Jabeen, "Some families of two-step simultaneous methods for determining zeros of non-linear equations," *ISRN Applied Mathematics*, vol. 2011, pp. 1–11, 2011.
- [11] N. A. Mir, M. Shams, N. Rafiq, S. Akram, and M. Rizwan, "Derivative free iterative simultaneous method for finding distinct roots of polynomial equation," *Alexandria Engineering Journal*, vol. 59, no. 3, pp. 1629–1636, 2020.
- [12] A. W. M. Anourein, "An improvement on two iteration methods for simultaneous determination of the zeros of a polynomial," *International Journal of Computer Mathematics*, vol. 6, no. 3, pp. 241–252, 1977.
- [13] G. H. Nedzhibov, "Iterative methods for simultaneous computing arbitrary number of multiple zeros of nonlinear equations," *International Journal of Computer Mathematics*, vol. 90, no. 5, pp. 994–1007, 2013.
- [14] P. D. Proinov and M. T. Vasileva, "On a family of Weierstrass-type root-finding methods with accelerated convergence," *Applied Mathematics and Computation*, vol. 273, pp. 957–968, 2016.
- [15] N. Rafiq, S. Akram, N. A. Mir, and M. Shams, "Study of dynamical behaviour and stability of iterative methods for non-linear equations with application in engineering," *Mathematical Problems in Engineering*, vol. 2020, p. 20, Article ID 3524324, 2020.
- [16] M. Shams, N. A. Mir, N. Rafiq, and S. Akram, "On dynamics of iterative techniques for non-linear equations with application in engineering," *Mathematical Problems in Engineering*, vol. 2020, p. 17, Article ID 5853296, 2020.
- [17] K. N. Weierstrass & Beweis, "Des Satzes dass jede ganze rationale Function einer Ver"anderlichen dargestellt werden kann als ein Product aus linearen Functionen derselben Ver"anderlichen," *Sitzungsber. K"onigl. Preuss. Akad. Wiss. Berlin II*, vol. 32, pp. 1085–1101, 1891.
- [18] F. Ahmad, E. Tohidi, and J. A. Carrasco, "A parameterized multi-step Newton method for solving systems of nonlinear equations," *Numerical Algorithms*, vol. 71, no. 3, pp. 631–653, 2016.
- [19] F. Ahmad, E. Tohidi, M. Z. Ullah, and J. A. Carrasco, "Higher order multi-step Jarratt-like method for solving systems of nonlinear equations: application to PDEs and ODEs," *Computers & Mathematics with Applications*, vol. 70, no. 4, pp. 624–636, 2015.
- [20] F. Soleymani, R. Sharma, X. Li, and E. Tohidi, "An optimized derivative-free form of the Potra–Pták method," *Mathematical and Computer Modelling*, vol. 56, no. 5–6, pp. 97–104, 2012.
- [21] D. V. Griffiths and I. M. Smith, *Numerical Methods for Engineers*, Chapman and Hall/CRC (Taylor and Francis Group), Special Indian Edition, Stanford, CL, USA, 2011.
- [22] M. G-Sanchez, M. Noguera, A. Grau, and J. R. Herrero, "On new computational local orders of convergence," *Applied Mathematics Letters*, vol. 25, no. 12, pp. 2023–2030, 2012.

Research Article

T-Shaped Control Plate Effect on Flow past a Square Cylinder at Low Reynolds Numbers

Maryam Shahab,¹ Shams Ul-Islam ,¹ and Ghazala Nazeer²

¹Department of Mathematics, COMSATS University Islamabad, Islamabad 44000, Pakistan

²The Government Sadiq College Women University, Bahawalpur 63000, Pakistan

Correspondence should be addressed to Shams Ul-Islam; islam_shams@comsats.edu.pk

Received 7 October 2021; Revised 31 October 2021; Accepted 22 November 2021; Published 2 December 2021

Academic Editor: Ahmed Zeeshan

Copyright © 2021 Maryam Shahab et al. This is an open access article distributed under the Creative Commons Attribution License, which permits unrestricted use, distribution, and reproduction in any medium, provided the original work is properly cited.

In this study, the influence of the T-shaped control plate on the fluid flow characteristics around a square cylinder for a low Reynolds numbers flow is systematically presented. The introduction of upstream attached T-shaped control plate is novel of its kind as T-shaped control plate used for the first time rather than the other passive control methods available in the literature. The Reynolds numbers (Re) are chosen to be $Re = 100, 150, 200,$ and 250 , and the T-shaped control plate of the same width with varying length is considered. A numerical investigation is performed using the single-relaxation-time lattice Boltzmann method. The numerical results reveal that there exists an optimum length of T-shaped control plate for reducing fluid forces. This optimum length was found to be 0.5 for $Re = 100, 150,$ and 200 and 2 for $Re = 250$. At this optimum length, the fluctuating drag forces acting on the cylinder are reduced by 134%, 137%, 133%, and 136% for $Re = 100, 150, 200,$ and 250 , respectively. Instantaneous and time-averaged flow fields were also presented for some selected cases in order to identify the three different flow regimes around T-shaped control plate and square cylinder system.

1. Introduction

Controlling of flow and suppression of fluid forces around bluff bodies is an important research area for engineers and scientists because of its practical importance in mechanical engineering, structures and buildings, aeronautical engineering etc., at high Reynolds number (Re). Applications at very low Reynolds number can be found in microdevices, such as in micro-electro-mechanical systems (MEMS), computer equipment's, and cooling of electronic devices. The flow past circular cylinders was mostly encountered in the earlier investigations. Among other bluff structures, square structure plays an important role in various engineering fields. The flow wake around the bluff structures can generate unsteady forces which have the potential to damage the structural integrity. Therefore, it is important to fully understand the flow characteristics and their resulting effects on the structure in order to control the structure integrity. Successful numerical simulation can show valuable flow

characteristics and information which can be very complicated to attain experimentally.

Successful flow control remarkably reduces the magnitude and effects of the fluctuating forces directly acting on the surfaces of the bluff body. One can use either active or passive techniques to control the wake and reduce the fluid forces. The passive technique does not require any external energy like the active technique. The previous experimental measurements and numerical studies for flow control include splitter plates [1–10] and control cylinders/rods [11–18] for Re between 80 and 2000. The development of passive methods of reduction of fluid forces and wake control is an active area of research.

Abdi et al. [1] numerically studied the flow characteristics over a circular cylinder using the commercial software COMSOL Multiphysics. It was concluded that single splitter plate and two splitter plates reduce the drag by about 15% and 23%, respectively. Islam et al. [2] studied numerically the reduction of fluid forces for flow past a square cylinder in the

presence of upstream, downstream, and dual splitter plates. The authors found that the drag force was reduced by up to 62.2%, 13.3%, and 70.2% for upstream, downstream, and dual splitter plates, respectively. Zhou et al. [3] experimentally observed that the upstream rigid splitter plate does not considerably reduce forces. Sharma and Eswaran [4] experimentally studied the flow past a square cylinder in presence of an attached flexible splitter plate at $Re = 400$. The authors observed that the drag coefficient varies non-monotonically due to various flow regimes. The experimental investigation was conducted to study the effect of an attached splitter plate on the rear side of the square cylinder at $Re = 485$ by Chauhan et al. [5]. They found 23% drag reduction and also found that the vortex shedding starts to suppress for the long length of the splitter plate. Dash et al. [6] numerically examined the fluid forces for flow past a square cylinder in presence of dual attached splitter plates. It was found that the drag was reduced by 21% for $Re = 100$. Soumya and Prakash [7] numerically studied the effect of downstream attached splitter plate with elliptic cylinder for Re between 50 and 200 using Streamline Upwind/Petrov–Galerkin (SUPG) based finite element method (FEM). It was concluded that the drag forces were significantly reduced as the length of the splitter plate increased. Several two-dimensional numerical investigations have thus been adopted in studies for the reduction of fluid forces using rigid, flexible, and dual splitter plates (e.g., Barman and Bhattacharyya [8], Sharma and Dutta [9], and Sarioglu [10]).

A numerical study on a flow past a circular cylinder in the presence of a control cylinder was carried out by Kim et al. [11]. They discussed in detail the flow characteristics by changing the positions of the control cylinder.

Islam et al. [12] numerically observed that the upstream control plate considerably reduced the drag forces and the shedding frequency for Re varying between 80 and 200 for flow past a square cylinder. Sharma and Dutta [13] experimentally examined the flow past a square cylinder in the presence of attached flexible foil, for different values of flexible foil length. Firat et al. [14] numerically examined the influence of a small control cylinder at the front of the square cylinder for various Reynolds numbers ($50 \leq Re \leq 200$), and it was found that the drag reduction occurs at gap spacing, $g = s/D = 2$ and 3. Here, s is the spacing between the control cylinder and the main square cylinder, and D is the size of the square cylinder. Yen et al. [15] experimentally examined the flow regimes, drag coefficient, lift coefficient, turbulence intensity, and vortex shedding frequency behind a square cylinder in the presence of an upstream control bar by varying the values of Re , rotation angles, and g values. They found that the upstream control bar reduces drag by about 57%. Zhu and Yao [16] numerically analyzed the effect of surrounding control cylinders for flow over a circular cylinder at intermediate Reynolds numbers. Different small control rods with the same diameter are placed around the main circular cylinder with uniform angle interval (θ) and gap spacing. For example, for four control rods, the angle interval is 9° . The authors found that the main circular cylinder attached to nine control rods with $\theta = 40^\circ$ and $g = 0.6$ can achieve a considerable vortex-induced vibration

suppression effect for a wide range of Reynolds numbers. A numerical study on a flow past a square cylinder in the presence of control rods was carried out by Zhu et al. [17] and Chauhan et al. [18]. They discussed in detail the suppression of vortex shedding and reduction of fluid forces. When one bluff body is placed in the wake of another bluff body, the fluid flow characteristics considerably depend on the gap spacing between the bluff bodies. Some representative numerical studies are those of Abbasi et al. [19] and Ahmad and Islam [20]. Abbasi et al. [19] numerically examined the flow fields and fluid forces around three inline cylinders and found considerable drag reduction for the downstream cylinders. Ahmad and Islam [20] observed various flow regimes and sensitivity of fluid forces for four cylinders in diamond arrangements. For a review of the various passive and active methods of drag reduction, the reader is referred to Rashdi et al. [21].

The flow past a square cylinder in the presence of an upstream attached T-shaped control plate is not studied yet. It is important to know how to control the wake and reduce the fluid forces with the different length of the upstream attached T-shaped control plate. The main motivation for the current work is to examine in detail whether the T-shaped control plate considerably reduced the fluid forces and suppressed the vortex shedding? Also, we aim to characterize wake structure behavior, as a function of the length of T-shaped control plate and Reynolds numbers. The other important aim is to identify the suitable length of the T-shaped control plate that is associated with minimum drag and maximum suppression of vortex shedding. To get reasonably reliable knowledge of important design parameters such as drag and lift forces, vortex shedding frequency, and wake size is very important. We believe that this study will further enrich the drag reduction database using a new passive technique (T-shaped control plate).

The paper is organized as follows. In Section 2, lattice Boltzmann method, problem description, boundary conditions, grid independence study, domain independence study, and validation of the developed code are presented with brief discussion. Section 3 includes the numerical results in detail. Finally, in Section 4, conclusions are drawn based on the present numerical results.

2. Lattice Boltzmann Method and Computational Details

Recently, the lattice Boltzmann method (LBM) has been applied successfully to a number of flow problems (see [19, 20] and some references cited in those works). The LBM is a compressible method, the Mach number, $Ma = U_\infty / \sqrt{RT}$ is set to less than 0.3 so that the compressible effect is negligible [22]. The reason is that we are interested in isothermal flow. In case of isothermal flow, $RT = 1/3$ is to be chosen in the units of $c = \delta x / \delta t = 1$. Here, $c = \delta x / \delta t$, δx , and δt are the lattice constant and the time step size, respectively. The governing differential equations for such fluid flow problems mainly consist of the equations of continuity and momentum, as follows:

Continuity:

$$\frac{\partial u_x}{\partial x} + \frac{\partial u_y}{\partial y} = 0. \quad (1)$$

Momentum:

$$\frac{\partial u_x}{\partial t} + u_x \frac{\partial u_x}{\partial x} + u_y \frac{\partial u_x}{\partial y} = -\frac{\partial p}{\partial x} + \frac{1}{\text{Re}} \left(\frac{\partial^2 u_x}{\partial x^2} + \frac{\partial^2 u_x}{\partial y^2} \right), \quad (2)$$

$$\frac{\partial u_y}{\partial t} + u_x \frac{\partial u_y}{\partial x} + u_y \frac{\partial u_y}{\partial y} = -\frac{\partial p}{\partial y} + \frac{1}{\text{Re}} \left(\frac{\partial^2 u_y}{\partial x^2} + \frac{\partial^2 u_y}{\partial y^2} \right). \quad (3)$$

In equations (1) to (3), u_x and u_y are the dimensionless velocity components along the x -direction and y -direction of a Cartesian coordinate system. Here, p is the pressure.

There are many different lattice Boltzmann methods. For a detailed study of the various LBM methods, the reader is referred to [22, 23]. This section briefly introduces the LBM. The lattice Bhatnagar–Gross–Krook (BGK) model [22] with single-relaxation-time (SRT) is given by [22]

$$f_i(\mathbf{x} + \mathbf{e}_i \delta t, t + \delta t) = f_i(\mathbf{x}, t) + \frac{1}{\tau} (f_i^{(\text{eq})}(\mathbf{x}, t) - f_i(\mathbf{x}, t)). \quad (4)$$

Here, $f_i(\mathbf{x}, t)$, $f_i^{(\text{eq})}(\mathbf{x}, t)$, \mathbf{e}_i , and τ are the particle distribution function at (\mathbf{x}, t) , equilibrium distribution function (the Maxwell–Boltzmann distribution function) at (\mathbf{x}, t) , the particle velocity along the i th direction, and the single-relaxation-time parameter, respectively. Note the two-sides of equation (4) represent the solution. The left hand side applies as a streaming step, and the right hand side gives the collision between the particles. The derivation of Navier–Stokes (N-S) equations from LBM is well known nowadays and can be found in some recently published books (e.g., see [22, 23]). The solution of N-S equations can be calculated iteratively from equation (4).

Collision step:

$$f_i^*(\mathbf{x}, t + \delta t) = f_i(\mathbf{x}, t) + \frac{1}{\tau} (f_i^{(\text{eq})}(\mathbf{x}, t) - f_i(\mathbf{x}, t)), \quad (5a)$$

Streaming step:

$$f_i(\mathbf{x} + \mathbf{e}_i \delta t, t + \delta t) = f_i^*(\mathbf{x}, t + \delta t). \quad (5b)$$

Here, f_i^* represents the postcollision state. One advantage of this is that the streaming step is local in LBM and no need for any computation.

The two-dimensional nine-velocity lattice model ($d2q9$, where d is the dimensions and q is the numbers of particles) [22] is used in this study. In the $d2q9$ (see Figure 1) model, \mathbf{e}_i denotes the nine discrete velocity set, as follows:

$$\mathbf{e}_i = 0, \quad \text{for } i = 0,$$

$$\mathbf{e}_i = c \left[\cos\left((i-1)\frac{\pi}{4}\right), \sin\left((i-1)\frac{\pi}{4}\right) \right], \quad \text{for } i = 1, 2, 3, 4,$$

$$\mathbf{e}_i = c\sqrt{2} \left[\cos\left((i-1)\frac{\pi}{4}\right), \sin\left((i-1)\frac{\pi}{4}\right) \right], \quad \text{for } i = 5, 6, 7, 8. \quad (6)$$

The equilibrium distribution function ($f_i^{(\text{eq})}(\mathbf{x}, t)$) can be solved from

$$f_i^{(\text{eq})} = \rho \omega_i \left[1 + \frac{3}{c^2} (\mathbf{e}_i \cdot \mathbf{u}) + \frac{4.5}{c^4} (\mathbf{e}_i \cdot \mathbf{u})^2 - \frac{1.5}{c^2} (\mathbf{u} \cdot \mathbf{u}) \right]. \quad (7)$$

Here, ω_i is the weighting coefficient. The weighting coefficient, is given by

$$\begin{aligned} \omega_i &= \frac{4}{9}, & \text{for } i = 0, \\ \omega_i &= \frac{1}{9}, & \text{for } i = 1, 2, 3, 4, \\ \omega_i &= \frac{1}{36}, & \text{for } i = 5, 6, 7, 8. \end{aligned} \quad (8)$$

The density and momentum fluxes in the discretized velocity space can be obtained as

$$\rho = \sum_{i=0}^8 f_i = \sum_{i=0}^8 f_i^{(\text{eq})}, \quad (9)$$

and

$$\mathbf{u} = \frac{1}{\rho} \sum_{i=1}^8 f_i = \frac{1}{\rho} \sum_{i=1}^8 f_i^{(\text{eq})}. \quad (10)$$

The pressure can be calculated through the equation of state and is

$$p = \rho c_s^2. \quad (11)$$

The speed of sound for the $d2q9$ model is $c_s = c/\sqrt{3}$ [22]. The corresponding kinematic viscosity in the N-S equations (2) and (3) derived from equation (4) is [22].

$$\nu = (\tau - 0.5)c_s^2 \delta t. \quad (12)$$

It is also known that the single relaxation time LBM is simple and good for parallel systems. Its difficulty lies in the necessity of taking the value of the relaxation time parameter. The stability of the single relaxation time LBM mostly appears at high Reynolds numbers. In such a situation, we need to refine the grids with various relaxation times and to check the results (note that viscosity in lattice units is correlated to the relaxation time). This single relaxation time LBM is conditionally stable and is valid for

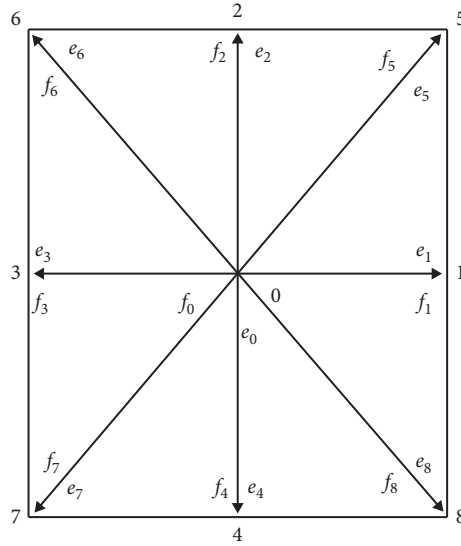


FIGURE 1: A two-dimensional nine-velocity lattice model ((d2q9).

$\tau > 0.5$. Here, in this problem, the values of τ for $Re = 100, 150, 200,$ and 250 are $0.5263, 0.5175, 0.5132,$ and $0.5105,$ respectively. One feature of LBM is that the pressure can be calculated through the equation of state instead of Poisson equation [22]. In LBM, we can find the pressure from the equation of state directly once knowing the density instead of using Poisson equation. For the LBM, the CFL (Courant–Friedrichs–Lewy) number is $CFL = e_i \delta t / \delta x = 1,$ which is fixed at unity.

Figure 2 presents the computational domain of flow past a square cylinder in the presence of an upstream attached T-shaped control plate. A square cylinder of size D is placed within the computational domain. A T-shaped control plate of length L is attached to the front surface of the square cylinder. $w = 0.1D$ is the width of the head of the T-shaped control plate. The distance between the left boundary of the domain and the front surface of the T-shaped control plate is $L_u = 10D,$ whereas the downstream distance of the domain from the rear surface of the square cylinder to the right boundary of the domain is $L_d = 39D.$ The distance between the upper and lower walls is kept as $L_y = 13D,$ resulting in a blockage ratio ($\beta = L_y/D$) = 13. $L_x = 50D$ is the length of the computational domain. A Cartesian grid was employed, and the origin $(0, 0)$ is set at the center of the main square cylinder. The details of the simulation parameters are summarized in Table 1. C_D and C_L are the drag forces and lift forces in the streamwise and transverse directions, respectively.

The following boundary conditions are incorporated in the present study.

- (i) At inlet, uniform inflow velocity is applied, $u = 0.04385, v = 0$
- (ii) At outlet, convective boundary condition is applied [24]

- (iii) At the upper and lower walls of the domain, no-slip ($u = v = 0$) is applied
- (iv) At the square cylinder and T-shaped control plate surfaces, no-slip boundary condition is imposed

The forces acting on the surfaces of the square cylinder can be calculated from the momentum-exchange method [25].

The implementation of the LBM is simple and straightforward. The following steps are presented for calculating forces and fluid properties:

- (i) Specify the streaming time step $\delta t.$ Calculate the single relaxation time parameter τ
- (ii) The local distribution function must be updated through collision step (equation (5a))
- (iii) The fluid particles are streamed to neighboring streaming lattice nodes through the streaming step (equation (5b))
- (iv) Implement suitable initial and boundary conditions for the distribution function
- (v) Calculate macroscopic variables (equations (9) and (10))
- (vi) Repeat steps (ii) to (iv) until the convergence criteria or the assigned maximum iteration numbers are reached

It is noticed that the lattice Boltzmann equation only requires the streaming step and collision step to evolve the fluid filled with complex nonlinearities. No special treatment is required for nonlinear terms in Navier–Stokes equations. The LBM explicitly calculates the pressure from the density. For computations, the simulation parameters are shown in Table 1.

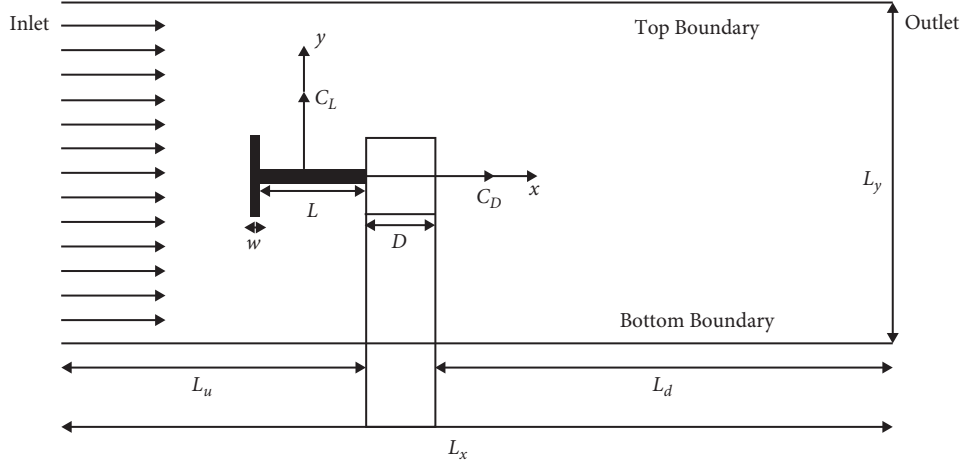


FIGURE 2: Schematic diagram of the proposed problem.

TABLE 1: Simulation parameters.

Re	U_∞	τ
100	0.04386	0.5263
150	0.04386	0.5175
200	0.04386	0.5132
250	0.04386	0.5105

The vorticity (dimensional) is defined as

$$\omega_z = \frac{\partial v}{\partial x} - \frac{\partial u}{\partial y}. \quad (13)$$

Here, u and v are the velocity components in the streamwise direction and transverse direction, respectively. It is to be noted that the vorticity is calculated by using a second-order central difference scheme and is then non-dimensionalized by the uniform inflow velocity (U_∞) and the side length of the square cylinder (D):

$$\phi_z = \frac{D\omega_z}{U_\infty^2}. \quad (14)$$

For analysis, we have defined the following non-dimensional parameters as given in equations (15)–(18)

$$Re = \frac{U_\infty D}{U}, \quad (15)$$

$$C_D = \frac{F_x}{0.5 \rho U_\infty^2 D}, \quad (16)$$

$$C_L = \frac{F_y}{0.5 \rho U_\infty^2 D}, \quad (17)$$

$$St = \frac{f_s D}{U_\infty}. \quad (18)$$

Here, Re , C_D , C_L , and St are the Reynolds number, drag coefficient, lift coefficient, and Strouhal number, respectively. It is to be noted here, F_x and F_y are the drag and lift forces experienced by the square cylinder along with the streamwise and transverse directions, respectively. These

forces are calculated using the momentum-exchange method [25]. f_s is the vortex shedding frequency calculated using the fast Fourier transformation (FFT) of the time series of the lift coefficient, C_L .

The stopping criteria once we get the steady state is

$$\frac{\sum_{ij} |u_{ij}^{(n+1)} - u_{ij}^n|}{\sum_{ij} |u_{ij}^{(n+1)}|} \leq 1 \times 10^{-6}. \quad (19)$$

It is noticed that $U_\infty = \delta x / \delta t U_{lb}$ represents the velocity in a system of lattice units. Here, U_{lb} represents the lattice Boltzmann velocity. In LBM, U_{lb} is proportional to the Mach number of the fluid. In Tables 2–5, the percentage deviation is also given in brackets. For $D = 10, 20, 30$, and 40 , the mean drag coefficient (C_{Dmean}), Strouhal number (St), root-mean-square value of drag coefficient (C_{Drms}), and lift coefficient (C_{Lrms}) values are as shown in Table 2. Here, $D (= \delta x)$ represents the lattice units on each side of the square cylinder and T-shaped control plate. The numerical results for C_{Dmean} , St , C_{Drms} , and C_{Lrms} in Tables 3–5 for different values of blockage ratio ($\beta = L_y/D$), L_u , and L_d , respectively. The results presented in Tables 2–5 have been performed at $Re = 250$ and $L/D = 5$. Inspection of Table 2 shows, however, that the D effect dies away as $D \geq 20$. Guo et al. [24] proposed and used that $D = 20$ is reasonably good to achieve good numerical results for the square cylinder. The blockage ratio β is 7.7%. It is observed that the β -value beyond 13 does not have any considerable influence on the integral parameters presented in Table 3. It was previously expressed that a good two-dimensional result can be achieved for flow of a square cylinder with a blockage ratio greater than about 5% [39]. One can also see the effect of L_u and L_d in Tables 4 and 5, respectively. In the present numerical study, the value of the blockage ratio is already more than 5%. $D = 20$, $\beta = 13$, $L_u = 10D$, and $L_d = 39D$ is, therefore, used for all computations in the present numerical study.

In order to ensure the validity of the code, we calculate the integral parameter values for $Re = 100, 150, 200$, and 250 for comparison with available data for flow past a square cylinder without T-shaped control plate. A comparison of

TABLE 2: Effect of different grids points for $Re = 250$, $L/D = 5$, $\beta = 13$, $L_u = 10D$, and $L_d = 39D$.

D	C_{Dmean}	St	C_{Drms}	C_{Lrms}
10	-0.2985 (5.0%)	0.1135 (4.6%)	0.0359 (4.7%)	0.3156 (4.1%)
20	-0.2846	0.1083	0.0342	0.3028
30	-0.2804 (1.5%)	0.1072 (1.0%)	0.0336 (1.8%)	0.2987 (1.4%)
40	-0.2812 (1.2%)	0.1072 (1.0%)	0.0337 (1.5%)	0.2995 (1.1%)

TABLE 3: Influence of β for $Re = 250$, $L/D = 5$, $L_u = 10D$, and $L_d = 39D$.

β	C_{Dmean}	St	C_{Drms}	C_{Lrms}
6	-0.2972 (4.4%)	0.1132 (4.3%)	0.0356 (4.0%)	0.3152 (4.0%)
13	-0.2846	0.1083	0.0342	0.3028
18	-0.2832 (0.5%)	0.1075 (0.7%)	0.0338 (1.2%)	0.3004 (0.8%)

TABLE 4: Influence of L_u for $Re = 250$, $L/D = 5$, $\beta = 13$, and $L_d = 39D$.

L_u	C_{Dmean}	St	C_{Drms}	C_{Lrms}
5	-0.2698 (5.5%)	0.1148 (5.7%)	0.0359 (4.7%)	0.3192 (5.1%)
10	-0.2846	0.1083	0.0342	0.3028
15	-0.2798 (1.7%)	0.1066 (1.6%)	0.0337 (1.5%)	0.2987 (1.4%)
20	-0.2803 (1.5%)	0.1066 (1.6%)	0.0338 (1.2%)	0.2998 (1.0%)

TABLE 5: Influence of L_d for $Re = 250$, $L/D = 5$, $\beta = 13$, and $L_u = 10D$.

L_d	C_{Dmean}	St	C_{Drms}	C_{Lrms}
15	-0.2739 (4.0%)	0.1132 (4.3%)	0.0356 (4.0%)	0.3165 (4.3%)
25	-0.2846	0.1083	0.0342	0.3028
35	-0.2802 (1.4%)	0.1069 (1.3%)	0.0337 (1.5%)	0.2987 (1.4%)
45	-0.2814 (1.1%)	0.1069 (1.3%)	0.0339 (0.9%)	0.3001 (0.9%)

the present results with the available data is given in Table 6. Our numerical results are generally in good agreement with available published data. The present results almost fell within the range of available numerical values, even some experimental values (Okajima [27], Norberg [28]). There are some slight differences between the present and experimental results. Their differences arise from experimental uncertainties, using various boundary conditions, the effect of blockage, grid structures, etc.

3. Results and Discussion

It is clear from previous investigations that the reduction of fluid forces and wake control depend on active and passive techniques. Keeping in view these importance, the present study was conducted to systematically analyze the importance of upstream attached T-shaped control plate length, ranging from $L/D = 0.5$ to 8 at Reynolds numbers, $Re = 100$, 150, 200, and 250. The present numerical results are calculated after the dynamic steady-state condition is reached (see equation (19)). The most important findings on the basis of our numerical investigation will be presented in this section in detail.

Figures 3(a)–3(e) presents the vorticity contours visualization around the square cylinder with and without a T-shaped control plate. Five different cases, one is without

T-shaped control plate ($L/D = 0$) and another four cases with different T-shaped control plate lengths ($L/D = 2, 4, 6, 8$) are considered for the various flow pattern investigation. The solid and dotted lines represent the positive and negative vortices, respectively. It can be seen from the figure that there is no vortex shedding from the T-shaped control plate at any length due to its attachment with the main square cylinder. Strouhal number (St) of the isolated cylinder and the square cylinder with upstream attached T-shaped control plate at lengths of 2, 4, 6, and 8 are 0.1510, 0.1618, 0.1316, 0.0896, and 0.1316, respectively. It is observed from the St values that the length of the T-shaped control plate caused a decrease and increase in the vortex shedding frequency of the main square cylinder. This decrease and increase can be further confirmed from the vorticity graphs. Qualitatively, the number of vortices that appeared behind the main square cylinder decreased from 13 to 10 for $L/D = 2$ and 4, to 6 for $L/D = 6$ and then increased from 6 to 11 for $L/D = 6$ and 8. It is observed that the formation of vortices is quite sensitive to the length of the upstream attached T-shaped control plate. From these figures, we can draw some important conclusions about flow characteristics. For all L/D values in Figures 3(a)–3(e), the alternate generation of shed vortices can be clearly seen behind the main square cylinder. This flow is called the single bluff-body flow regime. Shed vortices travel in alternate fashion throughout the flow field. We further divided the single bluff-

TABLE 6: Comparison of present results of flow past a square cylinder with available results.

Re = 100	C_{Dmean}	St	C_{Drms}	C_{Lrms}
Present	1.4125	0.1450	0.0035	0.1780
Dash et al. [6] (num)	1.460	0.1440	...	0.1840
Luo et al. [26] (exp)	...	0.142–0.145
Okajima [27] (exp)	...	0.140
Norberg [28] (exp)	...	0.140
Sohankar et al. [29] (num)	1.444	0.1450	0.0019	0.130
Saha et al. [30] (num)	0.0030	0.122
Re = 150	C_{Dmean}	St	C_{Drms}	C_{Lrms}
Present	1.4012	0.1520	0.0172	0.2732
Okajima [27] (exp)	...	0.1420
Norberg [28] (exp)	...	0.1550
Sohankar et al. [29] (num)	1.4080	0.1610	0.0061	0.1770
Saha et al. [30] (num)	0.0170	0.2740
Re = 200	C_{Dmean}	St	C_{Drms}	C_{Lrms}
Present	1.4268	0.1510	0.0294	0.3250
Okajima [27] (exp)	...	0.1440
Norberg [28] (exp)	...	0.1520
Sohankar et al. [29] (num)	1.424	0.165	0.0121	0.240
Saha et al. [30] (num)	0.0260	0.305
Dutta et al. [31] (exp)	1.410	0.154
Re = 250	C_{Dmean}	St	C_{Drms}	C_{Lrms}
Present	1.4432	0.1482	0.0348	0.4050
Sohankar et al. [29] (num)	1.4490	0.1510	0.0162	0.375
Saha et al. [30] (num)	0.0320	0.150

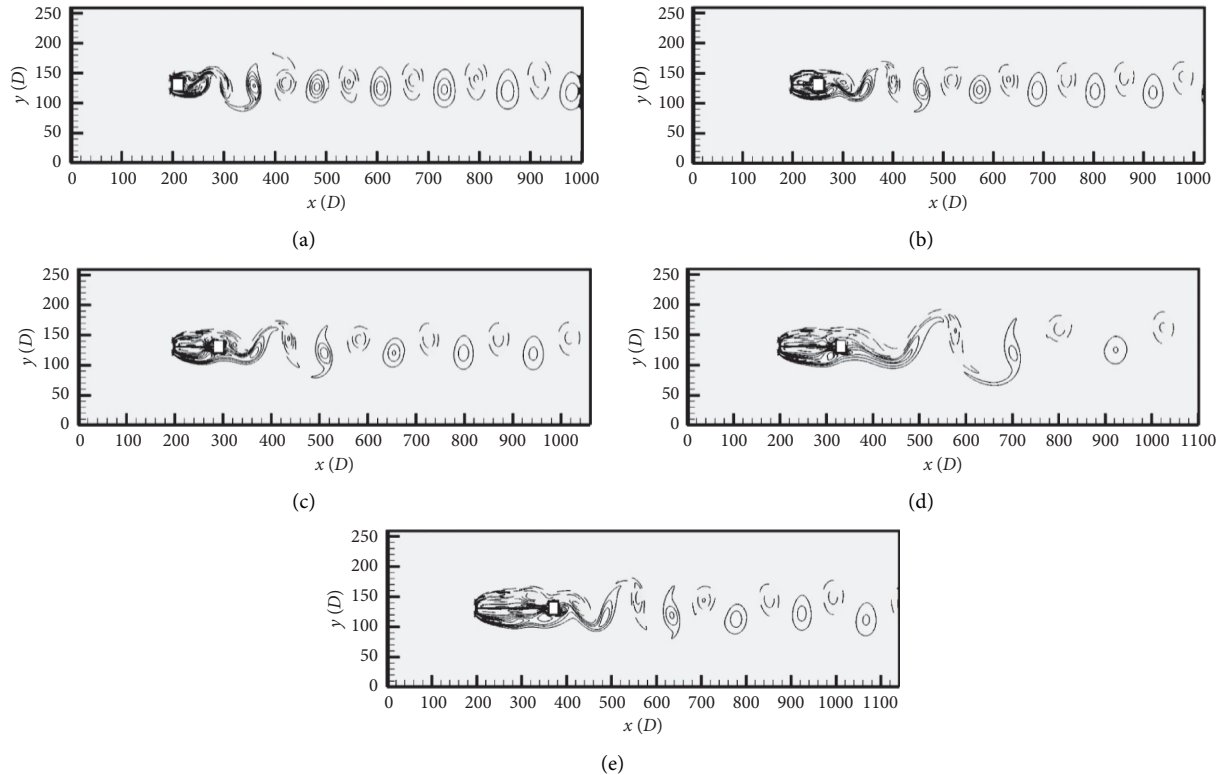


FIGURE 3: Instantaneous vorticity contours visualization of square cylinder in presence of attached T-shaped control plate at $Re = 200$. (a) Square cylinder without T-shaped control plate. (b) $L/D=2$. (c) $L/D=4$. (d) $L/D=6$. (e) $L/D=8$.

body flow regime into two different flow regimes. One is called the single bluff body with primary vortex shedding frequency (regime-I), and the second one is called the single

bluff body with secondary frequencies together with primary vortex shedding frequency (regime-II). In the case of regime-I, one can see only one dominant shedding frequency peak in

the power spectra (see Figures 4(a) and 4(b)). While in the case of regime-II, one can see some minor extra peaks called secondary frequencies together with the dominant vortex shedding frequency (Figures 4(c) and 4(d)). It can also be seen from Figures 3(b)–3(e), the generated shear layers from the bottom and top side of the head of the T-shaped control plate attach to the front and bottom and top sides of the main square cylinder, and then, they combined with the generated shed vortices from the main square cylinder.

Figures 5(a)–5(e) shows the instantaneous streamlines at different T-shaped control plate lengths at $Re = 200$. It is observed that the T-shaped control plate length will affect flow features, especially in the wake region.

At $L/D = 0$ (Figure 5(a)) where it is the single bluff body flow pattern, one bigger eddy is located behind the rear surface of the square cylinder without T-shaped control plate. In Figure 5(b) as $L/D = 2$, there is a small eddy at the bottom of the main square cylinder. The streamline graph further confirms that the shear layers separated from the top and bottom surfaces of the head of the control plate directly reattach to the main square cylinder. Some waviness was also observed in the wake region for all cases presented in Figures 5(a)–5(e). It is clear from Figure 5(c) that there is no close recirculation zone behind the main square cylinder. The streamline graphs further confirm that the separation point changes due to T-shaped attached control plate as compared to the square cylinder (without T-shaped control plate).

Figures 6(a)–6(e) shows the instantaneous pressure contours at different T-shaped control plate length at $Re = 200$. The use of an upstream attached T-shaped control plate, irrespective of what the flow regime is, reduces the pressure difference between the front surface of the T-shaped control plate and the rear surface of the main square cylinder. As a result, a reduction of the mean drag coefficient in comparison with an isolated occurs. Furthermore, as the L/D value increases, the pressure distribution above and below the length of the T-shaped control plate also changes.

As we have seen from the vorticity contours and streamlines that flow changes its characteristics from single bluff body to steady flow and then from steady flow to unsteady flow by changing the values of L/D . This can also be analyzed from Figures 7(a) and 7(b) which presents the time histories of C_D and C_L at various values of L/D and shows that the amplitude of forces changed by varying L/D values. It is seen from Figure 6(a) that the C_D variation is very sensitive to the T-shaped control plate length. The variation of C_D for $L/D = 4, 6,$ and 8 are more sensitive than that for $L/D = 2$. The oscillations amplitude for the C_L in comparison with an isolated cylinder (without T-shaped control plate) decreases.

The power spectrum of lift coefficients at $L/D = 2, 4, 6,$ and 8 are shown in Figures 4(a)–4(d). The highest peak in the graphs refers to the primary vortex shedding frequency (St_p), and the other small peaks represent the secondary frequencies (St_s). In the power spectra graph, ‘E’ stands for energy. The single dominant peak confirms the periodic nature of lift coefficients at $L/D = 2$ and 4 (Figure 6(b)). Some

small modulation exists for $L/D = 6$ and 8 in lift coefficients, and as a result, one can see one or two extra small peaks together with the primary vortex shedding frequency.

The instantaneous vorticity contours visualization shown in Figures 8(a)–8(d) clearly illustrates the influence of Re on the flow characteristics. It should be noted that, in the case $L/D = 5$ at $Re = 100$, we observed complete suppression of vortex shedding. This flow regime is called the steady flow regime (regime-III). In steady flow regime only, the streamline can be seen behind the cylinder without any recirculation or shed vortices. These figures clearly illustrate the basic difference between steady flow and single bluff-body flow. Flow behind the main square cylinder, identified by Karman vortex street at $Re = 150$, has almost similar vortices in alternating fashion from upper and lower surface of the main square cylinder (Figure 8(b)). This flow is called regime-I. In addition, as Reynolds number increased, we observed regime-II. Figures 8(c) and 8(d) show that periodic vortex shedding is further maintained when we increased the Reynolds number Re to 250 . As Re increases above 100 , the number of shed vortices increases, and consequently, the drag force decreases; see Figure 9(a). It is also noted that the vortices are shed alternatively, and the sizes of the shed vortices from the top and bottom surfaces of the main square cylinder are different. The latter tends to elongate in the near wake, and the former is almost round. This is because of the upstream attached T-shaped control plate length and increased Reynolds numbers. Furthermore, its strength increases as the value of Re increases. As a result, the Strouhal numbers of the square cylinder with the upstream attached T-shaped control plate at Reynolds numbers of $150, 200,$ and 250 are $0.1024, 0.1056,$ and 0.1104 , respectively.

Figures 10(a)–10(d) show the pressure distributions along the front and back sides of the main square cylinder with different Reynolds numbers at $L/D = 5$. As shown, the pressure distribution on the back side for all Reynolds numbers is considerably changed; thus, the remarkable differences in drag forces are mainly due to the differences in the pressure distribution along the surfaces of the length of the T-shaped control plate. It is observed that the maximum value of pressure exists at the center point of the front surface. However, as the value of Re changes, the pressure distribution on the surfaces of the length of the control plate changes considerably.

The graphical representation of C_D and C_L shown in Figures 9(a) and 9(b) further indicate the flow transitions. The lift coefficient represents the transverse force component which represents the magnitude of the vortex shedding, since no vortices shed from the main square cylinder; that is why, the lift force is steady for $Re = 100$ at $L/D = 5$. It is noticed that due to the steady flow nature the straight constant line can be clearly seen for C_D and C_L in Figures 9(a) and 9(b). The profiles of C_L confirm the periodic nature of the flow except for the C_D at $Re = 150, 200,$ and 250 . The periodic nature confirms that the vortices shed from the upper and lower sides of the cylinder with the same frequency. It is also observed that the C_L amplitude is somewhat increased as the value of Re increased. The negative drag

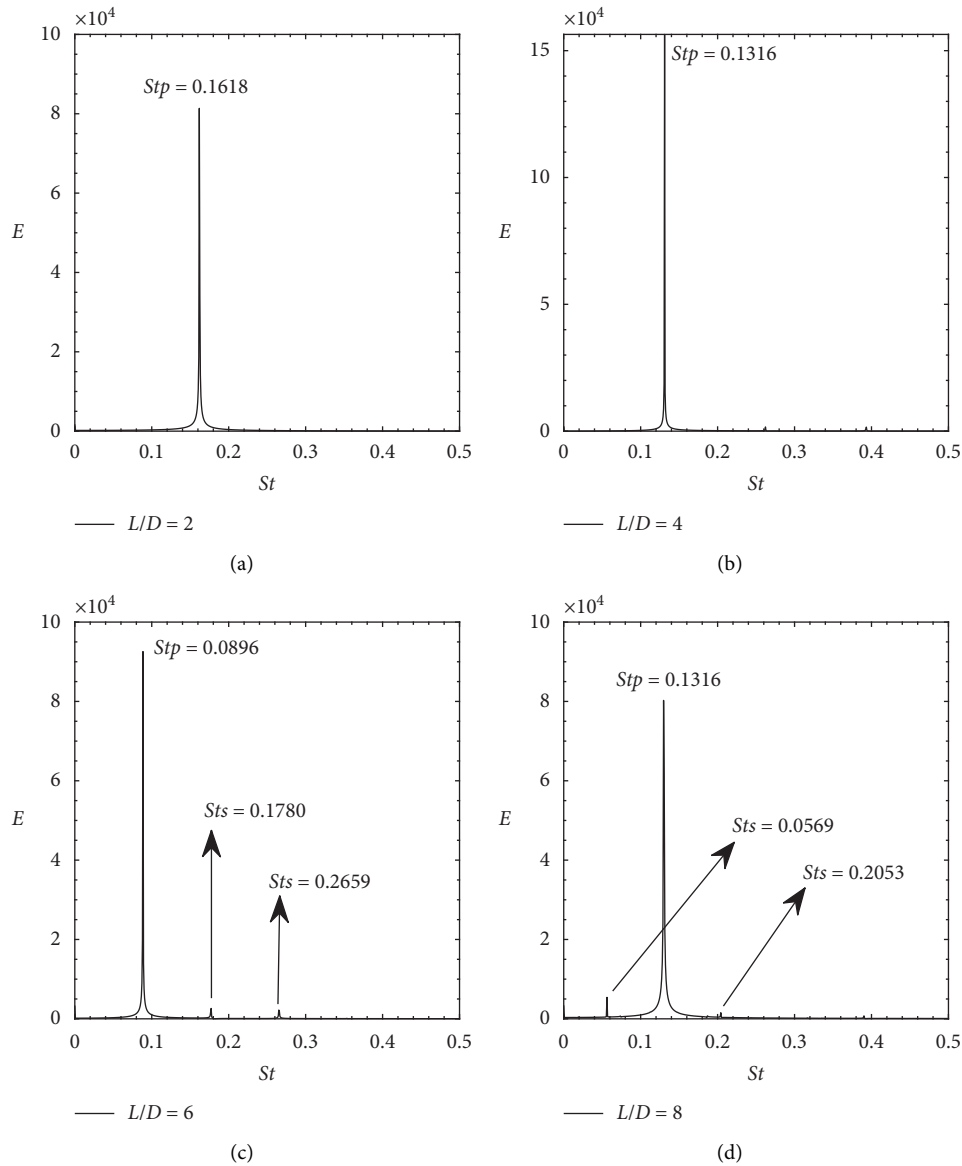


FIGURE 4: Power spectra analysis of fluctuating lift coefficient at $Re = 200$ for different T-shaped control plate length: (a) $L/D = 2$, (b) $L/D = 4$, (c) $L/D = 6$, and (d) $L/D = 8$.

value is observed for $Re = 150, 200,$ and 250 . Due to the presence of T-shaped control plate no periodic nature is observed for $Re = 150, 200,$ and 250 .

Figures 11(a)–11(c) shows the spectra analysis of the fluctuating lift coefficient at $L/D = 5$ for different Reynolds numbers. It is to be noted that due to the constant nature of C_L for $Re = 100$, no vortex shedding is observed behind the cylinder. The power spectra show two minor peaks together with the dominant vortex shedding frequency in the case of regime-II. But still, the primary vortex shedding frequency is the dominant frequency. The dominant primary vortex shedding frequency peak is seen in all the chosen cases presented in Figures 11(a)–11(c), which confirms the single frequency observed in the time trace analysis of lift coefficient C_L .

The instantaneous vorticity contour visualization shown in Figures 12(a)–12(e) clearly illustrates the influence of L/D

on the flow characteristics. It is clear from Figures 12(a)–12(d) that the vortices are shed alternatively from the upper and lower surfaces of the main square cylinder. The spacing between the two shed vortices is almost constant. However, the size of the vortex shed from the upper side of the square cylinder is comparatively larger than the size of the vortex shed from the lower side of the square cylinder. This may be due to the length of the T-shaped control plate, but still alternating vortex shedding can be clearly seen behind the square cylinder. The T-shaped control plate length effect can be seen more clearly from streamlines in Figure 12(e) for $L/D = 6$. In Figure 12(e), the flow is completely suppressed, and no alternate vortex shedding can be seen behind the square cylinder. This is called the steady flow regime (regime-III). It is also seen that the vortex formation length becomes longer, and the transverse spacing

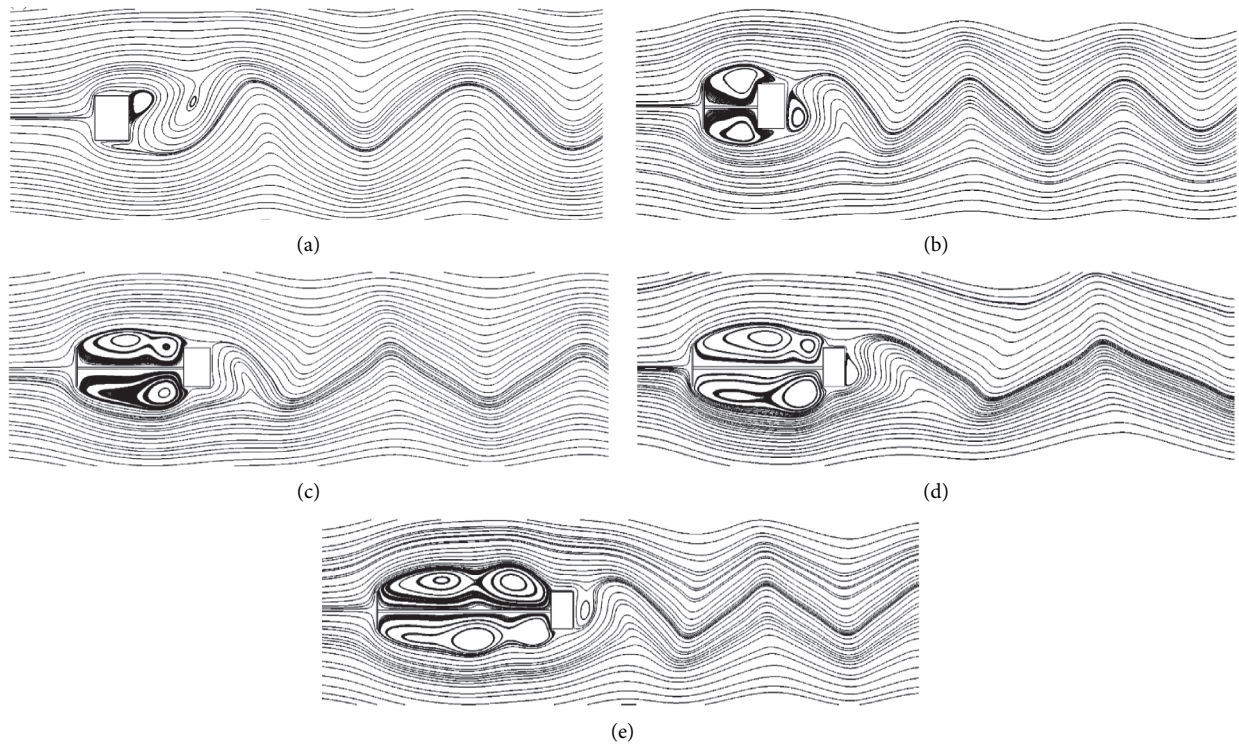


FIGURE 5: Comparison of the streamlines in the near wake of the main square cylinder with and without an upstream T-shaped control plate at at $Re = 200$: (a) square cylinder without T-shaped control plate, (b) $L/D = 2$, (c) $L/D = 4$, (d) $L/D = 6$, and (e) $L/D = 8$.

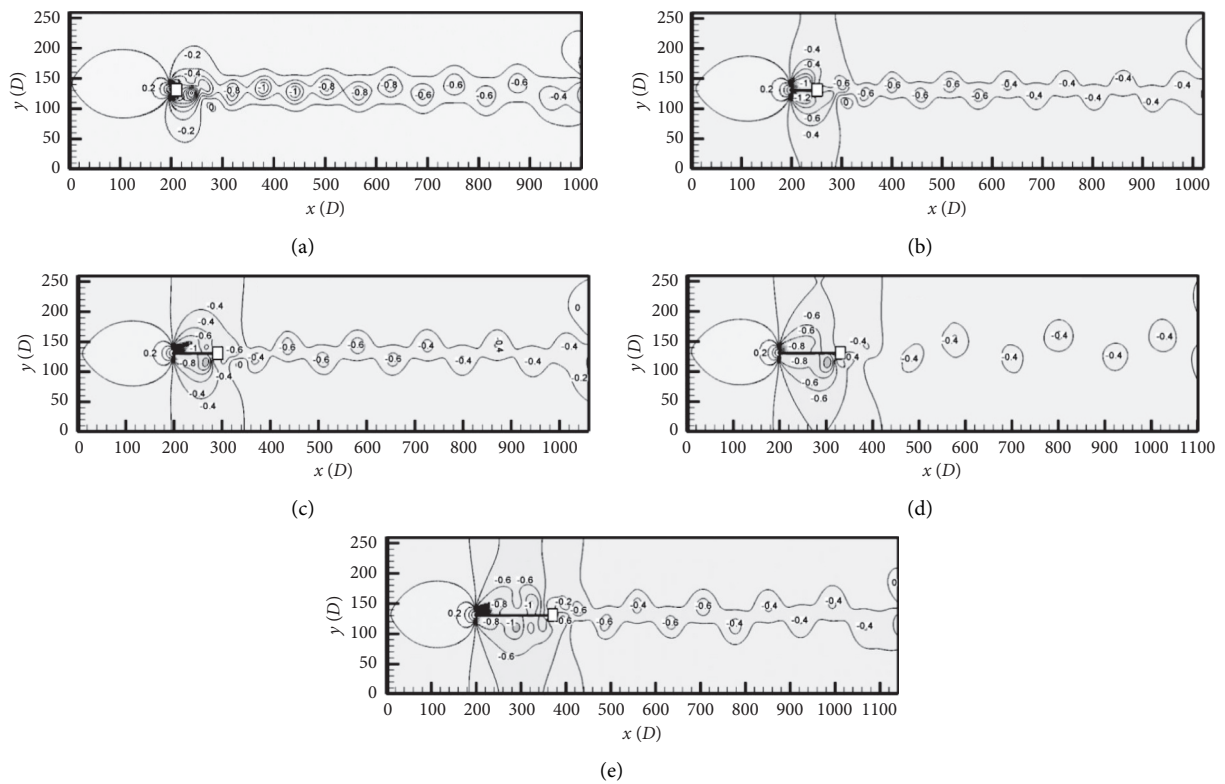


FIGURE 6: Pressure contours visualization of square cylinder in presence of attached T-shaped control plate at $Re = 200$: (a) square cylinder without T-shaped control plate, (b) $L/D = 2$, (c) $L/D = 4$, (d) $L/D = 6$, and (e) $L/D = 8$.

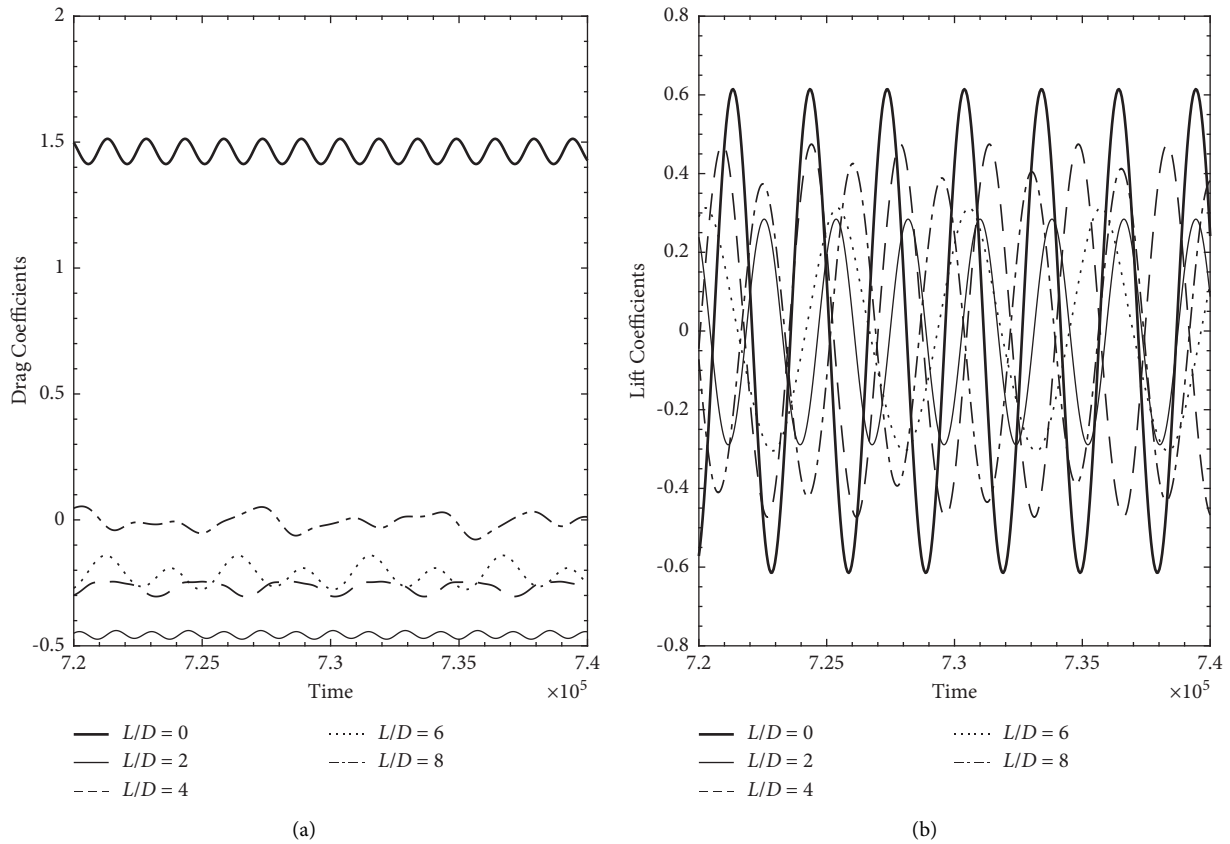


FIGURE 7: Time histories of (a) drag coefficients and (b) lift coefficients of square cylinder at $Re = 200$ for different T-shaped control plate length.

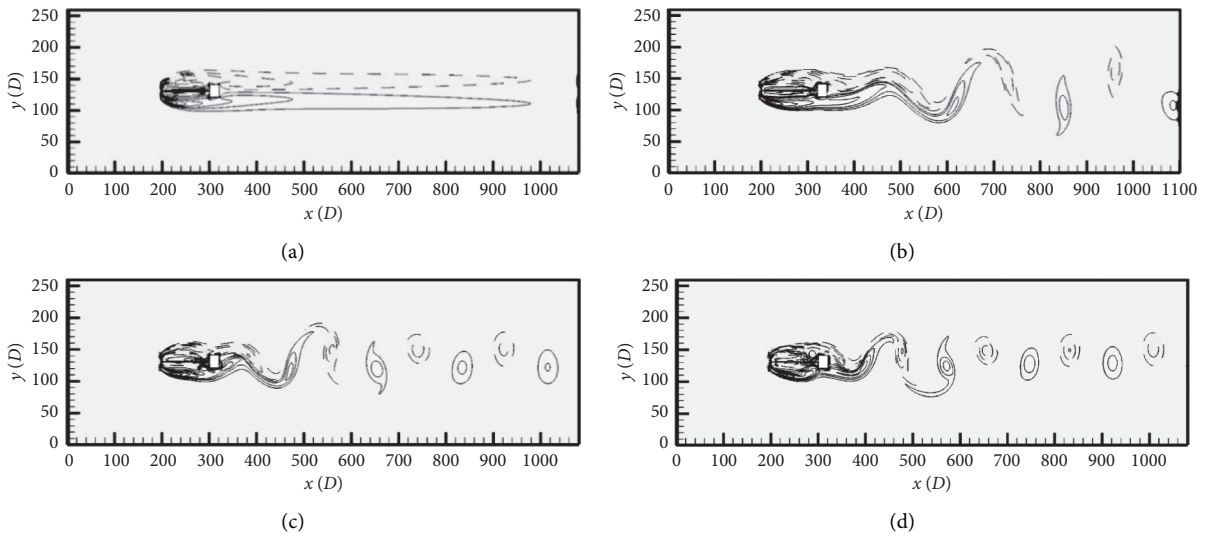


FIGURE 8: Instantaneous vorticity contours visualization at $L/D = 5$: (a) $Re = 100$, (b) $Re = 150$, (c) $Re = 200$, and (d) $Re = 250$.

between the shed vortices becomes smaller as the value of L/D increased from 0 to 4. Such observations were found by Zhou et al. [32] for flow past a circular cylinder using tripping rods at angles $(\theta) = 40^\circ$ and $Re = 200$. This confirms that the T-shaped control plate can also be used to understand the flow characteristics behind the bluff body.

As we have seen from the vorticity contours and streamlines that flow changes its characteristics from single bluff body to steady flow regime by changing the values of L/D . This can also be analyzed from Figures 13(a) and 13(b) which present the time histories of C_D and C_L at various values of L/D and show that the amplitude of forces changed by varying L/D

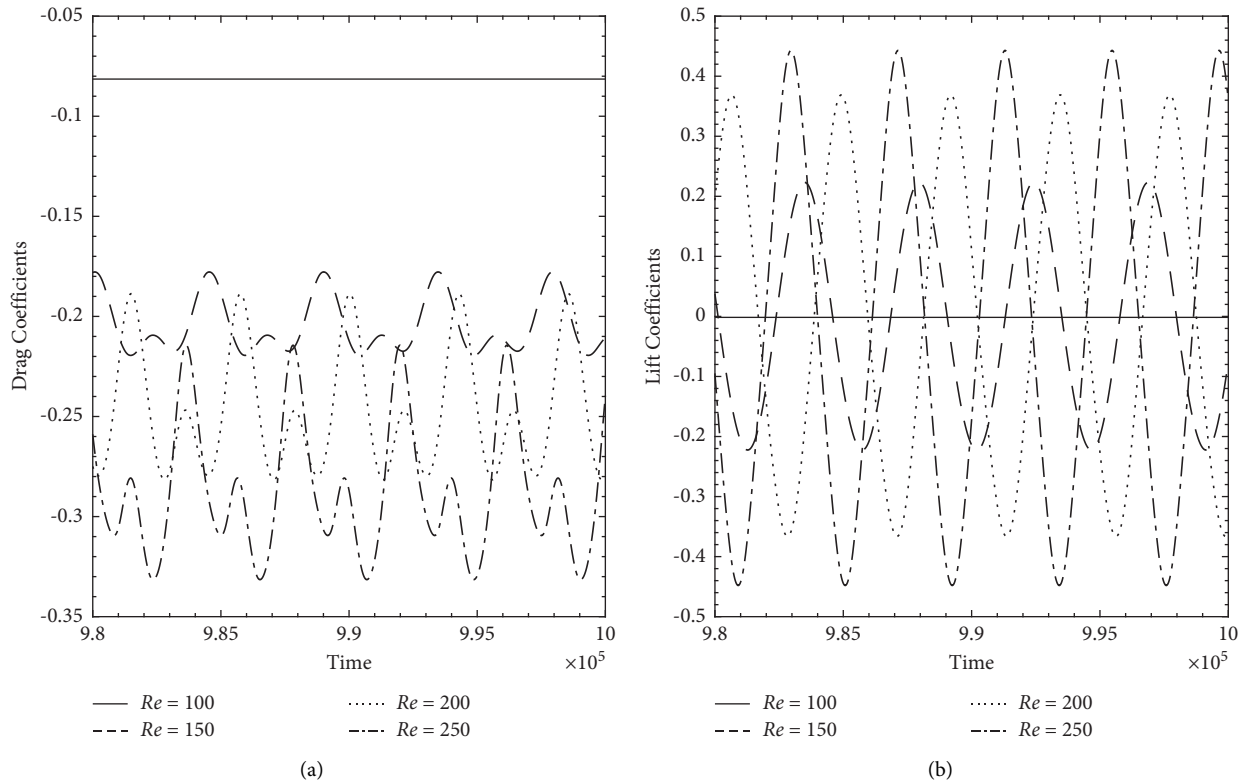


FIGURE 9: Time histories of (a) C_D and (b) C_L of square cylinder at $L/D=5$ for different Reynolds numbers.

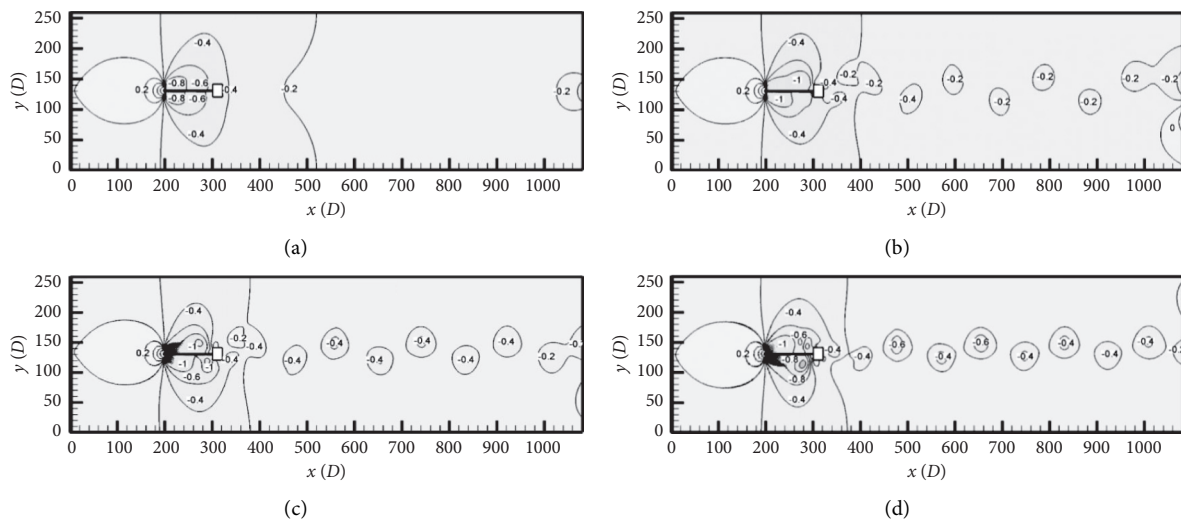


FIGURE 10: Pressure contours visualization at $L/D=5$: (a) $Re=100$, (b) $Re=150$, (c) $Re=200$, and (d) $Re=250$.

values. The lift coefficient of $L/D=1, 2,$ and 4 has periodic nature with smaller amplitude cycle compared to those observed for flow past an isolated cylinder ($L/D=0$) in Figure 13(b). At $L/D=6$, the constant behavior can be observed for the square cylinder. The periodic nature of C_L confirms the alternate shedding behaviour from cylinder at $L/D=0, 1, 2,$ and 4 . The periodic nature of C_L shows the periodic nature of the flow with almost constant amplitude. This periodic nature confirms that the vortices shed from the upper

and lower surface of the main square cylinder with same frequency. One can also observe that the C_L amplitude is somewhat increased in the case of $L/D=2$ than $L/D=4$.

The forces acting on the square cylinder in the streamwise and transverse directions by the fluid are the important criteria to analyze the flow characteristics quantitatively, and thus, the $C_{Dmean} St, C_{Drms}$ and C_{Lrms} are depicted in Figures 14(a)–14(h), respectively, where the solid and dotted straight lines refer to the case of a square cylinder

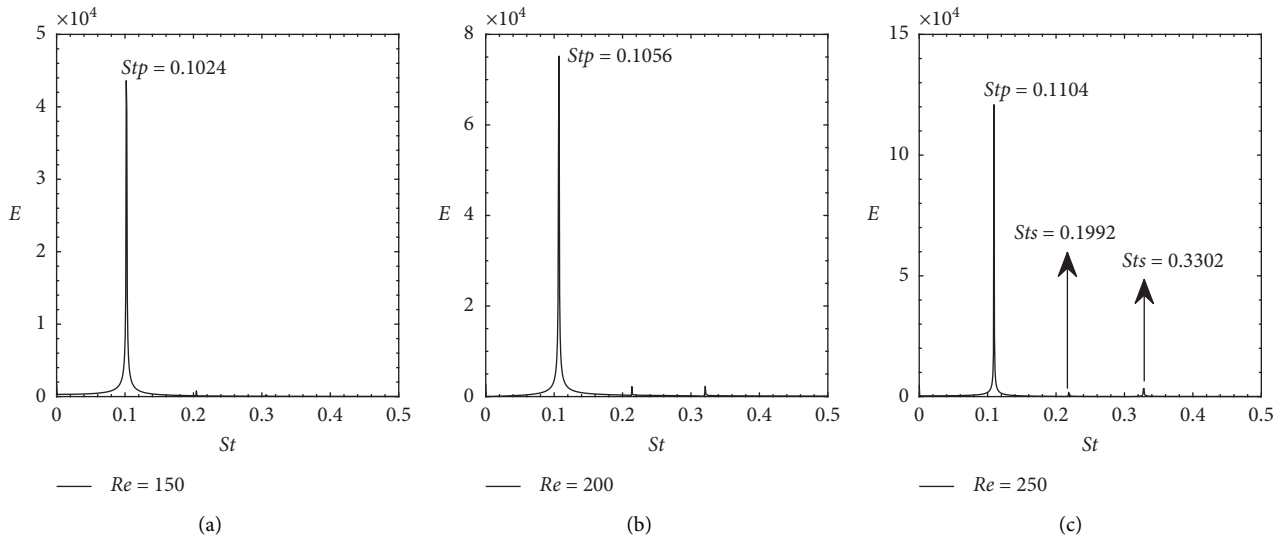


FIGURE 11: Spectra analysis of C_L using the FFT at $L/D=5$ for various Reynolds numbers: (a) $Re = 150$, (b) $Re = 200$, and (c) $Re = 250$.

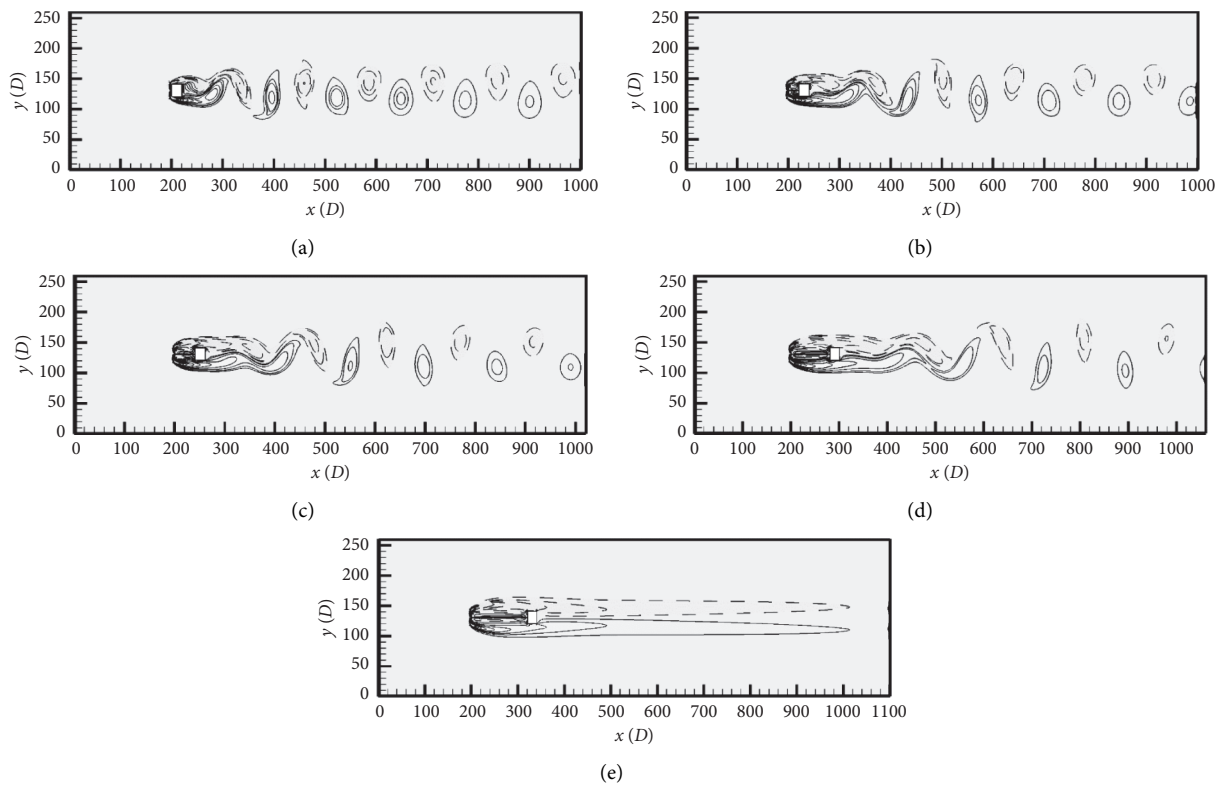


FIGURE 12: Instantaneous vorticity contours visualization at $Re = 100$: (a) $L/D=0$, (b) $L/D=1$, (c) $L/D=2$, (d) $L/D=4$, and (e) $L/D=6$.

without the T-shaped control plate. It is seen from Figures 14(a) and 14(b) that C_{Dmean} of the square cylinder with T-shaped control plate is lower than that of an isolated cylinder without the T-shaped control plate ($L/D=0$) for all considered Reynolds numbers. It is seen that the C_{Dmean} slightly increases with increasing Re . A maximum value of 0.1538 of C_{Dmean} is observed for $(L/D, Re) = (8, 200)$ and a

minimum value of -0.520 of C_{Dmean} is noticed for $(L/D, Re) = (0.5, 150)$. As the vortex length increases with narrow wake, the pressure on the rear surface of the square cylinder increases, and as a result, the drag reduces.

It is noticed that the St number decreases with the increase in L/D and experiences sudden jump at $L/D=7$ at $Re = 100, 150$, and 200 , which confirms the changes in flow

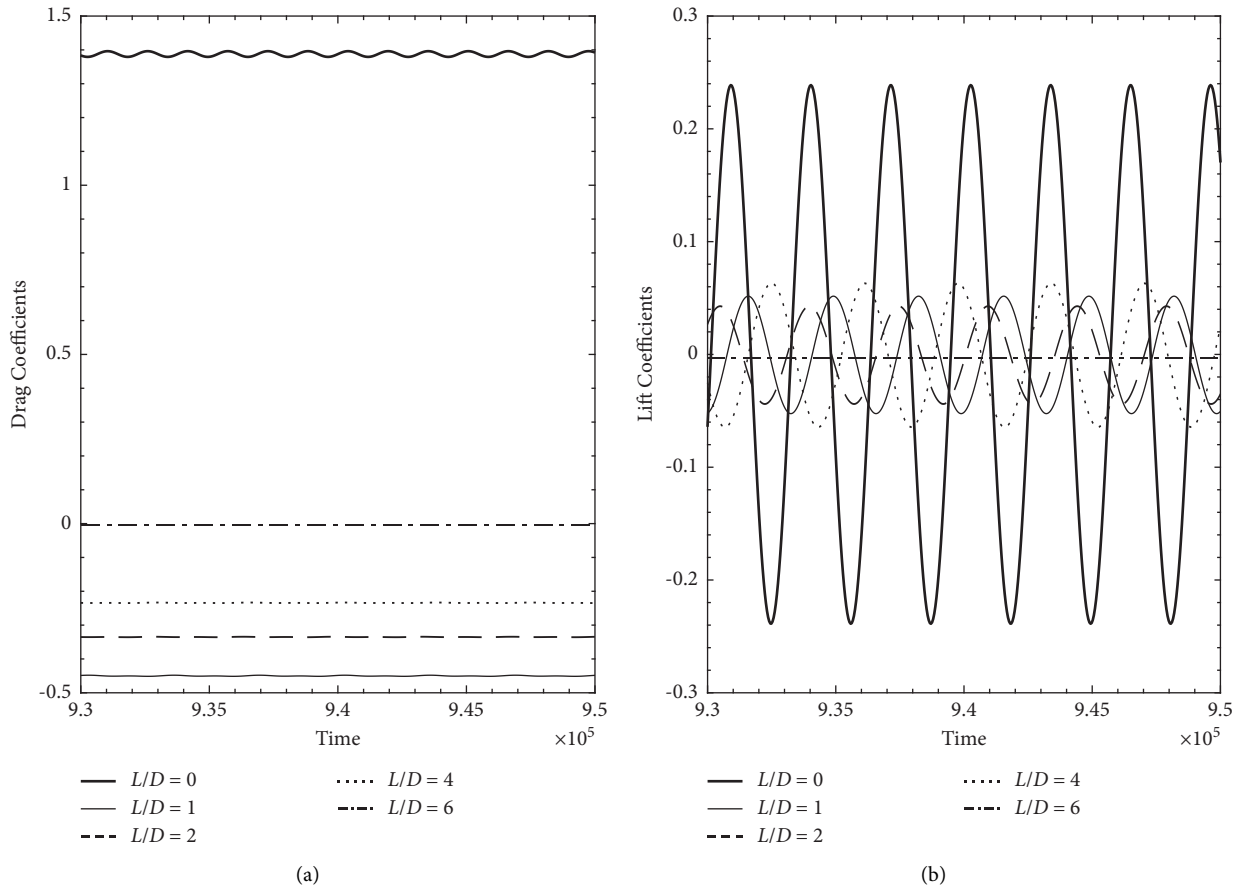


FIGURE 13: Time histories of (a) drag coefficients and (b) lift coefficients of square cylinder at $Re = 100$ for different T-shaped control plate length.

characteristics. The value of St for $L/D \geq 2.5$ exceeds the value of the single cylinder for $Re = 150, 200,$ and 250 (Figures 14(c) and 14(d)). It is to be noted that the variation trend of the St number with L/D is opposite to those of C_{Dmean} . There is a quick jump in St number for $Re = 150$ at $L/D = 7$. It was observed that two flow regimes (regime-I to regime-II) appear intermittently. The results further show that the Strouhal values are considerably lower than the isolated cylinder as the value of L/D increased. Generally, the St number of the square cylinder became lower than the isolated cylinder as the value of L/D increased. The slight increase in C_{Dmean} and quick decrease in Strouhal number is closely related to the wake structure changes behind the square cylinder.

It is seen from Figure 14(f) that, as the value of L/D increased, considerable changes in C_{Drms} are produced at $Re = 250$. It is noted that the effect of L/D on the C_{Drms} for $Re = 200$ and 250 (Figure 14(f)) as compared to $Re = 100$ and 150 (Figure 14(e)). The C_{Drms} for $L/D = 6$ to 8 at $Re = 250$ is much higher than that for a single square cylinder without T-shaped control plate (Figure 14(f)). In all other considered cases, the lift is smaller. As already discussed, flow features qualitatively above, when the L/D value increases, the C_{Lrms} increase. When the L/D value reaches a particular value, for example, 3.5 at $Re = 150$ (Figure 14(g)), there occurs a

maximum value. As L/D increases, C_{Lrms} increases first and reaches their maximum values for all Re values and then decreases (Figures 14(g) and 14(h)). It is found that, for $Re = 150, 200,$ and 250 the maximum value occurs at $L/D = 3.5, 3,$ and 3.5 , respectively. The C_{Lrms} associated with the square cylinder with the upstream attached T-shaped control plate for $Re = 100$ is lower than that of the isolated cylinder.

The C_{Lrms} values at $Re = 250$ (Figure 14(f)) are more scattered and either increased or decreased while changing the value of L/D . It can be seen from Figure 14(e) that the cylinder with the upstream attached T-shaped control plate had lower values of C_{Lrms} than the isolated cylinder at $Re = 100$ as the value of L/D increased. This can be attributed to the main reason that the shear layers downstream of the square cylinder are delayed by the use of the upstream attached T-shaped control plate. It can also be clearly seen that, for $Re = 150$ by increasing L/D up to 2.5 , the C_{Lrms} has a fixed value and considerably lower than the isolated cylinder value. However, by further increasing the length ($3 \leq L/D \leq 5.5$), C_{Lrms} increases and attains its maximum value and then starts to decrease slowly. In some specific cases, the value is more than the isolated cylinder. In general, increasing the length of T-shaped control plate from $L/D = 4$ onwards did not have a considerable effect on integral parameters.

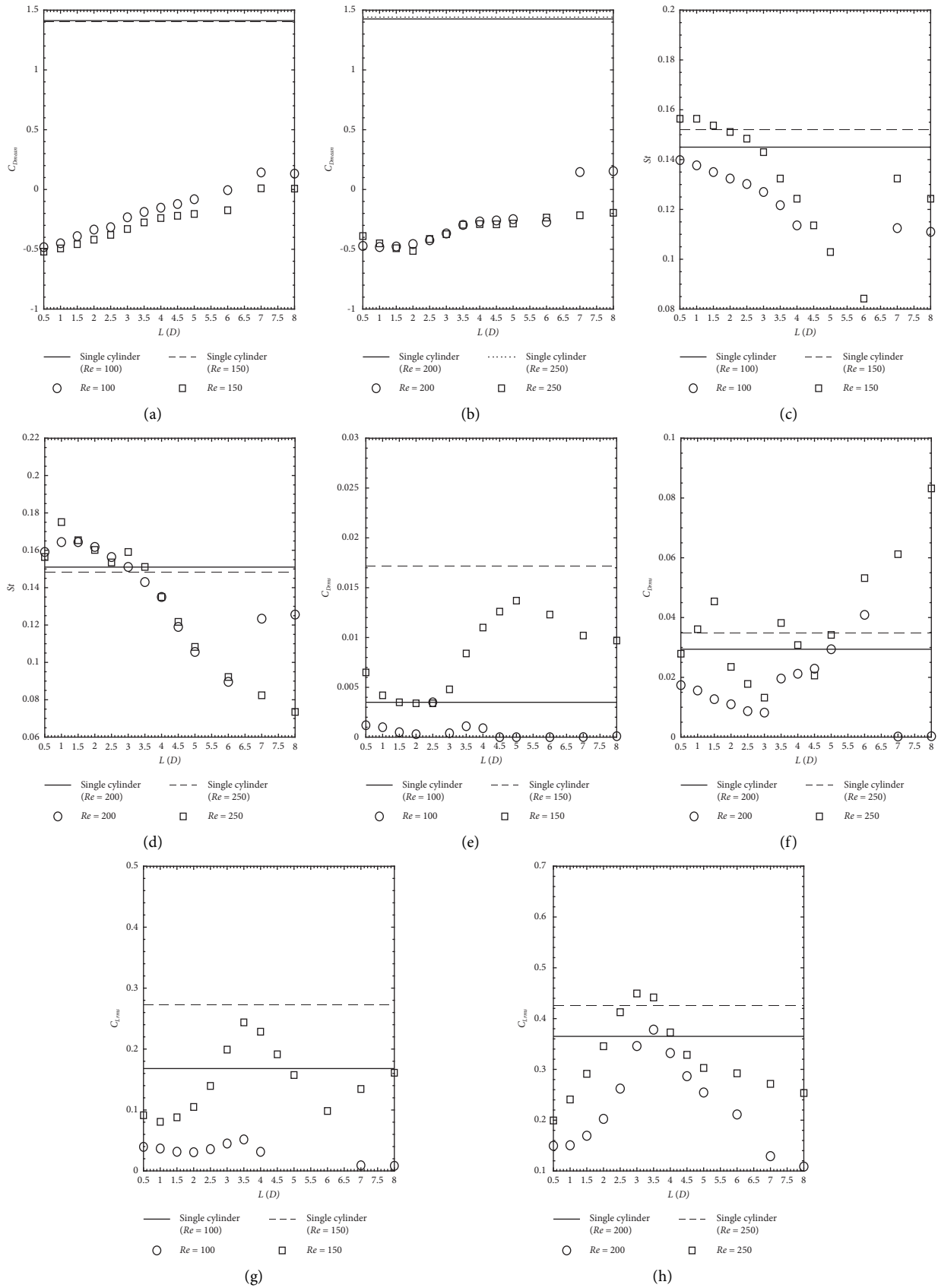


FIGURE 14: Variation of integral parameters of square cylinder with and without attached T-shaped control plate as a function of L/D at different fixed Re values: (a, b) C_{Dmean} (c, d) St , (e, f) C_{Drms} and (g, h) C_{Lrms} .

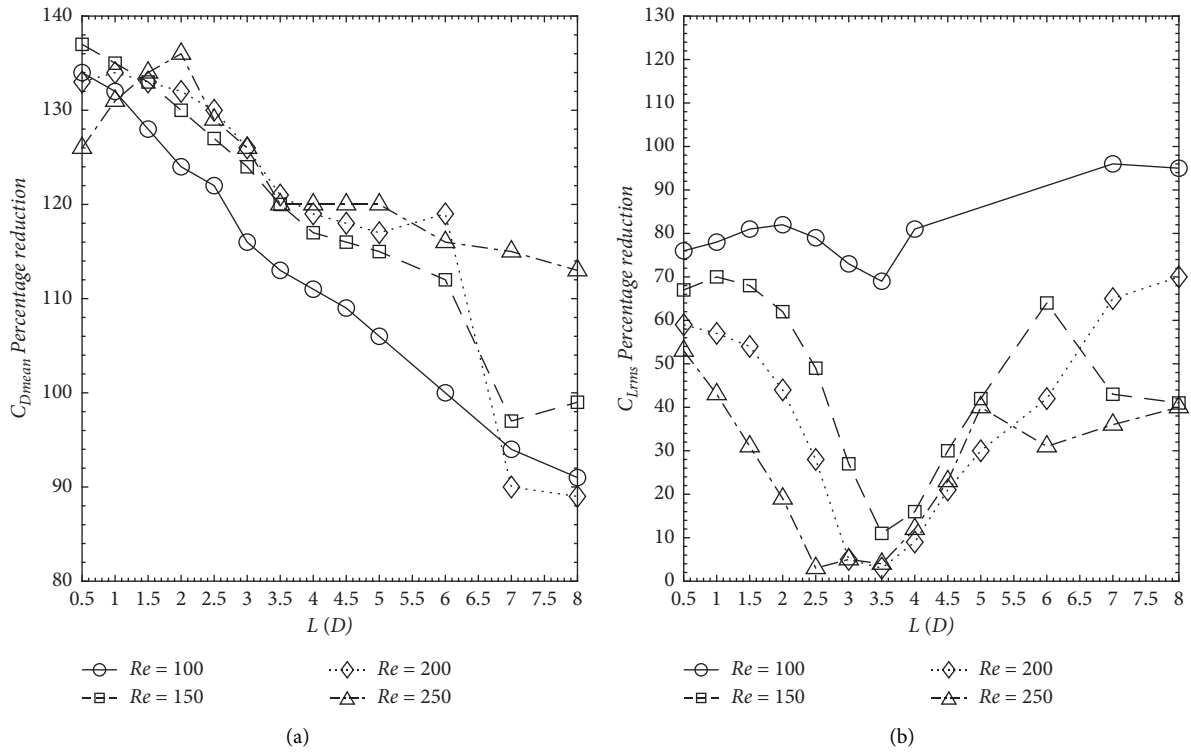


FIGURE 15: Percentage variation of (a) C_{Dmean} and (b) C_{Lrms} as a function of L/D at different fixed Re values.

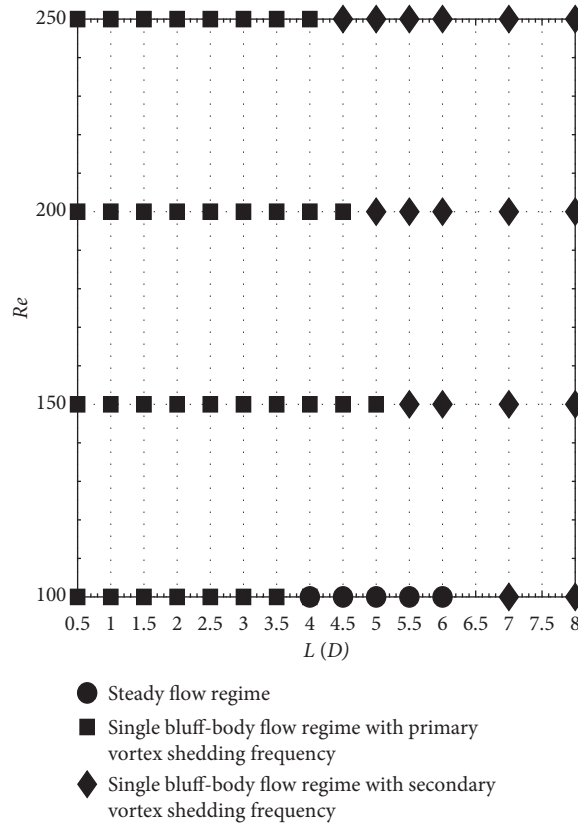


FIGURE 16: Flow regimes map as a function of L/D and Re .

TABLE 7: Wake length (L_w/D) of flow past a square cylinder in presence of upstream attached T-shaped control plate.

L/D	Re = 100	Re = 150	Re = 200	Re = 250
0.0	1.0	1.0	0.5	2.0
0.5	2.0	1.0	1.0	1.5
1.0	2.5	1.5	1.0	0.5
1.5	0.75	1.25	0.5	0.5
2.0	1.25	1.5	1.0	1.0
2.5	1.0	0.5	0.75	1.0
3.0	0.5	1.0	1.25	1.0
3.5	0.5	1.25	1.25	0.5
4.0	1.0	1.0	2.5	0.75
4.5	2.75	0.5	1.5	0.75
5.0	2.5	0.5	1.75	2.0
5.5	2.0	1.0	1.0	1.5
6.0	2.5	1.5	0.75	1.0
7.0	2.0	0.75	1.0	1.0
8.0	1.5	0.5	1.0	1.5

Figures 15(a) and 15(b) depicts the percentage variation of C_{Dmean} and C_{Lrms} for all the considered cases of T-shaped control plate length. It is noticed that, with increasing L/D , the percentage reduction in terms of C_{Lrms} increases. The previous studies suggest that the usually very small length of the splitter is good enough for maximum drag reduction and fluid forces suppression. Here we also observed that a small length ($L/D \geq 1.5$) of T-shaped control plate considerably reduced the drag forces. For example, at Re = 250, the reduction in C_{Dmean} is 126%, 131%, 134%, 136%, 129%, 126%, 120%, 120%, 120%, 120%, 116%, 115%, and 113% for the T-shaped plate with $L/D = 0.5, 1, 1.5, 2, 2.5, 3, 3.5, 4, 4.5, 5, 5.5, 6, 7, \text{ and } 8$, respectively.

According to the values of L/D and Re and based on the investigation of the time-averaged and instantaneous vorticity contours visualization on the T-shaped control plate and square cylinder, three major flow regimes are found in this numerical study and shown in Figure 16. One flow regime, $L/D = 4.5$ to 6 at Re = 100, is a steady flow regime in which no vortex shedding is observed behind the square cylinder. Another flow regime is the single bluff body flow regime. In the case of a single bluff body flow regime, a regular von Karman vortex street is observed behind the main square cylinder. In the case of a single bluff body flow regime, we further observed two different flow regimes. Single bluff body with Stp and Sts . Stp and Sts stand for dominant primary vortex shedding frequency and secondary frequencies together with primary vortex shedding frequency, respectively. Single bluff bodies with Stp are found at $(L/D, Re) = (0.5-4, 100), (0.5-5, 150), (0.5-4.5, 200), \text{ and } (0.5-4, 250)$. Single bluff bodies with Sts are found at $(L/D, Re) = (7-8, 100), (5.5-8, 150), (5-8, 200), \text{ and } (4.5-8, 250)$.

The wake length (L_w/D) is quantitatively calculated and is given in Table 7. The data confirms that wake lengths changed as the value of L/D increased from 0.5 to 8. As shown, the L_w/D for all the considered L/D values is changed. For cases with Re = 100 and $4.5 \leq L/D \leq 7$, the more L_w/D values are observed due to steady flow behavior behind the square cylinder.

4. Conclusions

A two-dimensional unsteady fluid flow around a square cylinder with an upstream attached T-shaped control plate was investigated numerically, and the important findings were reported in the present study. The flow characteristics and fluid forces were examined at Re = 100, 150, 200, and 250. The length of the T-shaped control plate is varied. A considerable effect of T-shaped control plate on the fluid forces around the square cylinder is observed, and accordingly, the following important conclusions can be drawn from the present computation:

- (i) It was found from the present computations that the vortex street behind the square cylinder was still maintained, but there was a significant decrease in drag. Decreasing the length of the upstream attached T-shaped control plate had a considerable effect on reduction of drag coefficient and rms value of lift coefficient. However, for $L/D \geq 5$, it did not have a considerable effect on the fluid forces. The minimum C_{Dmean} was observed at $L/D = 0.5$ for Re = 100, 150, and 200 and at $L/D = 2$ for Re = 250. At $L/D = 0.5$, 134%, 137%, 133%, and 136% reduction of C_{Dmean} was achieved for Re = 100, 150, 200, and 250, respectively. It was also found that when the length of T-shaped control plate is short, for instance, $L/D \leq 3$, the effect of the length of the T-shaped control plate on controlling the flow past a square cylinder becomes noticeable.
- (ii) A complete vortex shedding suppression for T-shaped control plate was achieved, at a T-shaped control plate length of $L/D = 4.5$ to $L/D = 6$ at Reynolds number 100. A maximum C_{Lrms} reduction of about 96% compared to the isolated cylinder was achieved at Re = 100 and $L/D = 7$ using T-shaped control plate. It was found that, as L/D increased, rms values of both drag coefficient and lift coefficient of square cylinder without T-shaped control plate considerably reduced compared with the isolated cylinder.
- (iii) Three different flow regimes were found in this study. The first one is the single bluff body flow regime with primary vortex shedding frequency (regime I). The second one is the single bluff body flow regime with secondary vortex shedding frequencies together with the primary vortex shedding frequency (regime II). The third one is the steady flow regime (regime III). In the case of regime-I, we found the dominance of primary vortex shedding frequency. On the other hand, in the case of regime-II, some extra minor peaks also exist in the power spectra.

Abbreviations

- C_D : Drag coefficient
 C_L : Lift coefficient
 C_{Dmean} : Mean drag coefficient

C_{Drms} :	Root-mean-square of drag coefficient
C_{Lrms} :	Root-mean-square of lift coefficient
c_s :	Speed of sound
Re:	Reynolds number ($Re = U_\infty D/\nu$)
St:	Strouhal number ($St = f_s D/U_\infty$)
Stp :	Strouhal number based on primary vortex shedding
Sts :	Strouhal number based on secondary vortex shedding frequencies
D :	Size of the main square cylinder
L :	Length of the T-shaped control plate
w :	Width of the T-shaped control plate head
f_s :	Vortex shedding frequency
U_∞ :	Uniform inflow velocity
L_u :	Upstream distance from the inlet position
L_d :	Downstream distance from the rear surface of the square cylinder
L_x :	Length of the computational domain
L_y :	Height of the computational domain
Ma:	Mach number
$f_i(\mathbf{x}, t)$:	Particle distribution function
$f_i^{(eq)}$:	Equilibrium distribution function
(\mathbf{x}, t) :	
p :	Pressure
ρ :	Density of the fluid
τ :	Single-relaxation-time parameter
δt :	Computational time-step
δx :	Lattice spacing
ν :	Kinematic viscosity of the fluid
ω_i :	Weighting coefficients
\mathbf{e}_i :	Discrete particle velocity
d :	Dimensions
q :	The number of particles
ω_z :	Vorticity
BGK:	Bhatnagar–Gross–Krook
LBM:	Lattice Boltzmann method
LGA:	Lattice gas automata
N-S:	Navier–Stokes
rms:	Root mean square
SRT:	Single-relaxation-time.

Data Availability

The data that support the main findings of this numerical study are available from the corresponding author upon request.

Conflicts of Interest

The authors declare that they have no known conflicts of interest that could have appeared to influence the numerical work reported in this study.

Acknowledgments

The second author Dr. Shams-ul-Islam is specially grateful to Higher Education Commission (HEC) Pakistan for providing funds under project no. 9083/Federal/NRPU/R&D/HEC/2017.

References

- [1] R. Abdi, N. Rezazadeh, and M. Abdi, "Reduction of fluid forces and vortex shedding frequency of a circular cylinder using rigid splitter plates," *European Journal of Computational Mechanics*, vol. 26, no. 3, pp. 225–244, 2017.
- [2] S. U. Islam, R. Manzoor, Z. C. Ying, M. M. Rashdi, and A. Khan, "Numerical investigation of fluid flow past a square cylinder using upstream, downstream and dual splitter plates," *Journal of Mechanical Science and Technology*, vol. 31, no. 2, pp. 669–687, 2017.
- [3] X. Zhou, J. Wang, and Y. Hu, "Experimental investigation on the flow around a circular cylinder with upstream splitter plate," *Journal of Visualization*, vol. 22, no. 4, pp. 683–695, 2019.
- [4] K. R. Sharma and S. Dutta, "Effect of rigid and flexible splitter plate attached to square cylinder on Strouhal number at moderate Reynolds number," in *Proceedings of the 24th National and 2nd International ISHMT-ASTFE Heat and Mass Transfer Conference (IHMT-2017)*, Hyderabad, India, December 2018.
- [5] M. K. Chauhan, S. Dutta, B. S. More, and B. K. Gandhi, "Experimental investigation of flow over a square cylinder with an attached splitter plate at intermediate Reynolds number," *Journal of Fluids and Structures*, vol. 76, pp. 319–335, 2018.
- [6] S. M. Dash, M. S. Triantafyllou, P. Valdivia, and Y. Alvarado, "A numerical study on the enhanced drag reduction and wake regime control of a square cylinder using dual splitter plates," *Computers & Fluids*, vol. 199, pp. 1–13, 2020.
- [7] S. Soumya and K. A. Prakash, "Effect of splitter plate on passive control and drag reduction for fluid flow past an elliptical cylinder," *Ocean Engineering*, vol. 141, pp. 351–374, 2017.
- [8] B. Barman and S. Bhattacharyya, "Control of vortex shedding and drag reduction through dual splitter plates attached to a square cylinder," *Journal of Marine Science and Application*, vol. 14, no. 2, pp. 138–145, 2015.
- [9] K. R. Sharma and S. Dutta, "Flow control over a square cylinder using attached rigid and flexible splitter plate at intermediate flow regime," *Physics of Fluids*, vol. 32, no. 1, p. 014104, 2020.
- [10] M. Sarioglu, "Control of flow around a square cylinder at incidence by using a splitter plate," *Flow Measurement and Instrumentation*, vol. 53, pp. 221–229, 2017.
- [11] S. Kim, J.-C. Yoon, and B.-S. Yim, "Suppression characteristics of flow-induced vibration in a test cylinder with varying locations of a control cylinder," *Journal of Mechanical Science and Technology*, vol. 32, no. 12, pp. 5685–5696, 2018.
- [12] S.-U. Islam, R. Manzoor, and A. Tareen, "Numerical investigation of flow around square cylinder with an upstream control plate at low Reynolds numbers in tandem," *Journal of the Brazilian Society of Mechanical Sciences and Engineering*, vol. 39, no. 4, pp. 1201–1223, 2017.
- [13] K. R. Sharma and S. Dutta, "Influence of length and effective stiffness of an attached flexible foil for flow over a square cylinder," *Journal of Fluids and Structures*, vol. 104, pp. 1–28, 2021.
- [14] E. Firat, Y. E. Akansu, and H. Akilli, "Flow past a square prism with an upstream control rod at incidence to uniform stream," *Ocean Engineering*, vol. 108, pp. 504–518, 2015.
- [15] S.-C. Yen, S.-F. Wu, and K.-C. San, "Modulation of wake flow and aerodynamic behaviors around a square cylinder using an

- upstream control bar,” *Experimental Thermal and Fluid Science*, vol. 70, pp. 139–147, 2016.
- [16] H. Zhu and J. Yao, “Numerical evaluation of passive control of VIV by small control rods,” *Applied Ocean Research*, vol. 51, pp. 93–116, 2015.
- [17] H. Zhu, J. Yao, Y. Ma, H. Zhao, and Y. Tang, “Simultaneous CFD evaluation of VIV suppression using smaller control cylinders,” *Journal of Fluids and Structures*, vol. 57, pp. 66–80, 2015.
- [18] M. K. Chauhan, S. Dutta, and B. K. Gandhi, “Wake flow modification behind a square cylinder using control rods,” *Journal of Wind Engineering and Industrial Aerodynamics*, vol. 184, pp. 342–361, 2019.
- [19] W. S. Abbasi, S. U. Islam, and H. Rahman, “Proximity effects on characteristics of flow around three inline square cylinders,” *Mathematical Problems in Engineering*, vol. 2019, Article ID 1752803, 14 pages, 2019.
- [20] S. Ahmad and S. Ul-Islam, “Numerical investigation of fluid flow past four cylinders at low Reynolds numbers,” *Mathematical Problems in Engineering*, vol. 2021, Article ID 1127324, 24 pages, 2021.
- [21] S. Rashdi, M. Hayatdavoodi, and J. A. Esfahani, “Vortex shedding suppression and wake control: a review,” *Ocean Engineering*, vol. 126, pp. 57–80, 2016.
- [22] T. Kruger, H. Kusumaatmaja, A. Kuzmin, O. Shardt, G. Silva, and E. M. Vigen, *The Lattice Boltzmann Method: Principles and Practice*, Springer, Berlin, Germany, 2017.
- [23] A. A. Mohamad, *Lattice Boltzmann Method: Fundamentals and Engineering Applications with Computer Codes*, Springer, Berlin, Germany, Second edition, 2019.
- [24] Z. Guo, H. Liu, L.-S. Luo, and K. Xu, “A comparative study of the LBE and GKS methods for 2D near incompressible laminar flows,” *Journal of Computational Physics*, vol. 227, no. 10, pp. 4955–4976, 2008.
- [25] D. Yu, R. Mei, L.-S. Luo, and W. Shyy, “Viscous flow computations with the method of lattice Boltzmann equation,” *Progress in Aerospace Sciences*, vol. 39, no. 5, pp. 329–367, 2003.
- [26] S. C. Luo, X. H. Tong, and B. C. Khoo, “Transition phenomena in the wake of a square cylinder,” *Journal of Fluids and Structures*, vol. 23, no. 2, pp. 227–248, 2007.
- [27] A. Okajima, “Strouhal numbers of rectangular cylinders,” *Journal of Fluid Mechanics*, vol. 123, pp. 379–398, 1982.
- [28] C. Norberg, “Flow around rectangular cylinders: pressure forces and wake frequencies,” *Journal of Wind Engineering and Industrial Aerodynamics*, vol. 49, no. 1-3, pp. 187–196, 1993.
- [29] A. Sohankar, L. Davidson, and C. Norberg, *Numerical Simulation of Unsteady Flow Around A Square Two-Dimensional Cylinder*, The University of Sydney, Sydney, Australia, 1995, https://www.researchgate.net/publication/292152601_Numerical_simulation_of_unsteady_flow_around_a_square_two-dimensional_cylinder.
- [30] A. K. Saha, G. Biswas, and K. Muralidhar, “Three-dimensional study of flow past a square cylinder at low Reynolds numbers,” *International Journal of Heat and Fluid Flow*, vol. 24, no. 1, pp. 54–66, 2003.
- [31] S. Dutta, P. K. Panigrahi, and K. Muralidhar, “Effect of orientation on the wake of a square cylinder at low Reynolds numbers,” *Indian Journal of Engineering and Materials Sciences*, vol. 11, pp. 447–459, 2004.
- [32] C. Y. Zhou, L. Wang, and W. Huang, “Numerical study of fluid force reduction on a circular cylinder using tripping rods,” *Journal of Mechanical Science and Technology*, vol. 21, no. 9, pp. 1425–1434, 2007.

Research Article

Numerical Computation of MHD Thermal Flow of Cross Model over an Elliptic Cylinder: Reduction of Forces via Thickness Ratio

Afraz Hussain Majeed , Rashid Mahmood , Waqas Sarwar Abbasi, and K. Usman

Department of Mathematics, Air University, PAF Complex E-9, Islamabad 44000, Pakistan

Correspondence should be addressed to Afraz Hussain Majeed; chafrazhussain@gmail.com

Received 30 July 2021; Revised 17 September 2021; Accepted 6 October 2021; Published 18 October 2021

Academic Editor: Akif Akgul

Copyright © 2021 Afraz Hussain Majeed et al. This is an open access article distributed under the Creative Commons Attribution License, which permits unrestricted use, distribution, and reproduction in any medium, provided the original work is properly cited.

The present work is concerned with a comprehensive analysis of hydrodynamic forces, under MHD and forced convection thermal flow over a heated cylinder in presence of insulated plates installed at walls. The magnetic field is imposed in the transverse direction of flow. The Galerkin finite element (GFE) scheme has been used to discretize the two-dimensional system of nonlinear partial differential equations. The study is executed for the varying range of flow behavior index (n) from 0.4 to 1.6, Hartmann number (Ha) from 0 to 100, Reynolds number (Re) from 10 to 50, Grashof number (Gr) from 1 to 10, thickness ratio (e) from 0.5 to 1.0, and Prandtl number (Pr) from 1 to 10, respectively. A coarse hybrid computational grid is developed, and further refinement is carried out for obtaining the highly accurate solution. The optimum case selection is based on flow patterns, drag and lift coefficients, and pressure drop reduction against cylinder thickness ratios and average Nusselt numbers. Drag coefficient increases with an increase in thickness ratio (e). The drag force reduction for $e = 0.5$ and $e = 0.75$ is also observed for a range of the power law index as compared with $e = 1.0$ cylinder. Maximum pressure drop over the back and front points of cylinder is reported at $Ha = 100$.

1. Introduction

Flow around bluff bodies of various shapes is a traditional study in fluid mechanics. With Reynolds (Re), the flow characteristics vary as the vortex structure changes behind the solid body when flow is separated. The situation becomes more fascinating when the flow is coupled with heat transfer, and therefore various theoretical, experimental, and simulation-based studies are present in the literature in different convective regimes. In the presence of multiple bluff bodies, the problem is more challenging, complex, and interesting. Expedient enhancements of the power industry introduce a new generation study that focuses mainly on the thermofluidic properties of convective force and mixed flow past multiple configurations of bluff body. Due to the interaction between vortices introduced on the cylinders, the phenomenon of shear layer transfer in these flow types provides

quite different signatures (see refs. [1–13]). The flow structures and the heat transfer features of a thermal transverse rectangular heated cylinder in the cross flow are analyzed numerically by Yang and Fu [1]. Zhao et al. [2] numerically investigated the characteristics of thermal flow for the laminar jet cluster, normally impinging on a plane wall. King and Chandratilleke [3] have reported the parametric study on impinged jets arranged in both square and hexagonal arrays shapes for maximum heat transfer. Nadeem et al. [4] reported the solution of similarity of the steady flow from a second-grade boundary layer with heat transfer via a horizontal circular cylinder. Yousefifard et al. [5] presented an unstructured grid using a particular vertex-based control volume framework. Flow evaluations have been carried out using structured and unstructured grids on the basis of Reynold numbers for steady and unstable flows. Shen et al. [6] numerically investigated the effects of thermal

features and rotational flow characteristics in ribbed channel at high Reynolds number and also computed the influence on the average Nusselt number. Zainuddin et al. [7] numerically examined the free oscillatory convection in the presence of heat generation around the horizontal circular cylinder of a Newtonian fluid by using the final differentiation method.

The broadest and most probable category of non-Newtonian fluids is pseudoplastic fluid. In these systems, the relation between viscosity and shear has an important technological effect, and a high degree of pseudoplasticity is generally undesirable because this implies poor flow at low shears. Esmaeili et al. [14] investigated that the selected non-Newtonian models are distinguished by the Carreau and Cross-Williamson models, which incorporate the tapering effects of blood flow. Xie and Jin [15] studied that the simulation of non-Newtonian free surface flow is based on the advantages of particulate methods in terms of handling large deformations and fragmentation. To capture the viscous characteristics of mixture flows, the cross-rheology equation has been chosen. Welahettige et al. [16] have numerically computed the effects of shear thinning fluid flow in an open channel. Mustafa et al. [17] have reported the rheology of cross-fluid flow over a steady rigid plate due to the flow rate gradient of pressure. Hauswirth et al. [18] simulated the effects of cross model fluid flow in permeable medium by using Lattice Boltzmann Method (LBM). A comprehensive literature review reveals that no due attention has been paid to the fluid cross that predicts the pseudoplastic nature of the fluid over a varying range of shear rate.

One of the most significant topics in the magnetohydrodynamic two-phase flows is to comprehend the motion of free fine particles under instantaneous gravity, buoyancy, hydrodynamic force, and Lorentz force. The clean metal manufacture excluding oxides and other kinds of nonmetallic inclusions is an example in electromagnetic metallurgy. If there is no magnetic field, both numerical simulations and experiments have fully investigated a solid particle generally modelled as a sphere. Sekhar et al. [19] simulated the steady and viscous fluid flux around a circular cylinder with a linear magnetic field. The multigrid procedure with deformity correction techniques is being used to obtain an accurate solution for the second order of complete nonlinear Navier–Stokes equations. Grigoriadis et al. [20] imposed a new MID configuration scheme for handling primarily MHD flows in complex domain. Tamoor et al. [21] investigated that the Newtonian MHD Casson fluid heating features are addressed by stretched cylinders moving at a linear velocity. Pan et al. [22–24] numerically investigated the effects of instability and transition of a vertical ascent or drop in a free field affected by a vertical magnetic field. Furthermore, they examined that the magnetic field can be used to destabilise the fluid solid system Chen et al. [25] numerically studied the effects of turbulent shear flow in the cylindrical container of an electrically conducting fluid. The flow is driven by the Lorentz azimuthal force, which results from a large number of small electrodes injecting the radial electrical currents on the base and the axial direction imposed magnetic field.

Flow analysis is fascinating as well as instigating. There are many technological applications and scientific challenges, but a wide range of fields requires further numerical and experimental research. The focus on frictional effects and heat exchange is on the viscous fluid flows over solid surfaces or within ducts and channels. The fluid properties must be evaluated to take into account of those effects. Either experimentally or theoretically the problem can be addressed. Various works have been proposed over the years to use numerical methods to solve incompressible Newtonian flow problems using finite differences, finite element, and finite volumes schemes. The most famous method is the classic PARDISO algorithm, which together with the pressure correction equation introduces the stalled grid concept. This method was used to resolve different 2D flow configurations successfully. In recent decades, three-dimensional numerical simulation of a variety of physical issues seems to have become widespread with the invention of fast, multiprocessor personal computers, including simple computer cluster management. It was noted that information still scarce is available in the literature in non-Newtonian fluid flows, especially polymer melts in molding process are evaluated in [26–32].

The aim of the present study is to compute reduction of forces based on thickness ratio (e) of elliptic obstacle submerged in cross-fluid flow. Such analysis of forces in conjunction with the cross model is new for CFD community. The rest of manuscript is organized as follows; in Section 2, flow configuration and governing equations are explained. Numerical scheme, grid convergence, and code validation are executed in Section 3. A detailed analysis of results is performed in Section 4. Finally, conclusion is mentioned in Section 5.

2. Flow Configuration and Governing Equations

The domain is a benchmark channel $\Omega = [0, 2.2] \times [0, 0.41]$ with a heated elliptic cylinder of diameter $D_L = 0.1$ placed in it having center at $C(0.2, 0.2)$ and h be the half height of the channel as revealed in Figure 1 while a consistent temperature T_h maintained on the surface of cylinder. Moreover, the thermophysical properties of fluids are considered to be free from temperature. Along the cylinder axis is imposed a homogenous vertical magnetic field with strength B . One of the parallel walls of the magnetic field is heated to a constant T_h wall temperature while the other surfaces are isolated thermally. The magnetic Reynolds number, which represents the relationship between the induced and applied magnetic field, is very small for a high Hartmann number. The magnetic field induced is thus negligible, and it is imposed in the z -direction only by that magnetic field. Also, the effects of viscous dissipation are neglected from the heat equation.

The steady, nonisothermal, and viscous incompressible fluid flow through a wildly long heated cylinders is the govern of continuity, dynamics, and energy equations. These equations are written as follows in their nondimensional forms (see ref. [33]):

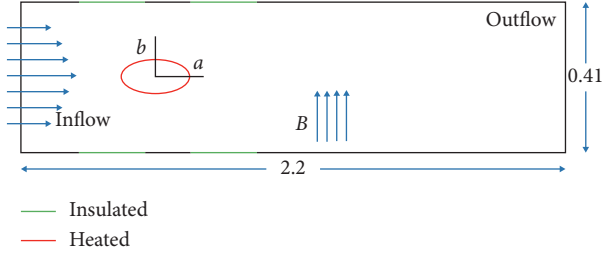


FIGURE 1: Schematic diagram of flow domain.

$$\frac{\partial u}{\partial x} + \frac{\partial v}{\partial y} = 0, \quad (1)$$

$$u \frac{\partial u}{\partial x} + v \frac{\partial u}{\partial y} = -\frac{\partial p}{\partial x} + \frac{1}{\text{Re}} \left(\frac{\partial \tau_{xx}}{\partial x} + \frac{\partial \tau_{xy}}{\partial y} \right), \quad (2)$$

$$u \frac{\partial v}{\partial x} + v \frac{\partial v}{\partial y} = -\frac{\partial p}{\partial y} + \frac{1}{\text{Re}} \left(\frac{\partial \tau_{yx}}{\partial x} + \frac{\partial \tau_{yy}}{\partial y} \right) + \frac{\text{Gr}}{\text{Re}^2} \theta - \frac{D_L \text{Ha}}{h \text{Re}} v, \quad (3)$$

$$u \frac{\partial \theta}{\partial x} + v \frac{\partial \theta}{\partial y} = \frac{1}{\text{Re Pr}} \left(\frac{\partial^2 \theta}{\partial x^2} + \frac{\partial^2 \theta}{\partial y^2} \right). \quad (4)$$

The velocity, pressure, and temperature u , v , p , and θ are nondimensional. The dimensionless aspects of the domain indicate that certain dimensional parameters, such as Reynolds, Grashof, Prandtl, and thickness ratio, govern the velocity and temperature profile in the current circumstances. The parameters are defined as follows:

- (i) Grashof number $\text{Gr} = g\beta(T_h - T_0)D_L^3/\mu^2$
- (ii) Prandtl number $\text{Pr} = \nu/\alpha$
- (iii) Hartmann number $\text{Ha} = hB\sqrt{\sigma/\rho\nu}$
- (iv) Thickness ratio $e = b/a$
- (v) Cross-fluid model [34] $\tau = (\mu_{\infty+}(\mu_0 - \mu_{\infty}/1 + (\lambda\dot{\gamma})^n))\dot{\gamma}$

All the parameters have been defined in the nomenclature section. These are complementary to the problem statement. Fluid with a parabolic profile in x -direction is entered at the entrance to this domain. For all variables, we set the Neumann condition at the outlet. On the other walls of the channel and on the surface of obstacle, no slip conditions have been imposed. In addition, obstacles are being uniformly heated while channel walls remain cold except the plates that are insulated.

Furthermore, computational results in the form of primitive variables (u , v , p , and θ) from the governing equations in consonance with the abovementioned domain boundary conditions have been obtained. In addition, the derived quantities are evaluated by way of drag coefficient, lift coefficient, and average Nusselt number, respectively.

The nondimensional net drag (F_d) and lift (F_l) forces act on the submerged cylinder in the flow and normal direction, while the drag and lift coefficients are

$$C_D = \frac{2F_d}{\rho U_{\text{mean}}^2 D_L}, \quad (5)$$

$$C_L = \frac{2F_l}{\rho U_{\text{mean}}^2 D_L}.$$

Here, the average velocity is $U_{\text{mean}} = 2/3U_{\text{max}}$ where $U_{\text{max}} = 0.3$ be the maximum velocity of parabolic profile. One more important quantity of interest is pressure drop $\delta p = p_L - p_R$ capitalizing with the front and back point of the cylinder, respectively. The local Nusselt (Nu_{local}) number on the surface of cylinder and on plates is estimated by $\text{Nu}_{\text{local}} = -(\partial\theta/\partial n_s)$. Such values have been averaged over the both surfaces (cylinder and plates) to obtain the average Nusselt (Nu_{avg}) number given as follows:

$$\text{Nu}_{\text{avg}} = \frac{1}{S} \int_S \text{Nu}_{\text{local}} dS, \quad (6)$$

where “ S ” and “ n_s ” are the surfaces of thermal region and normal direction of the surface; it is reasonable to postulate that the drag coefficient is function of Re whereas the Nusselt number depends on the Pr .

3. Numerical Scheme and Grid Convergence

Because of the two-dimensional development flow territory and the nonlinearity of the cross-fluid model, analytical solutions of mass, momentum, and energy equations cannot be exhibited; therefore, a numerical scheme based on finite element discretization is used to calculate the solution for various configurations. The discretized version of nonlinear equations is linearized by the Newton method, and an efficient and robust linear solver PARDISO has been utilized for inner computations. Finite element space involving quadratic polynomials (\mathbb{P}_2) has been selected to approximate the velocity and temperature component whereas the pressure approximation is done using the space of linear polynomials (\mathbb{P}_1). For the computation of accurate drag and lift forces, a very fine mesh is created in the vicinity of the obstacle as shown in Figure 2. To avoid potential problems of convergence, the solution has been initialized with zero value systems of velocity and temperature at each point in the grid.

Grid independence studies were carried out by computing Nu_{avg} for all cases of thickness ratio (e), and the results are presented in Tables 1–3. The values of other parameters are set as $n = 1$, $\text{Ha} = 0$, $\text{Re} = 20$, $\text{Pr} = 6.2$, and $\text{Gr} = 10$. A regular grid refinement is performed for all the three meshes from level 1 to level 8. No significant changes in Nu_{avg} were observed with further grid refinement at higher levels in space. All results were therefore calculated at mesh level 8. The corresponding number of element (#EL) and degree of freedom (#DOF) is provided in Tables 1–3.

The code has also been validated for steady flow in order to strengthen the reliability of the results to be achieved for the proposed study. Finally, the current code has also been validated against the study by Mahmood et al. [31] in Table 4.

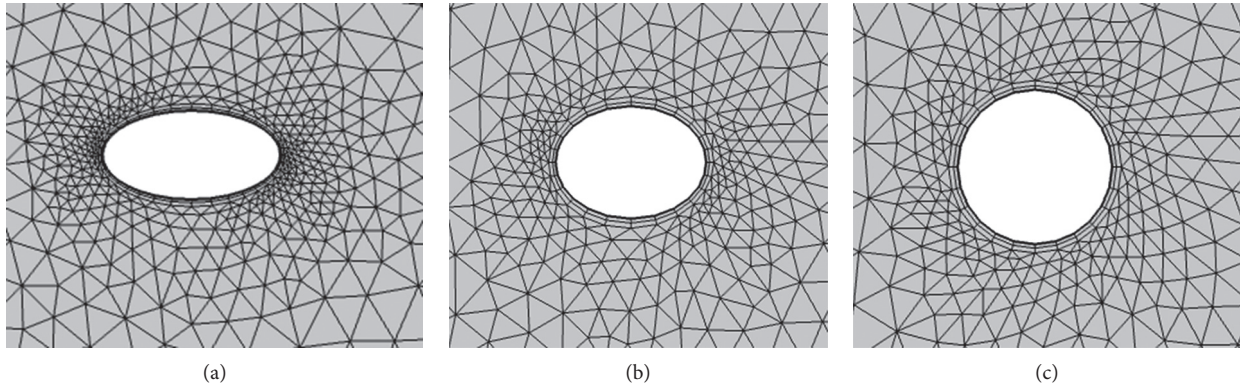


FIGURE 2: Computational hybrid grid at coarse level: (a) $e = 0.5$; (b) $e = 0.75$; (c) $e = 1.0$.

TABLE 1: Grid convergence study for $e = 0.5$.

Refinement level	#EL	#DOF	Nu_{avg}
1	1156	8733	5.5884
2	1790	13404	5.6196
3	2806	20530	5.6428
4	4976	35659	5.6511
5	7314	51641	5.652
6	12562	86773	5.6562
7	27892	191815	5.6577
8	64922	442155	5.6582

TABLE 2: Grid convergence study for $e = 0.75$.

Refinement level	#EL	#DOF	Nu_{avg}
1	1054	8023	5.8913
2	1606	12113	5.8991
3	2570	18901	5.9863
4	4584	32968	6.0024
5	6840	48417	6.0026
6	12154	83978	6.0169
7	26916	185471	6.0276
8	64862	441909	6.0291

TABLE 3: Grid convergence study for $e = 1.0$.

Refinement level	#EL	#DOF	Nu_{avg}
1	948	7287	6.0562
2	1584	11970	6.2515
3	2414	17840	6.3187
4	4562	32826	6.3668
5	6668	47299	6.3674
6	11886	82188	6.3774
7	27196	187387	6.3969
8	65518	446365	6.3992

TABLE 4: Validation of code for comparison of drag and lift coefficients for $e = 1.0$ (circular) cylinder.

Fluid forces	Mahmood et al. [31]	Cold cylinder	Heated cylinder
C_D	5.5785	5.5785	5.5785
C_L	0.0106	0.0106	-0.0007

4. Results and Discussion

In this section, the computational results for dimensionless equations (1)–(4) are presented. The values of cross model parameters, namely, μ_{∞} , μ_0 , and λ are taken from [34]. The pure

hydrodynamic flow and temperature properties are obtained in Figures 3 and 4 before imposing the magnetic effects. Figures 3 and 4 show velocity profile and isotherm contours for different thickness ratios in the vicinity of the cylinder and without the effect of the magnetic field $Ha = 0$, $Re = 20$, $Pr = 5$, and $\lambda = 0$ (Newtonian) externally used. The usual steady flow nature and the thermal fields are shown. Behind the cylinder forms a closed, steady recirculating area composed of vortices. The isotherms appear symmetrical in the wake region around the symmetry

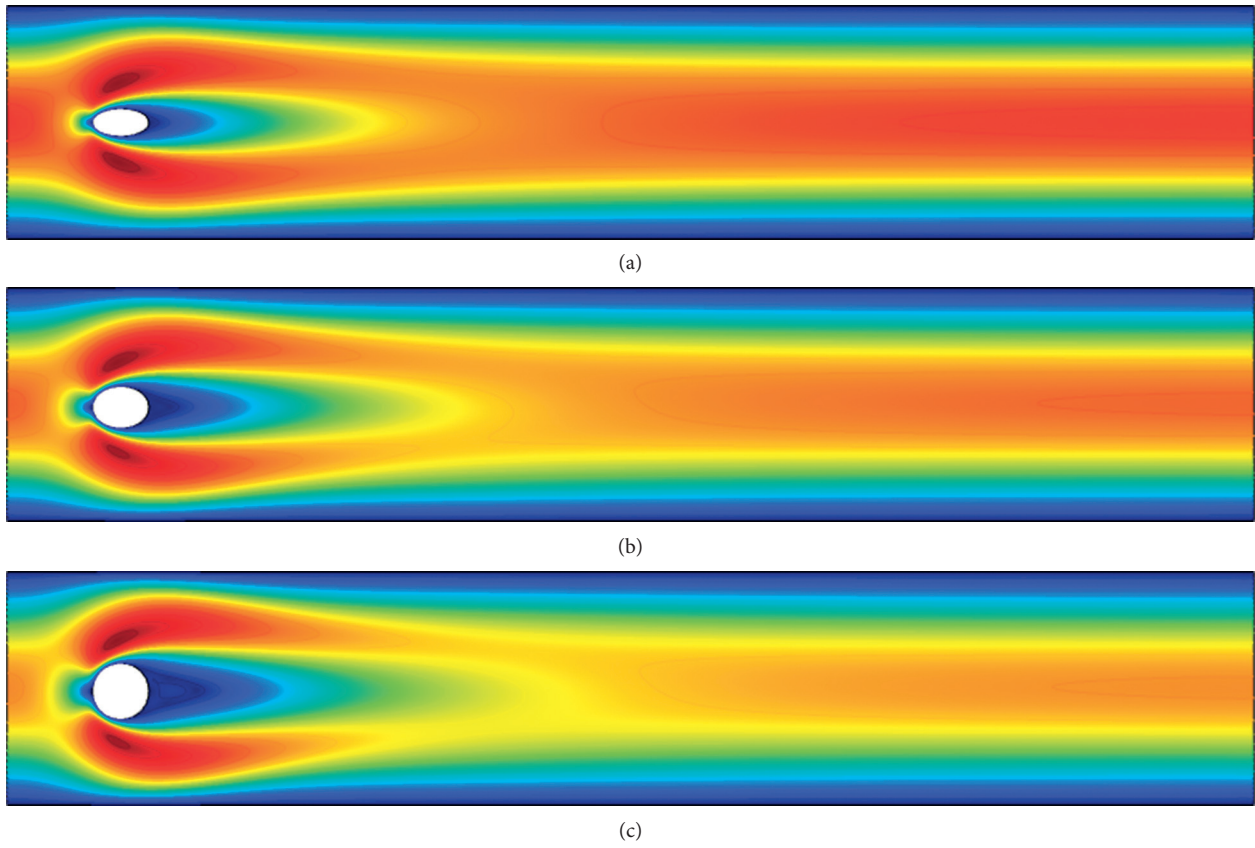


FIGURE 3: Shape effects on velocity profile for different e with $Re = 20, Pr = 5$, and $Ha = 0$: (a) $e = 0.5$; (b) $e = 0.75$; (c) $e = 1.0$.

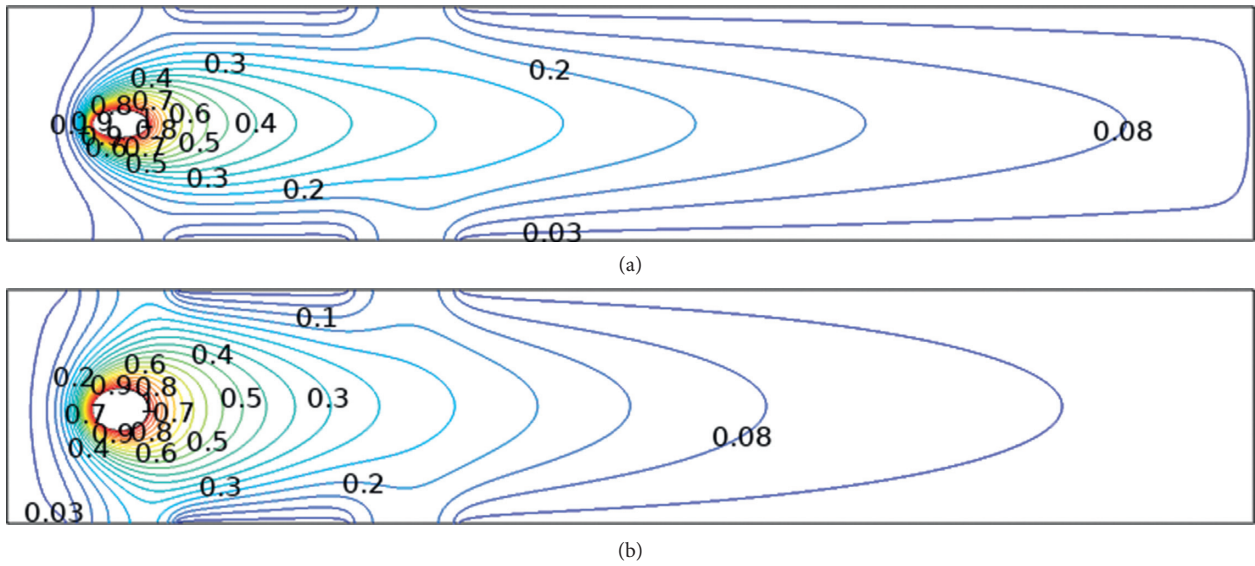


FIGURE 4: Continued.

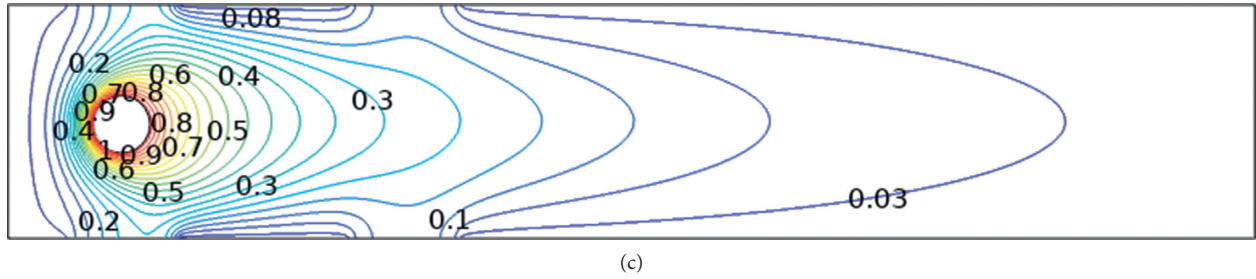


FIGURE 4: Shape effects on isotherm profile for different e with $Re = 20$, $Pr = 5$, and $Ha = 0$: (a) $e = 0.5$; (b) $e = 0.75$; (c) $e = 1.0$.

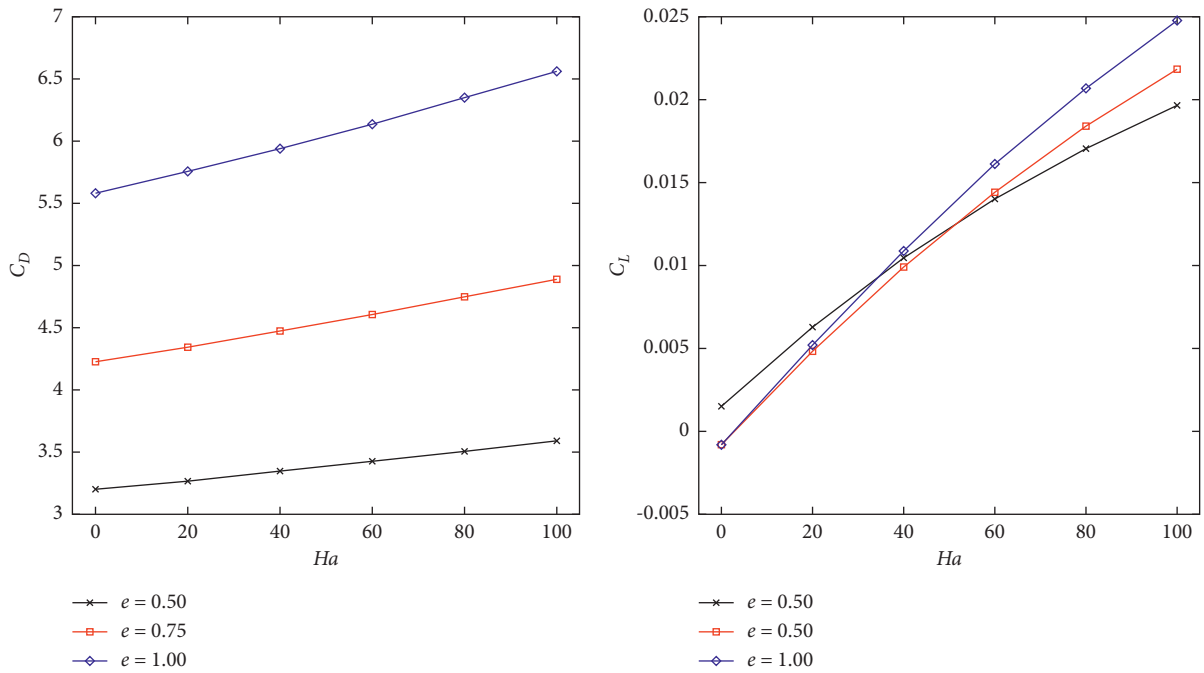


FIGURE 5: Shape effects on drag and lift coefficients against Ha for different e with $Re = 20$.

line. The isothermal plots indicate that in the near-wake area, temperature contours are lower with an increasing thickness ratio e . These figures also indicate that the cylinders' front surface is the most isothermal clustering, resulting in high thermal gradients compared with some other points on the cylinder surface. One of the main objectives is to determine the complete heat transfer from the isothermal cylinder to the fluid. By analyzing the heat transfer rate of the cylinder, the efficacy of the flow behavior particularly on heat exchange can be reported.

A majority of flow parameters including the drag coefficient, lift coefficient, and pressure drop have been computed in order to acquire the quantitative view of the aforementioned effects. Figure 5 shows variation of the drag and lift coefficients for various e against the Hartmann number Ha . In addition, with increase in both the Hartmann number Ha and e at fixed Re , drag coefficient increases. Moreover, lift coefficient increases with the increase in e for $Ha \geq 40$, while lift coefficients in the lateral direction for $Ha \leq 40$ are suppressed. In Figure 6, different values of Re are illustrated for the effects of e

versus drag and lift coefficients. It is observed that the drag coefficient decreases while the lift coefficient increases due to viscous forces in order to enhance Re . Figure 7 demonstrates the effects on drag and lift coefficients of the Hartmann number Ha and Reynolds number Re . Drag and lift coefficients are expected to increase with the increase in the Hartmann number Ha as drag coefficients decrease and lift coefficients increase for increasing Re . Figures 8 and 9 show that eccentricity influences on drag and lift coefficients against Prandtl numbers Pr and Grashof number Gr . Furthermore, drag is increased due to increased viscosity, while lift decreases against both thermal quantities Pr and Gr numbers.

The addition of one or more cylinders to the single body has been shown to significantly impact fluid forces according to earlier research. In this study, we also focused at this phenomenon. For this purpose, for every single combination of multiple cylinders examined in this study, a percentage reduction is calculated related to the circular cylinder for the drag coefficient, the lift coefficient, and the pressure drop of

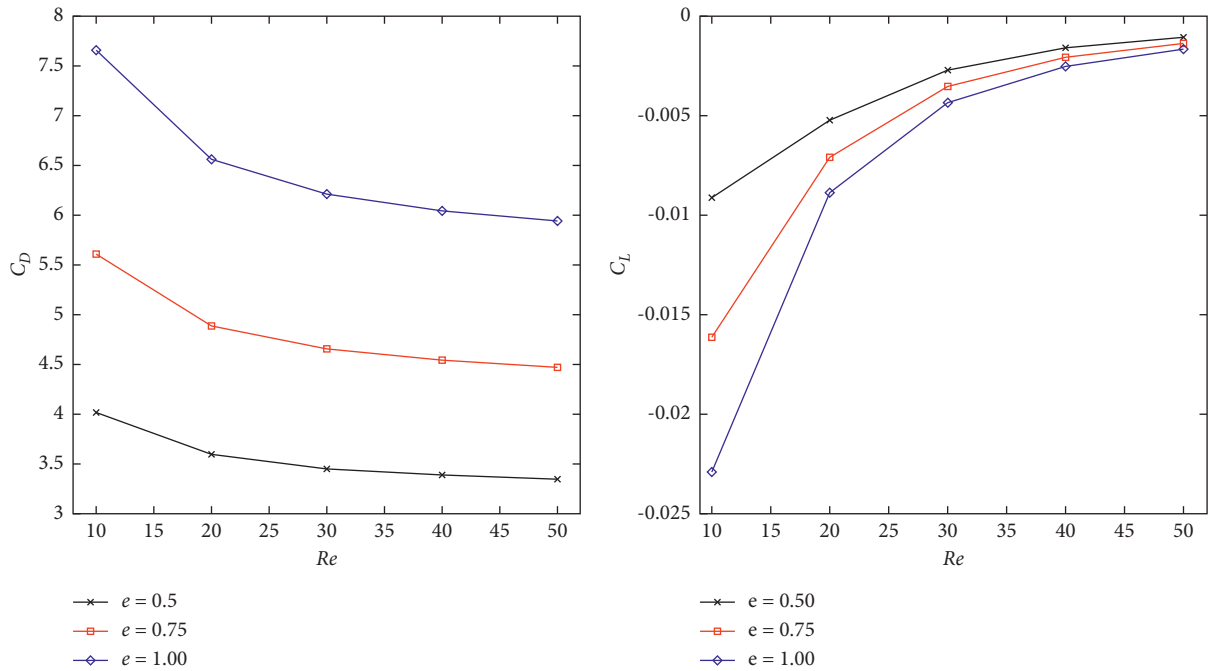


FIGURE 6: Shape effects on drag and lift coefficients against Re for different e with $Ha = 20$.

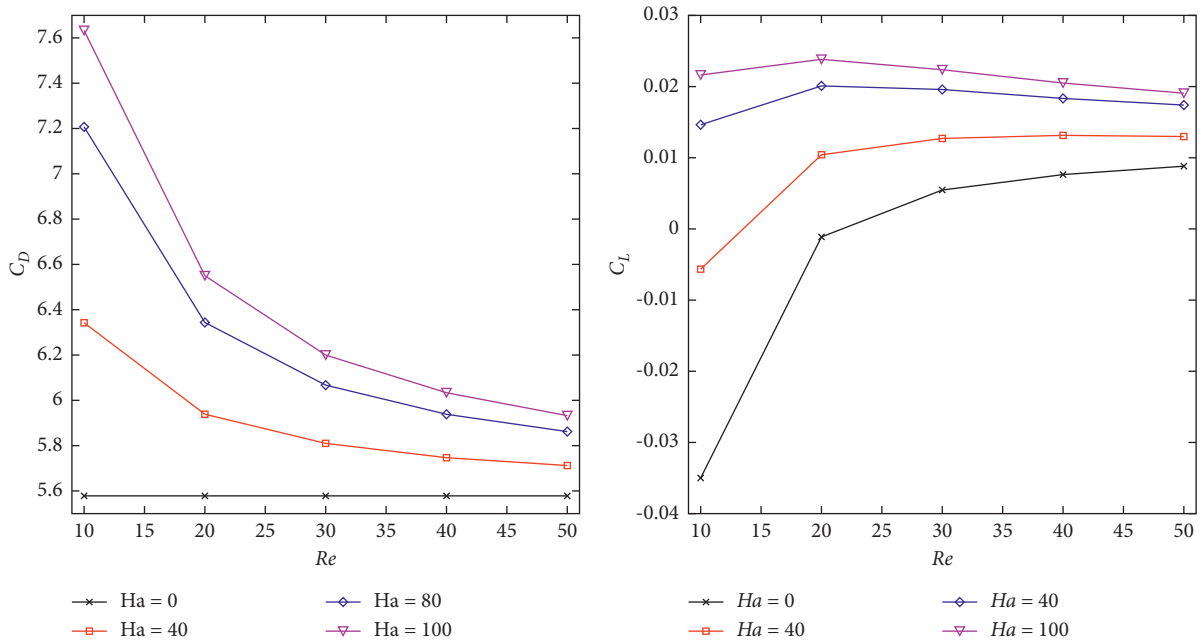


FIGURE 7: Impacts on drag and lift coefficients against Re for different Ha with $Gr = 1$ and $Pr = 5$.

the circular cylinder ($e = 1$). Tables 5–7 show the data of percentage reduction in drag, lift, and pressure drop for n verses thickness ratio (e) at fixed values of Re and Ha . Maximum reduction in drag and lift coefficients is reported at ($e = 0.5$) as compared with other values of (e) while for the pressure drop, highest reduction is seen at ($e = 0.75$). We may conclude that the more elliptical the bodies are, the greater will be the reduction in the strength of the wake. Table 8 displays the impact of Ha on pressure drop against e ,

and it is observed that for a fixed Ha , reduction is high for $e = 0.5$; however, for a fixed thickness ratio e , the reduction is directly proportional to Ha . Moreover, reduction in pressure drop is inversely related with Re as evident from Table 9.

While the velocity profile and isothermal contours represent the flow and temperature fields visually, they help to delineate the local hot/cold region that is relevant to the handling of temperature sensitive materials, sensitive materials in process

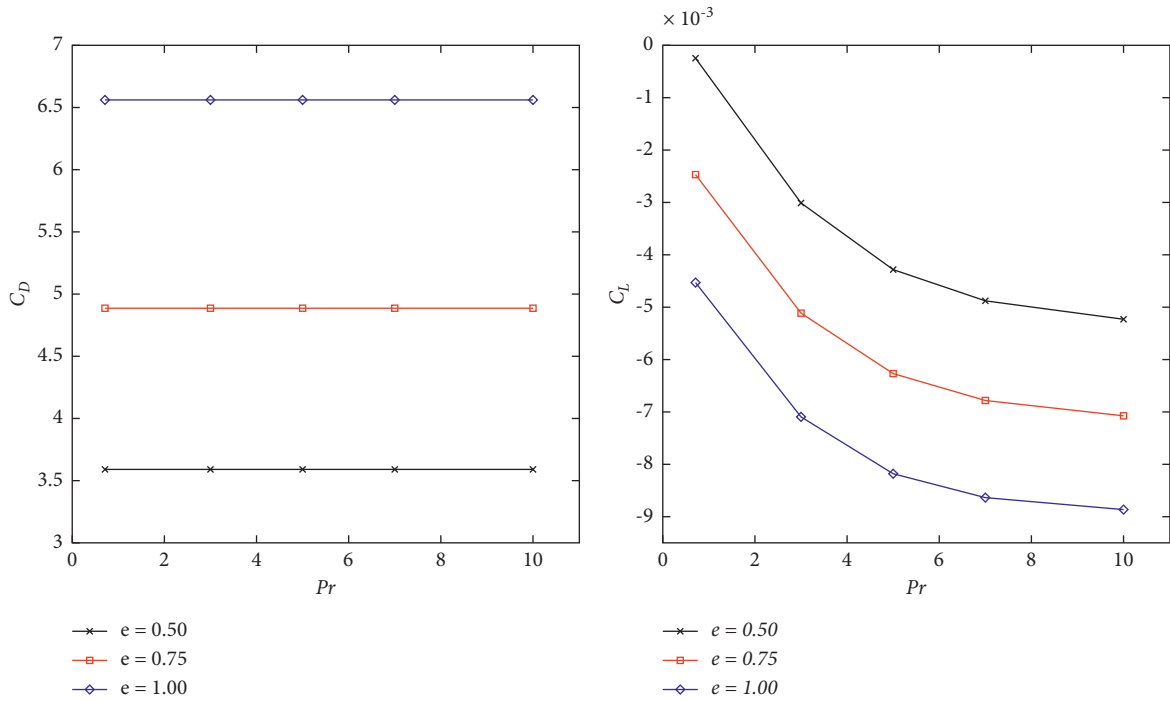


FIGURE 8: Impacts on drag and lift coefficients against Pr for different e with $Gr = 1$ and $Ha = 20$.

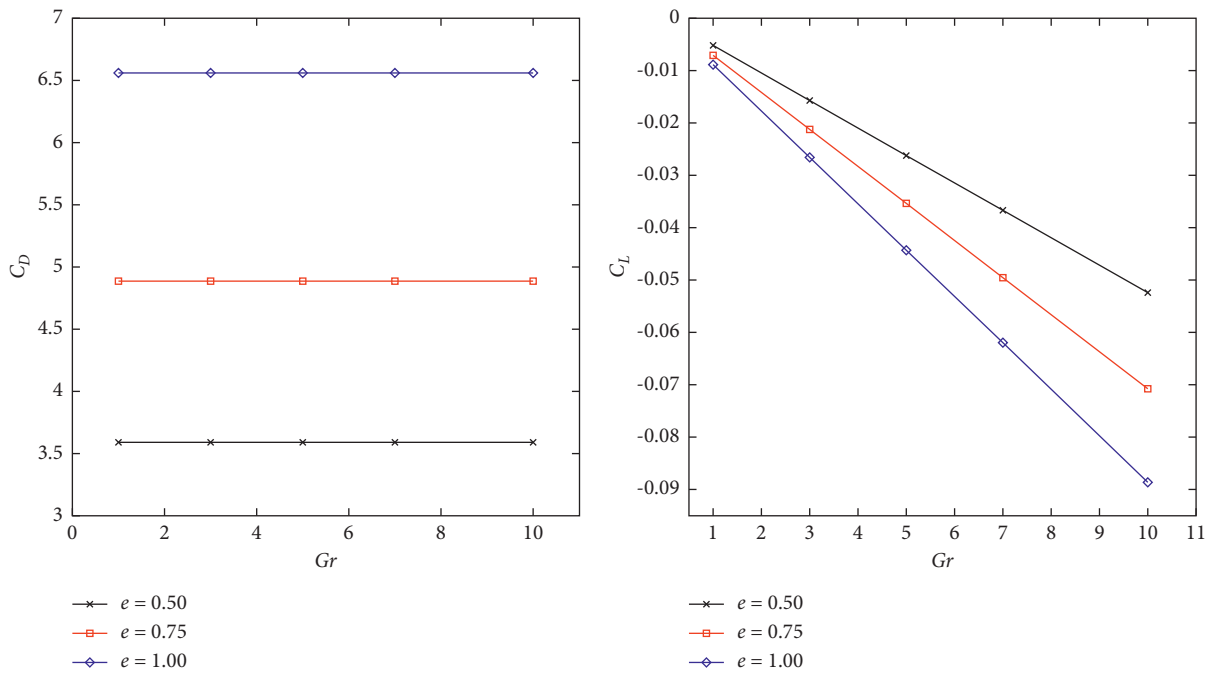


FIGURE 9: Impacts on drag and lift coefficients against Gr for different e with $Pr = 5$ and $Ha = 20$.

engineering and calculations require accurate heat transfer coefficient given by average Nusselt number Nu_{avg} . Figure 10 illustrates functional dependence on Reynolds number, Prandtl number, and Grashof number for the average Nusselt number. Under all circumstances, the average Nusselt number is strong for the value of e as set out in the previous section according to

Re , Pr , and Gr . The increasing thickness ratios e also endorse the heat transfer rate due to a reduction in efficient fluid viscosity at or near the cylindrical surface. For analysis, steady flow is considered in a two-dimensional space. The speed impact for both Re and Hartmann number Ha is marked exactly at $(x = 2)$, and components u and v are considered for minute

TABLE 5: Influence on percentage reduction in drag $e = 1.0$ for $e = 0.75$ and $e = 0.5$ at $Re = 20$ and $Ha = 20$.

n	$e = 1.0$	$e = 0.75$	% reduction	$e = 0.5$	% reduction
0.4	5.356412	4.070569	24.00	3.101553	42.09
0.6	5.378040	4.086737	24.01	3.113913	42.09
0.8	5.399516	4.102802	24.02	3.126193	42.10
1.0	5.420852	4.118770	24.02	3.138408	42.10
1.2	5.442058	4.134651	24.02	3.150560	42.11
1.4	5.463141	4.150447	24.03	3.162652	42.11
1.6	5.484107	4.166163	24.03	3.174686	42.11

TABLE 6: Influence on percentage reduction in lift coefficient for e against n with $Re = 20$ and $Ha = 20$.

n	$e = 1.0$	$e = 0.75$	% reduction	$e = 0.5$	% reduction
0.4	-0.01219	-0.0105	13.86	-0.00875	28.22
0.6	-0.01219	-0.0105	13.86	-0.00874	28.30
0.8	-0.01219	-0.0105	13.86	-0.00874	28.30
1	-0.01219	-0.0105	13.86	-0.00874	28.30
1.2	-0.0122	-0.0105	13.93	-0.00874	28.36
1.4	-0.0122	-0.0105	13.93	-0.00873	28.44
1.6	-0.0122	-0.0105	13.93	-0.00873	28.44

TABLE 7: Influence on percentage reduction in pressure drop for e against n with $Re = 20$ and $Ha = 20$.

N	$e = 1.0$	$e = 0.75$	% reduction	$e = 0.5$	% reduction
0.4	0.11538	0.107049	7.22	0.107986	6.41
0.6	0.115567	0.10723	7.21	0.108229	6.35
0.8	0.115753	0.10741	7.21	0.108471	6.29
1.0	0.115938	0.107591	7.20	0.108715	6.23
1.2	0.116122	0.107771	7.19	0.108959	6.17
1.4	0.116306	0.107951	7.18	0.109203	6.11
1.6	0.116489	0.108131	7.17	0.109448	6.04

TABLE 8: Impact of Ha on reduction in pressure drop for different e .

Ha	$e = 1.0$	$e = 0.75$	% reduction	$e = 0.5$	% reduction
0	0.117615	0.111998	4.76	0.109765	6.67
20	0.119741	0.113753	5.00	0.111084	7.23
40	0.122249	0.115795	5.28	0.112615	7.88
80	0.128146	0.118536	7.50	0.116157	9.36
100	0.131421	0.120145	8.58	0.118102	10.13

TABLE 9: Impact of Re on reduction in pressure drop for different e .

Re	$e = 1.0$	$e = 0.75$	% reduction	$e = 0.5$	% reduction
10	0.122247	0.112795	7.73	0.112615	7.68
20	0.119741	0.110753	7.51	0.111084	7.23
30	0.118987	0.110133	7.44	0.110619	7.03
40	0.118626	0.109836	7.41	0.110396	6.94
50	0.118415	0.109662	7.39	0.110265	6.88

analysis. The Reynolds number effect (Re) against u and v velocities on the ($x = 2$) channel is displayed in Figure 11. A fluctuation for all Re values is observed in the v -velocity. Now, for u -velocity, the parabolic forms with overlaps are again found

and the terminal velocity is 0.3 (approximately). Plots indicate the reliance on Re and Ha on stream lines. The fluidity becomes much higher for Ha than the rest of Ha. The progressive increase in nonlinearity due to increase in Ha is seen in Figure 12.

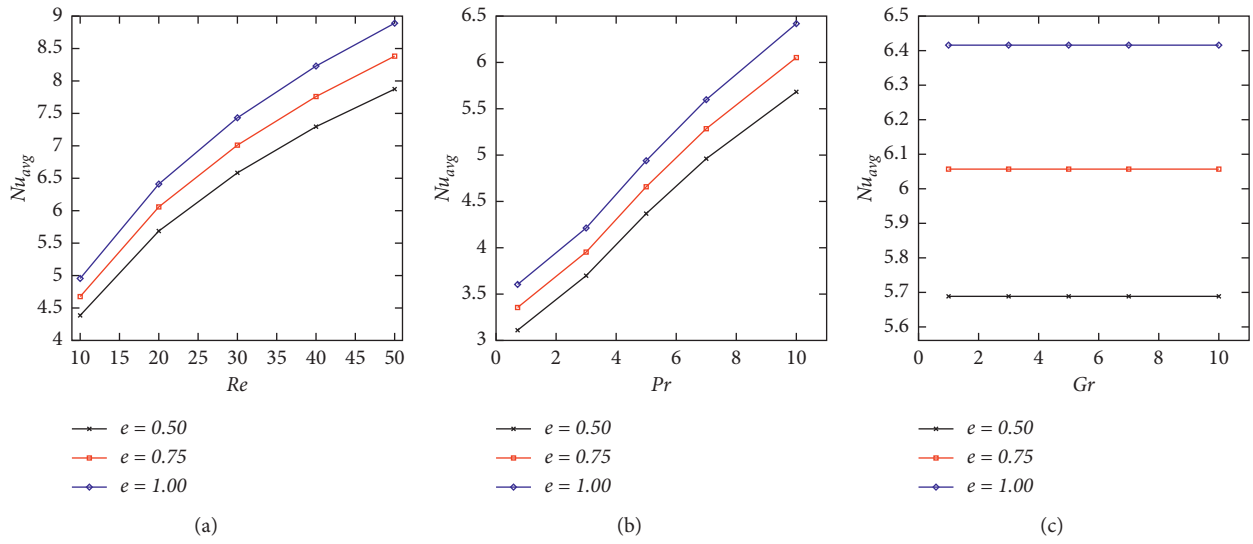


FIGURE 10: Impacts on the average Nusselt number against different parameters for different e : (a) Re ; (b) Pr ; (c) Gr .

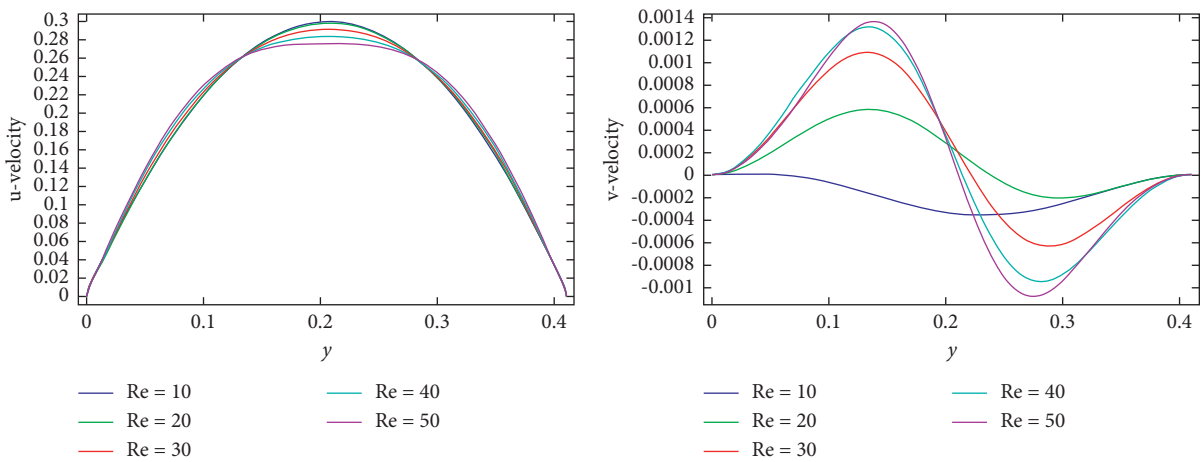


FIGURE 11: Impact on velocity line profile for different Re at $x = 2$ over circular cylinder with $Ha = 20$.

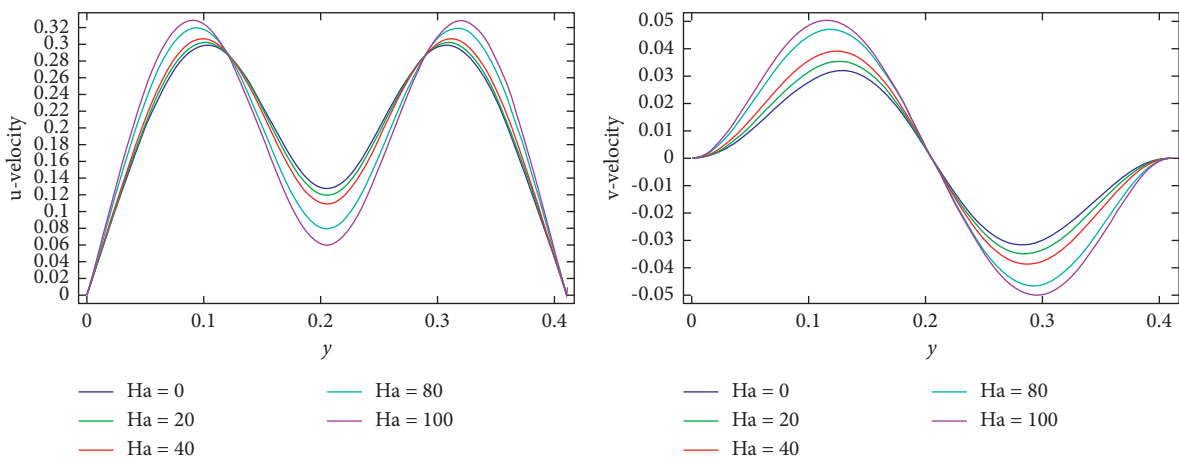


FIGURE 12: Impact on velocity line profile for different Ha at $x = 2$ over circular cylinder with $Re = 20$.

5. Conclusions

The present numerical work is concerned with the investigation of the flow past an elliptic cylinder for various thickness ratios (e). The objective was to see the reduction in hydrodynamic forces in comparison with e and heat transfer characteristics in presence of magnetic field. Simulations have been performed on the different scale of the flow behavior index (n) from 0.4 to 1.6, Hartmann number (Ha) from 0 to 100, Reynolds number (Re) from 10 to 50, Grashof number (Gr) from 1 to 10, Prandtl number (Pr) from 1 to 10, and the thickness ratio (e) from 0.5 to 1.0. The key results of this study are concluded as follows:

- (i) Reynolds number (Re) is instrumental in investigating the phenomenon of flow and heat transfer. The flow compoment changes from slower to quicker mode as it increases.
- (ii) On a heated cylinder, the average Nusselt number Nu_{avg} is rising. At $e = 1$, the maximum heat transfer was found.
- (iii) The pressure drop significantly reduced by 10.13% at $Ha = 100$ and increases the pressure on the circular ($e = 1$) cylinders.
- (iv) By enhancing thickness ratio (e), the lift coefficient (C_L) enriches and drag coefficient (C_D) decreases all values of significant factors.
- (v) Nu_{avg} increases with thickness ratio (e).
- (vi) For a fixed (e), reduction in pressure drop is directly proportional to Ha whereas it is inversely related with Re .

The current work can be extended to a nonstationary framework at high Re giving raise to periodic flows and vortex shedding behind the obstacles.

Greek Symbols

Nomenclature

u, v :	Dimensionless velocity components
θ :	Dimensionless temperature
p :	Dimensionless pressure
n :	Flow behavior index
D_L :	Diameter of cylinder
L_D :	Reference length
μ_o :	Viscosity at zero shear rate
μ_{∞} :	Viscosity at infinite shear rate
τ :	Stress tensor
$\dot{\gamma}$:	Shear rate
U_{mean} :	Reference velocity
Re :	Reynolds number
h :	Height of half channel
Pr :	Prandtl number
Gr :	Grashof number
F_D :	Drag force
C_D :	Drag coefficient
F_L :	Lift force
C_L :	Lift coefficient

Nu_{avg} :	Average Nusselt number
Nu_{local} :	Local Nusselt number
∇ :	Gradient operator
B :	Magnetic field
g :	Gravitational acceleration
e :	Thickness ratio
Ha :	Hartmann number.
α :	Thermal diffusivity
ρ :	Density
β :	Volumetric expansion
ν :	Kinematic viscosity
σ :	Magnetic permeability
λ :	Material cross time constant.

Abbreviations and Acronyms

#EL:	Number of elements
#DOF:	Number of degrees of freedom.

Data Availability

The relevant author can provide the data supporting the main findings of this numerical study upon request.

Conflicts of Interest

The authors declare that there are no conflicts of interest.

Acknowledgments

This work was supported by HEC-Pakistan through NRPJ Project no. 14038.

References

- [1] S.-J. Yang and W.-S. Fu, "Numerical investigation of heat transfer from a heated oscillating rectangular cylinder in a cross flow," *Numerical Heat Transfer: Applications*, vol. 39, no. 6, pp. 569–591, 2001.
- [2] W. Zhao, K. Kumar, and A. S. Mujumdar, "Impingement heat transfer for a cluster of laminar impinging jets issuing from noncircular nozzles," *Drying Technology*, vol. 23, no. 1-2, pp. 105–130, 2005.
- [3] A. J. C. King and T. T. Chandratilleke, "Heat transfer characteristics in impinging jet arrays," *Australian Journal of Mechanical Engineering*, vol. 4, no. 1, pp. 59–64, 2007.
- [4] S. Nadeem, A. Rehman, C. Lee, and J. Lee, "Boundary layer flow of second grade fluid in a cylinder with heat transfer," *Mathematical Problems in Engineering*, vol. 2012, Article ID 640289, 13 pages, 2012.
- [5] M. Yousefifard, P. Ghadimi, and R. Zamanian, "Unstructured grid solutions for incompressible laminar flow over a circular cylinder using a particular finite volume-finite element method," *Journal of Engineering*, vol. 2013, Article ID 795237, 9 pages, 2013.
- [6] Z. Shen, Y. Xie, D. Zhang, and G. Xie, "Numerical calculations on flow and heat transfer in smooth and ribbed two-pass square channels under rotational effects," *Mathematical Problems in Engineering*, vol. 2014, Article ID 981376, 7 pages, 2014.

- [7] N. Zainuddin, M. Ismoen, R. Roslan, and I. Hashim, "Oscillatory free convection about a horizontal circular cylinder in the presence of heat generation," *Mathematical Problems in Engineering*, vol. 2014, Article ID 946495, 8 pages, 2014.
- [8] Y. Fu, X. Zhao, X. Wang, and F. Cao, "Computation of flow past an in-line oscillating circular cylinder and a stationary cylinder in tandem using a CIP-based model," *Mathematical Problems in Engineering*, vol. 2015, Article ID 568176, 9 pages, 2015.
- [9] S. Ajith Kumar, S. A. Lal, and A. Sameen, "Flow past a moderately heated horizontal cylinder at low Reynolds number," *Proceedings of the Institution of Mechanical Engineers—Part G: Journal of Aerospace Engineering*, vol. 230, no. 7, pp. 1224–1239, 2016.
- [10] P. Welahettige, C. Berg, J. Lundberg, B. Lie, and K. Vaagsaether, "Computational fluid dynamics study of the effects of drill cuttings on the open channel flow," *International Journal of Chemical Engineering*, vol. 2019, Article ID 6309261, 9 pages, 2019.
- [11] F. Hussain, A. Hussain, and S. Nadeem, "Thermophoresis and brownian model of pseudo-plastic nanofluid flow over a vertical slender cylinder," *Mathematical Problems in Engineering*, vol. 2020, Article ID 8428762, 10 pages, 2020.
- [12] S. Bilal, A. H. Majeed, R. Mahmood, I. Khan, A. H. Seikh, and E.-S. M. Sherif, "Heat and mass transfer in hydromagnetic second-grade fluid past a porous inclined cylinder under the effects of thermal dissipation, diffusion and radiative heat flux," *Energies*, vol. 13, no. 1, 2020.
- [13] A. H. Majeed, S. Bilal, R. Mahmood, and M. Y. Malik, "Heat transfer analysis of viscous fluid flow between two coaxially rotated disks embedded in permeable media by capitalizing non-Fourier heat flux model," *Physica A: Statistical Mechanics and its Applications*, vol. 540, 2020.
- [14] M. Esmaeili, A. Javadzadegan, and S. E. Marashi, "The modeling of pulsatile blood flow as cross-williamson and carreau fluids in an artery with a partial occlusion," in *Proceedings of the 2008 Second UKSIM European Symposium on Computer Modeling and Simulation*, pp. 191–196, Liverpool, UK, September 2008.
- [15] J. Xie and Y.-C. Jin, "Parameter determination for the cross rheology equation and its application to modeling non-Newtonian flows using the WC-MPS method," *Engineering Applications of Computational Fluid Mechanics*, vol. 10, no. 1, pp. 111–129, 2016.
- [16] P. Welahettige, B. Lie, and K. Vaagsaether, "Computational fluid dynamics study of shear thinning fluid (drilling fluid) viscosity models in an open venturi channel," *International Journal of Petroleum Science and Technology*, vol. 13, no. 1, pp. 9–20, 2019.
- [17] M. Mustafa, A. Sultan, and M. Rahi, "Pressure-driven flow of cross fluid along a stationary plate subject to binary chemical reaction and arrhenius activation energy," *Arabian Journal for Science and Engineering*, vol. 44, no. 6, pp. 5647–5655, 2019.
- [18] S. C. Hauswirth, C. A. Bowers, C. P. Fowler et al., "Modeling cross model non-Newtonian fluid flow in porous media," *Journal of Contaminant Hydrology*, vol. 235, no. August, Article ID 103708, 2020.
- [19] T. V. S. Sekhar, R. Sivakumar, H. Kumar, and T. V. R. Ravi kumar, "Effect of aligned magnetic field on the steady viscous flow past a circular cylinder," *Applied Mathematical Modelling*, vol. 31, no. 1, pp. 130–139, 2007.
- [20] D. G. E. Grigoriadis, I. E. Sarris, and S. C. Kassinos, "MHD flow past a circular cylinder using the immersed boundary method," *Computers & Fluids*, vol. 39, no. 2, pp. 345–358, 2010.
- [21] M. Tamoor, M. Waqas, M. I. Khan, A. Alsaedi, and T. Hayat, "Magnetohydrodynamic flow of Casson fluid over a stretching cylinder," *Results in Physics*, vol. 7, pp. 498–502, 2017.
- [22] J.-H. Pan, M.-J. Ni, and N.-M. Zhang, "A consistent and conservative immersed boundary method for MHD flows and moving boundary problems," *Journal of Computational Physics*, vol. 373, pp. 425–445, 2018.
- [23] J.-H. Pan, N.-M. Zhang, and M.-J. Ni, "Instability and transition of a vertical ascension or fall of a free sphere affected by a vertical magnetic field," *Journal of Fluid Mechanics*, vol. 859, pp. 33–48, 2019.
- [24] J.-H. Pan, N.-M. Zhang, and M.-J. Ni, "Wake structure of laminar flow past a sphere under the influence of a transverse magnetic field," *Journal of Fluid Mechanics*, vol. 873, pp. 151–173, 2019.
- [25] L. Chen, A. Pothérat, M. J. Ni, and R. Moreau, "Direct numerical simulation of quasi-two-dimensional MHD turbulent shear flows," *Journal of Fluid Mechanics*, vol. 915, 2021.
- [26] R. Mahmood, S. Bilal, A. H. Majeed, I. Khan, and E.-S. M. Sherif, "A comparative analysis of flow features of newtonian and power law material: a new configuration," *Journal of Materials Research and Technology*, vol. 9, no. 2, pp. 1978–1987, 2019.
- [27] S. Bilal, R. Mahmood, A. H. Majeed, I. Khan, and K. S. Nisar, "Finite element method visualization about heat transfer analysis of newtonian material in triangular cavity with square cylinder," *Journal of Materials Research and Technology*, vol. 9, no. 3, pp. 4904–4918, 2020.
- [28] R. Mahmood, S. Bilal, A. H. Majeed, I. Khan, and K. S. Nisar, "CFD analysis for characterization of non-linear power law material in a channel driven cavity with a square cylinder by measuring variation in drag and lift forces," *Journal of Materials Research and Technology*, vol. 9, no. 3, pp. 3838–3846, 2020.
- [29] R. Mahmood, S. Bilal, A. H. Majeed, I. Khan, and K. S. Nisar, "Assessment of pseudo-plastic and dilatant materials flow in channel driven cavity: application of metallurgical processes," *Journal of Materials Research and Technology*, vol. 9, no. 3, pp. 3829–3837, 2020.
- [30] A. Mehmood, R. Mahmood, A. H. Majeed, and F. J. Awan, "Flow of the bingham-papanastasiou regularized material in a channel in the presence of obstacles: correlation between hydrodynamic forces and spacing of obstacles," *Modelling and Simulation in Engineering*, vol. 2021, no. April, 14 pages, Article ID 5583110, 2021.
- [31] R. Mahmood, N. Kousar, K. Usman, and A. Mehmood, "Finite element simulations for stationary Bingham fluid flow past a circular cylinder," *Journal of the Brazilian Society of Mechanical Sciences and Engineering*, vol. 40, no. 9, pp. 1–9, 2018.
- [32] A. H. Majeed, F. Jarad, R. Mahmood, and I. Saddique, "Topological characteristics of obstacles and nonlinear rheological fluid flow in presence of insulated fins: a fluid force reduction study," *Mathematical Problems in Engineering*, vol. 2021, Article ID 9199512, 15 pages, 2021.
- [33] W. K. Hussam, M. C. Thompson, and G. J. Sheard, "Dynamics and heat transfer in a quasi-two-dimensional MHD flow past a circular cylinder in a duct at high Hartmann number," *International Journal of Heat and Mass Transfer*, vol. 54, no. 5–6, pp. 1091–1100, 2011.

- [34] Y. I. Cho and K. R. Kensey, "Effects of the non-Newtonian viscosity of blood on flows in a diseased arterial vessel. Part 1: steady flows," *Biorheology*, vol. 28, no. 3-4, pp. 241-262, 1991.

Research Article

Flow Characteristics and Fluid Forces Reduction of Flow Past Two Tandem Cylinders in Presence of Attached Splitter Plate

Ali Ahmed ¹, Abdul Wahid,² Raheela Manzoor,³ Noreen Nadeem,³ Naqib Ullah,⁴ and Shazia Kalsoom³

¹Department of Mathematics, COMSATS University Islamabad, Park Road, Tarlai Kalan 45550, Islamabad, Pakistan

²Balochistan University of Information Technology Engineering and Management Science, Quetta, Balochistan, Pakistan

³Department of Mathematics, Sardar Bahadur Khan Women University, Quetta, Balochistan, Pakistan

⁴University of Central Punjab Islamabad Campus, Islamabad, Pakistan

Correspondence should be addressed to Ali Ahmed; alihmd87@gmail.com

Received 15 April 2021; Accepted 19 July 2021; Published 8 September 2021

Academic Editor: Irfan Kaymaz

Copyright © 2021 Ali Ahmed et al. This is an open access article distributed under the Creative Commons Attribution License, which permits unrestricted use, distribution, and reproduction in any medium, provided the original work is properly cited.

Numerical simulations are carried out to study the flow around two tandem square cylinders (SC) under the effect of spacing ratio (g/D) and splitter plate length (l/D) for a fixed Reynolds number (Re) = 100. The g/D is varied from 0 to 10 and l/D is varied from 0.5 to 10. The splitter plate length is found to have strong effect on vortex shedding and fluid forces. The maximum reduction in mean drag coefficient is observed at $l/D = 8$, that is 15% and 78% for upstream and downstream cylinders, respectively. The maximum reduction in root-mean-square value of lift coefficient is found at $l/D = 10$, that is 99%. The flow pattern at both of these points is steady flow. There is 100% vortex shedding suppression for $l/D > 5$. The observed flow patterns for flow past tandem cylinders without splitter plate are; single bluff body (SBB), steady flow (SF), quasi-steady flow (QSF), fully developed flow (FDF) and fully developed two-row vortex street flow (FDTRVS) regimes. SBB, QSF and SF regimes were observed in presence of splitter plate.

1. Introduction

The study of fluid forces and vorticity dynamics through the bluff body has been greatly improved in the last few decades. Most of these studies have been taken for single cylinder. However, much less attention has been paid to multiple cylinders flow compared to single cylinder. The addition of another bluff body can change the different aspects of flow such as fluid forces and transition threshold. To study the flow interference different models such as side-by-side, tandem and staggered models have been used. Among these models, tandem is the simplest one. A number of experimental and numerical studies have been conducted for flow past tandem cylinders. Kondo and Matsukuma [1] numerically analyzed the salient flow features through two tandem circular cylinders at $Re = 1000$. They found that the forces exerted on the last cylinder are substantially higher than those exerted on the first cylinder. While in case of

tandem square cylinders, the upstream cylinder forces are larger than those of the downstream cylinder [2]. Azuma et al. [3] experimentally measured forces acting on square structures both side-by-side and in tandem. They observed that the drag forces of two tandem cylinders changed significantly when the separation ratio was greater than $g/D = 3$ (where g is the spacing between cylinders and D is cylinder diameter) as compared to side-by-side arrangement. Abbasi et al. [4] numerically analyzed the flow regime transitions over the flow around three tandem cylinders for the g/D between 0.5 and 16 at $Re = 200$ and found five different types of flow regimes. In addition, they noted that the g/D is the important analysis parameter. Abbasi et al. [5] analyzed the flow regime transitions around two-, three- and four-tandem cylinders for Re ranging from 1 to 130 at $g/D = 2$ and 5. They observed two separate trends in terms of flow transitions for $g/D = 2$ and 5. The more reduction in terms of drag is observed at $g/D = 2$. Mittal et al. [6] numerically

analyzed the flow characteristics through two cylinders for $Re=100$ and 1000 and found that the shedding starts at $Re=100$. Abbasi et al. [7] numerically found three various types of flow features for two tandem cylinders. Vikram et al. [8] also analyzed the salient flow features past tandem cylinders. They observed that compared to downstream cylinder the upstream cylinder experience higher lift force. Sharman et al. [9] numerically analyzed the flow through two inline cylinders under the influence of g/D varying from 2 to 10 for $Re=100$. They identified $g/D=3.75-4$ as critical spacing, where the flow characteristics changes abruptly. Liu and Jerry [10] experimentally analyzed flow on two cylinders in tandem with $Re=2000-16000$ and $g/D=1.5-9$. They reported hysteresis with two discontinuous jumps associated with different flow regimes. Sohankar and Etminan [11] analyzed flow and heat transfer across cylinders arranged inline for $Re=1-200$. They found that vortex shedding formation begins in the range $35 \leq Re \leq 40$.

The addition of an eddy promoter improved the heat transfer of the downstream cylinder and controls the C_D . Bearman [12, 13] used the splitter plates to increase the formation length and reduce the drag. One of the most important studies was carried out by Zdravkovich [14], which divided the vortex suppression into three different branches, namely: (i) surface protrusions, (ii) shrouds and (iii) near-wake stabilizers. In literature both active and passive methods exist. Active control procedures generally require continuous external energy to reduce the drag forces and improve the lift [15, 16]. While for the passive methods there is no need internal energy, these include tripping rods [17], control cylinder [18–20], splitter plate [21], T-shaped plate [22] etc.

Anderson and Szewczyk [23] experimentally analyzed the impacts of low length splitter plates for the flow through circular cylinder and noticed that less than $D/8$ splitter length appreciably affect the wake zone for $Re=2700$ to $46,000$. You et al. [24] observed that significant noise reduction can take place for flow around circular cylinder once the splitter plate length is identical to the cylinder diameter. Uffinger et al. [25] analyzed the effects of different shapes on flow control behind a cylinder and found that the wedge shape behind the square body significantly control the flow. Ali et al. [26] computationally analyzed the influence of splitter plate length on a cylinder at $Re=150$.

To the best of ours' knowledge, for the proposed problem there is no numerical and experimental study reported in the literature. Hopefully, this work will help engineer's working on fluid forces reduction. The main motivation is to examine the splitter plate effect on flow regimes. The other main objective is to stabilize the critical gap spacing. Furthermore, we want to systematically examine the change over behavior of the mechanism of wake structure behind the downstream cylinder and amplitude variation of fluid forces.

This paper is ordered as follows: The proposed problem, numerical method, initial and boundary conditions are discussed in Section 2. The effect of computational domain and code validation is done in section 3. The computed results are presented in section 4. Finally, the conclusion is presented in section 5.

2. Problem Description and Numerical Details

2.1. Problem Description. A schematic representation of the flow through two fixed tandem SCs in presence of attached splitter plate is shown in Figure 1. D , l and g are the width of the cylinder, length of the splitter plate and spacing between the cylinders, respectively. C_1 and C_2 are the first and second cylinders, respectively. L_u , L_d , L_x , and L_y are the upstream location, downstream location, length, and height of the domain, respectively. Parabolic velocity profile is adopted at the entrance position of the domain, while the convective boundary condition is adopted at the exit of the domain [27]. No-slip boundary condition is applied to the surface of the cylinders and splitter plate [28]. Free-slip boundary condition is adopted at the top and bottom lateral boundaries of the channel [29]. The method of momentum exchange [30] is used for the calculation of forces.

2.2. Lattice Boltzmann Method. We have established the 2-D code for the flow through two tandem SCs with and without attached splitter at $(g/D, l/D) = (0-10, 0.5-10)$ for $Re=100$. The lattice Boltzmann method (LBM) is applied for the numerical results obtained in this paper. As compared to well known numerical techniques, the LBM is relatively new technique [28]. It was developed by Frisch et al. [31].

Here we will present a short overview of this method. In this study we applied Q_2N_9 (where Q is the space dimension and N is the number of particles) lattice model. In this model, each computational node consists of a rest particle ($i=0$) along with eight moving particles ($i=1-8$) (see Figure 2).

The density evolution equation is given by;

$$g_i(x + e_i, t + 1) = g_i(x, t) - \frac{[g_i(x, t) - g_i^{(0)}(x, t)]}{g_i(x, t) - \tau}, \quad (1)$$

where, g_i , $g_i^{(0)}$, t , x , e_i and τ are the particle distribution function, the corresponding equilibrium distribution function, dimensionless time, position of particles, velocity directions, and single relaxation time, respectively.

The corresponding equilibrium distribution function is:

$$g_i^{(0)} = \rho \omega_i (1 + 3(e_i \cdot u) + 4.5(e_i \cdot u)^2 - 1.5u^2). \quad (2)$$

Here, ρ , u , and ω_i are the fluid density, velocity and corresponding weighting functions ($\omega_i = 0$ for $i=0$, $\omega_i = 1/9$ for $i=1-4$, and $\omega_i = 1/36$ for $i=5-8$), respectively. Equation (1) can be solved by two steps: collision which use a Bhatnagar-Gross-Krook (BGK) operator [32, 33] and propagation. These steps can be defined as:

Collision:

$$g_i^{(\text{new})}(x, t) = g_i(x, t) - \frac{[g_i(x, t) - g_i^{(0)}(x, t)]}{g_i(x, t) - \tau}. \quad (3)$$

Streaming:

$$g_i(x + e_i, t + 1) = g_i^{(\text{new})}(x, t). \quad (4)$$

Equations (5) and (6) are used to calculate the density and velocity at each computational node

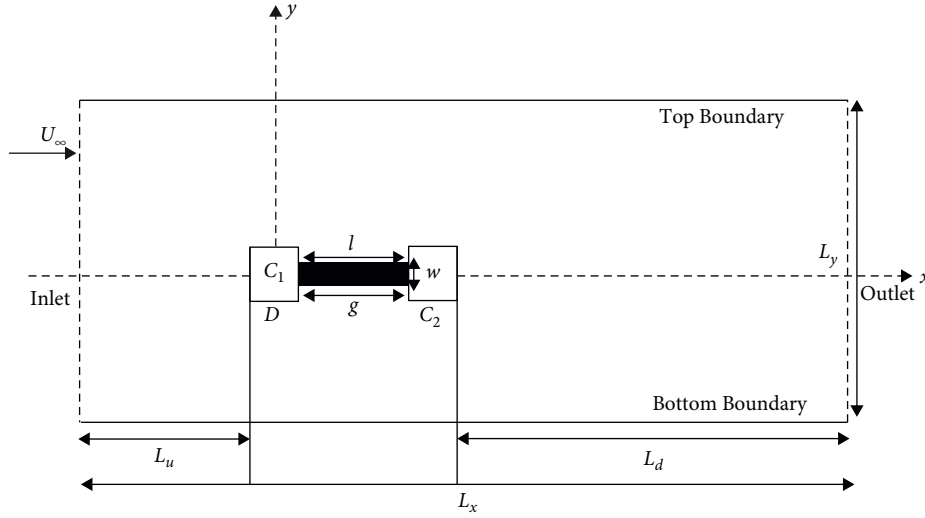


FIGURE 1: Schematic diagram of flow past two inline square cylinders in confined channel.

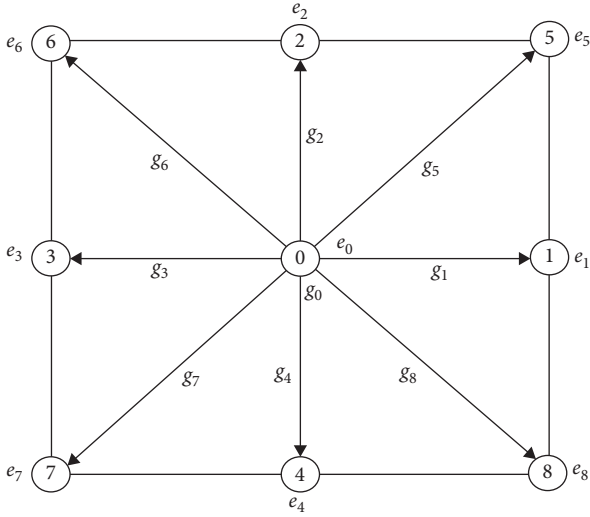


FIGURE 2: LBM lattice velocities on square structure.

$$\rho = \sum_i g_i, \quad (5)$$

$$\rho u = \sum_i g_i e_i. \quad (6)$$

The boundary conditions are applied after the streaming step (equation (4)), and the entire process is solved iteratively. The pressure can be calculated from the equation of state: $p = \rho c_s^2$; where c_s is the speed of sound and its value is $1/\sqrt{3}$.

3. Computational Domain Study and Code Validation

In this section we will present the grid independence and code validation.

3.1. Grid Independence Study. Table 1 presents the grid independence study. We have taken the error with respect to $D = 30$. From the results it is observed that as the size of D is increased from 20 to 30, the maximum variation in mean drag coefficient ($C_{D\text{mean}}$) and Strouhal number ($St = fs D/U_\infty$, where fs is the vortex shedding frequency) are 0.336% and 0.9%, respectively. Therefore, for the rest of simulation we used $D = 20$.

3.2. Computational Domain. The computational domain size strongly affects characteristics of flow around bluff bodies. The small change in computational domain changes the vortex shedding procedure, which affects the physical parameters. We have calculated the $C_{D\text{mean}}$ and St for different values of L_u , L_d and L_y , so that we can choose a suitable domain. The data in Table 2 shows that there is a slight difference in between the resulted values. So we can consider any case given in Table 2. We will simulate the given problem by using $L_u = 8D$; $L_d = 25D$ and $L_y = 10D$. The numbers 1 and 2 in subscripts represents the physical parameters of upstream and downstream cylinders.

3.3. Code Validation. The validation of code is done for the flow past single cylinder for $Re = 100$. For the validation of the code we have used only two parameters that is $C_{D\text{mean}}$ and St . For comparison the numerical results of Dutta et al. [34] as well as experimental data of Norberg et al. [35] and Okajima [36] are given in Table 3. The results shows that the present calculations of $C_{D\text{mean}}$ and St are in good agreement with the experimental data of Norberg et al. [35] and Okajima [36] and numerical data of Dutta et al. [34].

4. Results and Discussion

A two-dimensional (2D) numerical study is carried out to study the effect of g/D and l/D at $Re = 100$. The splitter plate is attached in the middle of the two cylinders. In this study

TABLE 1: Cylinder size effect on integral parameters at $Re = 100$.

D	10	20	30
C_{Dmean}	1.1916 (2.79%)	1.1622 (0.34%)	1.1583
St	0.1271 (3.78%)	0.1235 (0.9%)	0.1223

TABLE 2: Effect of computational domain at $g/D = 1$.

L_u	L_d	L_y	C_{Dmean1}	C_{Dmean2}	St_1	St_2
8D	25D	10D	1.0873 (3.08%)	-0.0828 (3.8%)	0.1018 (3.41%)	0.1018 (3.41%)
8D	40D	10D	1.1208	-0.0796	0.1054	0.1054
12D	25D	10D	1.1144 (2.43%)	-0.0860 (3.86%)	0.0987 (3.05%)	0.0989 (3.04%)
8D	25D	10D	1.0873 (3.53%)	-0.0828 (2.90%)	0.1018 (3.59%)	0.1018 (3.60%)
8D	25D	14D	1.0489	-0.0852	0.1056	0.1058

TABLE 3: Comparison of present and previous results.

	Present	Dutta et al. [34]	Norberg et al. [35]	Okajima [36]
C_{Dmean}	1.162	1.15	1.44	1.6
St	0.124	0.13	0.145	0.14

we will discuss the vorticity contours visualization, time analysis of C_D and C_L and power spectra of C_L . During this study the g/D will be varied from 0 to 10 and l/D will be varied from 0.5 to 10.

4.1. The Flow Over Two Tandem Square Cylinders without Splitter Plate. Figures 3(a)–3(f) presents the instantaneous flow visualization of flow field through two SCs in tandem arrangement without splitter plate. The different g/D values in Figures 3(a)–3(f) represented the flow field characteristics is SBB ($g/D = 0.5$ and 1), SF regime ($g/D = 2$ and 3), FDF regime ($g/D = 5$) and FDTRVS regime ($g/D = 9$), respectively. The pattern of vortex was a single row in SBB flow regime (Figure 3(a)). The phenomenon was analogous to the flow past a single SC. When the value of g/D is increased up to 1, the shear layers detached from the C_1 reattach on the upper surface of the C_2 (Figure 3(b)). When the g/D is increased to 2 and 3, no vortex shedding occurs behind the second cylinder (Figures 3(c), and 3(d)). When $g/D = 5$, the fully developed vortex shedding can be clearly seen behind the upstream square cylinder. Under these conditions, the flow behind the downstream SC was almost matching to that around single cylinder, and there was a little affect by the upstream SC (Figure 3(e)). On the other hand, the downstream SC was still affected by the upstream SC, appearing to be a two-rows vortex street at $g/D = 9$ (Figure 3(f)).

In the FDF regime, the two inline cylinders separately shed vortices at the same frequency. Igarashi [37] also reported that the two inline circular cylinders shed vortices at the same frequency at reasonably large spacing ratio. It is observed that the FDF or co shedding flow regime occurs at $g/D = 5$ where the vortices shed separately from the two cylinders but with same frequency. The negative vortex shedding from C_1 hits the front face of the C_2 and at the same

time the negative and positive shed vortices develop from the cylinder C_2 . These different shed vortices interact with each other and results in a FDTRVS regime with multi-frequency variation in the spectra of the lift coefficient of C_2 (ref. spectrum in Figure 4(j)).

Instantaneous streamline visualization shows the alternate generation of negative and positive shed vortices presented in Figures 5(a)–5(f). It is found that the wake width and vortex formation length are considerably dependent on spacing ratio. In SBB regime, the shear layers separated from the front edges of C_1 quickly reattached on the lateral surface of C_2 , forming two small recirculation regions within the cylinders (Figure 5(b)). Due to strong suction a negative drag value is observed for C_2 . At $g/D = 5$, both the cylinders (C_1 and C_2) shed vortices and the flow characteristics is called a FDF regime.

Time variation C_D and C_L of both cylinders are shown in Figures 6(a)–6(l) for different spacing ratios. As spacing ratio increases, the amplitude of drag coefficient also increases for FDF regime and FDTRVS regime (Figures 6(i), and 6(k)). It is observed that the C_D of C_2 is modulated. At $g/D = 0.5$ and 1, the C_L become sinusoidal, and the first cylinder and second cylinder shed vortices result in an inphase mode (Figures 6(b), and 6(d)). At $g/D = 2$, the C_L of both cylinders becomes constant (Figure 6(f)).

The spectra graph shows a single dominant peak corresponding to the primary frequency; no secondary frequency was observed in the spectra in case of single bluff body flow regime (Figures 4(a)–4(d)). The small peak in the power spectra (Figures 4(h) and 4(j)) suggests that the second cylinder flow is still affected by the first cylinder.

4.2. The Flow Around Two Tandem Square Cylinders with Attached Splitter Plate. Figures 7(a)–7(e) presents the vorticity contours visualization of flow field around through inline SCs. The different splitter plate length within the spacing between the two cylinders represented the flow field characteristics in reattachment flow regime ($g/D = l/D = 0.5$ and 1) and steady flow regime ($g/D = l/D = 2.5, 5$ and 10). In shear layers reattachment flow (SLR) regime, the shear layers separated from the C_1 reattach on the upper surface of the C_2 (Figures 7(a) and 7(b)). When $g/D = l/D \geq 2.5$, the steady flow regime can be clearly seen behind both cylinders (Figures 7(c)–7(e)). Under these circumstances, the flow behind the upstream and downstream SCs was almost similar, and it was hardly affected by the downstream SC. Inspection of Figures 8(a)–8(e) further confirms that the flow through the downstream SC becomes steady only in existence of the splitter plate of $l/D \geq 2.5$.

The higher upward mean lift force is observed for the downstream SC when the two cylinders are closely spaced as the viscous effect is more towards the lower face of the downstream square cylinder. From Figures 9(a), 9(c), 9(e) and 9(g) it can be seen that at $l/D = 0.5, 1, 2.5$ and 10 the C_{D1} and C_{D2} are both constants. Furthermore, the C_{D2} having negative drag coefficient at $l/D = 0.5, 1$ and 2.5. On the other hand, the lift force has periodic behaviour with decreasing amplitude as the value of l/D increased. Furthermore, at l/D

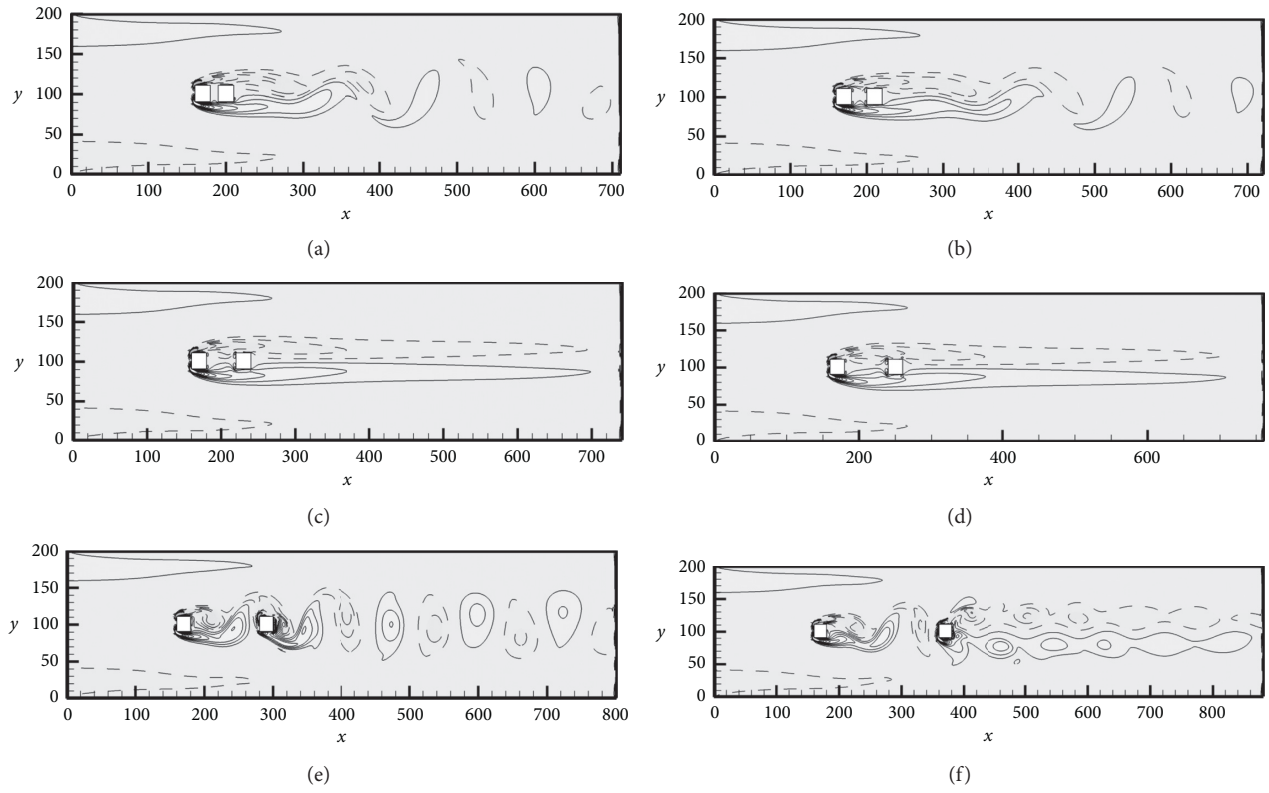


FIGURE 3: (a–f). Instantaneous vorticity contours visualization at different spacing ratios.

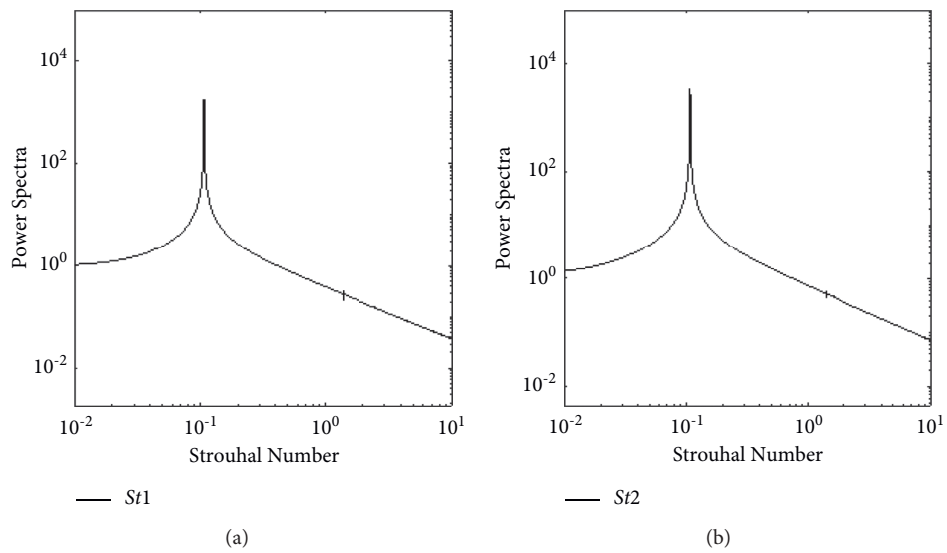
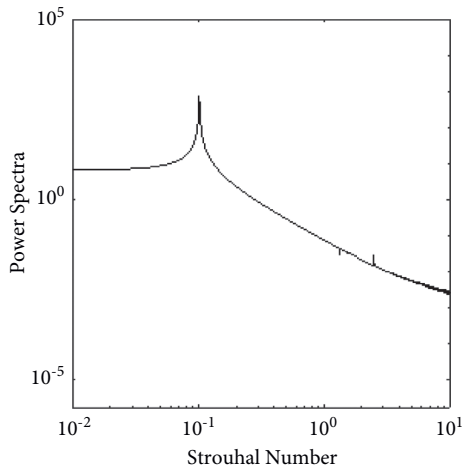
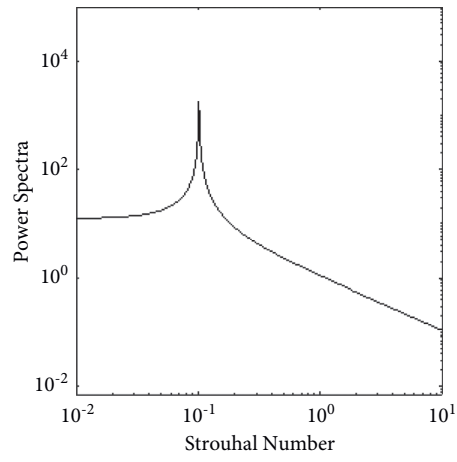


FIGURE 4: Continued.



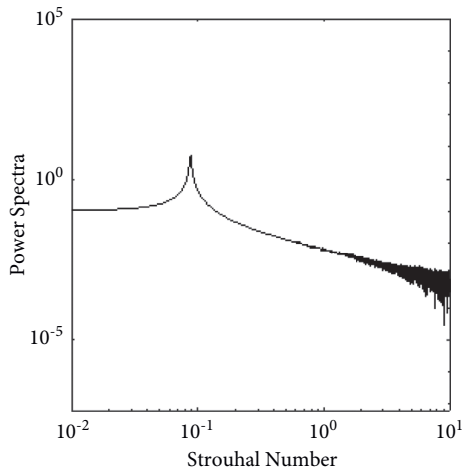
— St1

(c)



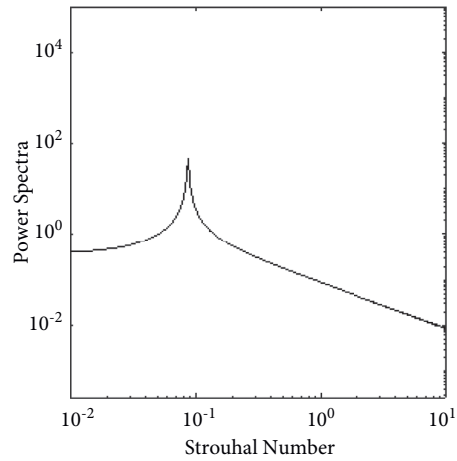
— St2

(d)



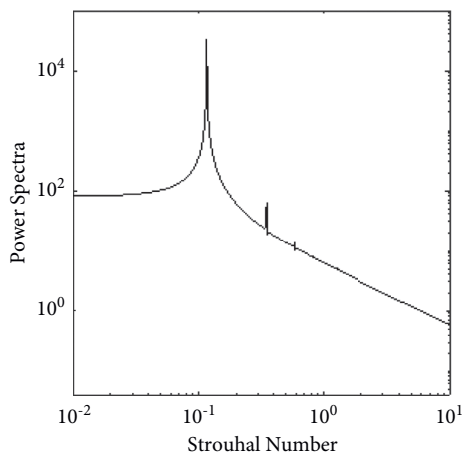
— St1

(e)



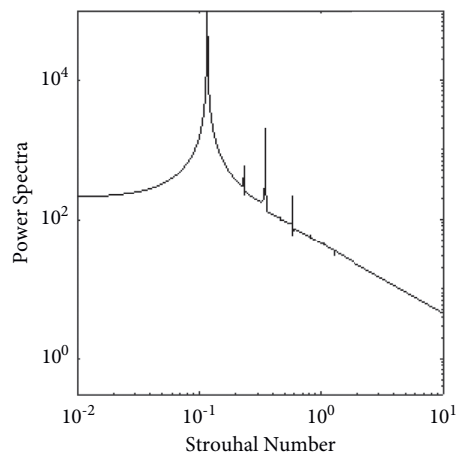
— St2

(f)



— St1

(g)



— St2

(h)

FIGURE 4: Continued.

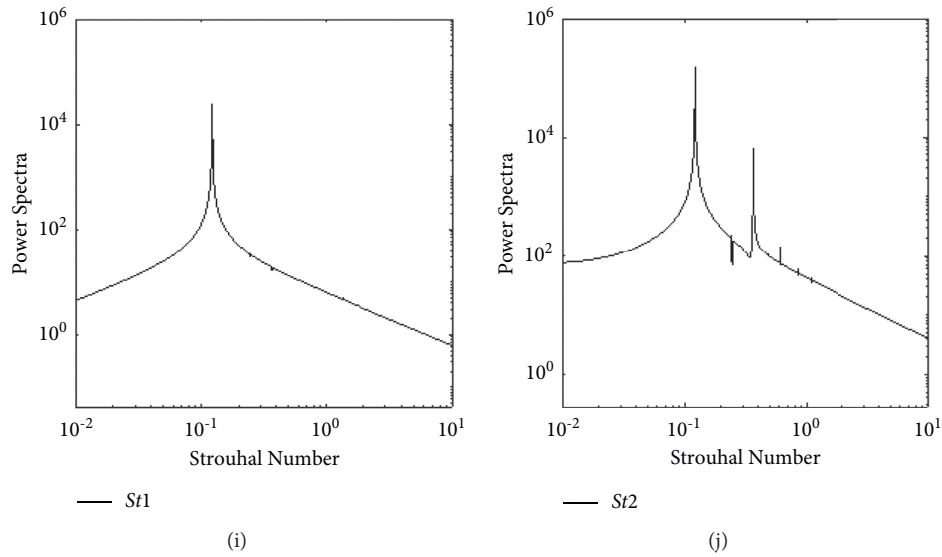


FIGURE 4: (a–j). Spectra analysis of lift coefficients at different spacing ratios.

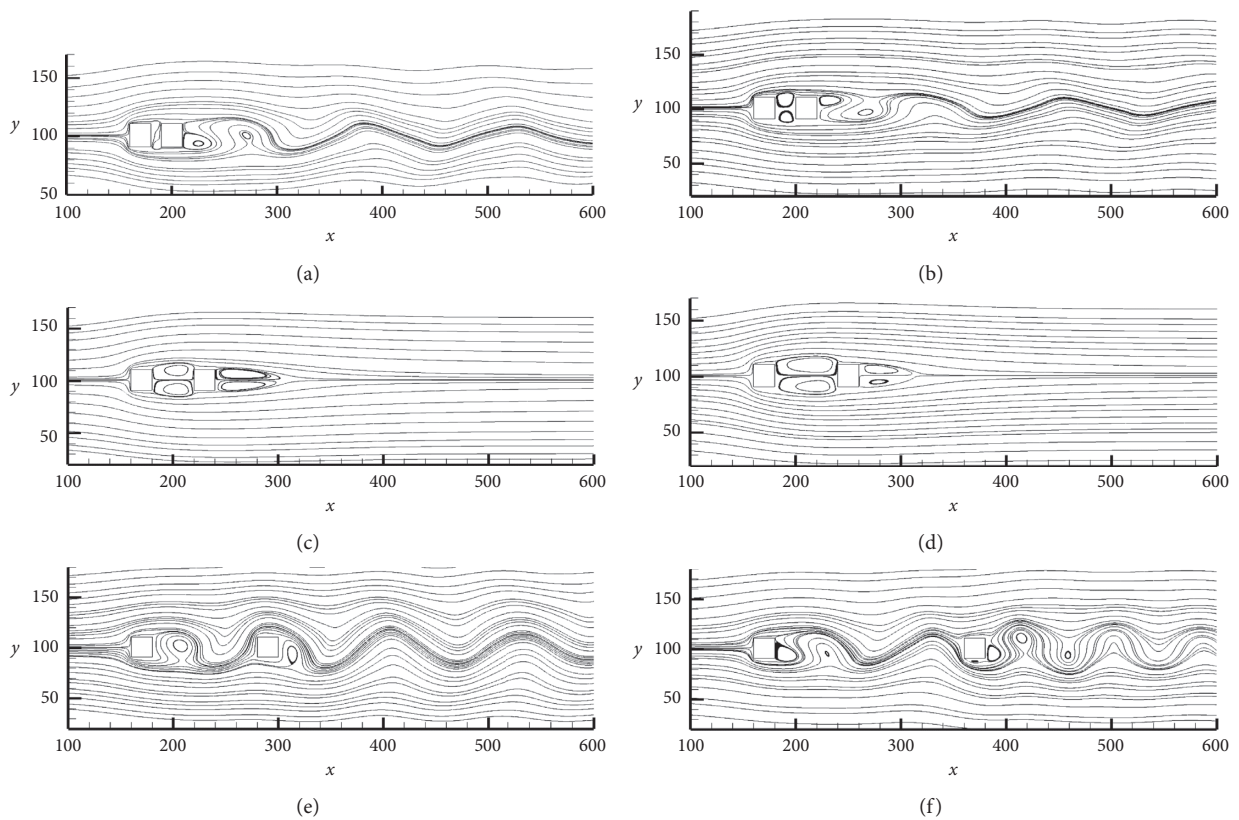


FIGURE 5: (a–f). Streamlines visualization at different spacing ratios.

$D = 10$, the lift force is a straight line due to steady flow behaviour behind the cylinders.

The power spectra of C_L of the two cylinders with different splitter plate length are shown in Figures 10(a)–10(f). At $l/D = 0.5$, the lift force oscillation of the upstream cylinder was stable, which ensures that the interference is weak between the cylinders. When the splitter plate length is

varied from 0.5 to 1, the power spectra not changed. With the further increase in splitter plate length, the interference among the two tandem cylinders slowly disappeared, and the oscillation became stable again. For the downstream cylinder, its lift force oscillation had almost the same behaviour as the upstream square cylinder. The difference was observed when the splitter plate length was varying from 5 to 10. Some

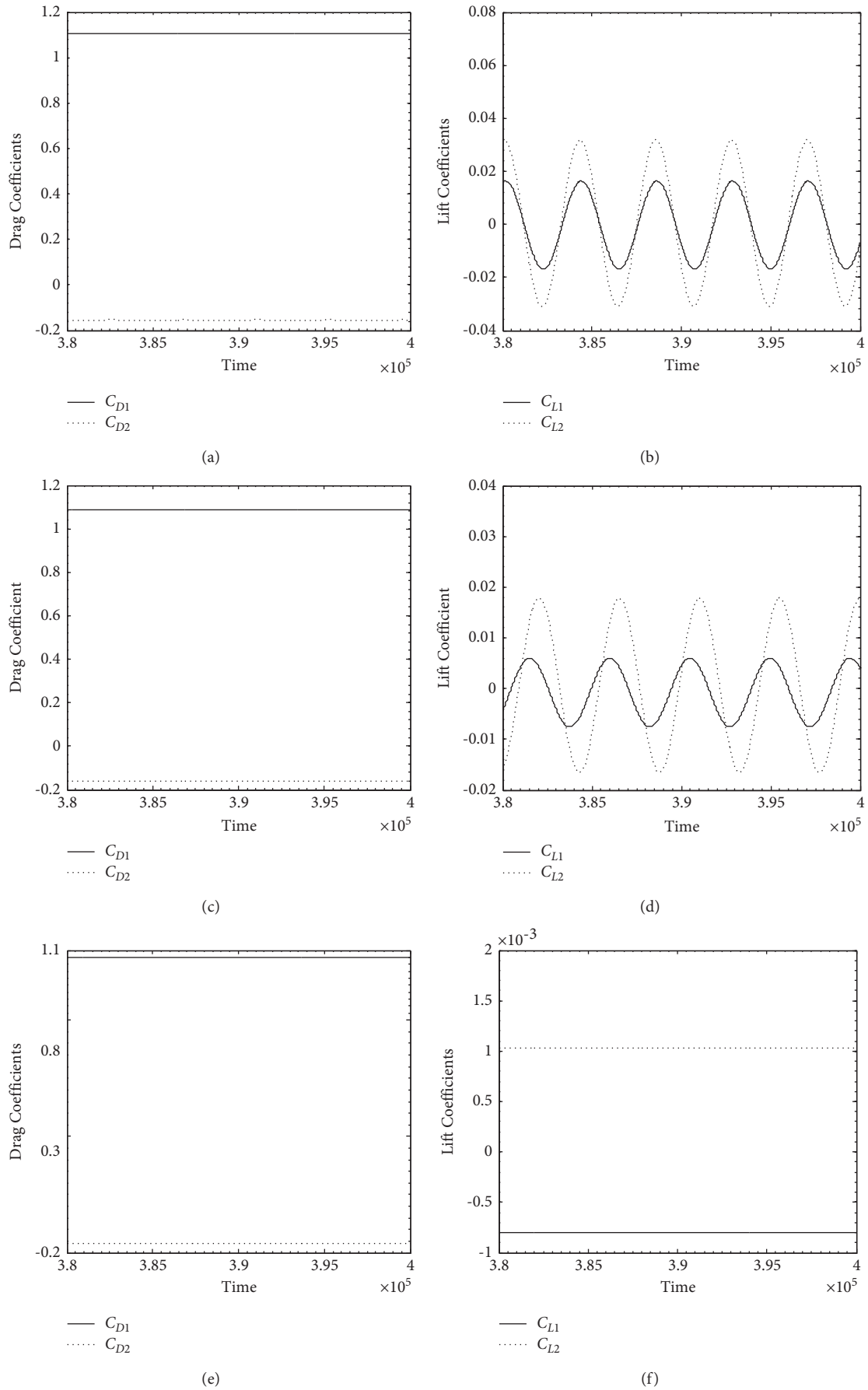
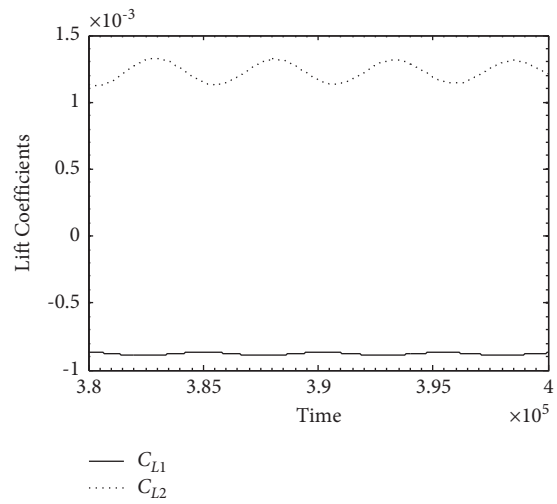
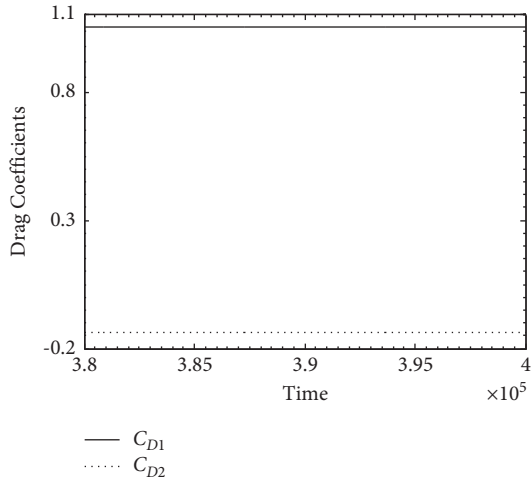
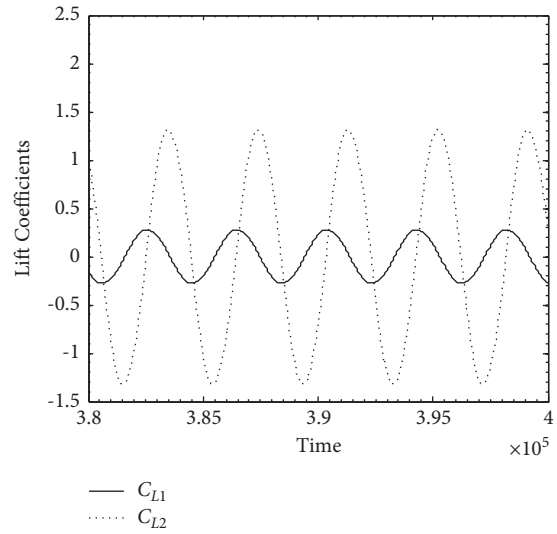
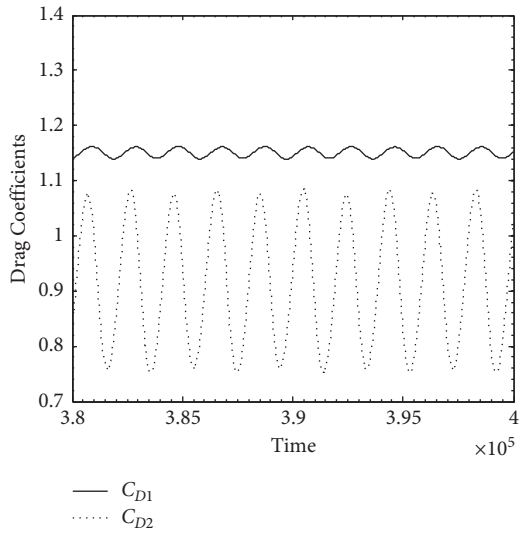


FIGURE 6: Continued.



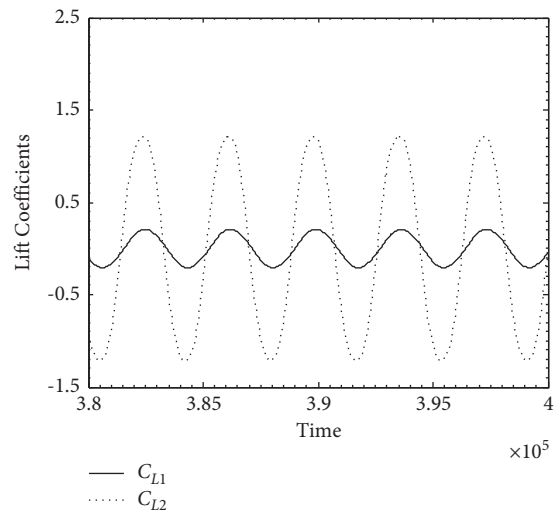
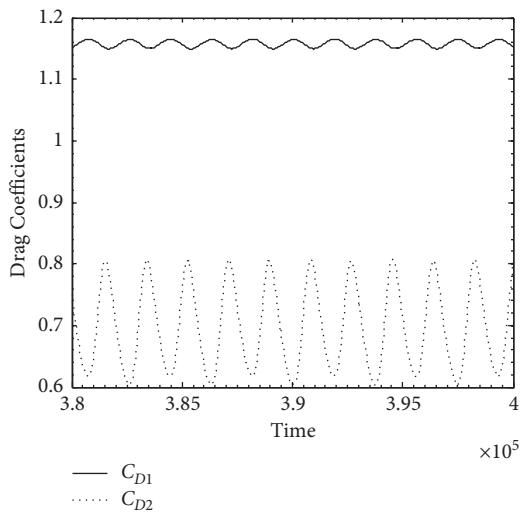
(g)

(h)



(i)

(j)



(k)

(l)

FIGURE 6: (a-l). Time variation of C_D and C_L at different spacing ratios.

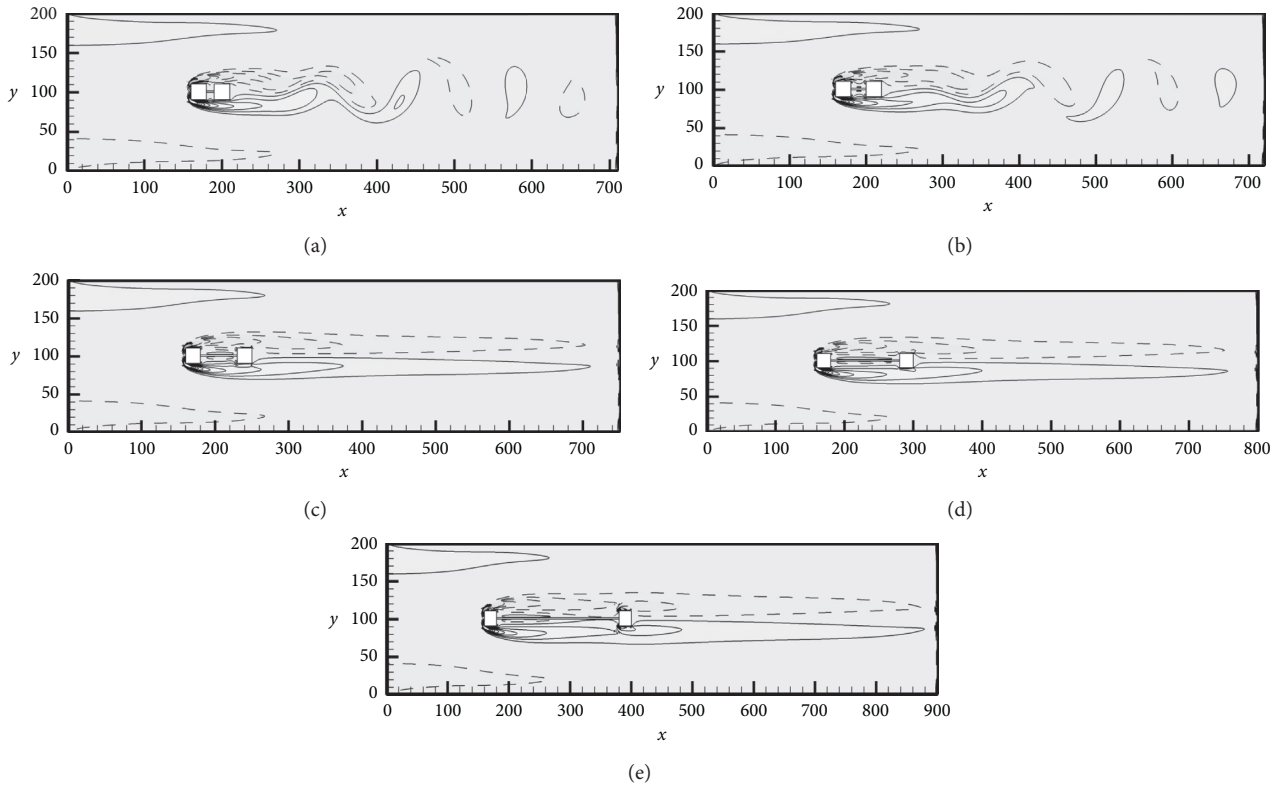


FIGURE 7: (a–e). Vorticity contours at different splitter plate lengths.

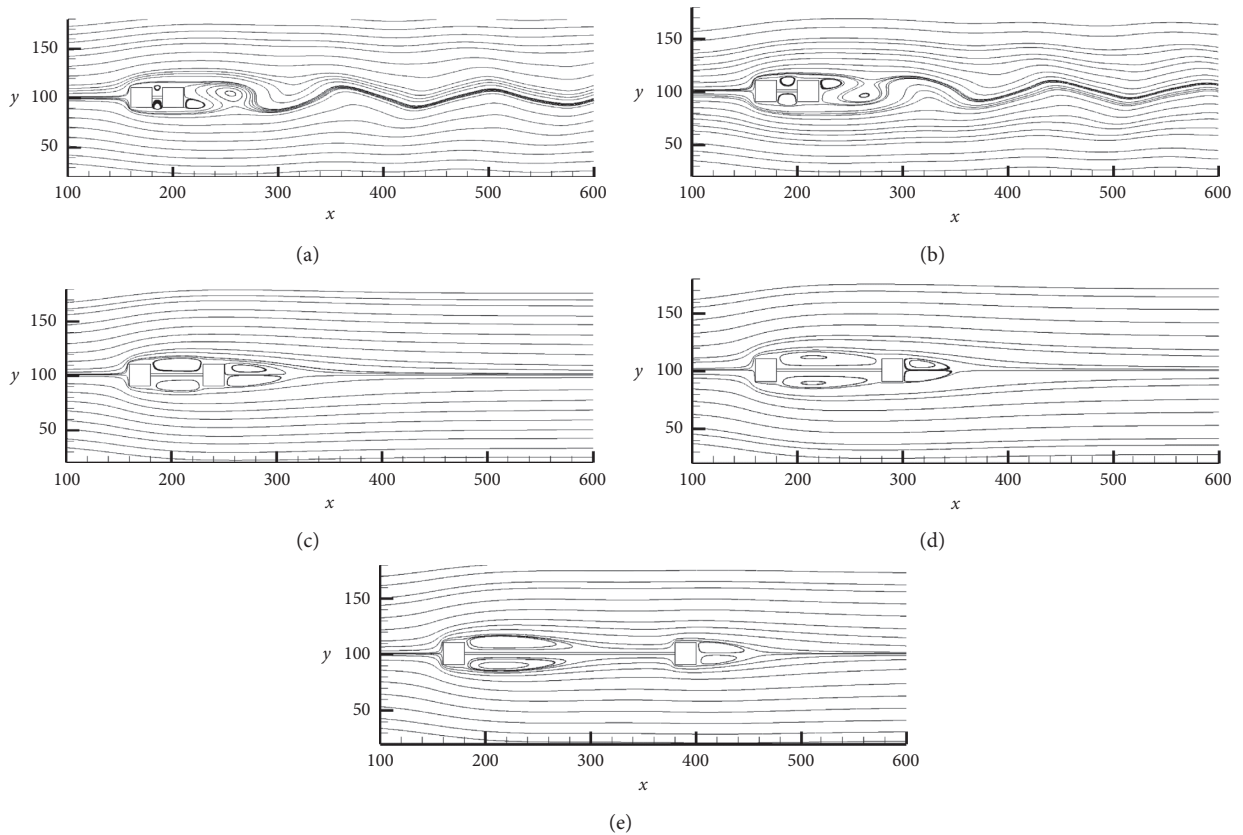
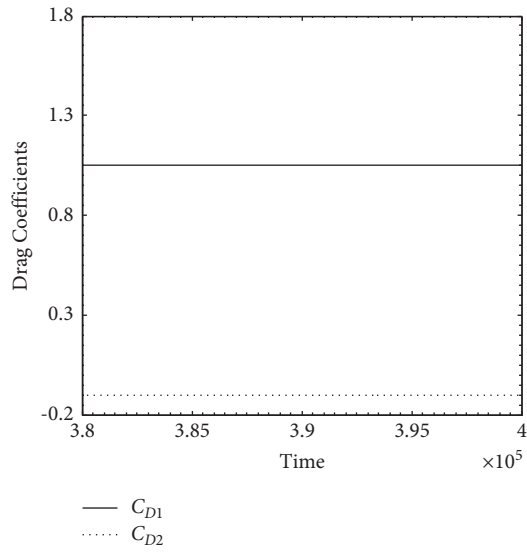
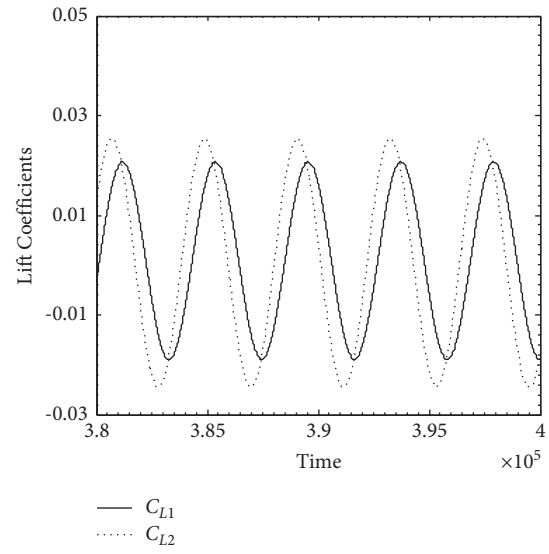


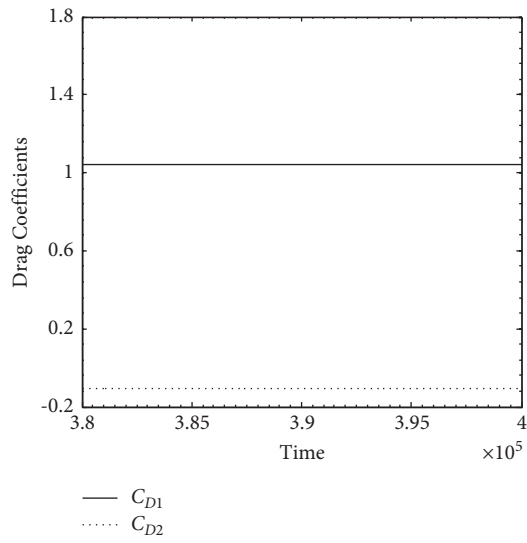
FIGURE 8: (a–e). Streamlines visualization at different values of splitter plate length.



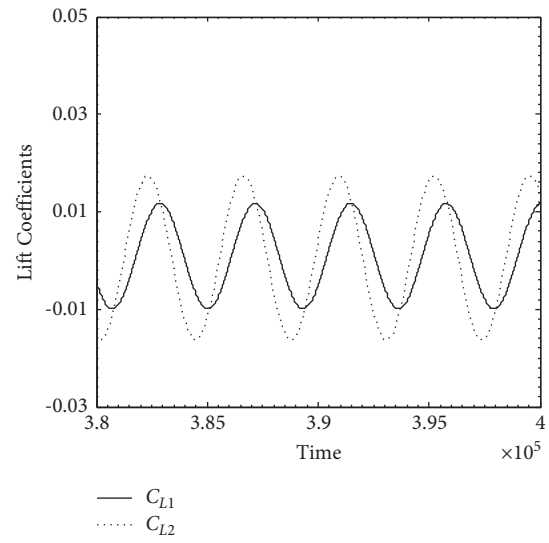
(a)



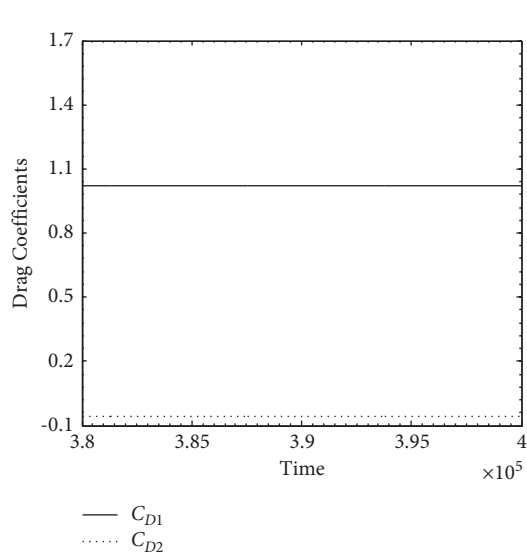
(b)



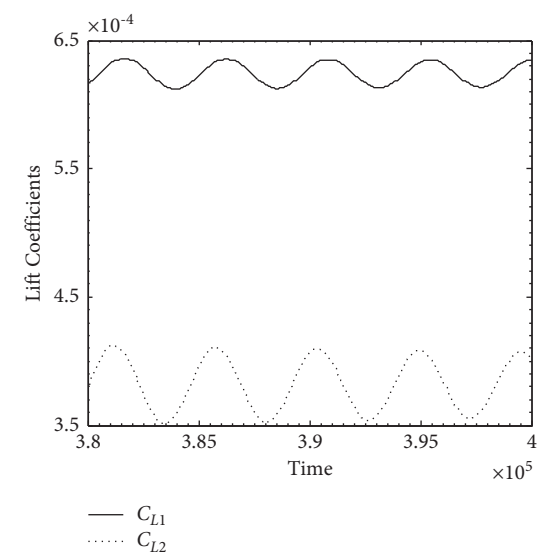
(c)



(d)



(e)



(f)

FIGURE 9: Continued.

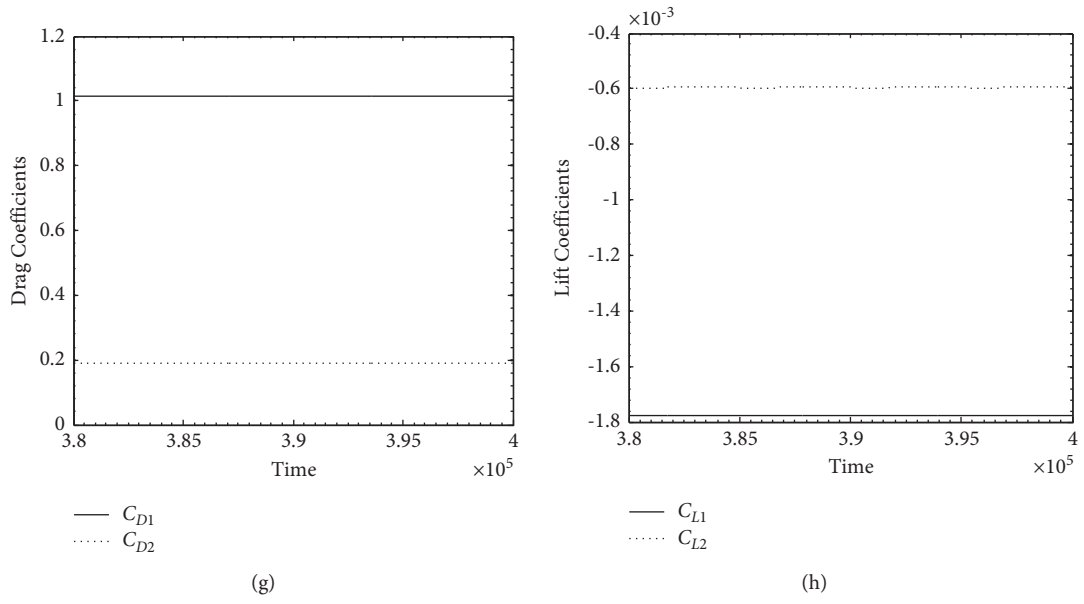


FIGURE 9: (a-h). Time variation of C_D and C_L at different l/D values.

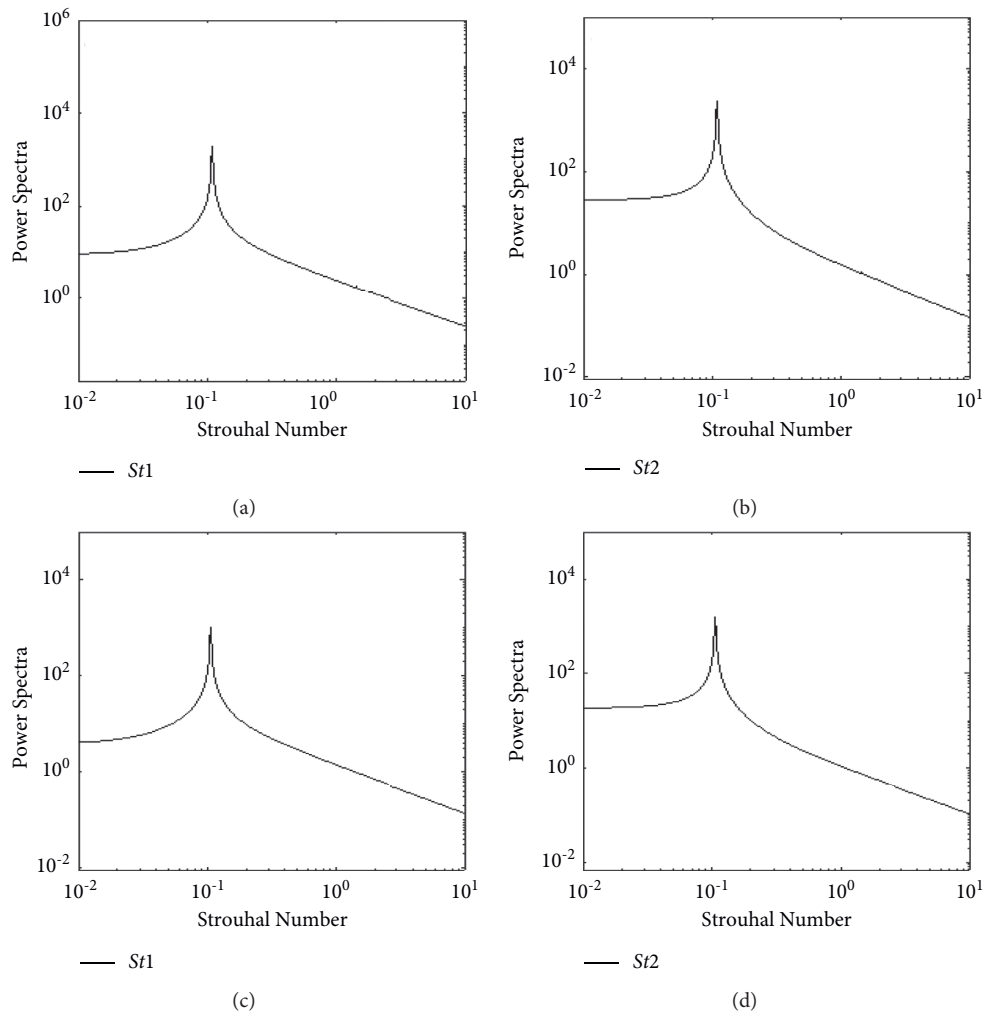


FIGURE 10: Continued.

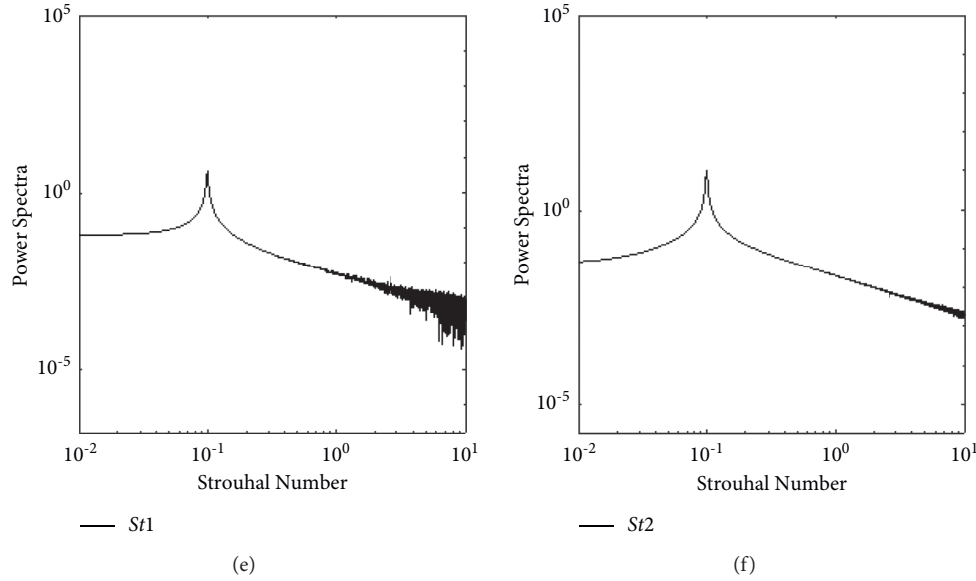


FIGURE 10: (a–f). The spectra analysis of lift coefficients at different l/D values.

minor peaks in the spectra of the upstream square cylinder were observed. This is due to the vortex generated by the C_1 directly acts on the C_2 .

The graphical representation of the different observed flow regimes is given in Figure 11. It can be observed that at small value of g/D and splitter plate length the single bluff body flow regime occurs. At intermediate values of g/D and l/D the shear layers reattachment flow regime occurs. The FDF regime and FDTRVS regime can be seen only for the two tandem square cylinders without splitter plate. It can also be observed from the flow diagram that the splitter plate considerably suppressed the vortex shedding behind the cylinders and completely convert it to steady flow regime.

4.3. Analysis of Force Statistics. In Figure 12(a), compared with the C_{Dmean} of a single SC, the C_{Dmean} of C_1 was slightly reduced up to $g/D = 4.5$ without splitter plate. As the g/D increased, the C_{Dmean} of the C_1 remained unchanged and was almost equal to an isolated cylinder. The C_{Dmean} of the C_2 was considerably smaller than that of single cylinder due to the influence by the wake of the upstream SC. The value of C_{Dmean} of the C_2 was negative when g/D is varied from 0.5 to 4. When the value of g/D increased to 4, the C_{Dmean} of C_2 changed from negative to positive. As the g/D continued to increase ($g/D > 4$), the C_{Dmean} of the downstream cylinder first increased and then slowly starts to decrease. The transition from shear layers reattachment flow regime to two-row vortex street flow regime was actually a positive-negative conversion of the C_{D2} . It is found that in presence with the splitter plate, the value of C_{Dmean} of the C_2 is considerably smaller than in the cases without splitter plate. The splitter plate length has marginal role on drag reduction for $g/D > 5$.

C_{Drms1} and C_{Drms2} are the root-mean-square drag values of the first cylinder and second cylinder, respectively (Figure 12(b)). The discontinuity is observed in C_{Drms2}

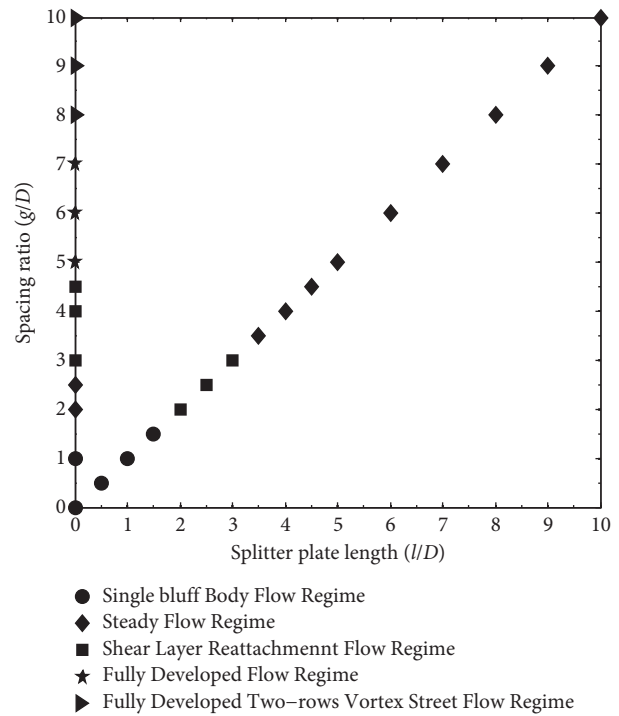


FIGURE 11: Flow regimes observed at different splitter plate lengths and spacing ratio.

without splitter plate in Figure 12(b) for the case of $g/D = 4.5$ due to transition of flow regime from shear layers reattachment flow regime ($g/D = 4$) to fully developed flow regime ($g/D = 4.5$). For a splitter plate length of l/D 1 to 10, the C_{Drms} of both cylinders is nearly equal to that of the isolated cylinder. However, it is found without splitter plate that the C_{Drms2} is irregular.

From Figure 13(a), it is seen that the C_L of the cylinder C_2 is more affected as compared to the cylinder C_1 due to the

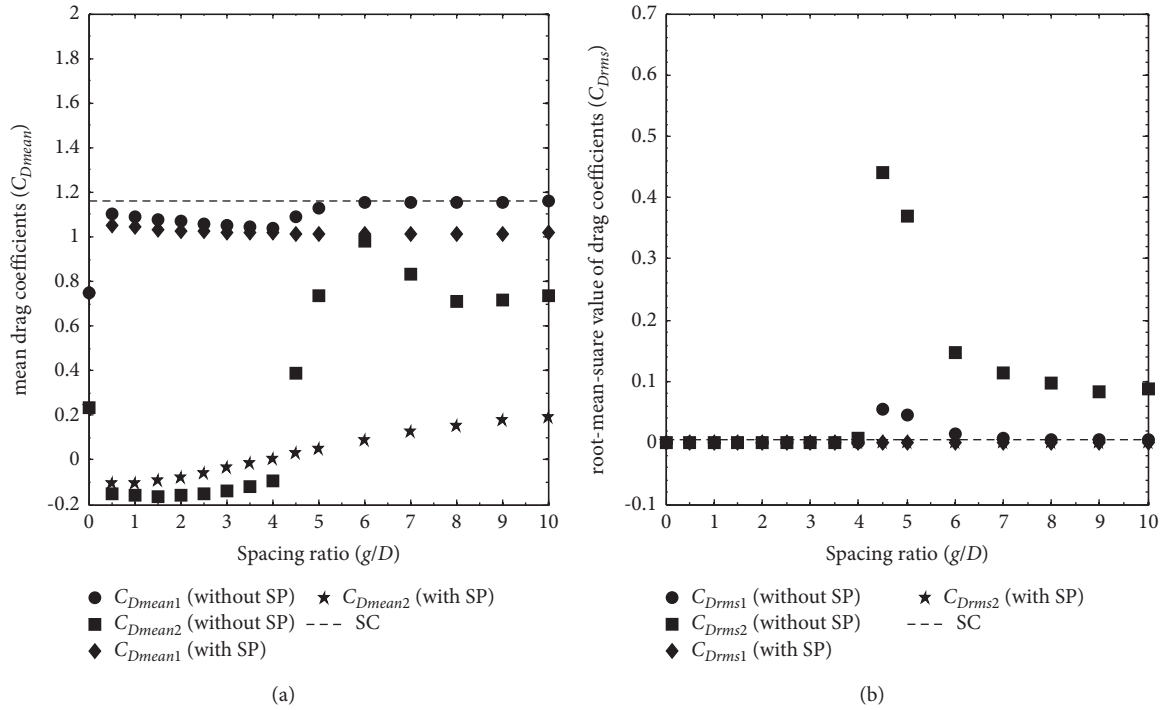


FIGURE 12: (a, b). Variation of C_{Dmean} and C_{Drms} as a function of spacing ratio.

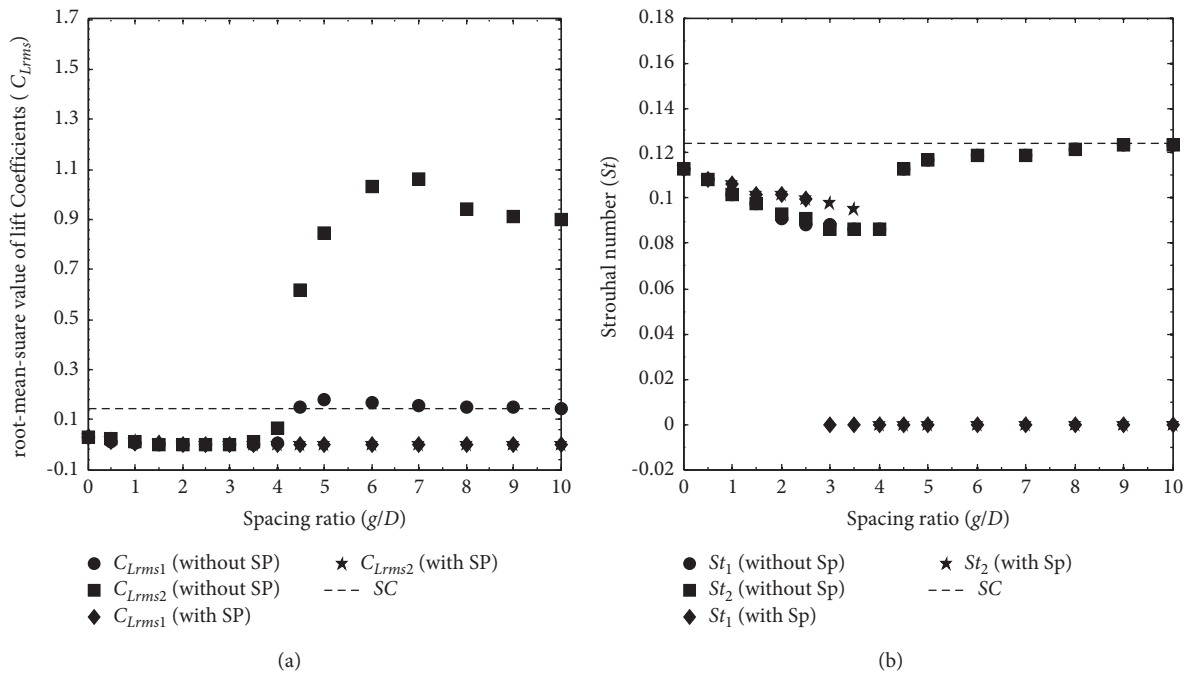


FIGURE 13: (a, b). Variation of C_{Lrms} and St as a function of spacing ratio.

change in g/D . The dependency of C_{Lrms2} is more pronounced at higher spacing ratios. On the increase of length of the splitter plate, the C_{Lrms2} apparently lower than the value of an isolated SC. The shedding frequency is one of the fluidic parameters which can affect the C_2 and alter wake dynamics. Similar to the numerical results of Sharman et al.

[30], the St values of the C_1 and C_2 are the same with all g/D values considered in this study.

Figure 14 presents the percentage reduction of C_{Dmean} of flow past two tandem cylinders. Regarding the C_{Dmean2} , the control effectiveness increases with increasing the splitter plate length: i.e., 49, 53.4, 57.2, 56.1, 62, 63.1, 67.1, 60, 53.1,

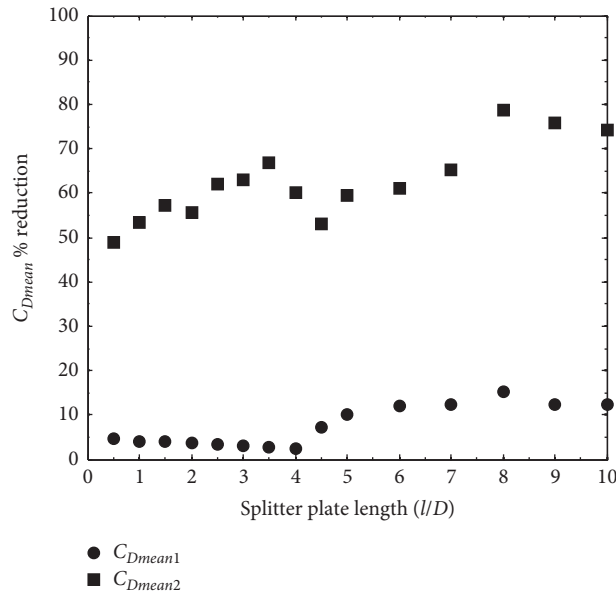


FIGURE 14: Percentage reduction of C_{Dmean} at different values of l/D .

59.4, 61, 65.2, 79.1, 76.1, and 74.2% for $l/D = 0.5, 1, 1.5, 2, 2.5, 3, 3.5, 4, 4.5, 5, 6, 7, 8, 9,$ and 10 , respectively. The larger splitter plate length will lead to a better control of fluid forces.

5. Conclusions

In this article, the numerical simulation for flow past two tandem cylinders in presence of attached splitter plate was carried out at $Re = 100$. This study investigates the drag reduction and the interference among the cylinders at various splitter plate length of $l/D = 0.5$ to 10 . The observed flow regimes were divided into five different regimes: single-bluff body, shear layers reattachment, steady, fully developed two-row vortex shedding and fully developed flow regimes. The C_{Dmean2} was negative when g/D is varied from 0.5 to 4 . We not found fully developed shed vortices between the cylinders in case of single-bluff body and shear layers reattachment flow regimes. The discontinuity is observed in C_{Drms2} without splitter plate for the case of $g/D = 4.5$ due to transition of flow regime from shear layers reattachment flow regime ($g/D = 4$) to fully developed flow regime ($g/D = 4.5$). The dependency of root-mean-square value of lift coefficient of the downstream cylinder (C_{Lrms2}) is more pronounced at higher spacing ratios. Regarding the mean drag coefficient of the downstream square cylinder, the maximum reduction about 79.1% is observed for $l/D = 8$.

Data Availability

Data will be provided on demand.

Conflicts of Interest

The authors declare that they have no conflicts of interest.

References

- [1] N. Kondo and D. Matsukuma, "Numerical simulation for aerodynamic characteristics of two circular cylinders in staggered arrangement by a third-order upwind finite element method," *International Journal of Computational Fluid Dynamics*, vol. 20, no. 8, pp. 1–20, 2006.
- [2] H. Sakamoto, H. Hainu, and Y. Obata, "Fluctuating forces acting on two square prisms in a tandem arrangement," *Journal of Wind Engineering and Industrial Aerodynamics*, vol. 26, no. 1, pp. 85–103, 1987.
- [3] A. Azuma, M. Iuchi, I. Watnabe, K. Fujii, K. Sida, and K. Watanabe, "Wind tunnel investigation of buildings and structures," *Journal of the Japan Society for Aeronautical and Space Sciences*, vol. 22, pp. 209–295, 1974, in Japanese.
- [4] W. S. Abbasi, S. U. Islam, and H. Rahman, "Proximity effects on characteristics of flow around three inline square cylinders," *Mathematical Problems in Engineering*, vol. 2019, 14 pages, 2019.
- [5] W. Sarwar Abbasi, S. Ul Islam, L. Faiz, and H. Rahman, "Numerical investigation of transitions in flow states and variation in aerodynamic forces for flow around square cylinders arranged inline," *Chinese Journal of Aeronautics*, vol. 31, no. 11, pp. 2111–2123, 2018.
- [6] S. Mittal, V. Kumar, and A. Raghuvanshi, "Unsteady incompressible flows past two cylinders in tandem and staggered arrangements," *International Journal for Numerical Methods in Fluids*, vol. 25, no. 11, pp. 1315–1344, 1997.
- [7] W. S. Abbasi and S. U. Islam, "Transition from steady to unsteady state flow around two inline cylinders under the effect of Reynolds numbers," *Journal of the Brazilian Society of Mechanical Sciences and Engineering*, vol. 40, no. 3, p. 168, 2019.
- [8] C. K. Vikram, Y. K. Gowda, H. V. Ravindra, and C. G. Gowda, "Numerical simulation of two dimensional unsteady flow past two square cylinders," *International Journal of Technology and Engineering System*, vol. 2, no. 3, pp. 355–360, 2011.
- [9] B. Sharman, F. S. Lien, L. Davidson, and C. Norberg, "Numerical predictions of low Reynolds number flows over two

- tandem circular cylinders,” *International Journal for Numerical Methods in Fluids*, vol. 47, no. 5, pp. 423–447, 2005.
- [10] C.-H. Liu and J. M. Chen, “Observations of hysteresis in flow around two square cylinders in a tandem arrangement,” *Journal of Wind Engineering and Industrial Aerodynamics*, vol. 90, no. 9, pp. 1019–1050, 2002.
- [11] A. Sohankar and A. Etminan, “Forced-convection heat transfer from tandem square cylinders in cross flow at low Reynolds numbers,” *International Journal for Numerical Methods in Fluids*, vol. 60, no. 7, pp. 733–751, 2009.
- [12] P. W. Bearman, “Investigation of the flow behind a two-dimensional model with a blunt trailing edge and fitted with splitter plates,” *Journal of Fluid Mechanics*, vol. 21, no. 2, pp. 241–255, 1965.
- [13] P. W. Bearman, “The effect of base bleed on the flow behind a two-dimensional model with a blunt trailing edge,” *Aeronautical Quarterly*, vol. 18, no. 3, pp. 207–224, 1967.
- [14] M. M. Zdravkovich, “Review and classification of various aerodynamic and hydrodynamic means for suppressing vortex shedding,” *Journal of Wind Engineering and Industrial Aerodynamics*, vol. 7, no. 2, pp. 145–189, 1981.
- [15] G. Artana, R. Sosa, E. Moreau, and G. Touchard, “Control of the near-wake flow around a circular cylinder with electro-hydrodynamic actuators,” *Experiments in Fluids*, vol. 35, no. 6, pp. 580–588, 2003.
- [16] J. H. M. Fransson, P. Konieczny, and P. H. Alfredsson, “Flow around a porous cylinder subject to continuous suction or blowing,” *Journal of Fluids and Structures*, vol. 19, pp. 1031–1048, 2004.
- [17] C. Y. Zhou, L. Wang, and W. Huang, “Numerical study of fluid force reduction on a circular cylinder using tripping rods,” *Journal of Mechanical Science and Technology*, vol. 21, no. 9, pp. 1425–1434, 2007.
- [18] Y. J. Chen and C. P. Shao, “Suppression of vortex shedding from a rectangular cylinder at low Reynolds numbers,” *Journal of Fluids and Structures*, vol. 43, pp. 15–27, 2013.
- [19] A. Gupta and A. K. Saha, “Suppression of vortex shedding in flow around a square cylinder using control cylinder,” *European Journal of Mechanics-B/Fluids*, vol. 76, pp. 276–291, 2019.
- [20] A. Ahmed, S.-U. Islam, C. Y. Zhou, and R. Manzoor, “Fluid dynamics around three cylinders in presence of small control cylinders,” *Canadian Journal of Physics*, vol. 98, no. 11, pp. 1060–1076, 2020.
- [21] K. Kwon and H. Choi, “Control of laminar vortex shedding behind a circular cylinder using splitter plates,” *Physics of Fluids*, vol. 8, pp. 479–486, 1996.
- [22] M. Mahbub Alam, H. Sakamoto, and Y. Zhou, “Effect of a t -shaped plate on reduction in fluid forces on two tandem cylinders in a cross-flow,” *Journal of Wind Engineering and Industrial Aerodynamics*, vol. 94, no. 7, pp. 525–551, 2006.
- [23] E. A. Anderson and A. A. Szewczyk, “Effects of a splitter plate on the near wake of a circular cylinder in 2 and 3-dimensional flow configurations,” *Experiments in Fluids*, vol. 23, no. 2, pp. 161–174, 1997.
- [24] D. You, H. Choi, M.-R. Choi, and S.-H. Kang, “Control of flow-induced noise behind a circular cylinder using splitter plates,” *AIAA Journal*, vol. 36, pp. 1961–1967, 1998.
- [25] T. Uffinger, S. Becker, and A. Delgado, “Investigations of the flow field around different wall-mounted square cylinder stumps geometries,” in *Proceedings of the 14th International Symposium on Application of Laser Techniques to Fluid Mechanics*, pp. 7–10, Lisbon, Portugal, July 2008.
- [26] M. Sukri Mat Ali, C. J. Doolan, and V. Wheatley, “The sound generated by a square cylinder with a splitter plate at low Reynolds number,” *Journal of Sound and Vibration*, vol. 330, no. 15, pp. 3620–3635, 2011.
- [27] Z. Guo, H. Liu, L.-S. Luo, and K. Xu, “A comparative study of the LBE and GKS methods for 2D near incompressible laminar flows,” *Journal of Computational Physics*, vol. 227, no. 10, pp. 4955–4976, 2008.
- [28] A. A. Mohammad, *Lattice Boltzmann Method: Fundamentals and Engineering Applications with Computer Codes*, Springer, Berlin, Germany, Second edition, 2019.
- [29] A. Sharma and V. Eswaran, “Heat and fluid flow across a square cylinder in the two-dimensional laminar flow regime,” *Numerical Heat Transfer, Part A: Applications*, vol. 45, no. 3, pp. 247–269, 2004.
- [30] R. Mei, D. Yu, W. Shyy, and L.-S. Luo, “Force evaluation in the lattice Boltzmann method involving curved geometry,” *Physical Review E*, vol. 65, pp. 1–28, 2002.
- [31] U. Frisch, B. Hasslacher, and Y. Pomeau, “Lattice-gas automata for the Navier-Stokes equation,” *Physical Review Letters*, vol. 56, no. 14, pp. 1505–1508, 1986.
- [32] M. Breuer, J. Bernsdorf, T. Zeiser, and F. Durst, “Accurate computations of the laminar flow past a square cylinder based on two different methods: lattice-Boltzmann and finite-volume,” *International Journal of Heat and Fluid Flow*, vol. 21, no. 2, pp. 186–196, 2000.
- [33] D. Sumner, S. S. T. Wong, S. J. Price, and M. P. Païdoussis, “Fluid behaviour of side-by-side circular cylinders in steady cross-flow,” *Journal of Fluids and Structures*, vol. 13, no. 3, pp. 309–338, 1999.
- [34] S. Dutta, P. K. Panigrahi, and K. Muralidhar, “Effect of orientation on the wake of a square cylinder at low Reynolds numbers,” *Indian Journal of Engineering and Materials Sciences*, vol. 11, no. 6, 2004.
- [35] C. Norberg, A. Sohankar, and L. Davidson, “Numerical simulation of unsteady flows around a square two-dimensional cylinder,” in *Proceedings of the Twelfth Australian Fluid Mechanics Conference*, Sydney, Australia, December 1995.
- [36] A. Okajima, “Strouhal numbers of rectangular cylinders,” *Journal of Fluid Mechanics*, vol. 123, pp. 379–398, 1982.
- [37] T. Igarashi, “Characteristics of the flow around two circular cylinders arranged in tandem: 1st report,” *Bulletin of JSME*, vol. 24, no. 188, pp. 323–331, 1981.

Research Article

Topological Characteristics of Obstacles and Nonlinear Rheological Fluid Flow in Presence of Insulated Fins: A Fluid Force Reduction Study

Afraz Hussain Majeed ¹, Fahd Jarad ^{2,3}, Rashid Mahmood ¹, and Imran Saddique⁴

¹Department of Mathematics, Air University, PAF Complex E-9, Islamabad 44000, Pakistan

²Department of Mathematics, Cankaya University, Etimesgut, Ankara, Turkey

³Department of Medical Research, China Medical University Hospital, China Medical University, Taichung, Taiwan

⁴Department of Mathematics, School of Science, University of Management and Technology, Lahore-54770, Pakistan

Correspondence should be addressed to Fahd Jarad; fahd@cankaya.edu.tr

Received 7 July 2021; Accepted 9 August 2021; Published 18 August 2021

Academic Editor: Shams -ul-Islam

Copyright © 2021 Afraz Hussain Majeed et al. This is an open access article distributed under the Creative Commons Attribution License, which permits unrestricted use, distribution, and reproduction in any medium, provided the original work is properly cited.

In this work, a comprehensive study of fluid forces and thermal analysis of two-dimensional, laminar, and incompressible complex (power law, Bingham, and Herschel–Bulkley) fluid flow over a topological cross-sectional cylinder (square, hexagon, and circle) in channel have been computationally done by using finite element technique. The characteristics of nonlinear flow for varying ranges of power law index ($0.4 \leq n \leq 1.6$), Bingham number ($0 \leq Bn \leq 50$), Prandtl number ($0.7 \leq Pr \leq 10$), Reynolds number ($10 \leq Re \leq 50$), and Grashof number ($1 \leq Gr \leq 10$) have been examined. Considerable evaluation for thermal flow field in the form of dimensionless velocity profile, isotherms, drag and lift coefficients, and average Nusselt number (Nu_{avg}) is done. Also, for a range of Bn , the drag forces reduction is observed for circular and hexagonal obstacles in comparison with the square cylinder. At $Bn = 0$ corresponding to Newtonian fluid, maximum reduction in drag force is reported.

1. Introduction

Since the last several decades, heat transfer from a single cylinder (circular, square) has been widely considered, given its significance in various fields of engineering mathematical problems. The key research factors for the design, maintenance of electric cooling system, evaporators, heat exchangers, thermal plants and automobile radiators, etc., can be reported. Moreover, thermal flow by natural, forced, and mixed convection from solid body to fluid stream has been simulated by many researchers in a variety of configurations. Ditchfield et al. [1] experimentally examined the effects of thermal flow on viscoplastic fluid by implementing a proposed model. Shyam et al. [2] considered the influence of nonisothermal and nonlinear viscous fluid flow over the pair of circular heaters at large Grashof number. Computations were reported by varying gap between cylinders to elucidate

its impact on thermal flow field. Laidoudi et al. [3, 4] analyzed the characteristics of mixed convection thermal flow of dual circular cylinders at low Reynolds number. They also computed fluid forces and average Nusselt number and observed high Nusselt number on second obstacle compared to the first one due to thermal buoyancy. Kefayati et al. [5] have numerically investigated the effects of double diffusion and entropy generation of viscous fluid flow over a cold cylinder in a duct by Lattice Boltzmann technique. In addition, an enhancement in heat transfer was noticed due to increase in the length of diameter of the cylinder. The buoyancy effects on thermal flow characteristics of confined circular cylinder submerged laminar Poiseuille fluid are studied by Laidoudi et al. [6]. Masoumi et al. [7] have examined the influence of nonisothermal viscoplastic fluid flow inside the circular duct and also imposed the Galerkin's Weighted Residual (GWR) scheme of FEM computation

with hybrid mesh. The influence of Richardson number on flow and heat transfer topologies of an obstacle at high Reynolds number are examined by Zafar and Alam [8]. Laidoudi et al. [9] considered the effects of the free convection fluid flow between two cylinders at high Reynolds number in a circular duct and also provided the correlation impacts of the average Nusselt number.

In order to design structures for non-Newtonian fluid exposed in polymer processing activities, reliable knowledge about fluid forces is often necessary, and in this regard, the flow and heat transfer in the free convection regime have been considerably studied in extensive research resources in recent years. Bharti et al. [10, 11] investigated the characteristics of steady, incompressible, non-Newtonian fluid flow over a confined cylinder at low Reynolds number $Re \leq 40$. They solved the model by using QUICK algorithm and finite volume scheme. Shyam et al. [12] numerically studied the influence of thermal flow of free convection over a constant heated block in a square duct and also reported the effects of average Nusselt number on Grashof and Prandtl number against power law index. Baranwal and Chhabra [13] considered an incompressible free convective thermal flow of power law fluid over a confined cylinder in square cavity. In addition, they examined the geometric effects of the cylinder on thermal flow fields. A. Pantokratoras [14] numerically reported the flow of power law fluid over a rotating cylinder solved by using finite volume scheme through commercial code FLUENT. Gangawane and Manikandan [15] have explored the thermal flow features over a hexagonal block with constant temperature, solved by using finite volume technique with QUICK discretization and SIMPLE algorithm. Asnaashari and Tohidi [16] investigated the effects of flow and heat transfer of power law fluid in an unconfined computational domain. Dhiman and Shyam [17] have examined the influence of Reynolds number on unsteady heat transfer over an equilateral triangular block and created grid by GAMBIT and solved it by using FLUENT.

Nirmalkar and Chhabra [18] studied the characteristics of Bingham fluid flow over a heated submerged cylinder using finite element computation. Patel and Chhabra [19] have extensively examined heat transfer, fluid forces, and yield stress results in steady flow regime. Mahmood et al. [20] have simulated a plastic fluid flow of square cavity by using the open-source software package FEATFLOW submerged in Papanastasiou regularization. Liu et al. [21] investigated the characteristics of Bingham fluid flow in deeply buried rock. Thakur et al. [22] have been considered a forced convective heat transport of a Bingham fluid over a rotating circular cylinder at low Reynolds number. Rem et al. [23] investigated the influence of unsteady Bingham fluid flow in a fractured channel.

The Herschel–Bulkley fluid model narrates the rheological influence of viscoplastic fluids which occurred in innumerable applications in industry. These viscous fluids are characterized by yield stress which requires a finite stress for flow. The relation between the shear stress and the shear rate is nonlinear. Since thermal flow is important in industrial applications with viscoplastic fluid flow like paint, cosmetic, and petroleum, many researchers have examined

the characteristics of thermal flow in such viscoplastic fluid flow regimes [24–32].

Zdanski and Vaz [33] have implemented a second-order finite difference scheme to simulate a flow problem of incompressible 3D viscous fluid flow in a channel. Abbasi et al. [34] have numerically analyzed the impacts of hydrodynamic forces over a cylinder-based Lattice Boltzmann Method (LBM) at low Reynolds number. Also, they compared their results with numerical and experimental data for single square cylinder case. Mahmood et al. [35] studied the non-Newtonian flow in a channel driven cavity by using $P_2 - P_1$ element pair for finite element computation. Abbasi et al. [36] examined the characteristics of fluid forces over square cylinders at varying range of gap spacing, solved by LBM computation. Khan et al. [37] imposed least square FEM computation of viscous fluid flow over a semicylinder block via COMSOL solver. Tomio et al. [38] implemented a numerical methodology, second-order finite difference scheme to solve a flow problem. Characterization of fluid forces of nonlinear material in a channel is based on FEM computation at low Reynolds number [39–41].

This manuscript is organized as follows. In Section 1 and Section 2, the introduction of the problem and the flow configuration and governing equations with constitutive relations are explained. Numerical scheme and grid convergence are described in Section 3. Also, the results are compared with literature for code validation. In Section 4, we explain in detail all the results and discussion of the article. Finally, conclusion is mentioned in Section 5.

2. Flow Configuration and Governing Equations

A cylinder (square, hexagon, and circle) of diameter $L_D = 0.1$ in an incompressible viscous polymer solution in laminar, steady, 2D flow regime is revealed in Figure 1. The surface of cylinders is maintained at a uniform temperature T_h and flow with average velocity U_∞ . The total length of given benchmark problem is $L_{up} + L_{down}$, where $L_{up} = 0.2$ is the upstream length and downstream length is $L_{down} = 2$ from the center of the cylinder and height of the channel is 0.41, respectively. Moreover, the thermophysical properties of fluids are considered to be free from temperature. Also, we have neglected the effects of viscous dissipation from heat equation.

The geometrical configuration of the problem is shown in Figure 1.

Continuity, momentum, and energy are the governing equations of steady, nonisothermal, and viscous incompressible fluid flow across an infinitely long channel in presence of heated cylinder. Their nondimensional forms of these equations are written as follows:

$$\nabla \cdot \mathbf{u} = 0, \quad (1)$$

$$\mathbf{u} \cdot \nabla \mathbf{u} + \nabla p = \frac{1}{Re} \nabla \cdot \boldsymbol{\tau} + \frac{Gr}{Re^2} \boldsymbol{\theta}, \quad (2)$$

$$\mathbf{u} \cdot \nabla \theta = \frac{1}{\text{RePr}} \nabla^2 \theta, \quad (3)$$

where τ represents the category of the chosen fluid. Here we have used three models, namely, power law, Bingham, and Herschel–Bulkley fluid defined as follows.

(i) Power law model:

$$\tau = m(\dot{\gamma})^n. \quad (4)$$

(ii) Bingham model:

$$\begin{cases} \dot{\gamma} = 0, & \tau \leq \tau_y, \\ \tau = \left(\frac{\tau_y}{\dot{\gamma}} + \mu_p \right) \dot{\gamma}, & \tau > \tau_y. \end{cases} \quad (5)$$

(iii) Herschel–Bulkley model:

$$\begin{cases} \tau = \tau_y + m\dot{\gamma}^n, \\ \eta = \frac{\tau_y}{\dot{\gamma}} + m\dot{\gamma}^{n-1}, & \tau > \tau_y. \end{cases} \quad (6)$$

The nondimensionalized equations (1)–(3) suggest that velocity, pressure, and temperature fields are dependent on dimensionless parameters, Reynolds number (Re), Grashof number (Gr), Prandtl number (Pr), and Bingham number (Bn). These parameters are defined as

$$\begin{aligned} \text{Reynolds number } \text{Re} &= \frac{U_\infty L_D}{\nu}, \\ \text{Grashof number } \text{Gr} &= \frac{g\beta(T_h - T_0)L_D^3}{\nu^2}, \\ \text{Prandtl number } \text{Pr} &= \frac{\nu}{\alpha}, \\ \text{Bingham number } \text{Bn} &= \frac{\tau_0 L_D}{\mu U_\infty}, \end{aligned} \quad (7)$$

where symbols have been defined in nomenclature. To compute the solution of equations (1)–(3), the system must be subject to some boundary conditions. At the inlet of this domain, fluid enters with parabolic profile in x -direction. At the outlet, the Neumann conditions for all variables have been imposed. On the surface of channel and obstacles there is no-slip boundary condition. Furthermore, fins are insulated and obstacles are heated uniformly while other walls of channel remain cold.

Ultimately, computational results from the preceding governing equations in the form of primitive variables (\mathbf{u} , p , and θ), together with the above boundary conditions of the domain are postprocessed to evaluate the derived quantities like drag coefficient, lift coefficient, and Nu_{avg} , respectively.

The nondimensional net drag (F_d) and lift (F_l) forces act on the submerged cylinder in the flow and normal direction, while the drag and lift coefficient are

$$\begin{aligned} C_D &= \frac{2F_d}{\rho U_\infty^2 L_D}, \\ C_L &= \frac{2F_l}{\rho U_\infty^2 L_D}. \end{aligned} \quad (8)$$

Here the reference velocity is $U_\infty = (2/3)U_{\text{max}}$, where $U_{\text{max}} = 0.3$ is the maximum velocity of given parabolic profile at the inlet. The local Nusselt (Nu_{local}) number on the surface of duct and fins is estimated by $\text{Nu}_{\text{local}} = -(\partial\theta/\partial n_s)$. Such values have been more averaged over both surfaces (cylinder and fins) to obtain the average Nusselt (Nu_{avg}) number given as

$$\text{Nu}_{\text{avg}} = \frac{1}{S} \int_S \text{Nu}_{\text{local}} dS, \quad (9)$$

where “ S ” and “ n_s ” are the surfaces of thermal region and normal direction of the surface; it is reasonable to postulate that the drag coefficient is function of Re whereas the Nu_{avg} depends on the Pr. This work endeavors to exhibit and develop more efficient functional relationship for circular cylinder in future.

3. Numerical Scheme and Grid Convergence

Due to nonlinearity of the governing equations as well as of non-Newtonian fluids, having plastic viscosity applied to channel flow, the energy and momentum equations cannot be supported with analytical solutions, so we implemented numerical scheme finite element method (FEM) for computing the optimized solution with different shapes of cylinder. The underlying discrete nonlinear system of equations has been solved by Newton method and the linearized inner system is solved with a direct solver PARDISO. The PARDISO solver utilizes LU matrix factorization and reduces the number of iterations required for the desired level of convergence. This reduces the number of the iterations required. The Lagrangian system was used for the velocity discretization (second order) of elements and pressures and temperatures (linear) as is shown in Figure 2.

Grid independence study has been performed for the C_D , C_L , and Nu_{avg} for the different cylinders and corresponding results are given in Table 1–Table 3 for all the three shapes of cylinders at $\text{Re} = 20$, $\text{Pr} = 6.2$, $\text{Bn} = 0$, $n = 1$, and $\text{Gr} = 10$. The benchmark results reveal the fact that results at levels 7 and 8 are in close agreement so to save computational cost, and we performed the rest of the simulation at level 7.

Finally, the current code has also been validated against the Schaefer and Turek [42] in Table 4 by setting the temperature on circular cylinder as zero.

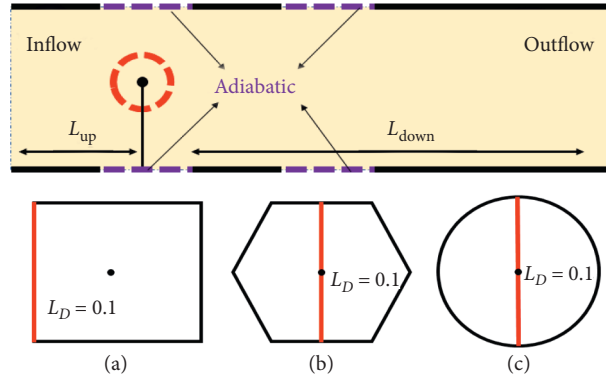


FIGURE 1: Schematic diagram of the problem: (a) square; (b) hexagon; (c) circle.

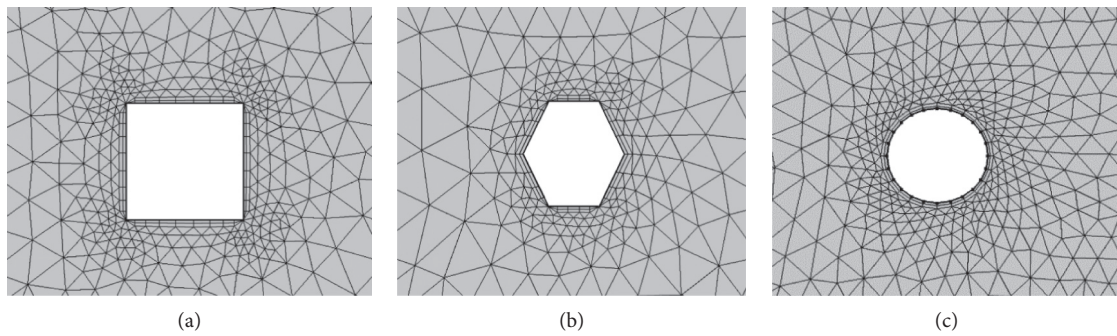


FIGURE 2: Complex computational grids at coarse level: (a) square; (b) hexagon; (c) circle.

TABLE 1: Grid convergence study for square cylinder.

#RL	#EL	DOF	C_D	C_L	Nu_{avg}
1	1,126	8,483	6.8482	0.0356	4.8973
2	1,790	13,396	6.9111	0.0619	4.9782
3	2,846	20,782	6.9246	0.0706	5.0401
4	5,160	36,943	6.9333	0.0720	5.1123
5	7,850	55,357	6.9347	0.0731	5.1496
6	13,648	94,160	6.9359	0.0728	5.1807
7	30,900	212,318	6.9389	0.0726	5.2426
8	72,496	493,199	6.9397	0.0721	5.2791

4. Results and Discussions

This work endeavors in three different cross-sectional cylinders with significant boundary conditions to elucidate the impact of non-Newtonian fluid flow and heat transfer behavior. The results shown in this study cover the range of parameters as: $0.4 \leq n \leq 1.8$, $10 \leq Re \leq 50$, $0 \leq Bn \leq 50$, $0.7 \leq Pr \leq 10$, and $1 \leq Gr \leq 10$, respectively. Here is a comment on the choice of these ranges. The value of the power law index is encountered in many products such as suspension and polymer fluids found in industrial practices. Moreover, Bn are considered adequate for determining their influence on flow and heat transfer characteristics. The lowest value of ($Bn = 0$) is Newtonian and the fluid in the very wide ($Bn \rightarrow \infty$) is plug-like and heat is transmitted only via conduction which is slightly increased by piston-like fluid motion. The selection of the range of parameters for present

work is based on a combination of the actual material characteristics and the anticipated fluid limiting conditions. Extensive results are discussed in the ensuing sections on lengths entrance, velocity profile and temperature, yield surfaces, and Nu_{avg} . It is, however, edifying first to determine the accuracy of the existing numeric assumptions and this objective is accomplished by presenting a number of benchmarks for a number of limiting circumstances and comparing the results available in literature.

4.1. Power Law Model. The velocity distribution illuminated in Figure 3 with varying cylinder shapes at Reynolds $Re = 20$ with Newtonian fluid $n = 1$ is restricted. Since the velocity of the parabola is induced at inlet, and other boundaries are kept in no-slip conditions, velocity variation close to channel obstacles is observed. A conclusion is

TABLE 2: Grid convergence study for hexagonal cylinder.

#RL	#EL	DOF	C_D	C_L	Nu_{avg}
1	1,098	8,279	6.1080	-0.0019	4.6590
2	1,796	13,413	6.1088	0.0004	4.7139
3	2,742	20,061	6.1096	0.0005	4.7385
4	4,984	35,706	6.1116	0.0016	4.7873
5	7,666	54,068	6.1124	0.0017	4.7847
6	13,298	91,768	6.1128	0.0018	4.8005
7	30,388	208,777	6.1135	0.0019	4.8355
8	71,232	484,604	6.1135	0.0019	4.8517

TABLE 3: Grid convergence study for circular cylinder.

#RL	#EL	DOF	C_D	C_L	Nu_{avg}
1	962	7,378	5.5349	-0.0075	4.8564
2	1,590	12,009	5.4785	-0.0087	4.9292
3	2,426	17,918	5.5207	-0.0036	4.9190
4	4,540	32,683	5.5510	-0.0019	4.9243
5	6,716	47,611	5.5538	-0.0018	4.9283
6	11,796	81,603	5.5605	-0.0015	4.9297
7	27,194	197,374	5.5754	-0.0008	4.9286
8	65,288	444,870	5.5786	-0.0008	4.9292

TABLE 4: Validation of code for comparison of drag and lift coefficients.

Coefficients of fluid forces	Schaefer and Turek [42]	Present study
C_D	5.5785	5.5785
C_L	0.0106	0.0106

reached that the parabolic nature of velocity profiles is similar in the entry. Figure 4 is plotted to evaluate pressure variation across the physical domain, particularly in vicinity of circular obstacle and constant $Re = 20$. From the figure, it is seen that pressure exhibits optimized nonlinear (power law, Bingham, and Herschel–Bulkley) fluids behavior close to the obstacle and gets linear downstream in channel flow as expected. Here, the optimum pressure is observed to have maximum value in front of the obstruction that interacts with fluid. It also appears that its pressures become linear when the fluid passes over the obstacle.

Figure 5 shows the effects of the shape of cylinder on C_D and C_L against n from 0.4 to 1.6 covering a wide range of Newtonian, shear-thinning (thixotropic), and shear-thickening (rheopectic) fluids. The reductions in the values of C_D and C_L are observed from square to circle cylinders. Moreover, reduction in power law index results in lowering the apparent fluid's viscosity beside the cylinder, thereby reducing the frictional drag strength. The shape effects for Newtonian fluid ($n = 1$) against Re are illustrated in Figure 6. Furthermore, the power law index influences the total drag coefficient which is decreasing gradually as the Re increases from 10 to 50. In Figure 7, the effect of drag and lift coefficients on obstacle shapes was shown; with increasing Prandtl numbers, C_D and C_L decrease. Both coefficients produce lower values for the case of circular cylinder as compared with the other two shapes.

The changes in the flow field because of the parametric values of n , Re , and Pr significantly impact the Nu_{avg} over the surface of cylinders. Towards this end, we presented in this section the effects on the Nu_{avg} for the different shapes of the cylinder for Pr , n , and Re . Figure 8(a) shows that increasing the Pr gives rise to an increment in the Nu_{avg} . The dependence of Nu_{avg} on n and Re for three different cylinders is shown in Figures 8(b) and 8(c). Nu_{avg} increases as the Re increases because the thermal boundary layer is progressively thinning. In addition, an increase in shear-thinning (decreased value of n) also improves the rate of thermal flow, due to the reduction of the apparent fluid viscosity because of steep gradients close to the submerged cylinders.

4.2. Bingham Model. In this case, the flow field comprises the yielded and unyielded zones, which vary with the choice of Bingham fluid which is nondimensional analog of yield stress. Figure 9 illustrates the areas where fluid moves like a rigid body in unyielding (plug) zones. The viscosity increases as the yield stress in the Bingham fluid gradually increases. In the vicinity of the submerged cylinder there is always a yielded region. Bingham fluid acts in the center of the channel like a solid. Figure 10 shows the isotherms around the cylinders for the Newtonian case at fixed Re . The isothermal profile reflects the physical phenomena observed through the analysis of patterns of streamlines. More thermal contours are crowded near the curved surface than

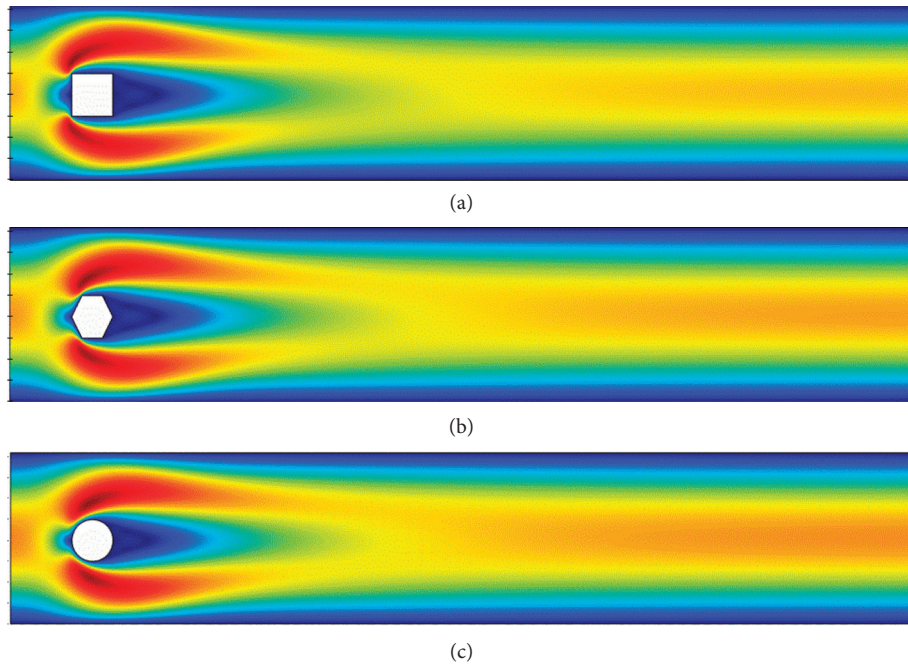


FIGURE 3: Shape effects on velocity profile for $n = 1$, $Pr = 5$, and $Re = 20$. (a) Square shape cylinder; (b) hexagon shape cylinder; (c) circular shape cylinder.

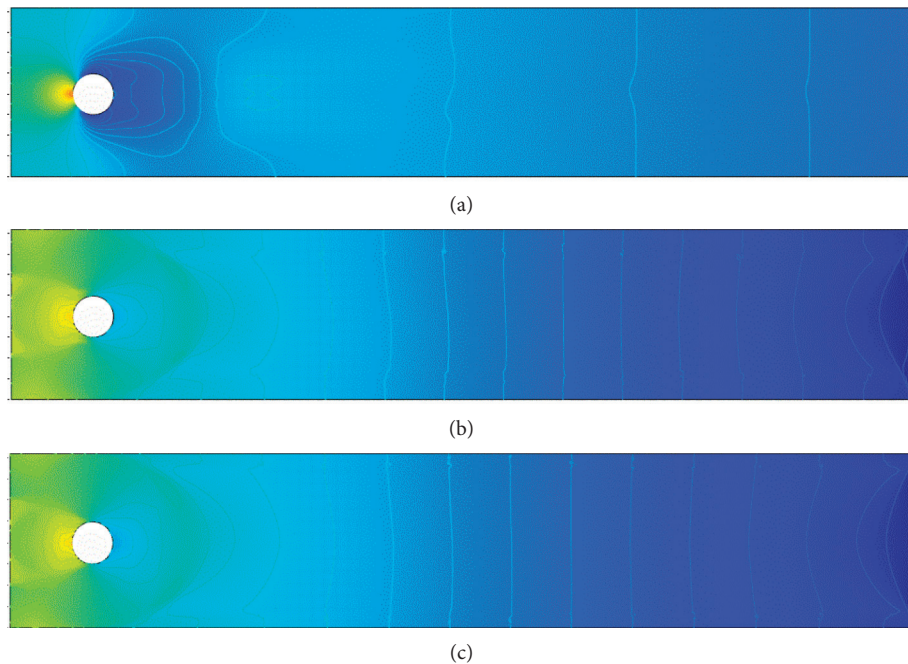


FIGURE 4: Fluid effects on pressure profile for $Re = 20$. (a) Power law fluid ($n = 0.4$). (b) Bingham fluid ($Bn = 20$). (c) Herschel-Bulkley fluid ($Bn = 20, n = 0.4$).

on the flat surface, which leads to a higher Nu_{avg} on the curved surface. The crowds of temperature contours depend on the Bn and Pr

The trend of C_D and C_L based on the shape of cylinders versus Bn can be seen in Figure 11. There is a linear growing profile for drag coefficient for all shapes. However, for a

square cylinder the C_D is higher as compared with the other cases because the fluid forces dominate at the surface of square cylinder. The C_L varies nonlinearly for all cylinders; for the square cylinder, however, the C_L decreases after a certain Bn threshold with an increase in the Bn . However, quantitative analysis of C_D and C_L for different Re is

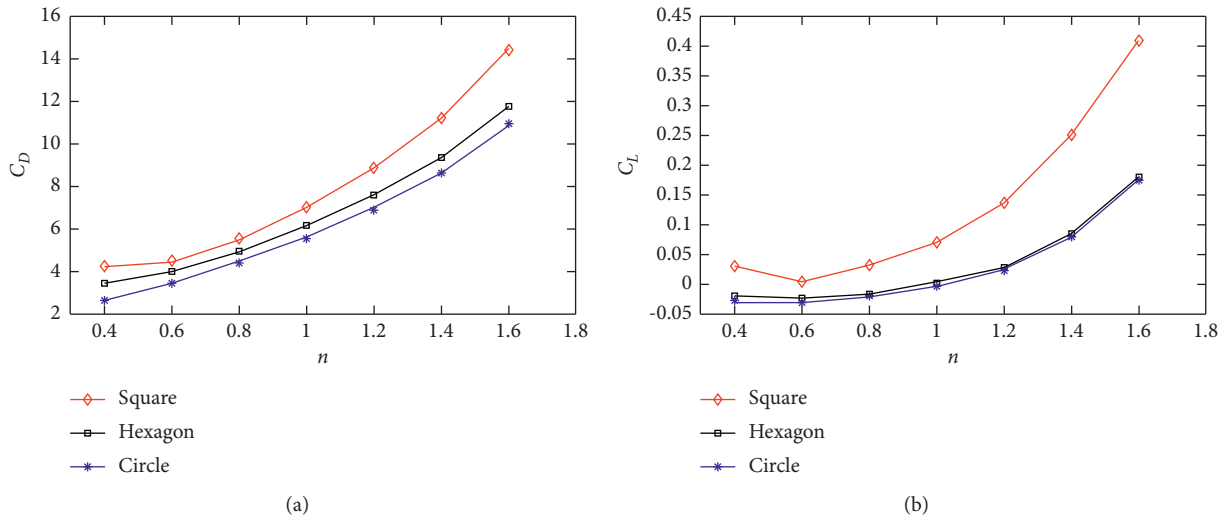


FIGURE 5: (a) Drag coefficient and (b) lift coefficient against n with $Pr = 5$ and $Re = 20$.

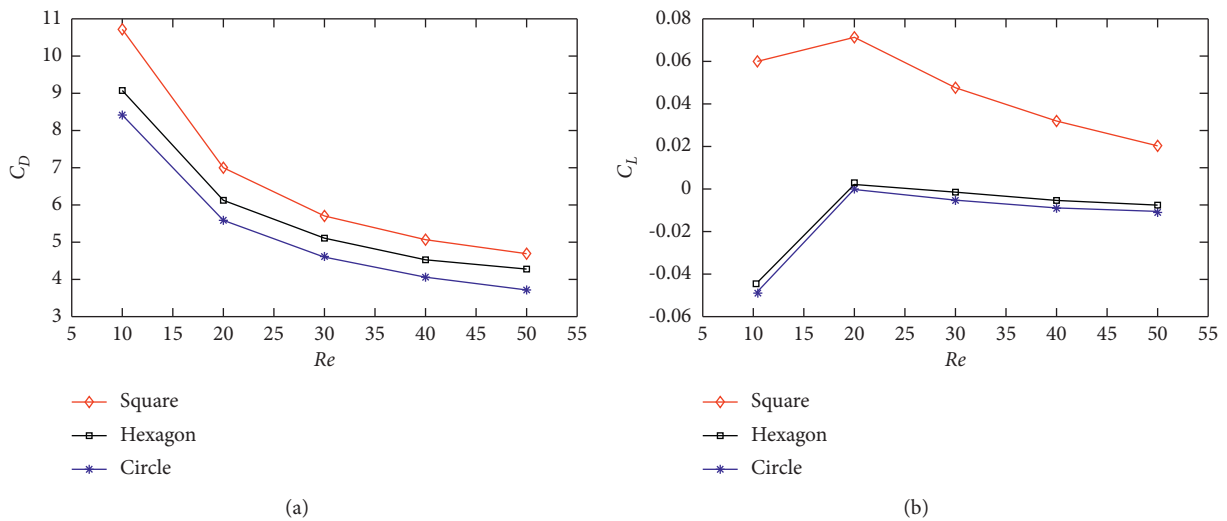


FIGURE 6: (a) Drag coefficient and (b) lift coefficient against Re with $Pr = 5$ and $n = 1$.

presented in Table 5. Table 6 shows that, in the case of three shaped cylinders, maximum reduction is observed for all Bn values. In addition, the maximum reduction can be seen at $Bn = 0$ for all cylinder combinations. In the range $0 \leq Bn \leq 50$, for all configurations that approach their corresponding minimum values, the values of a percent reduction decrease.

Figure 12 reveals the disparity of the Nu_{avg} based on the shapes of cylinder and with the Bn . The Nu_{avg} has been shown to dominate in case of square cylinder.

4.3. Herschel–Bulkley Model. The fluid model Herschel–Bulkley combines the characteristics of Power Law and Bingham models. The fluid flow of Herschel–Bulkley thus shares the features of power law and of Bingham fluid. The effect on the flow components is similar from the power

index and Bingham number. For this reason, only those flow characteristics over the cylinder that were not described above will be discussed in this case. Such as the Bingham fluid, a fluid region is formed around the cylinder when there is a flow over the cylinder, while the medium is a rigid substance on the periphery. The fluid region is mainly based on the number of Bingham: the larger the amount of Bingham, the lesser the region of fluid.

The size depends simultaneously on the power index: the lower the n , the smaller the fluid region. It can thus be concluded that a perturbation of the cylinders is reduced if the rheology of the fluids is non-Newtonian, if the number of the Bingham and/or the power index is lower. In strongly non-Newtonian fluids, dependence on the drag and kinematic features of the flow is less significant than in Newtonian fluids. The responsiveness of the flow properties to relative velocity changes is weakened as the non-Newtonian fluid properties

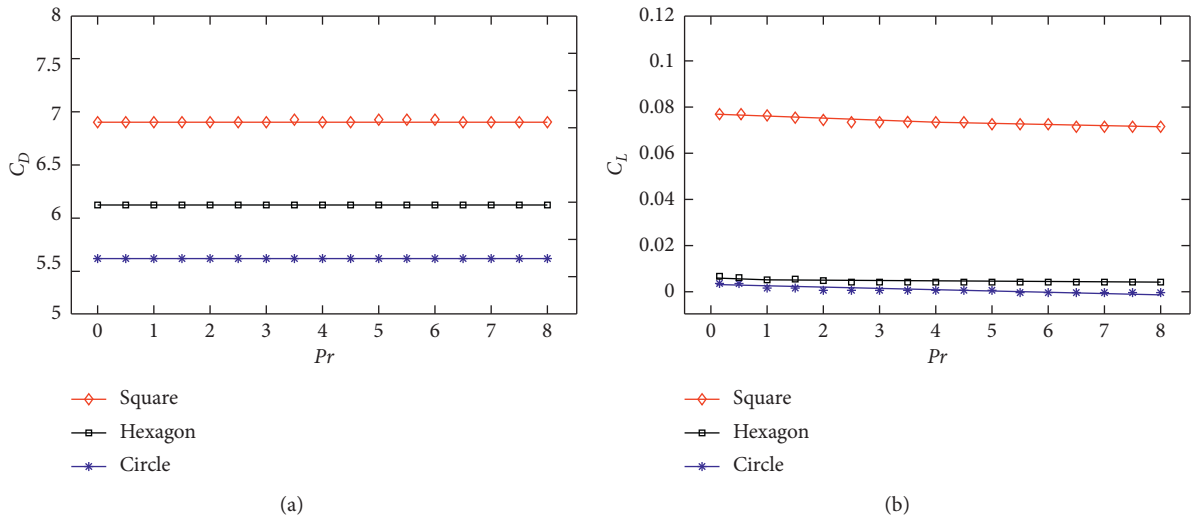
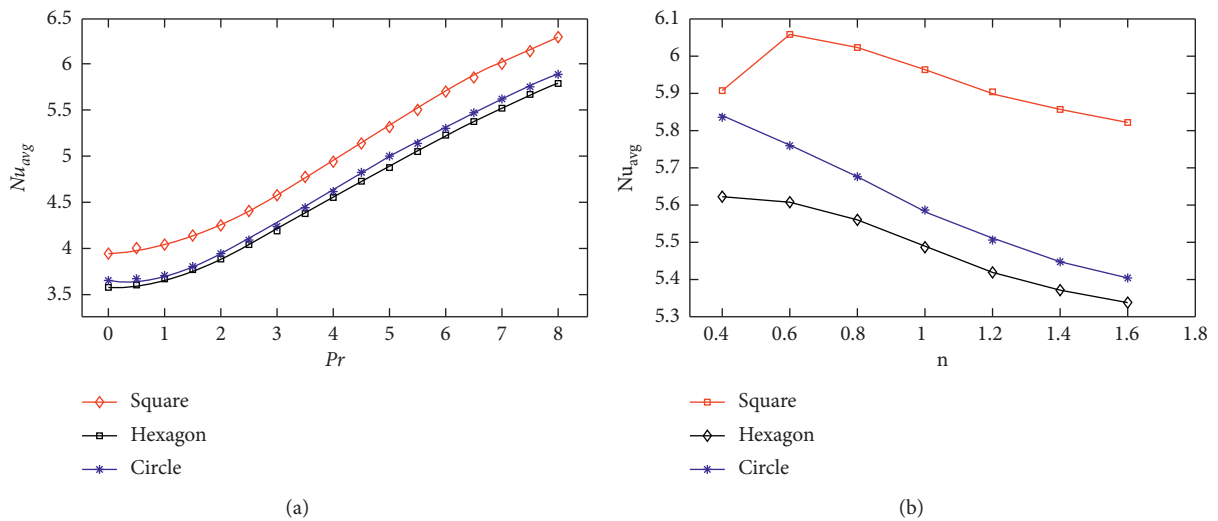
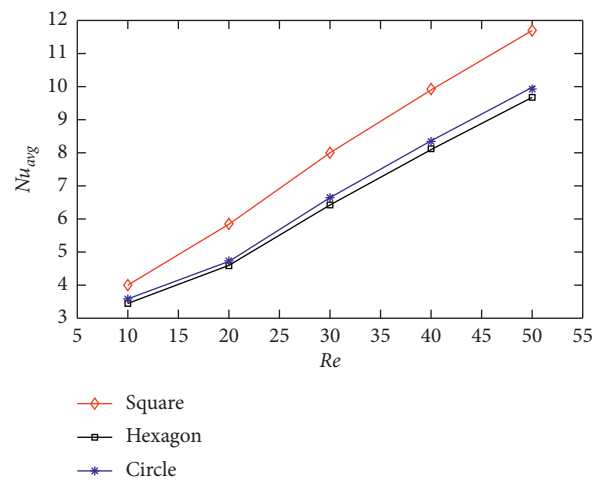


FIGURE 7: (a) Drag coefficient and (b) lift coefficient against Pr with $n = 1$ and $Re = 20$.



(a) (b)



(c)

FIGURE 8: (a): Average Nusselt number (Nu_{avg}) against Pr with $n = 1$ and $Re = 20$. (b) Average Nusselt number (Nu_{avg}) against n with $Pr = 5$ and $Re = 20$. (c) Average Nusselt number (Nu_{avg}) against Re with $n = 1$ and $Pr = 5$.

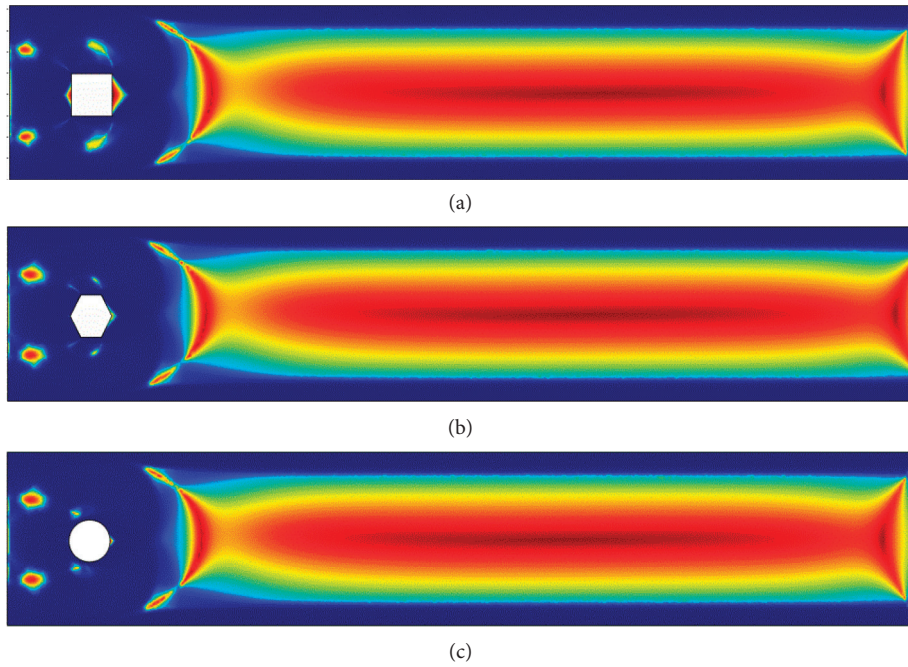


FIGURE 9: Shape effects on viscosity field for $Bn = 20$ and $Re = 20$. (a) Square shape cylinder; (b) hexagon shape cylinder; (c) circular shape cylinder.

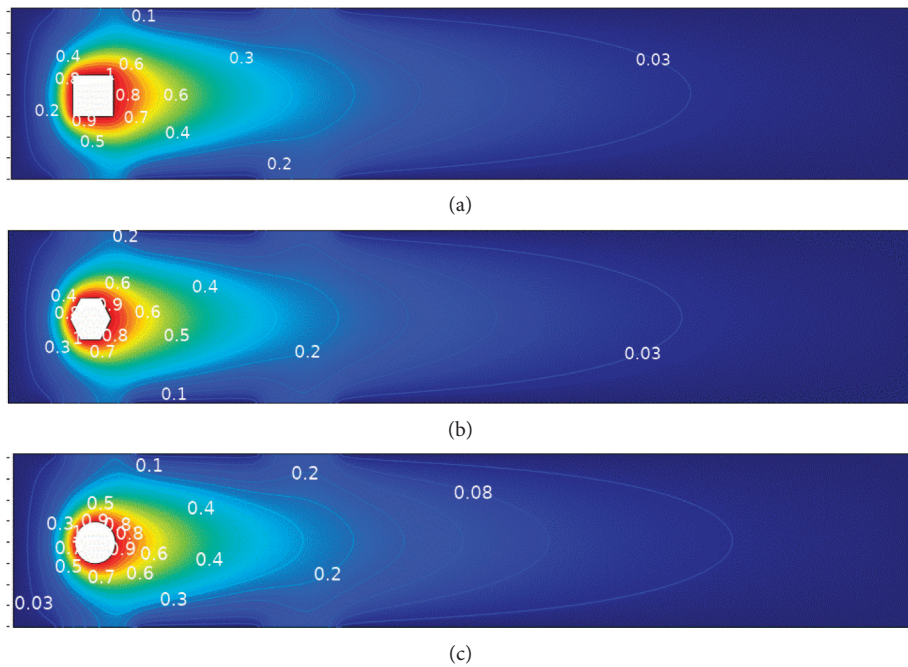


FIGURE 10: Shape effects on isotherm contour for $Bn = 20$ and $Re = 20$. (a) Square shape cylinder; (b) hexagon shape cylinder; (c) circular shape cylinder.

increase. Figure 13 reveals the characteristics of drag and lift coefficient against Bingham number for different fluid properties over the different cylinders. The drag trend for Bn is the same across the fluid, but the drag values for the rheopectic fluid are higher as the boundaries are nonsmooth

compared to the thixotropic fluid. The lift values demonstrate an increasing trend for Bn from 0 to 10 and reveal a decreasing trend for a further increase in the Bingham number for each fluid case. Figure 14 reveals the effects of cylinder shapes on average Nusselt number against Bn for complex

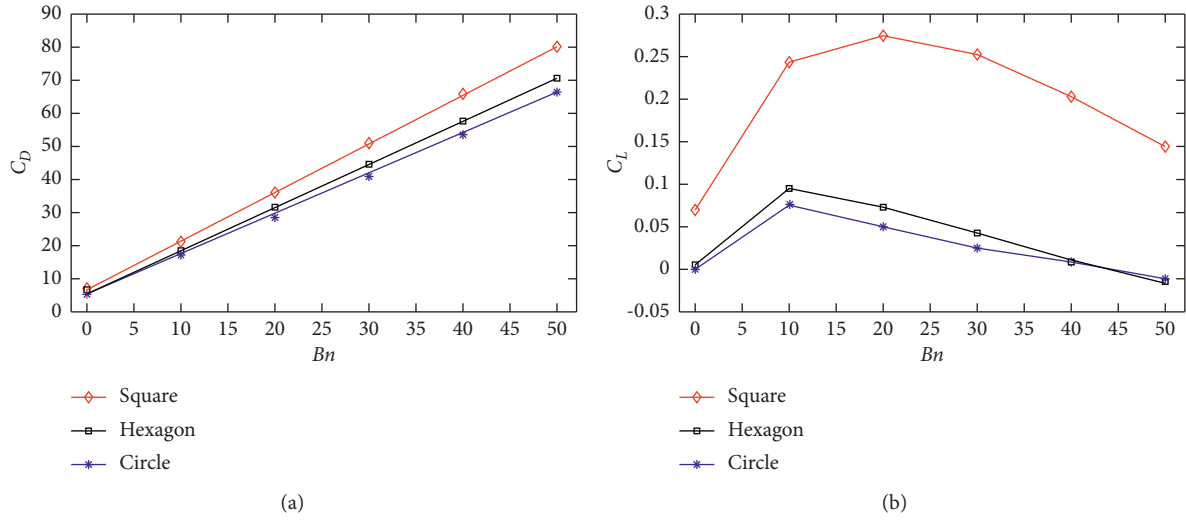


FIGURE 11: (a) Drag coefficient C_D and (b) lift coefficient C_L against Bn with $Pr = 5$ and $Re = 20$.

TABLE 5: Impact on drag and lift coefficients against Bn for different Re values.

Bn	$Re = 10$		$Re = 30$		$Re = 50$	
	C_D	C_L	C_D	C_L	C_D	C_L
0	8.428736	-0.04927	4.571563	-0.00557	3.694473	-0.01109
10	58.36013	0.120413	9.431011	0.044435	5.201851	0.015601
20	107.898	0.001741	14.68912	0.044090	6.969524	0.025137
30	156.8559	-0.13567	20.02938	0.030733	8.793285	0.028560
40	205.5070	-0.29718	25.40788	0.015660	10.65577	0.026068
50	253.8652	-0.44502	30.81171	0.003527	12.53580	0.020911

TABLE 6: Percentage reduction in drag coefficient: square versus hexagonal and circular case.

Bn	Square	Hexagon	% reduction	Circle	% reduction
0	6.9397	6.1135	14.94	5.5786	19.61
5	13.9553	12.0237	14.41	11.2657	19.55
10	21.4478	18.4166	14.13	17.2796	19.43
15	28.9459	24.8896	14.01	23.3732	19.25
20	36.4354	31.4094	13.79	29.5111	19.00
25	43.8990	37.9431	13.57	35.6571	18.77
30	51.3235	44.4747	13.34	41.8024	18.55
35	58.7175	51.0029	13.14	47.9443	18.35
40	66.0861	57.5283	12.95	54.0775	18.17
45	73.4365	64.0466	12.79	60.1993	18.03
50	80.7721	70.5589	12.64	66.3107	17.90

fluids. Figure 15 shows the variation of the Nu_{avg} with Bn on both shape cylinders and theGr. The Nu_{avg} increases with Gr as usual.

A line graph is shown in Figure 16 to depict the impact of rheology of fluid on velocity profiles. The velocity profile changes as the yield stress increases, from a parabola to a flat

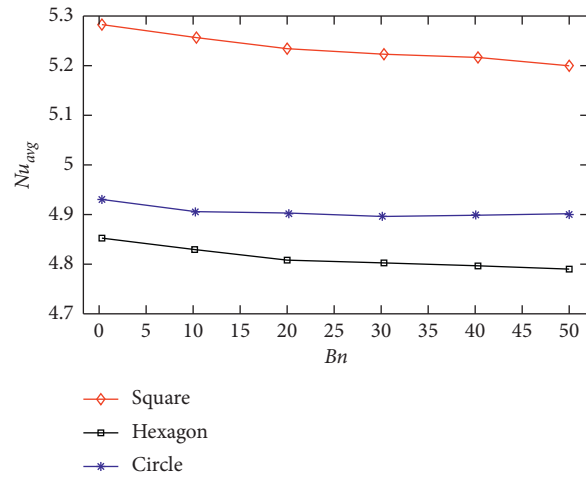


FIGURE 12: Average Nusselt number (Nu_{avg}) against Bn with $Re = 20$ and $Pr = 5$.

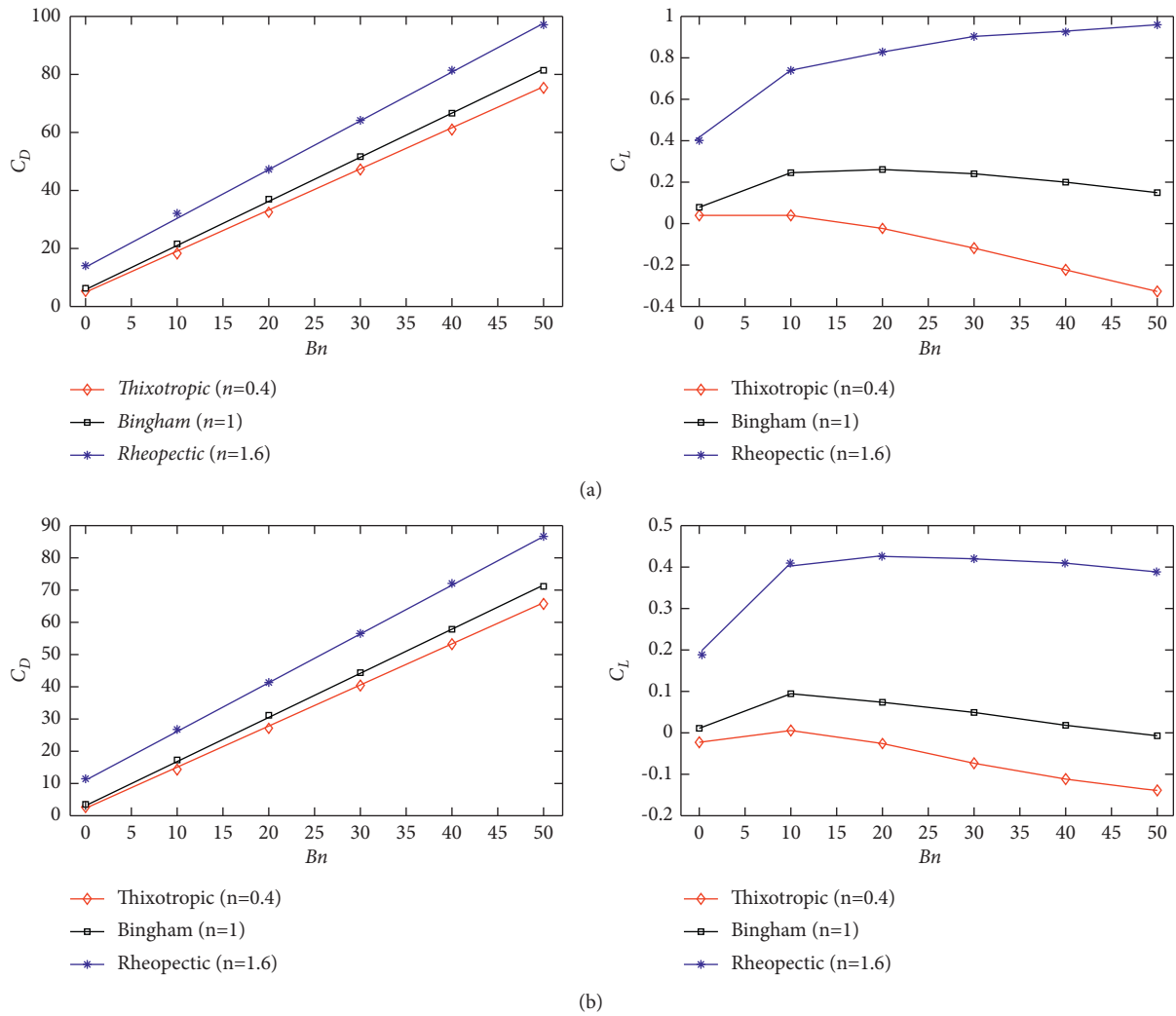
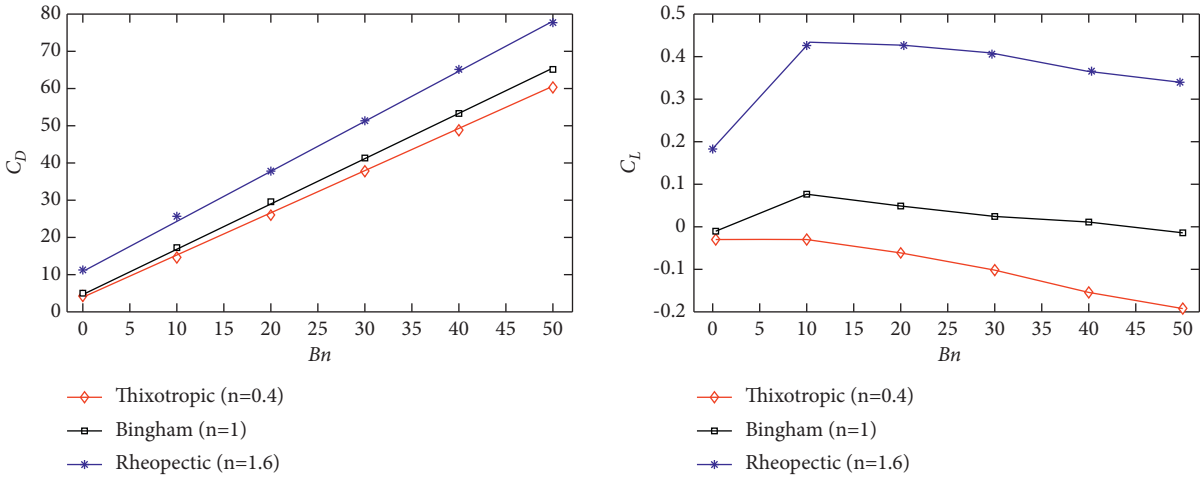
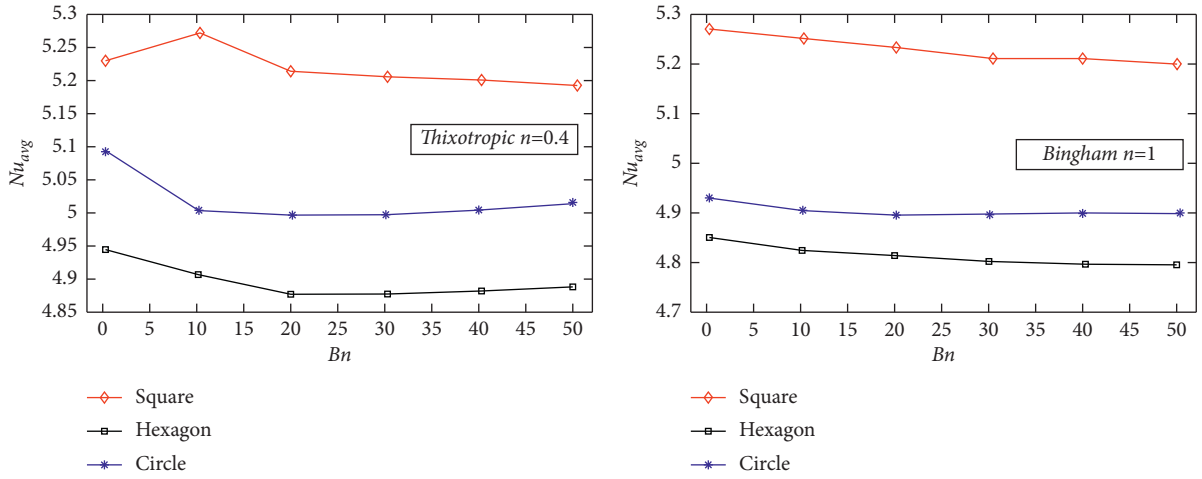


FIGURE 13: Continued.



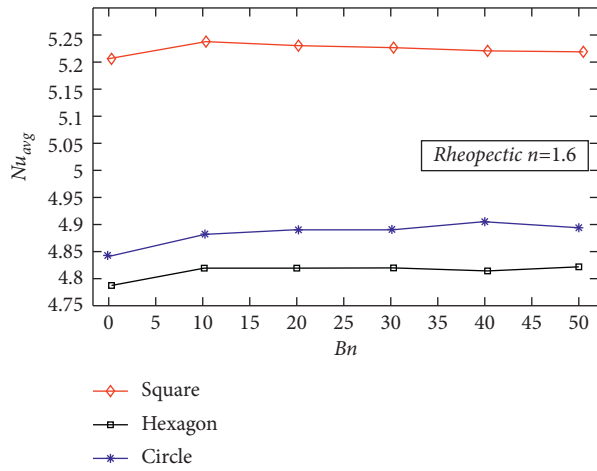
(c)

FIGURE 13: Drag and lift coefficients against Bn with Pr = 5 and Re = 20. (a) Square cylinder; (b) hexagonal cylinder; (c) circle cylinder.



(a)

(b)



(c)

FIGURE 14: Average Nusselt number (Nu_{avg}) for different fluids against Bn with Pr = 5 and Re = 20. (a) Thixotropic ($n = 0.4$); (b) Bingham ($n = 1$); (c) rheopectic ($n = 1.6$).

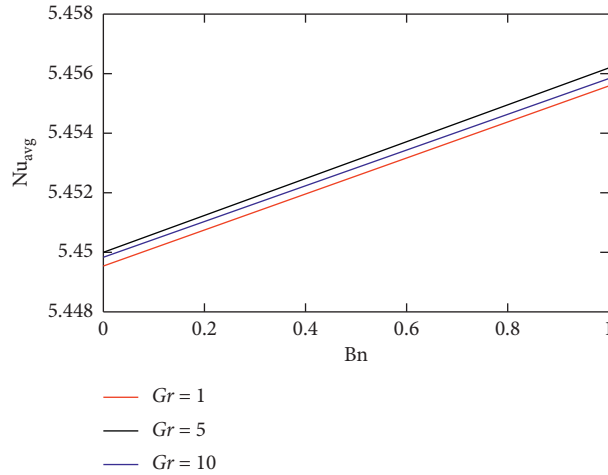


FIGURE 15: Impact of average Nusselt number (Nu_{avg}) against Bn for different Gr values.

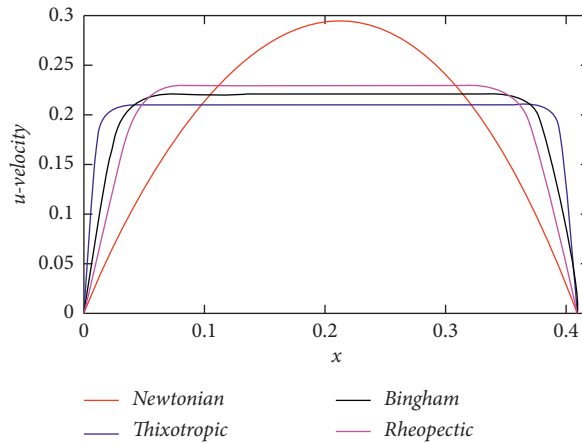


FIGURE 16: Velocity profile for various fluid models at $x = 2$ with $Re = 20$.

plateau in the channel central region, which represents the unyielded material.

5. Conclusions

In this manuscript, extensive computations have been carried out to elucidate the thermal flow features based on the topology of the obstacles. The results revealed herein enhance over the following varying ranges of nondimensional parameters: n from 0.4 to 1.6, Bn from 0 to 50, Re from 10 to 50, Pr from 0.7 to 10, and Gr from 1 to 10, respectively. In nonlinear fluid, C_D decreases from square to circle by order to optimize cylinder. The results for the development and completion of the velocity profile and thermal flow and Nu_{avg} for three typical shapes of partially insulated cylinders are detailed. The main findings include the following:

- (i) Drag and lift coefficients increase against n and Pr while they decrease along Re over all the topologies of cylinders

- (ii) For the Newtonian case, reduction in C_D is maximum while reduction is decreasing for increasing the Bn
- (iii) The rate of thermal flow tends to increase as the Re values increase due to a decline in the n
- (iv) The Nu_{avg} increases with increasing both Bn and Gr
- (v) The velocity profile shifts from a parabolic to a smooth plateau in the center along the channel when the yield stress increases indicating a plug zone in the center of the channel

Nomenclature

- u : Dimensionless velocity
- θ : Dimensionless temperature
- p : Dimensionless pressure
- m : Dimensional stress growth parameter
- n : Flow behavior index
- ρ : Density

g : Gravitational acceleration
 L_D : Reference length

Greek

τ_y : Yield stress
 μ_p : Plastic viscosity
 τ : Stress tensor
 $\dot{\gamma}$: Shear rate
 U_∞ : Reference velocity
 Re : Reynolds number
 Bn : Bingham number
 Pr : Prandtl number
 Gr : Grashof number
 F_D : Drag force
 C_D : Drag coefficient
 F_L : Lift force
 C_L : Lift coefficient
 Nu_{avg} : Average Nusselt number
 Nu_{local} : Local Nusselt number
 ∇ : Gradient operator
 α : Thermal diffusivity
 ν : Kinematic viscosity

Abbreviations

#EL: Number of elements
 #DOF: Number of degrees of freedom.

Data Availability

The data underlying the results presented in the study are available within the article.

Conflicts of Interest

The authors state that there are no conflicts of interest.

Acknowledgments

This work was supported by HEC-Pakistan through NRPU Project No. 14038.

References

- [1] C. Ditchfield, C. C. Tadini, R. K. Singh, and R. T. Toledo, "Velocity and temperature profiles, heat transfer coefficients and residence time distribution of a temperature dependent Herschel-Bulkley fluid in a tubular heat exchanger," *Journal of Food Engineering*, vol. 76, no. 4, pp. 632–638, 2006.
- [2] R. Shyam, C. Sasmal, and R. P. Chhabra, "Natural convection heat transfer from two vertically aligned circular cylinders in power-law fluids," *International Journal of Heat and Mass Transfer*, vol. 64, no. 17, pp. 1127–1152, 2013.
- [3] H. Laidoudi and M. Bouzit, "Mixed convection heat transfer from confined tandem circular cylinders in cross-flow at low Reynolds number," *Mechanika*, vol. 23, no. 4, pp. 522–527, 2017.
- [4] H. Laidoudi and M. Bouzit, "Suppression of flow separation of power-law fluids flow around a confined circular cylinder by superimposed thermal buoyancy," *Mechanika*, vol. 23, no. 2, pp. 220–227, 2017.
- [5] G. R. Kefayati and H. Tang, "Double-diffusive natural convection and entropy generation of Carreau fluid in a heated enclosure with an inner circular cold cylinder (Part I: heat and mass transfer)," *International Journal of Heat and Mass Transfer*, vol. 120, pp. 731–750, 2018.
- [6] H. Laidoudi and M. Bouzit, "Mixed convection in Poiseuille fluid from an asymmetrically confined heated circular cylinder," *Thermal Science*, vol. 22, no. 2, pp. 821–834, 2018.
- [7] H. Masoumi, M. S. Aghighi, A. Ammar, and A. Nourbakhsh, "Laminar natural convection of yield stress fluids in annular spaces between concentric cylinders," *International Journal of Heat and Mass Transfer*, vol. 138, pp. 1188–1198, 2019.
- [8] F. Zafar and M. M. Alam, "Mixed convection heat transfer from a circular cylinder submerged in wake," *International Journal of Mechanical Sciences*, vol. 183, no. 1, pp. 83–88, 2020.
- [9] H. Laidoudi, M. Helmaoui, M. Bouzit, and A. Ghenaim, "Natural convection of newtonian fluids between two concentric cylinders of a special cross-sectional form," *Thermal Science*, vol. 45, p. 190, 2020.
- [10] R. P. Bharti, R. P. Chhabra, and V. Eswaran, "Steady flow of power law fluids across a circular cylinder," *Canadian Journal of Chemical Engineering*, vol. 84, no. 4, pp. 406–421, 2006.
- [11] R. P. Bharti, R. P. Chhabra, and V. Eswaran, "Two-dimensional steady Poiseuille flow of power-law fluids across a circular cylinder in a plane confined channel: wall effects and drag coefficients," *Industrial & Engineering Chemistry Research*, vol. 46, no. 11, pp. 3820–3840, 2007.
- [12] R. Shyam, M. Sairamu, N. Nirmalkar, and R. P. Chhabra, "Free convection from a heated circular cylinder in confined power-law fluids," *International Journal of Thermal Sciences*, vol. 74pp. 156–173, C, 2013.
- [13] A. K. Baranwal and R. P. Chhabra, "Free convection in confined power-law fluids from two side-by-side cylinders in a square enclosure," *Heat Transfer Engineering*, vol. 37, no. 18, pp. 1521–1537, 2016.
- [14] A. Pantokratoras, "Steady flow of power-law fluids across a circular rotating cylinder," *Progress in Computational Fluid Dynamics, An International Journal*, vol. 17, no. 4, pp. 239–249, 2017.
- [15] K. M. Gangawane and B. Manikandan, "Laminar natural convection characteristics in an enclosure with heated hexagonal block for non-Newtonian power law fluids," *Chinese Journal of Chemical Engineering*, vol. 25, no. 5, pp. 555–571, 2017.
- [16] M. Asnaashari and A. Tohidi, "Conjugate heat transfer from a circular cylinder to a power-law non-Newtonian fluid," *Heat Transfer - Asian Research*, vol. 48, no. 4, pp. 1466–1482, 2019.
- [17] A. Dhiman and R. Shyam, "Unsteady heat transfer from an equilateral triangular cylinder in the unconfined flow regime," *ISRN Mechanical Engineering*, vol. 2011, Article ID 932738, 13 pages, 2011.
- [18] N. Nirmalkar and R. P. Chhabra, "Momentum and heat transfer from a heated circular cylinder in Bingham plastic fluids," *International Journal of Heat and Mass Transfer*, vol. 70, pp. 564–577, 2014.
- [19] S. A. Patel and R. P. Chhabra, "Heat transfer in Bingham plastic fluids from a heated elliptical cylinder," *International Journal of Heat and Mass Transfer*, vol. 73, pp. 671–692, 2014.
- [20] R. Mahmood, N. Kousar, M. Yaqub, and K. Jabeen, "Numerical simulations of the square lid driven cavity flow of bingham fluids using nonconforming finite elements coupled

- with a direct solver,” *Advances in Theoretical and Mathematical Physics*, vol. 2017, Article ID 5210708, 9 pages, 2017.
- [21] X. Liu, H. Cheng, J. Lin, C. Rong, M. Li, and H. Xu, “Study of the mechanism of fracture grouting in deeply buried rock strata based on bingham fluid slurry,” *Advances in Civil Engineering*, vol. 2019, Article ID 6943239, 10 pages, 2019.
- [22] P. Thakur, N. Tiwari, and R. P. Chhabra, “Forced convection in a Bingham plastic fluid from a heated rotating cylinder,” *Journal of Chemical Engineering of Japan*, vol. 52, no. 9, pp. 730–742, 2019.
- [23] B. Ren, L. Wang, H. Fan, K. Ding, K. Wang, and C. Jiang, “Unsteady approximate model of grouting in fractured channels based on bingham fluid,” *Geofluids Journal*, vol. 16, 2021.
- [24] C. Nouar, M. Lebouché, R. Devienne, and C. Riou, “Numerical analysis of the thermal convection for Herschel-Bulkley fluids,” *International Journal of Heat and Fluid Flow*, vol. 16, no. 3, pp. 223–232, 1995.
- [25] J.-G. Yoo and K.-W. Kim, “Numerical analysis of grease thermal elasto-hydrodynamic lubrication problems using the Herschel-Bulkley model,” *Tribology International*, vol. 30, no. 6, pp. 401–408, 1997.
- [26] C. Nouar, C. Desaubry, and H. Zenaidi, “Numerical and experimental investigation of thermal convection for a thermodependent Herschel-Bulkley fluid in an annular duct with rotating inner cylinder,” *European Journal of Mechanics-B: Fluids*, vol. 17, no. 6, pp. 875–900, 1998.
- [27] C. Nouar, “Thermal convection for a thermo-dependent yield stress fluid in an axisymmetric horizontal duct,” *International Journal of Heat and Mass Transfer*, vol. 48, no. 25–26, pp. 5520–5535, 2005.
- [28] N. Labsi, Y. Benkahla, M. B. Feddaoui, and A. Boutra, “Viscous dissipation effect on the flow of a thermodependent herschel-bulkley fluid,” *Thermal Science*, vol. 19, no. 5, pp. 1553–1564, 2015.
- [29] M. A. Hassan, M. Pathak, and M. K. Khan, “Rayleigh-benard convection in herschel-bulkley fluid,” *Journal of Non-newtonian Fluid Mechanics*, vol. 226, pp. 32–45, 2015.
- [30] A. A. Gavrilov, K. A. Finnikov, and E. V. Podryabinkin, “Modeling of steady herschel-bulkley fluid flow over a sphere,” *Journal of Engineering and Thermophysics*, vol. 26, no. 2, pp. 197–215, 2017.
- [31] L. Hermany, G. Lorenzini, R. J. Klein et al., “Constructal design applied to elliptic tubes in convective heat transfer cross-flow of viscoplastic fluids,” *International Journal of Heat and Mass Transfer*, vol. 116, pp. 1054–1063, 2018.
- [32] T. Hoshino, “Analysis of the flow properties of a Herschel-Bulkley fluid using short back extrusion viscometry and considering time-dependent and stress growth behaviors,” *Rheologica Acta*, vol. 54, pp. 809–819, 2020.
- [33] P. S. B. Zdanski and M. Vaz, “A numerical method for simulation of incompressible three-dimensional Newtonian and non-Newtonian flows,” *Numerical Heat Transfer, Part B: Fundamentals*, vol. 59, no. 5, pp. 360–380, 2011.
- [34] W. Sarwar Abbasi, S. Ul Islam, L. Faiz, and H. Rahman, “Numerical investigation of transitions in flow states and variation in aerodynamic forces for flow around square cylinders arranged inline,” *Chinese Journal of Aeronautics*, vol. 31, no. 11, pp. 2111–2123, 2018.
- [35] R. Mahmood, S. Bilal, A. H. Majeed, I. Khan, and E.-S. M. Sherif, “A comparative analysis of flow features of Newtonian and power law material: a New configuration,” *Journal of Materials Research and Technology*, vol. 12, 2019.
- [36] W. S. Abbasi, S. U. Islam, and H. Rahman, “Proximity effects on characteristics of flow around three inline square cylinders,” *Mathematical Problems in Engineering*, vol. 2019, Article ID 1752803, 14 pages, 2019.
- [37] I. Khan, “Finite element least square technique for Newtonian fluid flow through a semicircular cylinder of recirculating region via COMSOL multiphysics,” *Jurnal Matematika*, vol. 2020, Article ID 8869308, 11 pages, 2020.
- [38] J. C. Tomio, M. M. Martins, M. Vaz, and P. S. B. Zdanski, “A numerical methodology for simulation of non-Newtonian viscoelastic flows,” *Numerical Heat Transfer Part B Fundam.* vol. 78, no. 6, pp. 1–15, 2020.
- [39] R. Mahmood, S. Bilal, A. H. Majeed, I. Khan, and K. S. Nisar, “CFD analysis for characterization of non-linear power law material in a channel driven cavity with a square cylinder by measuring variation in drag and lift forces,” *Journal of Materials Research and Technology*, vol. 67, 2020.
- [40] S. Bilal, R. Mahmood, A. H. Majeed, I. Khan, and K. S. Nisar, “Finite element method visualization about heat transfer analysis of Newtonian material in triangular cavity with square cylinder,” *Journal of Materials Research and Technology*, vol. 9, no. 3, pp. 4904–4918, 2020.
- [41] A. Mehmood, R. Mahmood, A. H. Majeed, and F. J. Awan, “Flow of the bingham-papanastasiou regularized material in channel in the presence of obstacles: correlation between hydrodynamic forces and spacing of obstacles,” *Modelling and Simulation in Engineering*, vol. 2021, Article ID 5583110, 14 pages, 2021.
- [42] M. Schaefer and S. Turek, “Benchmark computations of laminar flow around a cylinder,” *Notes on Numerical Fluid Mechanics*, vol. 52, pp. 547–566, 1996.

Research Article

Numerical Investigation of Fluid Flow past Four Cylinders at Low Reynolds Numbers

Shafee Ahmad and Shams Ul-Islam 

Mathematics Department, COMSATS University Islamabad, Islamabad Campus, Islamabad 44000, Pakistan

Correspondence should be addressed to Shams Ul-Islam; islam_shams@comsats.edu.pk

Received 16 April 2021; Revised 24 June 2021; Accepted 10 July 2021; Published 27 July 2021

Academic Editor: Ahmed Zeeshan

Copyright © 2021 Shafee Ahmad and Shams Ul-Islam. This is an open access article distributed under the Creative Commons Attribution License, which permits unrestricted use, distribution, and reproduction in any medium, provided the original work is properly cited.

A numerical investigation on the effects of separation ratios and Reynolds numbers on the flow around four square cylinders in diamond arrangement has been carried out using the lattice Boltzmann method. The separation ratios between the cylinders vary from $g^* = 1$ to 15. The Reynolds numbers based on the diameter of the square cylinder and the inlet uniform inflow velocity are selected from $Re = 80$ to 160. The computations show that a total of five different flow regimes are observed over the selected ranges: single bluff-body, quasi-unsteady, chaotic flow, in-phase synchronized vortex shedding, and antiphase synchronized vortex shedding flow regimes. It is found that the flow features significantly depend on both the separation ratio and Reynolds number, with the former's influence being more than the latter's. We found that the critical spacing for four square cylinders in diamond arrangement for selected Reynolds numbers ($80 \leq Re \leq 160$) is in the range of $2 \leq g^* \leq 5$. The results reveal that the presence of secondary cylinder interaction frequencies indicates that, for chaotic flow regime, the wake pattern is not stable and there is a strong interaction of gap flows and continuous change in the direction of shed vortices behind the cylinders. The effects of the g^* and Re on fluid forces, vortex shedding frequency, and flow separation have been examined in detail.

1. Introduction

Fluid-structure interactions occur in a number of engineering fields. Study on wake structure and fluid forces on multiple bluff bodies is of practical importance in a number of engineering applications, such as chimneys, offshore structures, towers, bridges, marine risers, and ocean platforms. It is also of importance in the analysis of fluid/structure interactions since the mechanism associated with the complex physical phenomena such as vortex shedding, flow separation, merging of vortices, and interaction of gap flows with the shed vortices is still not fully understood.

A typical irregular variation of wake structures is when multiple bluff bodies is subject to a cross flow. When the separation ratio (g^*) is too small between the cylinders, the vortices strongly interact, thus substantially increasing the drag forces. Separation ratio g^* is defined as $g^* = S/D$, where S and D are the surface-to-surface distance between the cylinders and diameter of the cylinder, respectively. Investigations into the effects of the g^* and Reynolds

number (Re) on multiple bluff bodies have also been carried out. The Reynolds number is defined based on the diameter of the cylinder as $Re = u_{\max} D/\nu$, where u_{\max} is the maximum velocity at the inlet and ν is the fluid kinematic viscosity. Kolar et al. [1] carried out an experimental investigation using the two-component laser Doppler velocimetry and discussed in detail the synchronized flow around two side-by-side square cylinders. The Reynolds number and separation ratio were focused on 23,100 and 2, respectively. Williamson [2] experimentally examined the flow features around two side-by-side circular cylinders at $0.5 < g^* \leq 5$ at low Reynolds numbers varying from 50 to 200. According to Guillaume and LaRue [3], flow around two side-by-side cylinders experiences different drag values and vortex shedding frequencies. Kang [4] have carried out a detailed numerical examination of flow around two side-by-side circular cylinders. The author found different flow regimes while changing the Reynolds numbers from 40 to 160 with $g^* < 5$. Agrawal et al. [5] conducted numerical investigation into the effects of g^* on the flow past two side-by-side square

cylinders at $Re = 73$ using the lattice Boltzmann method (LBM). A basic study of flow around two side-by-side square cylinders was carried out by Inoue et al. (2006). They studied the effects of the separation ratios and observed various flow regimes at $Re = 150$. Alam and Zhou [6] conducted an experimental study to examine the flow features around two side-by-side square cylinders, and they observed different flow regimes at $Re = 300$ and $1 \leq g^* \leq 5$. There has been much numerical work on the flow past multiple cylinders arranged side-by-side, such as the work by Ding et al. [7], Burattini and Agrawal [8], Han et al. [9], and Islam et al. [10]. It is known from these studies that the flow regimes strongly depend on the g^* value between the cylinders.

The separation ratio between the inline cylinders has great impact on the flow regimes and force statistics (Zdravkovich [11]). The experimental investigations carried out by Yen et al. [12] were for the Re and g^* for flow around two tandem square cylinders. They observed different flow regimes by changing the values of the Re and g^* . Etminan et al. [13] did a finite volume study on flow past tandem square cylinders using finite volume method at low Reynolds numbers at $g^* = 5$. The authors found that the flow changes its state from steady to unsteady at $Re = 40$. A number of numerical studies on flow past two tandem square cylinders have also been carried out with the motivation to examine the transition of flow regimes from one state to another by changing the spacing between the cylinders (see Sohankar [14] and Zhao et al. [15]).

Experimental studies have been carried out for flow around four circular cylinders in an inline square configuration by Sayers [16]. Lam and Lo [17] experimentally examined various types of flow regimes and their corresponding Strouhal number (St) for four circular cylinders in an inline square configuration at $Re = 2100$ and g^* ranging from 1.28 to 5.96. The authors observed different flow regimes by changing the value of g^* . Strouhal number St is defined as $St = f_s D / u_{\max}$, where f_s is the vortex shedding frequency. Farrant et al. [18] numerically examined vortex shedding from arrays of cylinders in various arrangements for different orientations and spacings at $Re = 200$ using the cell boundary element method. They found well-known flow features such as in-phase vortex shedding, antiphase vortex shedding, and vortex shedding flow regimes, which are well-known flow characteristics and observed mostly in case of two-cylinder arrangement. Song et al. [19] studied numerically various flow regimes and force statistics for flow around four square cylinders in an inline square configuration using the finite volume method (FVM). They systematically investigated the effect of spacing between the cylinders for $Re = 300$. The authors found that $g^* = 3.5$ is the critical spacing and the flow regime changes from a bistable shielded flow regime to a vortex shedding flow regime by changing the values of g^* from 1.5 to 8. Lam et al. [20] numerically studied flow interference effects of four cylinders at $Re = 100$ and 200 with $1.5 \leq g^* \leq 5$ and observed different flow regimes. Lin et al. [21] numerically studied the different flow regimes at $Re = 200$ for flow around four circular cylinders by changing the value of g^* . They found that the flow becomes critical at $g^* = 3$. Abbasi et al. [22]

numerically examined the effects of Re and g^* on flow around four square cylinders in an inline square configuration. Experimental studies have been carried out for flow around four square cylinders in a square configuration (Liu et al. [23]). The authors experimentally measured the lift (C_L) and drag (C_D) forces at $Re = 4.58 \times 10^4$ and $g^* = 3.45, 4.14, \text{ and } 5.17$ for four different angles of attacks. The authors found that the four cylinders forces are slightly different by changing the value of g^* . Lift coefficient is defined as $C_L = 2F_y / \rho u_{\max}^2 D$, where F_y is the lift force in the transverse direction. Similarly, the drag coefficient is defined as $C_D = 2F_x / \rho u_{\max}^2 D$, where F_x is the drag force in the streamwise direction. Zhang et al. [24] experimentally investigated the flow features and forces for array of four square cylinders at different g^* and orientations at $Re = 8000$ using the Particle Image Velocimetry (PIV). They observed three different flow regimes while changing the values of pitch ratio from 2 to 5 and incidence angles from 0° to 45° . Gao et al. [25] performed numerical simulations of vortex-induced vibrations of four circular cylinders in a square configuration at a low Reynolds number of 150 and mass ratio of 2 using the commercial software package Ansys Fluent 16.0. They examined in detail the effect of incident angle α varying from 0° to 45° and reduced velocity V_r varying from 3 to 14. The authors found that the incident angle has a considerable effect on the vibration amplitudes and force coefficients of the four circular cylinders, especially for the cylinders arranged at the downstream positions, where the maximum force coefficients and vibration amplitudes occur. The fluid flow plays an important role in engineering applications [26]. The nature of the flow around multiple bluff bodies is highly dependent on the separation ratio between the cylinders and practically very important [27–30].

Knowledge of the effect of g^* on the flow characteristics around the square cylinders in diamond arrangement is scarce. It is not clear how g^* and Re affect the fluid dynamics as compared to isolated cylinder, tandemly arranged cylinders, and side-by-side arranged cylinders. Numerical and experimental studies for flow past four square cylinders in diamond arrangement are far from complete as compared to circular cylinders. More specifically, an example is how a change in g^* from 1 to 15 will affect forces, flow transitions, and Strouhal numbers of the four cylinders, for a given Re . The main motivation of present numerical examination is to explore systematically further insight about the flow mechanism past four square cylinders in diamond arrangement, to get in-depth knowledge of important parameters, such as C_D, C_L, St , transition of flow regimes, and power spectra of C_L by changing the values of Re and g^* . Furthermore, two important aspects will be presented in more detail: (i) merging of jet flows and shear layer reattachment at low spacings and (ii) variation in the wake size. Five Reynolds numbers and eleven separation ratios are investigated. Due to two-dimensional limitations, we chose Re up to 160 [31].

The paper is organized as follows. In Section 2, the details of lattice Boltzmann method, problem description, effect of computational domain, grid independence, and code

validation study are presented. The computed results are presented and analyzed in Section 3. Finally, the most important conclusions are drawn in Section 4.

2. Numerical Method and Computational Details

Flow past four square cylinders in diamond shape is governed by the unsteady two-dimensional (2D) incompressible Navier–Stokes equations. The Cartesian coordinate system for the proposed problem is as follows:

$$\frac{\partial u_i}{\partial t} + u_j \frac{\partial u_i}{\partial x_j} = -\frac{1}{\rho} \left(\frac{\partial p}{\partial x_i} \right) + \nu \frac{\partial^2 u_i}{\partial x_j \partial x_j}, \quad (1)$$

$$\frac{\partial u_i}{\partial x_i} = 0. \quad (2)$$

Here, p is the pressure, ρ is the fluid density, ν is the kinematic viscosity of fluid, and u_i (or u_j) is the velocity component in the x_i (or x_j) coordinate direction.

Instead of trying to discretize (1) and (2), a discretization of the Boltzmann equation is good enough to deal with the fluid flow problems. Computational fluid dynamics (CFD) has become very popular and plays an important role in analysis of fluid flow studies. The LBM has developed quickly in many aspects in the last twenty years and nowadays has become a powerful and attractive CFD tool for fluid flows. The LBM has some advantages compared to other CFD techniques. First, in the LBM the pressure is calculated from the equation of state [32]. This means once the density field is known, one can directly obtain the pressure fields. Second, no-slip boundary condition can be handled easily by bounce-back scheme [33]. Third, the fundamental Boltzmann equation is directly discretized [34]. Today, researchers use LBM in a number of disciplines [35–39]. In the above-mentioned references, one can easily find the streaming; collision; equilibrium distribution; discretization in time, space, and velocity; derivation of weighting coefficients; and recovery of the governing continuity and Navier–Stokes equations.

The LBM can be derived from the Bhatnagar, Gross, and Krook (BGK) (1954) approximation of the Boltzmann equation [40] without body force:

$$\partial_t f + \zeta \Delta f = \Omega. \quad (3)$$

Here, $f(x, \zeta, t)$ is the particle distribution function in the phase space (x, ζ) . x and ζ are the position vector and the microscopic velocity, respectively. Ω is the collision operator. The simplest collision operator that can be used for Navier–Stokes simulations is the Bhatnagar–Gross–Krook (BGK) operator defined as follows:

$$\Omega = \frac{[f^{(\text{eq})} - f]}{\tau}. \quad (4)$$

Here, $f^{(\text{eq})}(x, \zeta)$ is the Maxwell–Boltzmann distribution function. τ is the single-relaxation time parameter which controls the stability. It is important to state here that the

viscosity must be positive for the chosen LBM model which requires the choice of $\tau > 0.5$. Now putting (4) into (3), we get

$$\partial_t f + \zeta \cdot \Delta f = \frac{[f^{(\text{eq})} - f]}{\tau}. \quad (5)$$

In the LBM-BGK method, for fluid flow, the discretized distribution function f_i is used. The discretized lattice Boltzmann equation [40] is

$$f_i(\mathbf{x} + \mathbf{e}_i \delta t, t + \delta t) = f_i(\mathbf{x}, t) + \delta t \frac{[f_i^{(\text{eq})}(\mathbf{x}, t) - f_i(\mathbf{x}, t)]}{\tau}. \quad (6)$$

Here, $f_i(\mathbf{x}, t)$ is the density distribution function and is linked to the discrete velocity direction i (see Figure 1). \mathbf{e}_i , t , and δt are the discrete velocities, time, and time increment, respectively. The relaxation parameter τ is related to the fluid kinematic viscosity by $\nu = c_s^2 (\tau - 0.5) \delta t$, where c_s is the speed of sound. To determine the macroscopic equations for the LBM, one may need to perform a Taylor expansion of (6). Equation (6) can be divided into two main steps. The first part is collision (or relaxation):

$$f_i^*(\mathbf{x}, t) = f_i(\mathbf{x}, t) + \delta t \frac{[f_i^{(\text{eq})}(\mathbf{x}, t) - f_i(\mathbf{x}, t)]}{\tau}. \quad (7)$$

Here, f_i^* represents the distribution function after collisions. It is to be noted that collision is simply an algebraic local operation. The second part is propagation (or streaming):

$$f_i(\mathbf{x} + \mathbf{e}_i \delta t, t + \delta t) = f_i^*(\mathbf{x}, t). \quad (8)$$

The $f_i^{(\text{eq})}(\mathbf{x}, t)$ in (6) can be calculated as [41]

$$f_i^{(\text{eq})}(\mathbf{x}, t) = w_i \rho \left[1 + \frac{(\mathbf{e}_i \cdot \mathbf{u})}{c_s^2} + \frac{(\mathbf{e}_i \cdot \mathbf{u})^2}{2c_s^4} - \frac{(\mathbf{u})^2}{2c_s^2} \right]. \quad (9)$$

Here, \mathbf{u} is the macroscopic velocity vector and w_i s are the weighting coefficients. It is important to mention here that in lattice Boltzmann equation we can deal with the low Mach number ($Ma = \delta t u_{\text{max}} / \delta x c_s) < 0.3$ for near incompressible flows; therefore, the terms higher than \mathbf{u}^2 are ignored in the equilibria. $d_2 q_9$ discrete velocity model is selected for this study (Figure 1). d and q represent the dimensions and number of particles, respectively. $c^2 s$ is defined as $c^2/3$ for $d_2 q_9$ model. Here, c is the lattice speed and is defined as $c = \delta x / \delta t$. In this study, we choose lattice spacing (δx) as 1 lattice unit and time step (δt) as 1 ts. The magnitudes of weighting coefficients w_i are defined as

$$w_i = \begin{cases} \frac{4}{9} & i = 0, \\ \frac{1}{9} & i = 1, 2, 3, 4, \\ \frac{1}{36} & i = 5, 6, 7, 8. \end{cases} \quad (10)$$

The discrete velocities for the $d_2 q_9$ model are given by [33]

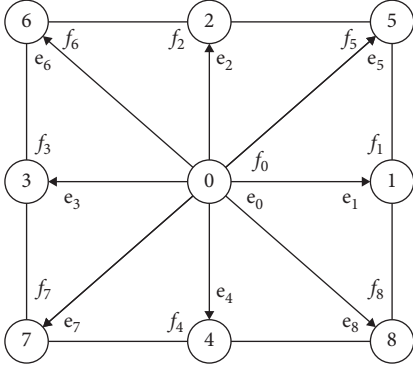


FIGURE 1: Lattice arrangement for the two-dimensional proposed problem.

$$\begin{cases} \mathbf{e}_i = 0, & i = 0, \\ \mathbf{e}_i = \left(\cos\left(\frac{\pi}{2}(i-1)\right), \sin\left(\frac{\pi}{2}(i-1)\right) \right), & i = 1, 2, 3, 4, \\ \mathbf{e}_i = \sqrt{2} \times \left(\cos\left(\frac{\pi}{2}\left(i-\frac{9}{2}\right)\right), \sin\left(\frac{\pi}{2}\left(i-\frac{9}{2}\right)\right) \right), & i = 5, 6, 7, 8. \end{cases} \quad (11)$$

The ρ and \mathbf{u} can be obtained from

$$\rho = \sum_{i=0}^8 f_i = \sum_{i=0}^8 f_i^{(eq)}, \quad \mathbf{u} = \frac{1}{\rho} \sum_{i=0}^8 f_i \cdot \mathbf{e}_i = \frac{1}{\rho} \sum_{i=0}^8 f_i^{(eq)} \cdot \mathbf{e}_i \quad (12)$$

One can use the equation of state to calculate the pressure as given in the following:

$$p = \rho c_s^2. \quad (13)$$

From the Chapman–Enskog expansion [35, 39], one can easily recover the governing Navier–Stokes equations (1) and continuity (2) from the lattice Boltzmann method.

In 2D case, the vorticity is calculated as

$$\omega_z = \frac{\partial v}{\partial x} - \frac{\partial u}{\partial y}. \quad (14)$$

Figure 2 shows a schematic view of four identical square cylinders in diamond arrangement, and the system is exposed in a coming uniform inflow velocity u_{\max} , where S is the spacing between the cylinders and D the diameter of the cylinder. The coming maximum velocity is assumed to be $2D$. C_1 , C_2 , C_3 , and C_4 represent the first, second, third, and fourth cylinders, respectively. The upstream distance (L_u) of the domain (the distance between the inlet boundary and the front surface of the first cylinder) and the downstream distance (L_d) of the computational domain (the distance between the rear surface of the second cylinder and the exit boundary) are assigned constant values of $10D$ and $35D$, respectively. L_x and L_y are the streamwise and transverse directions, respectively. A Cartesian coordinate system (x, y) is used to describe the flow where x and y are incoming flow direction and perpendicular to the stream direction, respectively. C_D and C_L are the drag and lift forces in the streamwise and transverse directions, respectively. The

variations of grid points for different separation values are presented in Table 1.

No-slip boundary conditions [33] are applied on the surfaces of the cylinders. Periodic boundary conditions [36] are applied at the top and bottom walls of the computational domain. Convective boundary condition [42] is incorporated at the exit of the domain. The forces on the surfaces of the cylinders are incorporated using the momentum exchange method [43]. The in-house computational code is developed for the Lahey Fortran Windows platform with 64 bits. All the computations are carried out in Intel i7-2600, dual core 3.2 GHz, 8 GB memory, and 320 GB hard disk for 64-bit Windows operating system. A typical calculation (10,00000-time steps) takes about 20 hours of CPU time. In Tables 2–4, the flow quantities mean drag coefficient ($C_{D\text{mean}}$), St , root-mean-square values of drag coefficient ($C_{D\text{rms}}$), and lift coefficient ($C_{L\text{rms}}$) are presented. In Table 3, $\beta = L_y/D$ is the blockage ratio of the computational domain. In Tables 2–5, the number within brackets gives the percentage deviation relative to the $D = 20$, $\beta = 13$, $L_u = 10D$, and $L_d = 35D$, respectively. In Tables 2–4, the parentage deviation in brackets is calculated from the following equation:

$$\% \text{ error} = \text{absolute} \left(\frac{\text{highest value} - \text{lowest value}}{\text{highest value}} \right) * 100. \quad (15)$$

Before starting simulations for proposed problem, the grid independence study is carried out first to select such grid size which does not affect the flow features and force statistics considerably. For this purpose, we choose 10-point grid, 20-point grid, and 30-point grid along the surface of the single square cylinder, at $Re = 160$. The flow parameters like $C_{D\text{mean}}$, St , $C_{D\text{rms}}$, and $C_{L\text{rms}}$ obtained from these simulations are given in Table 2. It can be seen that the 10-point grid considerably affected the results in terms of percentage difference as compared to the 20-point grid. Furthermore, the 30-point grid takes more computational time as compared to the 20-point grid, and the difference in terms of percentage is almost negligible. Therefore, we have chosen $D = 20$ on each surface of the cylinder. Similar grid size was chosen by [44].

We also studied the effect of computational domain for flow past isolated cylinder at $Re = 160$. The computational domain significantly affects the flow parameters and fastens or slows the vortex shedding process [45]. Table 3 indicates that $\beta = 13$ is a good choice for height of computational domain. There is some difference in terms of percentage observed between $\beta = 13$ and 19 for $L_u = 10D$ and $L_d = 35D$. Table 4 shows that by fixing $\beta = 13$ and $L_d = 35D$, respectively, it can be seen that after $L_u = 10D$ the influence of upstream location almost vanishes. Interestingly, at $L_u = 15D$ the physical parameters show slight increasing behavior. Furthermore, by fixing $\beta = 13$ and $L_u = 10D$, respectively, there is negligible difference between the computed results at $L_d = 35D$ and $50D$. Even the difference with $L_d = 20D$ is also negligible. We will use $L_d = 35D$ as downstream distance from the rear surface of the C_2 to the exit of the computational domain (see Table 5), so that there is reasonably large enough space for flow past multiple cylinders.

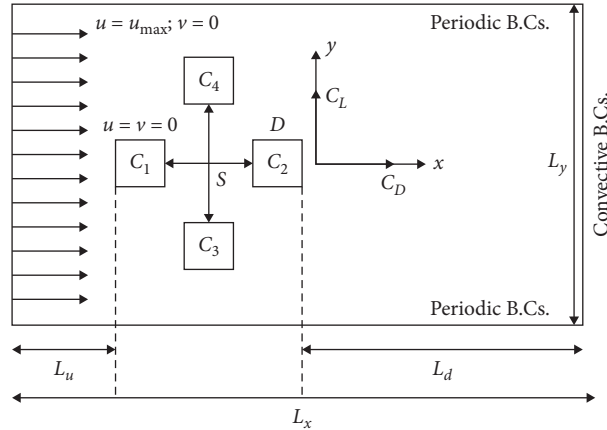


FIGURE 2: Schematic diagram of the proposed problem.

TABLE 1: Selected separation ratios for diamond-shaped arranged cylinders.

Cases	$L_x \times L_y$
$g^* = 1$	301 × 961
$g^* = 2$	321 × 981
$g^* = 3$	341 × 1001
$g^* = 4$	361 × 1021
$g^* = 5$	381 × 1041
$g^* = 6$	401 × 1061
$g^* = 7$	421 × 1081
$g^* = 8$	441 × 1101
$g^* = 9$	461 × 1121
$g^* = 10$	481 × 1141
$g^* = 15$	581 × 1241

TABLE 2: Effect of cylinder size on flow past single square cylinder.

	C_{Dmean}	St	C_{Drms}	C_{Lrms}
$D = 10$	1.5833 (3.9%)	0.2068 (21%)	0.0256 (20%)	0.3593 (16%)
$D = 20$	1.5221	0.1644	0.0206	0.3029
$D = 30$	1.5108 (0.7%)	0.1644 (0%)	0.0198 (3.9%)	0.3012 (0.6%)

TABLE 3: Effect of β on flow past single square cylinder for $L_u = 10D$ and $L_d = 35D$.

β	C_{Dmean}	St	C_{Drms}	C_{Lrms}
7	1.8208 (16.4%)	0.1901 (13.5%)	0.0237 (13%)	0.3595 (15.7%)
13	1.5221	0.1644	0.0206	0.3029
19	1.4627 (4%)	0.1601 (2.6%)	0.0202 (1.9%)	0.2978 (1.7%)

TABLE 4: Influence of L_u on flow past isolated cylinder for $\beta = 13$ and $L_d = 35D$.

Cases	C_{Dmean}	St	C_{Drms}	C_{Lrms}
$L_u = 5D$	1.5334 (0.7%)	0.1671 (1.6%)	0.0202 (1.9%)	0.2911 (3.9%)
$L_u = 10D$	1.5221	0.1644	0.0206	0.3029
$L_u = 15D$	1.5381 (1%)	0.1644 (0%)	0.0211 (2.3%)	0.3102 (2.2%)

Calculations were first carried out for a single square cylinder in a cross flow with $Re = 80, 100, 120, 140,$ and 160 to obtain a baseline for comparison. The results for C_{Dmean} and St are compared with available experimental and

numerical results in Figures 3(a)–3(d). The present C_{Dmean} results are very close to the numerical results of Malekzadeh and Sohankar [31]. The present C_{Drms} results are almost identical to the numerical results of Sen et al. [46].

TABLE 5: Influence of L_d on flow past isolated cylinder for $\beta = 13$ and $L_u = 10D$.

Cases	$C_{D\text{mean}}$	St	$C_{D\text{rms}}$	$C_{L\text{rms}}$
$L_d = 20D$	1.5229 (0.1%)	0.1644 (0%)	0.0204 (1%)	0.3037 (0.3%)
$L_d = 35D$	1.5221	0.1644	0.0206	0.3029
$L_d = 50D$	1.5216 (0.03%)	0.1644 (0%)	0.0207 (0.5%)	0.3030 (0.03%)

The $C_{D\text{mean}}$, St , $C_{D\text{rms}}$, and $C_{L\text{rms}}$ all show a good agreement with the reported data. Figure 4(a) shows the alternate generation of negative and positive shed vortices, i.e., the well-known Karman vortex street. The streamline visualization in Figure 4(b) further confirms the regular generation of shed vortices behind the cylinder. Figures 4(c) and 4(d) show the C_D and C_L force histories. It can be observed that the C_D settles to a periodic behavior with a mean value around 1.5221. The C_L also settles to a regular sinusoidal function after the onset of wake instability leads to vortex shedding. The power spectra analysis of C_L is presented in Figure 4(e). The Strouhal number is obtained using the fast Fourier transform (FFT). The frequency of the C_L is found to be 0.1644.

3. Results and Discussion

The calculations are carried out for flow around four cylinders arranged in diamond shape. The separation ratio changes from 1 to 15 while the Re varies from 80 to 160. 1, 2, 3, and 4 in subscript of flow quantities represent the first, second, third, and fourth cylinders, respectively. For comparison, we also add the single-cylinder (SC) data in Figures 5(a)–5(d) and 8(a)–8(d). We assign the names to flow regimes on the basis of wake interactions, shear layer reattachment, gap flows, variation of forces, and spectra behavior of lift coefficients. The vorticity contour and streamline visualization for flow around cylinders at different combinations of Re and g^* are plotted in Figures 9(a)–9(f) and 10(a)–10(f), respectively. These graphs help us understand the wake structure mechanism near downstream of the cylinders and its effect on the downstream region. At $g^* = 1$ and $Re = 100$, there is no flow through the gaps. In this case, alternate vortex shedding is composed of negative and positive vortex forms behind the last cylinder (Figure 9(a)). Similar flow features were also observed for other chosen Reynolds numbers at $g^* = 1$. Similar to that of a flow around an isolated cylinder, a single vortex street is observed behind the cylinders. This flow behavior is named as single bluff-body flow regime (SBBFR). The corresponding time variations of C_D and C_L for SBBFR are presented in Figures 11(a) and 11(b). This graph clearly indicates that there is no modulation in the signals. The drag coefficient for the C_1 is relatively smaller than those for the other three cylinders. The power spectra further confirm the regular alternate generation of shed vortices behind the cylinder (see Figures 12(a)–12(d)). The power spectra also confirm that the primary vortex shedding dominates the flow and the small one extra harmonic in C_2 does not affect the flow behind the cylinders. The same shedding values are observed for the side-

by-side cylinders ($St_3 = St_4 = 0.0820$). Kang [4] numerically suggests that the single bluff-body flow regime occurs for flow around two side-by-side cylinders at $g^* \leq 0.4$. At $g^* = 2$ and $Re = 80$, there is a shear layer reattachment from C_1 onto C_2 . The flow through gaps is also not affected too much by the near downstream vortices. The flow pattern behind cylinders is almost steady and shows some unsteadiness near exit of the computational domain (Figure 9(b)). That is why this flow regime is named as quasi-unsteady flow regime (QUFR). At $(Re, g^*) = (140, 2)$, the combination of shear layer and strong jet effect through the gaps considerably changes the flow characteristics behind the cylinders (Figure 9(c)). The irregular variation of vortex shedding is because the gap flows are considerably stronger. At $g^* = 2$, the shed vortices behind the cylinders do not travel in alternate fashion as they move downstream and merge, and distortion can be seen in the flow field. The flow features of each cylinder are significantly influenced by upstream cylinder due to small spacing between the cylinders. The vortex shedding that occurs from two side-by-side cylinders (C_3 and C_4) does not have strong influence on the forces and wake structures. One can see noticeable modulations in C_D and C_L for cylinders C_1 and C_2 as compared to the other two cylinders (Figures 11(e) and 11(f)). This type of flow regime is named as chaotic flow regime (CFR). Lin et al. [21] had similar numerical observation for flow around four circular cylinders in an inline square configuration at $Re = 200$ and $g^* = 3$. From Figure 9(d), we observe that the fully developed shed vortices from C_1 reattach to C_2 while at the downstream of C_2 these shed vortices are not regular as they move downstream. Due to two gap flows, the shed vortices behind the cylinders C_3 and C_4 show some irregularity as they shed, and move downstream and interact with the shed vortices of C_2 . Again, the flow shows chaotic nature at far downstream of the domain. The flow regime is named as CFR again. At $g^* = 5$ (Figure 11(g)), we observe that the shed vortices within the spacing have a strong interaction with the cylinder C_2 . Moreover, at the downstream position of C_2 , the shed vortices travel in strong fashion. As a result, one can see higher drag value for C_1 compared to C_2 . In antiphase synchronized vortex shedding flow regime (ASVSFR), at $Re = 100$ and $g^* = 15$, the vortices can be clearly seen within the gap between C_1 and C_2 as well as in the downstream region of C_2 (Figure 9(e)), because the flow finds enough space between C_1 and C_2 to roll up in the form of shed vortices. Near exit of the domain, they are interacting with each other. The modulation in the C_D and C_L of C_1 and C_2 is due to the shed vortices within the gap of cylinders. Figure 9(e) confirms that, in case of $g^* = 15$, the four single-cylinder wakes are completely synchronized. The well-known von Karman vortex street is clearly found behind each cylinder at this large separation ratio between the cylinders. The minor modulation in the C_{D2} and C_{L2} occurs due to minor difference between the vortex shedding frequencies of C_2 . According to the spectrum analyses, the primary vortex shedding frequency dominates the flow. At this separation ratio, the shedding frequencies of the cylinders C_3 and C_4 are close to the isolated cylinder case for all Reynolds numbers. Figure 9(f) confirms that, in case of $g^* = 9$ and $Re = 120$,

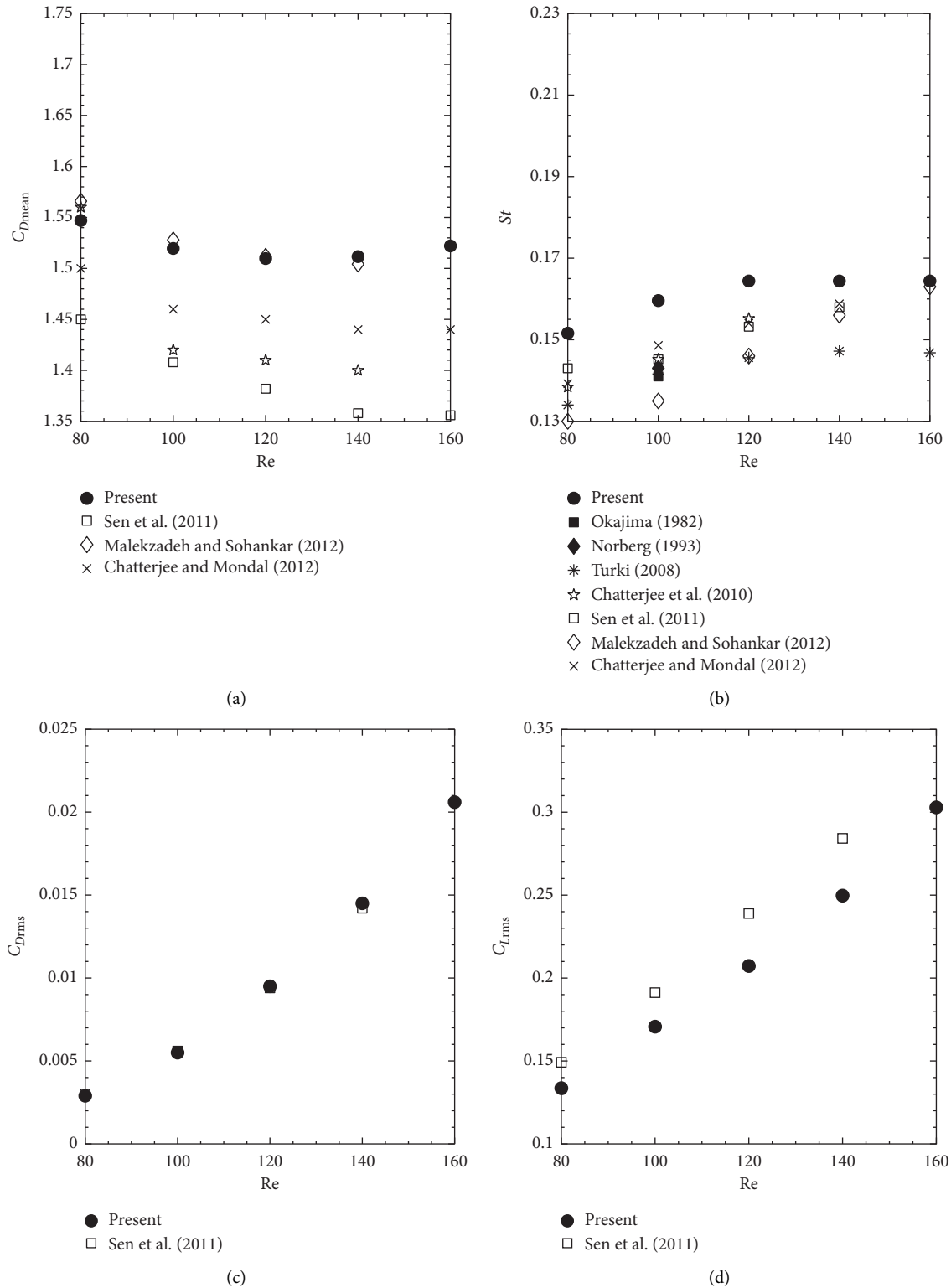


FIGURE 3: Variation of (a) C_{Dmean} , (b) St , (c) C_{Drms} , and (d) C_{Lrms} as a function of Re.

the four single-cylinder wakes are completely synchronized. In addition, the shedding behind cylinders C_3 and C_4 is in-phase. According to the spectrum analyses, the primary vortex shedding frequency dominates the flow. At this separation ratio, the shedding frequencies of the

cylinders C_3 and C_4 are close to the isolated cylinder case for all Reynolds numbers. That is why this flow regime is named as in-phase synchronized vortex shedding flow regime (ISVSFR). Furthermore, in ASVSFR and ISVSFR, the cylinders C_3 and C_4 confirm the antiphase and in-

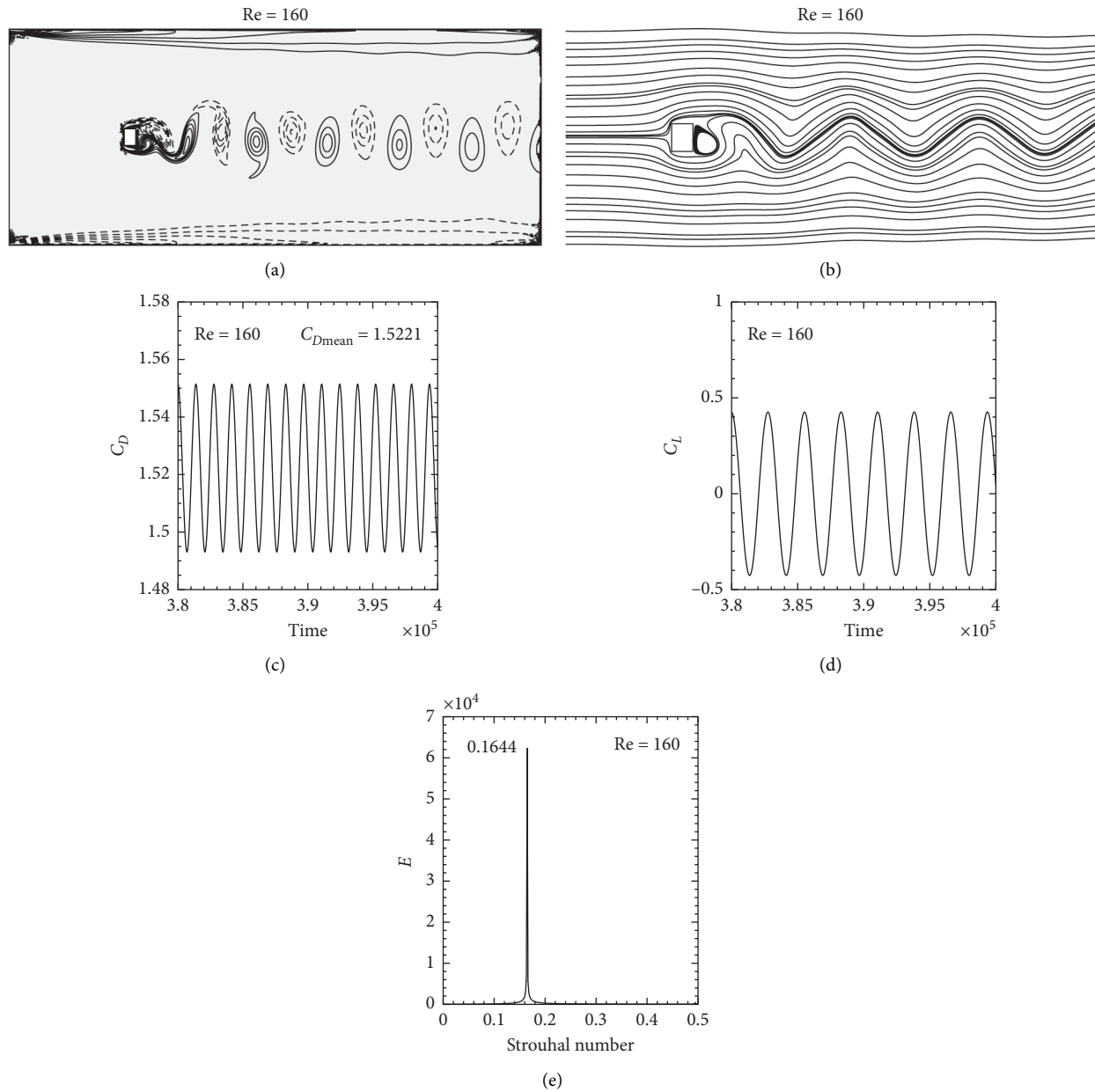


FIGURE 4: (a) Instantaneous vorticity contour visualization. (b) Streamline visualization. (c, d) Force time history. (e) Power spectra analysis of the C_L , $Re = 160$.

phase synchronized vortex shedding behind these two cylinders. Previous experimental study of Kolar et al. [1] for flow around two side-by-side square cylinders and numerical study of Farrant et al. [18] for flow around four circular cylinders in an inline square configuration also suggest the in-phase synchronized vortex shedding for large separation ratio. From these graphs, it can be observed that, along with g^* , the Reynolds numbers also have significant influence on the change of flow features around four cylinders. Such observations are also consistent with the available experimental studies of Williamson [2] for $Re = 100$ to 200 and Zhou et al. [47] for $Re = 150$ to 450 for flow past two side-by-side cylinders.

As presented in Figure 10(b), there is no vortex shedding in the gap between C_1 and C_2 , but small recirculation zones are clearly seen behind cylinder C_1 . The gap flows can generate large lift on cylinder C_4 . As a result, one can see only two small eddies behind the cylinders (Figure 10(a)). As g^* is increased to 2, there is no recirculation within the gaps and some unsteadiness is seen at far downstream of the domain. These characteristics belong to QUFR and are observed only for $Re = 80$ at this specific separation ratio (Figure 10(b)). At $(Re, g^*) = (140, 2)$, the interaction of shed vortices and interference becomes very complex and strong within the cylinders due to narrow jet flows through the gaps. The wake of C_1 significantly shrinks and narrows, because the gap

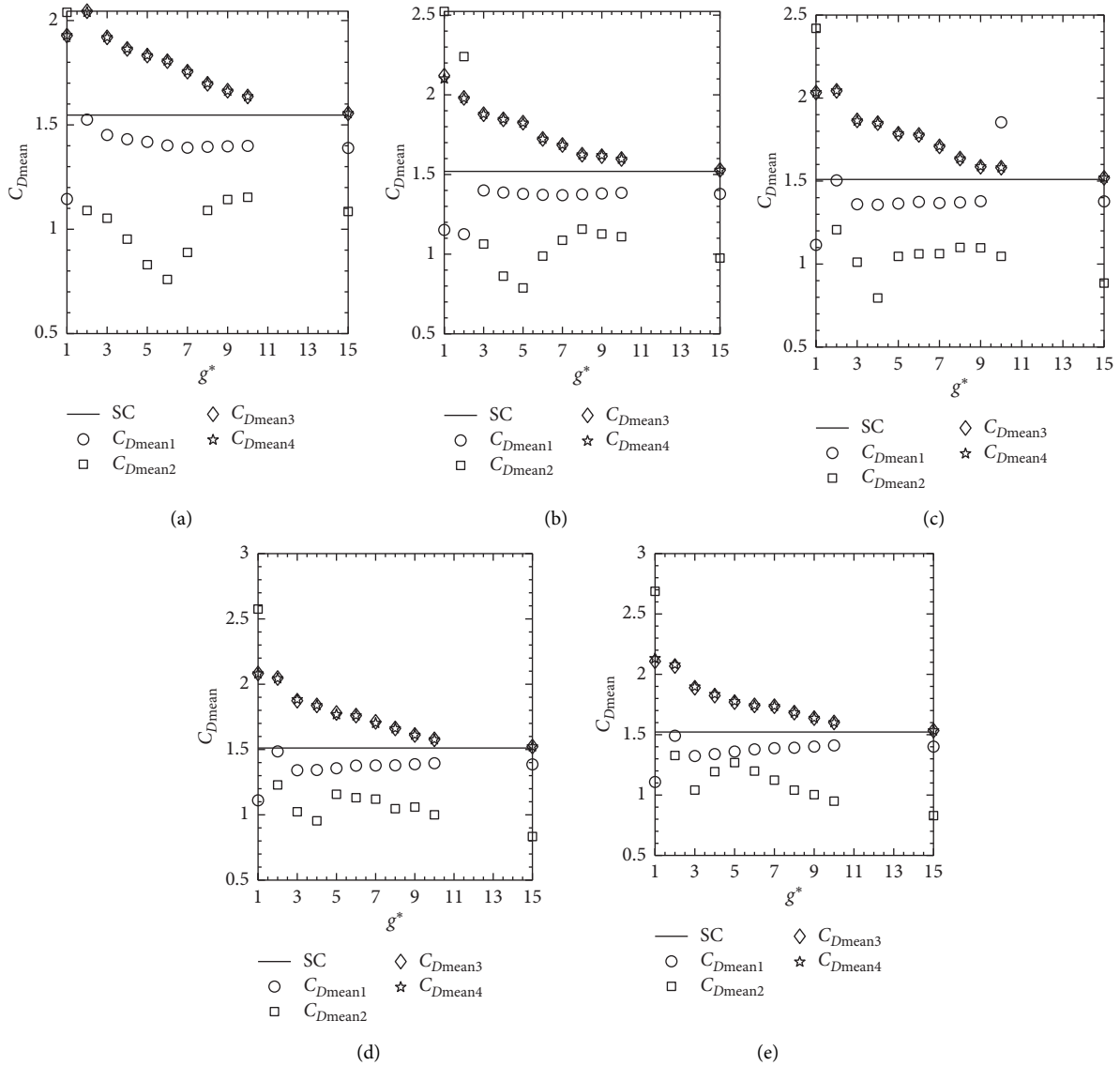


FIGURE 5: Variation of C_{Dmean} as a function of g^* for (a) $Re = 80$, (b) $Re = 100$, (c) $Re = 120$, (d) $Re = 140$, and (e) $Re = 160$.

flows from each side rush into the central region. The shear layer reattachment from C_1 onto C_2 generates a very complex region behind C_2 , C_3 , and C_4 in terms of small and large eddies (Figure 10(c)). When g^* is increased to 5, the effect of gap flows is slightly reduced and the recirculation observed behind each cylinder further confirms that the wake deviates either downward or upward and does not affect the shed vortices from C_1 . This recirculation confirms the irregular generation of vortices observed at far downstream of the computational domain (Figure 10(d)). As a result of such instability, one can see some more peaks in the power spectra together with the primary vortex shedding frequency (see Figures 12(m)–12(p)). We believe that the CFR for the four square cylinders in diamond arrangement lies between 3 and 5 for all chosen Reynolds numbers. At $g^* = 9$ and 15, the streamline visualization shows that the shear layer of the C_1 rolls up into a fully developed vortex and impinges onto the cylinder C_2 . Due to reasonably large

spacing in presence of C_1 and C_2 , the vortex shedding of side-by-side cylinders C_3 and C_4 becomes antiphase for $g^* = 9$ (Figure 10(f)) and in-phase for $g^* = 15$ (Figure 10(e)). As a result of large separation ratio, the vortex shedding frequency of the cylinders is almost close to that of an isolated cylinder for all chosen Reynolds numbers.

Figures 11(a)–11(l) show the time variation of drag and lift forces for different observed flow regimes at different values of Re and g^* . At $g^* = 1$ and $Re = 100$, the time analysis of C_D and C_L of four cylinders for single bluff-body flow regime shows periodic behavior without any modulations (Figures 11(a) and 11(b)). Furthermore, at $g^* = 2$ and $Re = 80$, the drag coefficient of cylinder C_1 shows steady behavior for QUFR (Figure 11(c)). The lowest drag observed for C_2 , C_{D3} , and C_{D4} shows antiphase behavior. The existence of a secondary cylinder interaction frequencies and its contribution in CFR can be clearly seen from the irregular variation of drag and lift forces presented in Figures 11(e)–

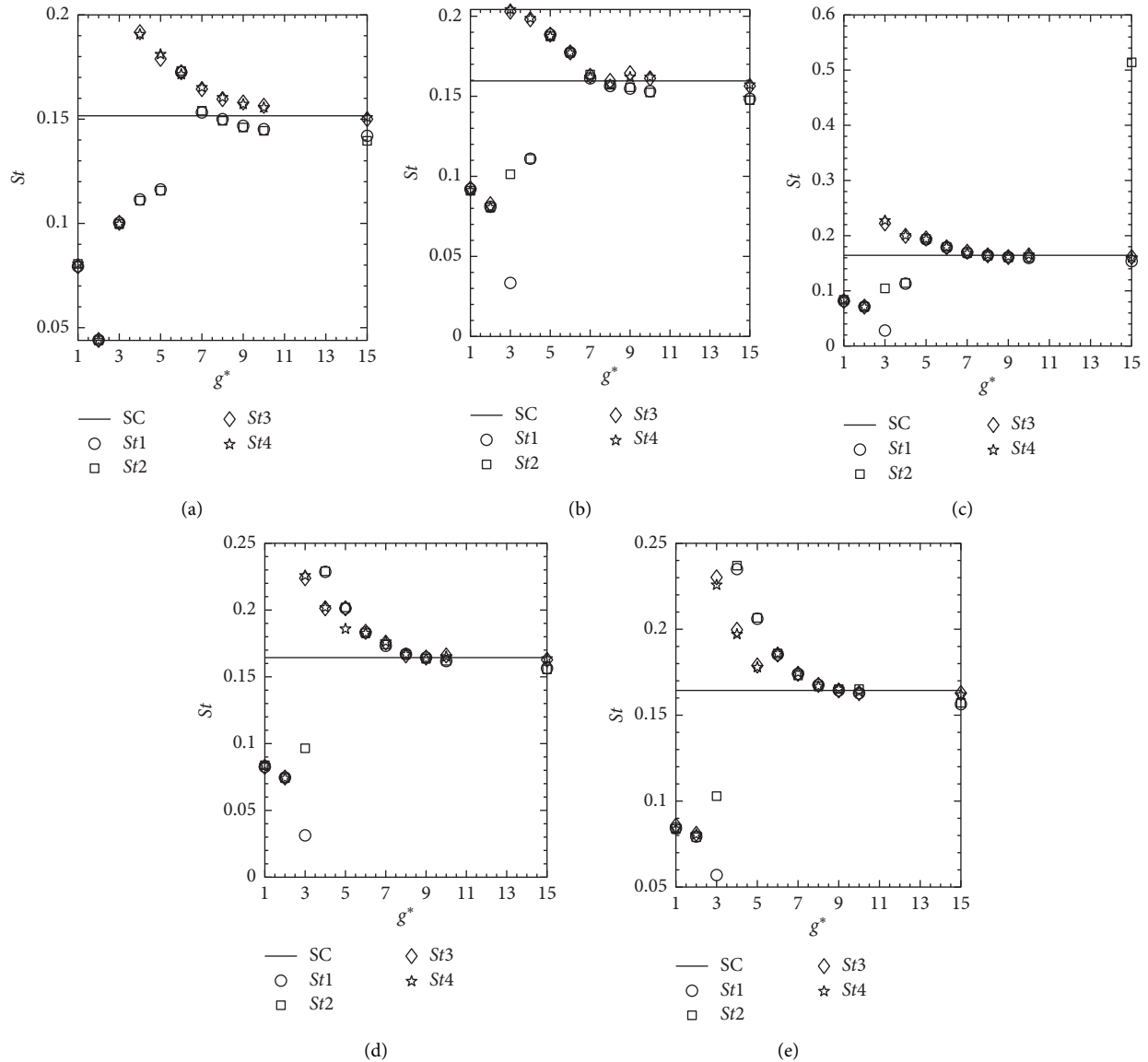


FIGURE 6: Variation of St as a function of g^* for (a) $Re = 80$, (b) $Re = 100$, (c) $Re = 120$, (d) $Re = 140$, and (e) $Re = 160$.

11(h) for different combinations of Re and g^* . The amplitude of forces continuously changes due to interaction of gap flows with the shed vortices behind the cylinders. The time variation of lift coefficients is becoming periodic for the ASVSFR and ISVSFR regimes except for the cylinder C_2 . The C_{L2} is strongly modulated and strongly interacts with other cylinders shed vortices. On the other hand, the drag coefficients show some minor modulations (Figures 11(i)–11(l)). In Figures 11(i)–11(l), the time signal analysis of lift coefficients confirms the existence of only primary vortex shedding frequency. Only C_{D2} and C_{L2} show some small modulation. This ensures that at reasonably large separation ratios the role of secondary cylinder interaction frequencies almost disappears for all four cylinders. The time variation of lift coefficients is sinusoidal for the three cylinders (C_1 , C_3 , C_4), with the amplitude for the cylinder C_2 being larger than that of the C_1 , C_3 , and C_4 cylinders. Furthermore, at low separation ratios, the drag coefficient in the cylinders C_3 and

C_4 is higher than that in the isolated cylinder. Zhou et al. [47] also reported that, at $g^* = 2$ and $Re = 0.35\text{--}1.04 \times 10^4$, the drag coefficients in the two side-by-side cylinders case were considerably higher than that in the isolated cylinder case.

To further examine the transition of flow regimes, FFT analyses of the lift coefficients are performed, and some representative cases are presented in Figures 12(a)–12(x). It can be seen in Figures 12(a)–12(x) that the influences of primary vortex shedding frequency and secondary cylinder interaction frequencies change once the flow regime changes from one state to another. Kumar et al. [48] proposed the secondary cylinder interaction frequency concept for the first time for flow around row of square cylinders. In SBBFR, the primary vortex shedding indicates that the vortex pattern behind the cylinders moves in alternate fashion. Different vortex frequencies (Figures 12(a) and 12(b)) are observed for cylinders C_1 and C_2 , and the same shedding frequencies (Figures 12(c) and 12(d)) are observed for C_3 and C_4 . One

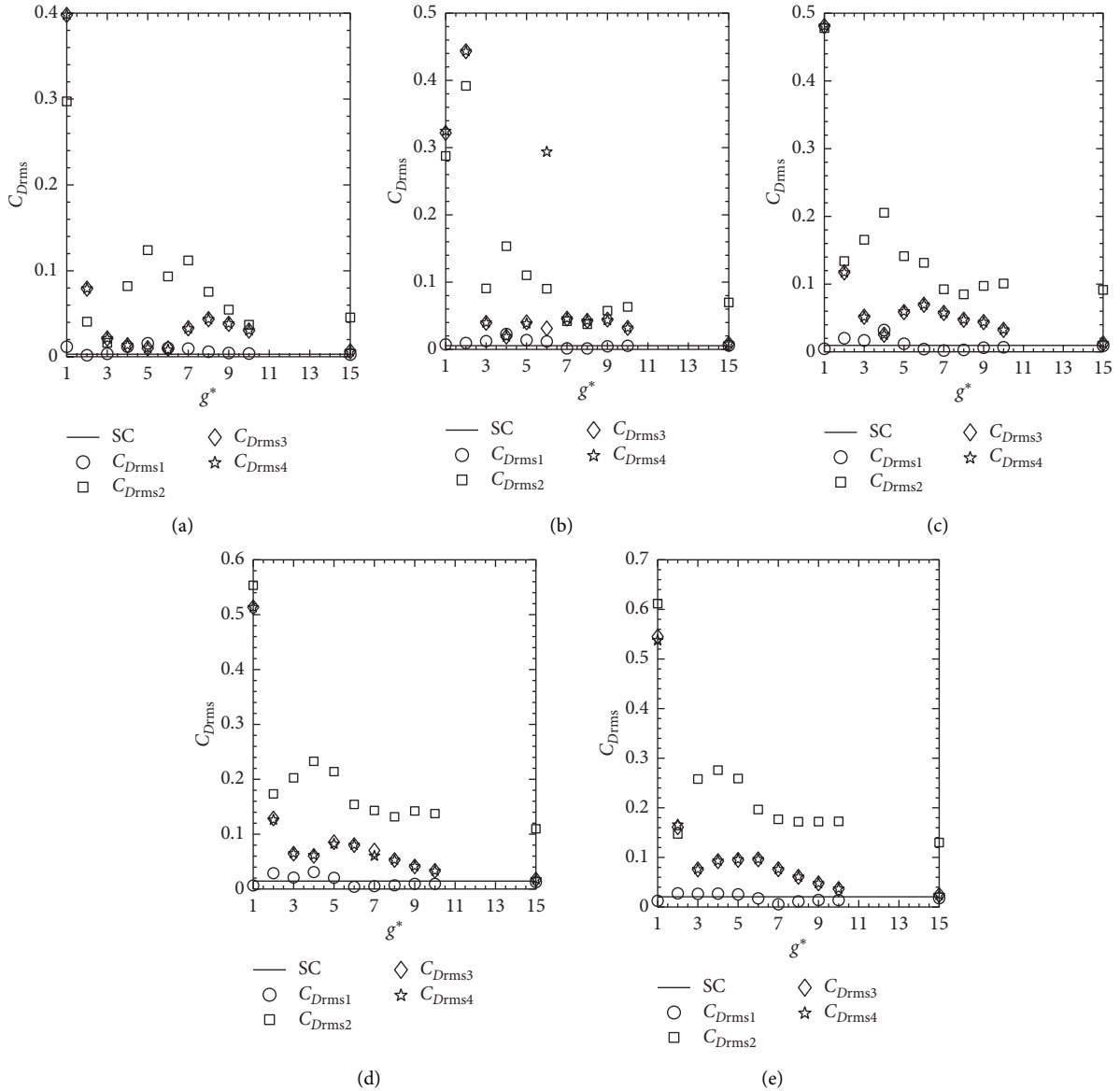


FIGURE 7: Variation of C_{Drms} as a function of g^* for (a) $Re = 80$, (b) $Re = 100$, (c) $Re = 120$, (d) $Re = 140$, and (e) $Re = 160$.

small peak is also found for C_1 and C_2 . In QFR, for $(Re, g^*) = (80, 2)$, there is no evidence of other harmonics in the spectra and the primary vortex shedding frequency dominates the flow (Figures 12(e)–12(h)). Almost the same shedding frequencies are observed for all cylinders with negligible difference. This is due to the unsteadiness nature of the flow near exit of the computational domain. To examine the frequency characteristics of the chaotic flow regime (CFR), two representative cases $((Re, g^*) = (140, 2)$ and $(160, 5)$) are presented in Figures 12(i)–12(p). The presence of secondary cylinder interaction frequencies indicates that, for CFR, the wake pattern is not stable and there is a strong interaction of gap flows and continuous change in the direction of shed vortices behind the cylinders. In this study, we found that the chaotic nature increased with increasing Reynolds numbers at $g^* = 2$. The highest peak in Figures 12(i)–12(l) ($St1 = 0.0735$ and $St2 = 0.0731$) for inline

cylinders (C_1 and C_2) and ($St3 = 0.0735$ and $St4 = 0.0731$) for side-by-side cylinders (C_3 and C_4) is the primary vortex shedding frequency. The power spectrum analysis at $(Re, g^*) = (160, 5)$ is shown in Figures 12(m)–12(p). It is found again that there exist secondary cylinder interaction frequencies even at reasonable spacing between the cylinders. A Strouhal number of 0.2060, 0.2075, 0.1765, and 0.1758 corresponds to the primary vortex shedding frequency for $C_1, C_2, C_3,$ and C_4 respectively. In the chaotic flow regime, due to some spacing between the cylinders, the gap flow effect becomes smaller and only one to two harmonics are seen in the spectra. This confirms the interaction of shed vortices behind the cylinders at far downstream of the domain. The secondary cylinder interaction frequencies together with the primary vortex shedding frequency are also observed by Abbasi et al. [22] for flow past four square cylinders in an inline square configuration. The spectra

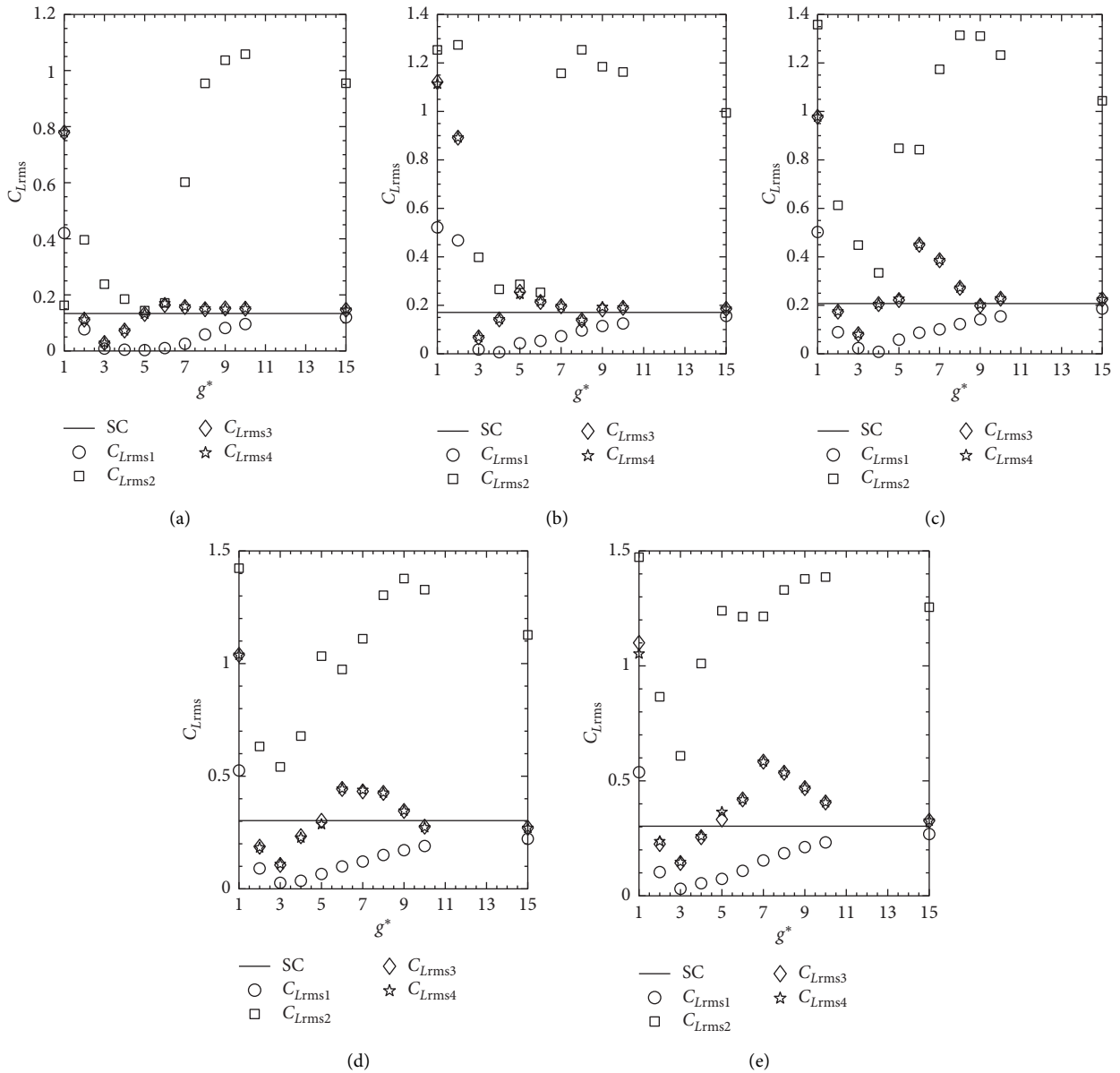


FIGURE 8: Variation of C_{Lrms} as a function of g^* for (a) $Re = 80$, (b) $Re = 100$, (c) $Re = 120$, (d) $Re = 140$, and (e) $Re = 160$.

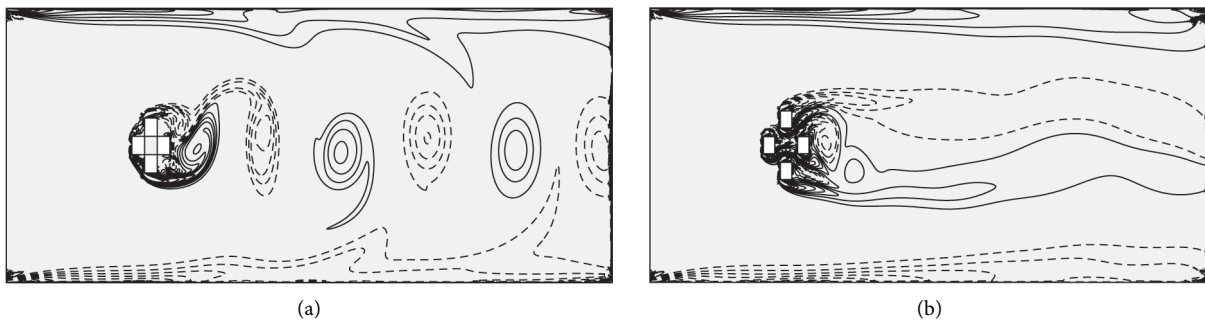


FIGURE 9: Continued.

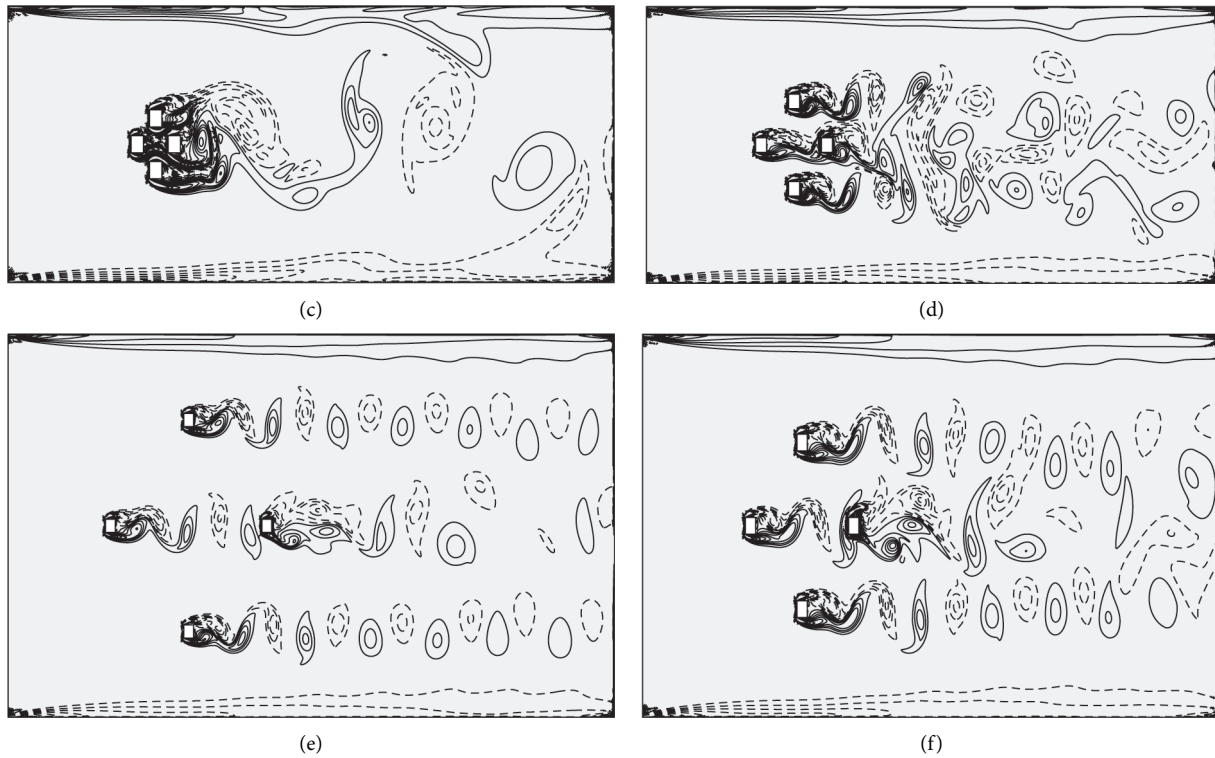


FIGURE 9: Vorticity contour representation at different combinations of Re and g^* . (a) $g^* = 1.0$ and $Re = 100$. (b) $g^* = 2.0$ and $Re = 80$. (c) $g^* = 2.0$ and $Re = 140$. (d) $g^* = 5.0$ and $Re = 160$. (e) $g^* = 15.0$ and $Re = 100$. (f) $g^* = 9.0$ and $Re = 120$.

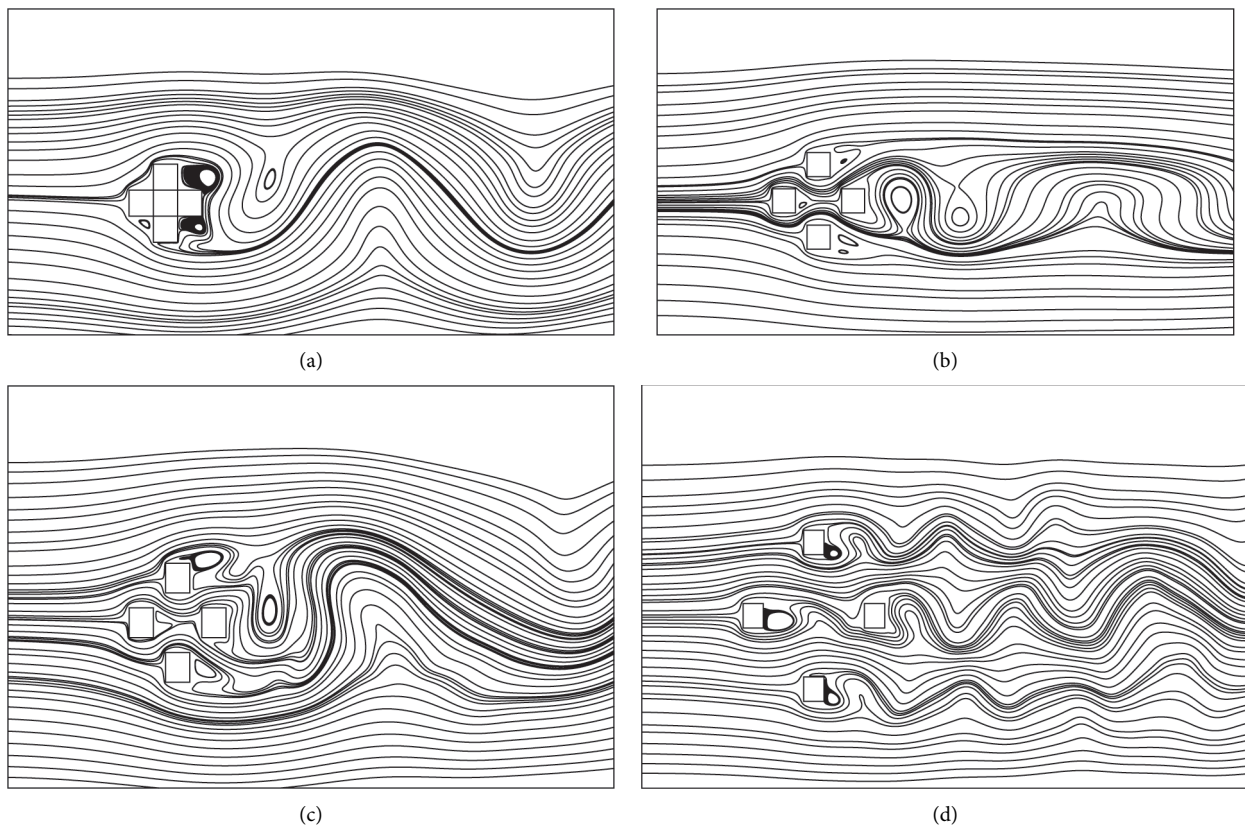


FIGURE 10: Continued.

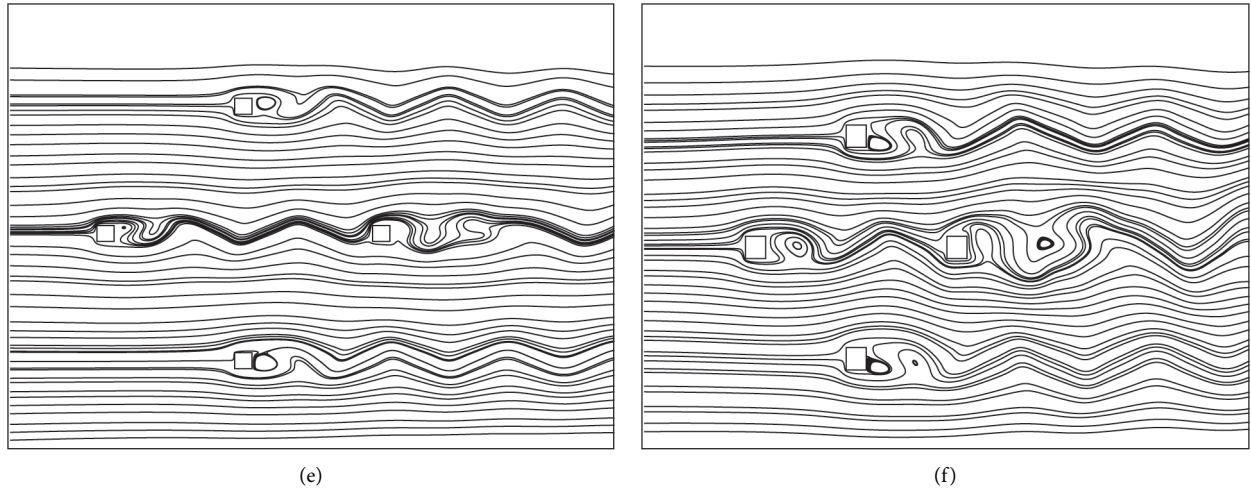


FIGURE 10: Streamline visualization at different combinations of Re and g^* . (a) $g^* = 1.0$ and $Re = 100$. (b) $g^* = 2.0$ and $Re = 80$. (c) $g^* = 2.0$ and $Re = 140$. (d) $g^* = 5.0$ and $Re = 160$. (e) $g^* = 15.0$ and $Re = 100$. (f) $g^* = 9.0$ and $Re = 120$.

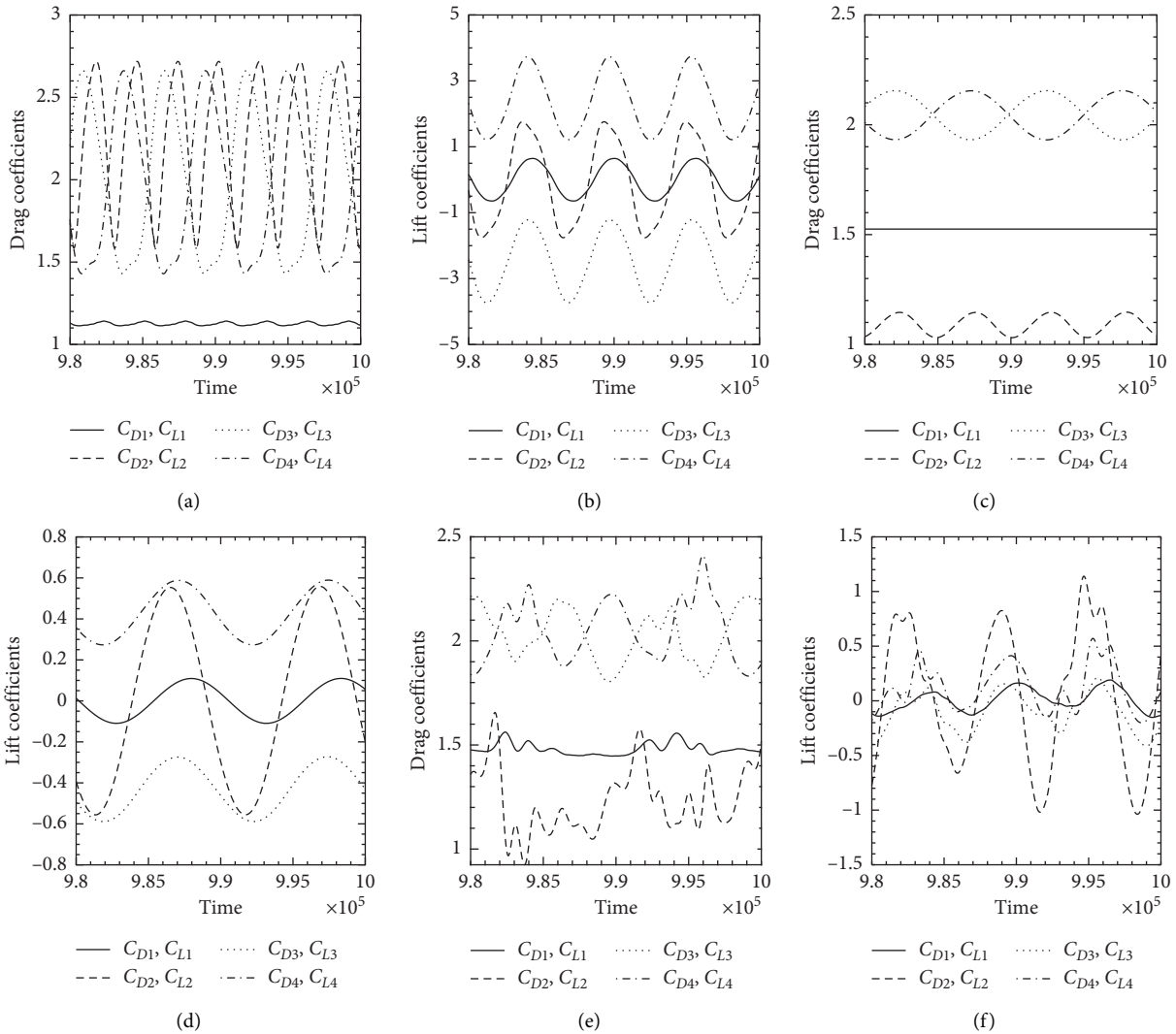


FIGURE 11: Continued.

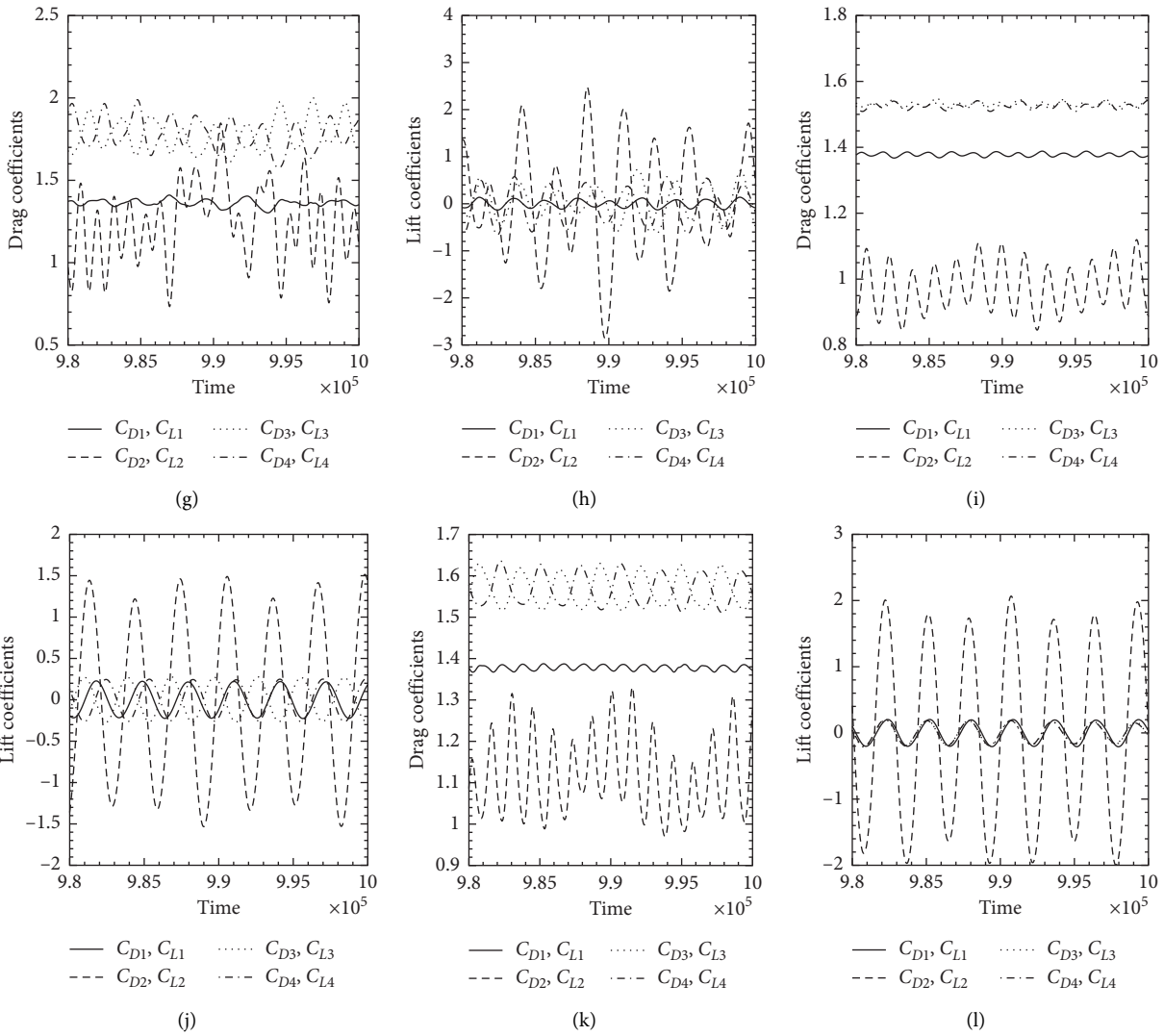


FIGURE 11: Time history analysis of C_D and C_L at different values of Re and g^* . (a) $g^* = 1.0$ and $Re = 100$. (b) $g^* = 1.0$ and $Re = 100$. (c) $g^* = 2.0$ and $Re = 80$. (d) $g^* = 2.0$ and $Re = 80$. (e) $g^* = 2.0$ and $Re = 140$. (f) $g^* = 2.0$ and $Re = 140$. (g) $g^* = 5.0$ and $Re = 160$. (h) $g^* = 5.0$ and $Re = 160$. (i) $g^* = 15.0$ and $Re = 100$. (j) $g^* = 15.0$ and $Re = 100$. (k) $g^* = 9.0$ and $Re = 120$. (l) $g^* = 9.0$ and $Re = 120$.

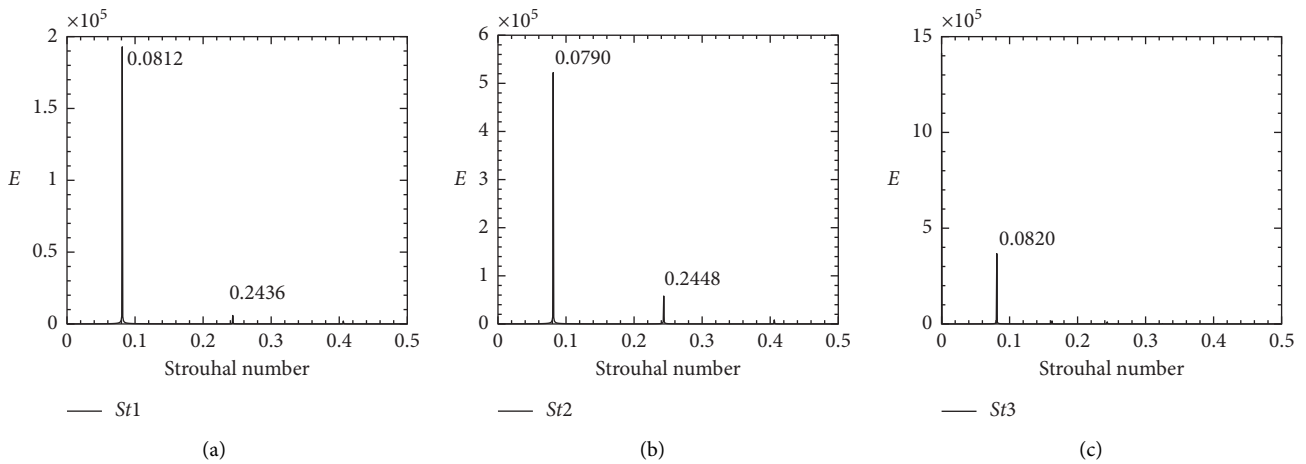
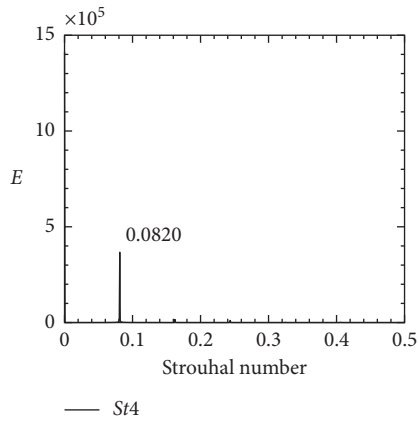
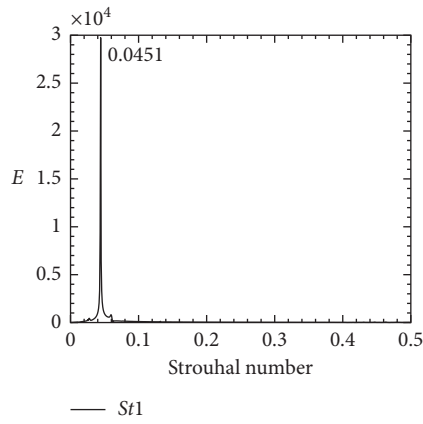


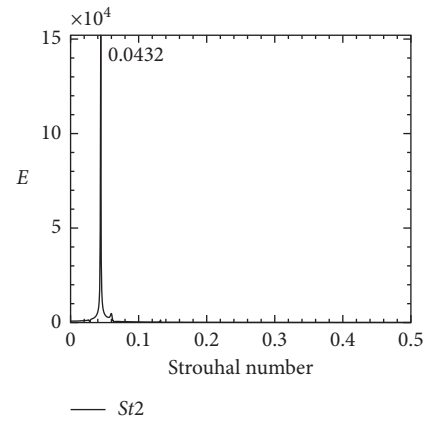
FIGURE 12: Continued.



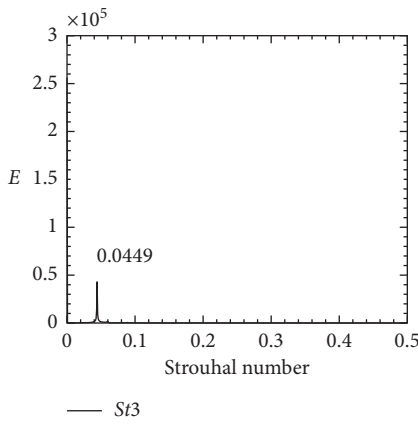
(d)



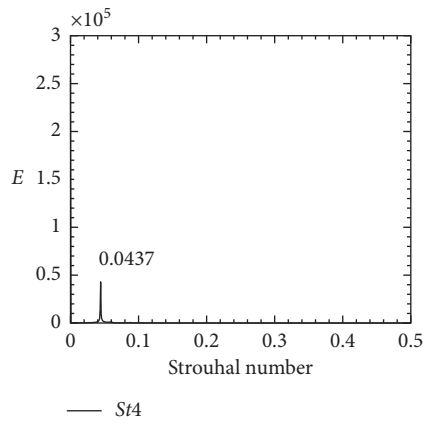
(e)



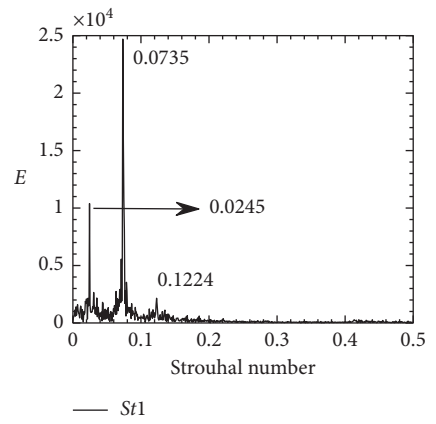
(f)



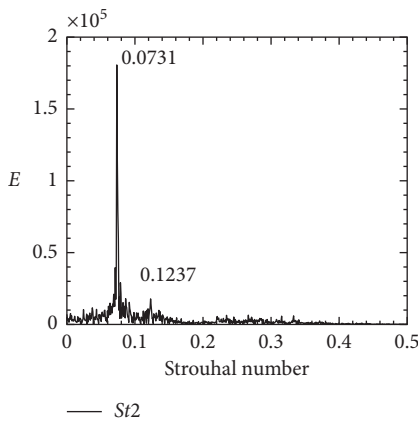
(g)



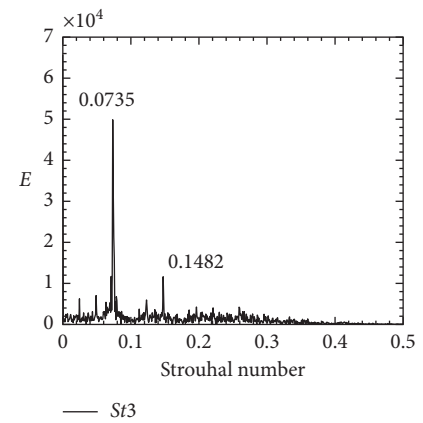
(h)



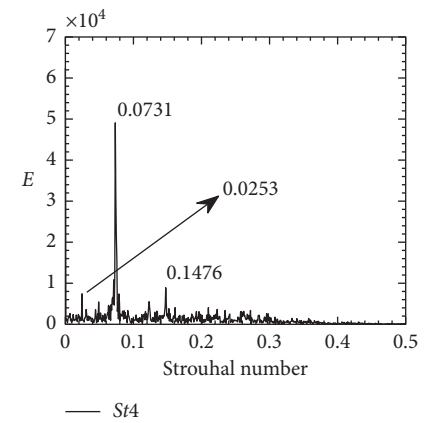
(i)



(j)

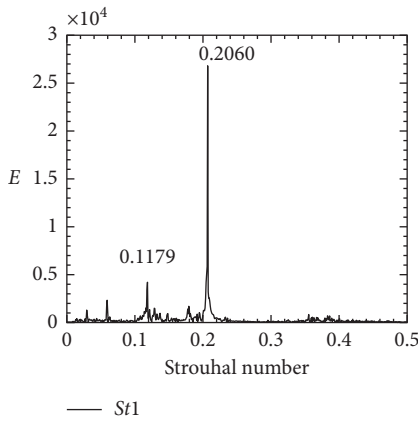


(k)

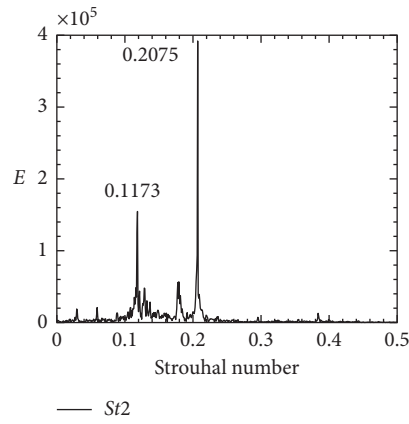


(l)

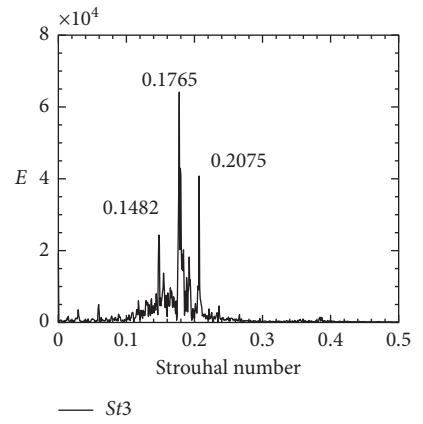
FIGURE 12: Continued.



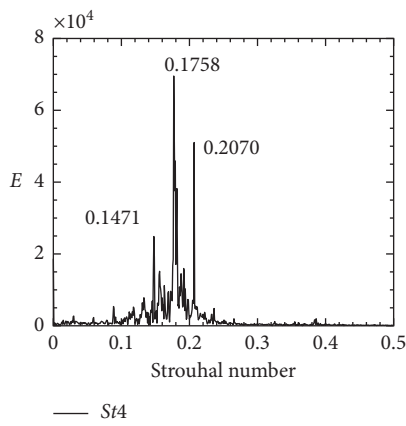
(m)



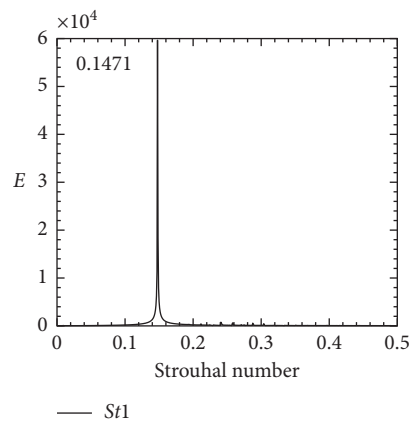
(n)



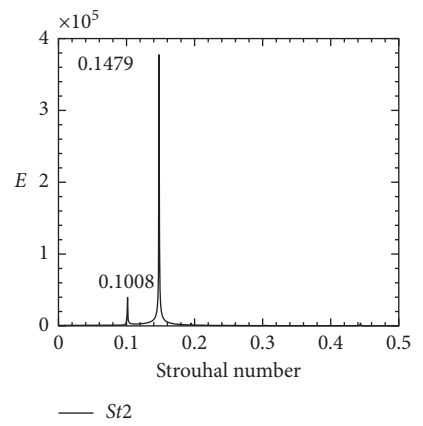
(o)



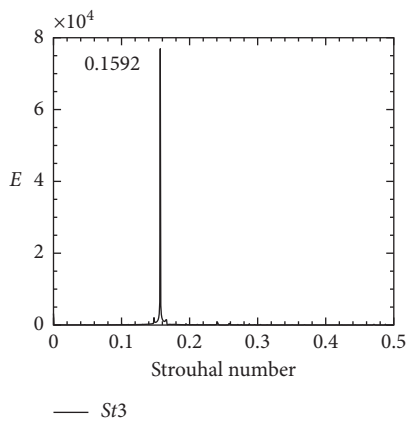
(p)



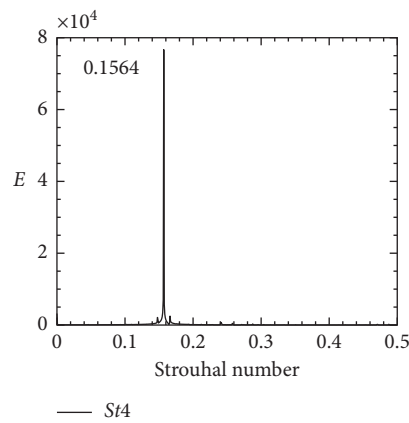
(q)



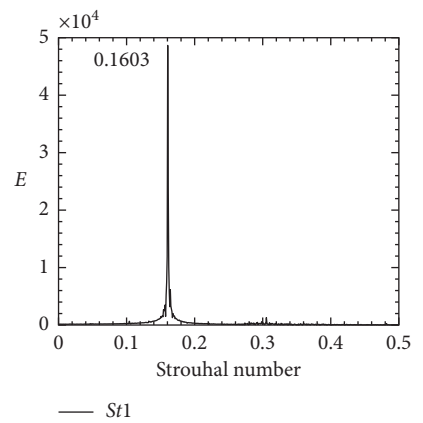
(r)



(s)



(t)



(u)

FIGURE 12: Continued.

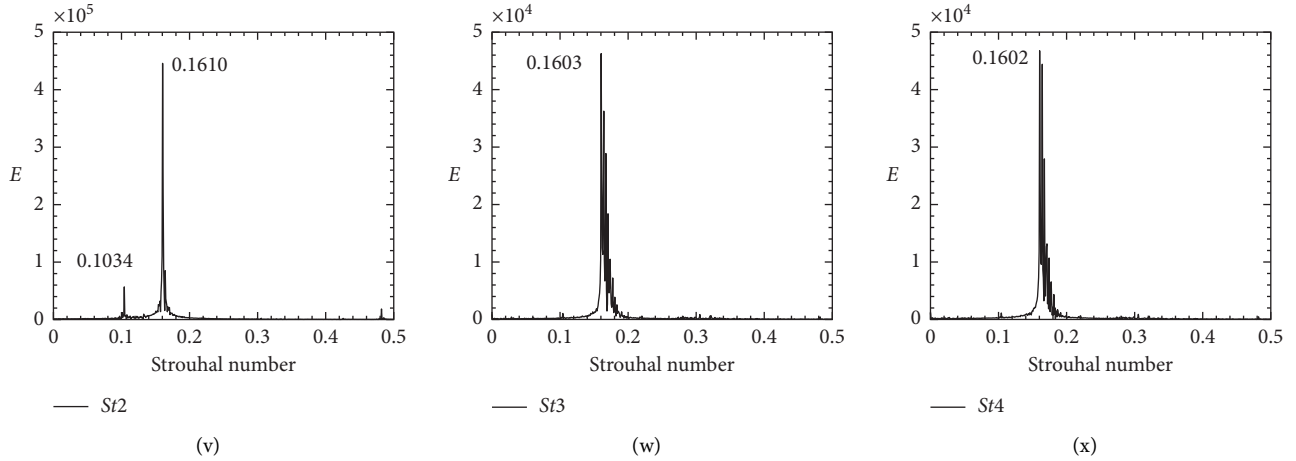


FIGURE 12: Power spectra analysis of C_L at various values of g^* and Re. (a) $g^* = 1.0$ and Re = 100. (b) $g^* = 1.0$ and Re = 100. (c) $g^* = 1.0$ and Re = 100. (d) $g^* = 1.0$ and Re = 100. (e) $g^* = 2.0$ and Re = 80. (f) $g^* = 2.0$ and Re = 80. (g) $g^* = 2.0$ and Re = 80. (h) $g^* = 2.0$ and Re = 80. (i) $g^* = 2.0$ and Re = 140. (j) $g^* = 2.0$ and Re = 140. (k) $g^* = 2.0$ and Re = 140. (l) $g^* = 2.0$ and Re = 140. (m) $g^* = 5.0$ and Re = 160. (n) $g^* = 5.0$ and Re = 160. (o) $g^* = 5.0$ and Re = 160. (p) $g^* = 5.0$ and Re = 160. (q) $g^* = 15.0$ and Re = 100. (r) $g^* = 15.0$ and Re = 100. (s) $g^* = 15.0$ and Re = 100. (t) $g^* = 15.0$ and Re = 100. (u) $g^* = 9.0$ and Re = 120. (v) $g^* = 9.0$ and Re = 120. (w) $g^* = 9.0$ and Re = 120. (x) $g^* = 9.0$ and Re = 120.

analysis of lift coefficients for $(Re, g^*) = (100, 15)$ and $(120, 9)$ for all four cylinders is presented in Figures 12(q)–12(x) for ASVSFR and ISVSFR. It is observed that there exists only primary vortex shedding frequency for both flow regimes due to large spacing between the cylinders. Only one extra small peak is observed for C_2 which is the way of C_1 . Interestingly, the power spectra of C_2 still show one small peak together with the primary vortex shedding frequency at large separation ratio ($g^* = 15$) shown in Figures 12(r) and 12(v).

As shown in Figures 13(a)–13(f), the streamwise velocity distribution at different cross-sections for different values of Re and g^* shows different characteristics. It is clear from these figures that the streamwise velocity at different cross-sections is considerably affected as the flow transition occurs. For example, in case of CFR (Figures 13(c)–13(d)), the irregular variation of velocities even at far downstream location confirms the mutual interaction of generated shed vortices along with the gap flows. It is observed that the downstream cylinder C_2 generally experiences large streamwise and transverse amplitudes.

The results of C_{Dmean} , St , C_{Drms} , and C_{Lrms} of four cylinders as a function of g^* for the different Re values are presented in Figures 5(a)–5(d), 6(a)–6(d), 7(a)–7(d), and 8(a)–8(d), respectively, together with the results of isolated cylinder for comparison. It can be seen from Figures 5(a)–5(d) for all chosen Reynolds numbers that the tandem cylinders (C_1 and C_2) are showing smaller mean drag forces than the side-by-side ones. As mean drag increases, wake interference decreases. In general, the C_{Dmean} values of C_1 and C_2 are considerably less than C_{Dmean} values of isolated cylinder at various separation ratios for all chosen Reynolds numbers. This confirms that the presence of cylinder in the wake of other cylinder reduces the forces. This finding agrees well with the results of Zdravkovich [11] for flow past tandem cylinders. Furthermore, we observed from the

figures that C_{Dmean3} and C_{Dmean4} decrease with the increase in g^* , except at Re = 80 and $g^* = 2$. This is due to the flow transition from single bluff-body flow regime to quasi-unsteady flow regime. However, the opposite trend is observed for the C_{Dmean2} ; i.e., it decreases first to $g^* = 6, 5, 4, 4,$ and 3 for Re = 80, 100, 120, 140, and 160, respectively; then starts to increase; and again decreases by increasing the values of g^* . The maximum average drag force can be observed at $g^* = 1$ for all Re values for C_{Dmean2} . As the spacing ratio increases, the C_{Dmean3} and C_{Dmean4} values approach SC value for all Reynolds numbers. The C_{Dmean2} values are mostly affected up to $g^* = 5$ due to critical flow regime observed at $2 \leq g^* \leq 5$. It is observed that the drag values are almost the same for cylinders C_3 and C_4 at $g^* \geq 1$ for all chosen Reynolds numbers. It is to be noted that, in case of two side-by-side cylinders, Guillaume and LaRue [3] experienced different drag values. In case of four cylinders in an inline square configuration, researchers observed negative drag values for the downstream cylinders (Sayers [16] and Abbasi et al. [22]). We did not find negative drag values for the downstream cylinders in diamond arrangement of four square cylinders.

At small spacings between the cylinders due to the complex interferences among the cylinders, the variations of the wakes appear to be more complicated than that of a flow past a single square cylinder. The g^* is found to have a strong effect on the wake structures and forces of the cylinder C_2 , rather than the cylinders C_3 and C_4 . It is clear from Figures 6(a)–6(e) that Strouhal number of all four cylinders shows abrupt changes up to $g^* = 5$ for different Reynolds numbers. Then, it shows increasing behavior and almost approaches the SC value. At $1 \leq g^* \leq 5$ and Re = 80, 100, 120, 140, and 160, we found multiple peaks in the power spectra because of secondary cylinder interaction frequencies. Further, at $g^* \geq 6$, we observed that generally the Strouhal number of tandem cylinders (C_1 and C_2) as

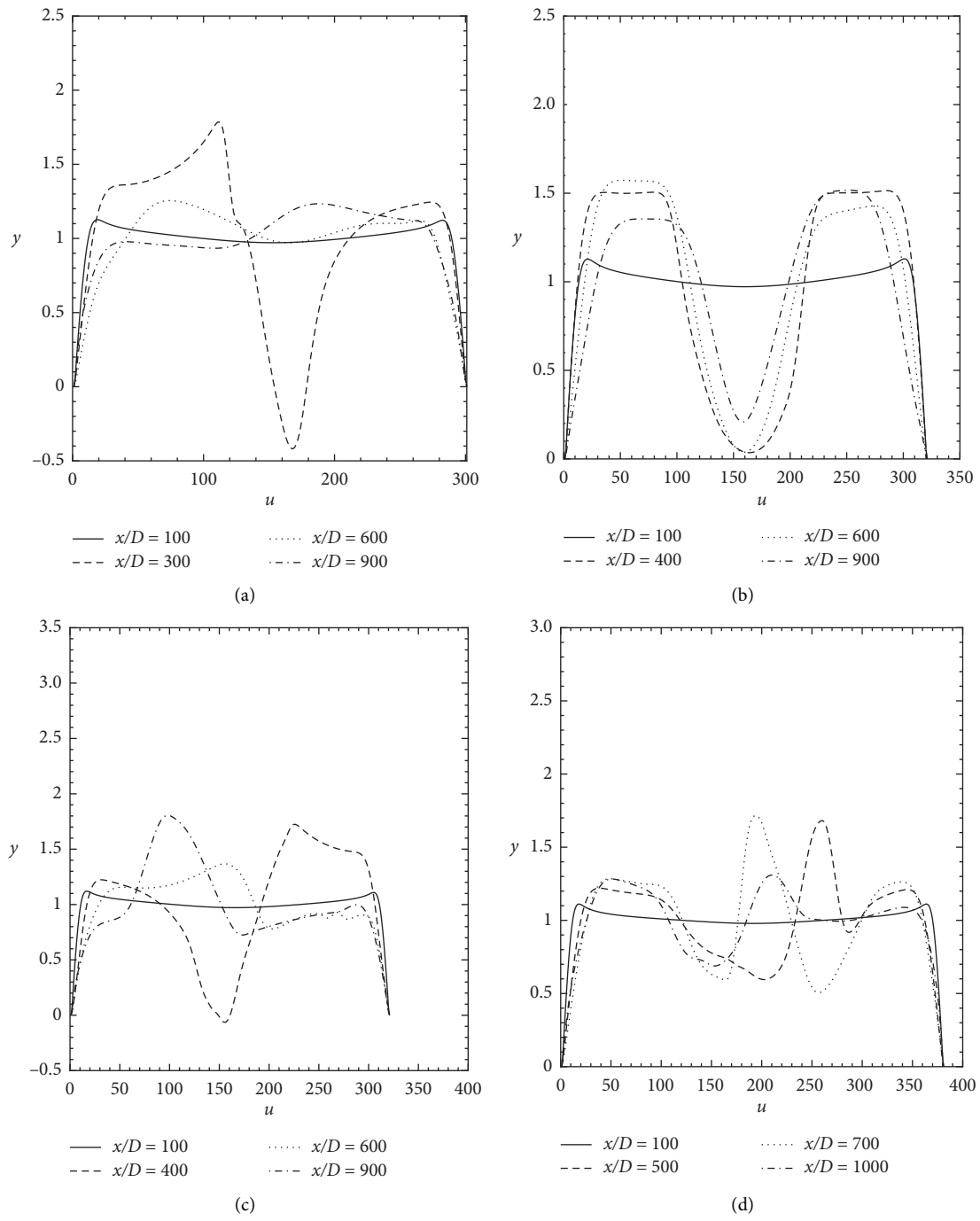


FIGURE 13: Continued.

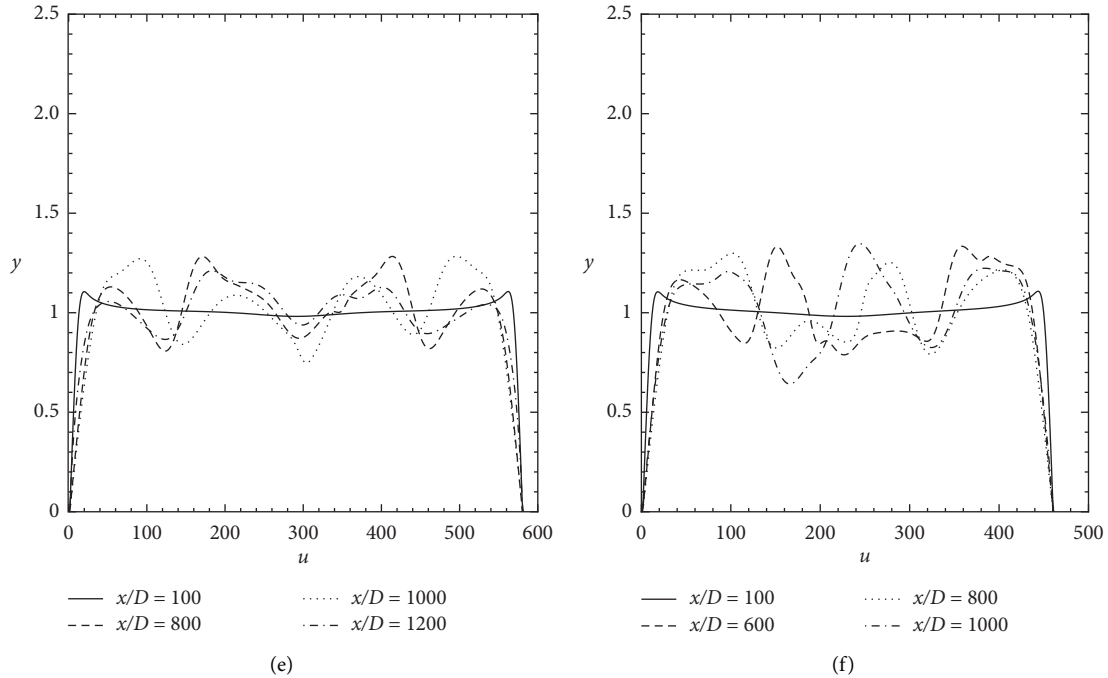


FIGURE 13: Streamwise velocity distribution at various cross-sections for different combinations of g^* and Re. (a) $g^* = 1.0$ and $Re = 100$. (b) $g^* = 2.0$ and $Re = 80$. (c) $g^* = 2.0$ and $Re = 140$. (d) $g^* = 5.0$ and $Re = 160$. (e) $g^* = 15.0$ and $Re = 100$. (f) $g^* = 9.0$ and $Re = 120$.

well as side-by-side cylinders (C_3 and C_4) is almost the same, which confirms that the primary vortex shedding frequencies are dominant. We further observed different vortex shedding frequencies for cylinders C_1 and C_2 for all selected Reynolds numbers at $g^* = 3$. This is due to the strong interaction of gap flows with the shed vortices behind the cylinders. The results indicate that when the spacing between the cylinders is reasonably large, the St approaches single-cylinder value. We found that the forces are slightly different for each individual cylinder by changing the value of g^* at fixed Re. Liu et al. [23] had similar experimental observations at $Re = 4.58 \times 10^4$ and $g^* = 3.45, 4.14,$ and 5.17 for flow around four square cylinders. Furthermore, the results show that the vortex shedding frequency considerably depends on the separation ratio, especially at $1 \leq g^* \leq 6$. For the antiphase and in-phase synchronized vortex shedding flow regimes, the vortex shedding frequency of cylinders is almost constant at $9 \leq g^* \leq 15$, very close to that ($St = 0.1516, 0.1596, 0.1644, 0.1644,$ and 0.1644 for $Re = 80, 100, 120, 140,$ and 160 , respectively) in the isolated cylinder case. Interestingly, the vortex shedding frequency drastically increases for cylinders C_1 and C_2 and decreases for cylinders C_3 and C_4 with increasing separation ratio for the chaotic flow regime.

The effects of separation ratios g^* on C_{Drms} of four cylinders are shown in Figures 7(a)–7(e). It can be seen from Figures 7(a)–7(e) that with g^* the values of C_{Drms} are generally reduced and approach SC value except at C_{Drms2} for all chosen Reynolds numbers. At $g^* = 1$, the C_{Drms1} values reach their minimum, and the other three cylinders attain the maximum values for all selected ranges of Reynolds numbers. It is observed that, due to chaotic flow

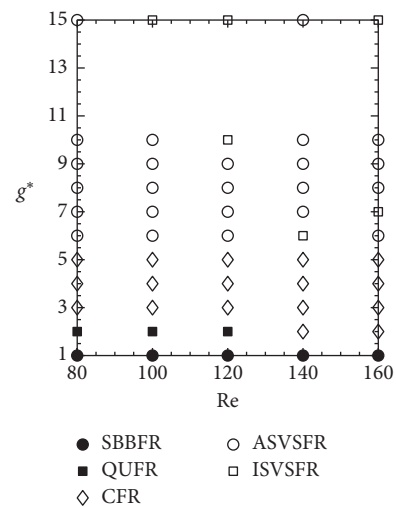


FIGURE 14: Flow regimes as a function of Re and g^* .

regime, the effect of g^* for all Reynolds numbers on the four cylinders C_{Drms} values is significant and becomes small when $g^* \geq 7$. As g^* increases, as shown in Figures 7(a)–7(e), the variation of C_{Drms1} is almost constant with minor variation in that of the SC. The $C_{Drms1}, C_{Drms3},$ and C_{Drms4} values appear to be smaller than those of the C_{Drms2} , except for the $g^* = 1$ and 2 for all chosen Reynolds numbers. At large separation ratio $g^* = 7$ to 9, the C_{Drms} of C_3 and C_4 is maintained at constant values, and the values for the cylinder C_2 is higher than those for the cylinders C_3 and C_4 . The differences of C_{Drms2} from C_{Drms3} and C_{Drms4} for $g^* = 7$ to 9 become higher as the Reynolds number increased.

When g^* increases to 15, the $C_{D_{rms1}}$, $C_{D_{rms3}}$, and $C_{D_{rms4}}$ are almost the same. However, the variation of $C_{D_{rms2}}$ is quite different.

In Figures 8(a)–8(e), the calculation results of $C_{L_{rms}}$ for various separation ratios at $80 \leq Re \leq 160$ are compared with the isolated cylinder data. It can be seen that, due to the shear layer reattachment from C_1 onto C_2 and the complex interaction of gap flows with the shed vortices behind C_3 and C_4 from $g^* = 2$ to 5, the variation of the $C_{L_{rms}}$ with separation ratios for four cylinders appears to be more complicated than that of the SC value. The $C_{L_{rms3}}$ and $C_{L_{rms4}}$ decrease with increasing g^* but are still larger than those of $C_{L_{rms1}}$. The results show that the $C_{L_{rms2}}$ is considerably affected by changing the value of g^* at fixed Reynolds number. A possible explanation for such observation is that the wake structure behavior for the cylinder C_2 is too complicated than that for the other cylinders, involving the gap flows from the upstream cylinders and the shear layers interaction with cylinder C_1 . It is seen from the $C_{L_{rms}}$ values that the flow regimes are very sensitive to the separation ratio up to $g^* \geq 7$. It is found that $C_{L_{rms1}}$ value is lower than the isolated cylinder value for all Reynolds numbers up to $g^* = 7$ and then approach SC value for $g^* \geq 8$. This mean that the effect of shear layer becomes less beyond $g^* = 7$. The root-mean-square values of C_3 and C_4 cylinders are almost the same for all selected ranges and approach SC value. The drastic changes in $C_{L_{rms2}}$ by changing the values of g^* for fixed Reynolds number confirm that the secondary cylinder interaction frequencies occur continuously due to gap flows interaction with shed vortices behind the cylinders. These characteristics further tell us that the shed vortices near downstream of C_2 are affected by the vortices generated from C_1 . Furthermore, with increasing g^* , the $C_{L_{rms1}}$ value first decreases to $g^* = 3$, then slightly increases, and finally approaches the SC value.

The graphical representation of various flow regimes, found in this numerical study, is given in Figure 14 at all separation ratios and Reynolds numbers. It can be seen that, at low separation ratios ($g^* = 1$) and $Re = 80, 100, 120, 140$, and 150 , the SBBFR occurs. In the small separation ratio ($g^* = 1$), the gap flow has almost no effect, and the shear layer on the C_1 cannot fall off freely. The four cylinders can act as a single bluff body, as shown in Figure 9(a). At $(Re, g^*) = (80, 2), (100, 2)$, and $(120, 2)$, the QUFR occurs. On the other hand, at $(Re, g^*) = (80, 3-5), (100, 3-5), (120, 3-5), (140, 2-5)$, and $(160, 2-5)$, the CFR is observed. At $(Re, g^*) = (80, 6-10 \text{ and } 15), (100, 6-10), (120, 6-9), (140, 7-10 \text{ and } 15), \text{ and } (160, 6 \text{ and } 8-10)$, the ISVSFR can be clearly seen. For $(Re, g^*) = (100, 15), (120, 10 \text{ and } 15), (140, 6), \text{ and } (160, 7 \text{ and } 15)$, the ASVSFR occurs. The flow features vary only slightly as Re increases for $g^* = 6$ to 15 . The ISVSFR is dominant as compared to ASVSFR. As shown in Figure 14, the critical spacing for four square cylinders in diamond arrangement for selected Reynolds numbers ($80 \leq Re \leq 160$) is in the range of $2 \leq g^* \leq 5$. It is to be noted that for the four cylinders in diamond arrangement, the critical spacing appears to be generally wider than that of two side-by-side square cylinders (Agrawal et al. [5]) and two tandem cylinders (Yen et al. [12]). It can be seen that the in-phase and antiphase nature of the cylinders C_3 and C_4 occurred when the separation ratio increased and the fully developed shed vortices existed between the cylinders C_1 and C_2 at higher separation

ratios. Williamson [2] also experimentally observed that the wakes behind the two side-by-side cylinders were either antiphase or in-phase when the separation ratio increased.

4. Conclusions

Two-dimensional computations have been performed to examine the influence of Re and g^* of four square cylinders in a diamond arrangement. The effects of the Re and g^* on the vortex shedding modes and dynamic responses of the four square cylinders are examined. The main conclusions are summarized as follows:

- (i) Numerical results showed that, by varying g^* from 1 to 15 and Re from 80 to 160, a total of five different kinds of flow regimes were identified: single bluff-body flow regime ($80 \leq Re \leq 160$ and $g^* = 1$), quasi-unsteady flow regime ($Re = 80, 100$, and 120 and $g^* = 2$), critical flow regime ($80 \leq Re \leq 160$ and $3 \leq g^* \leq 5$; also at $g^* = 2$ for $Re = 140$ and 160), antiphase synchronized vortex shedding flow regime ($(Re, g^*) = (140 \text{ and } 160, 2), (80, 100, 120, \text{ and } 160, 7), (80 \leq Re \leq 160, 8), (80 \leq Re \leq 160, 9), (80, 100, 140, \text{ and } 160, 10), (80 \text{ and } 140, 15)$), and in-phase synchronized vortex shedding flow regime ($(Re, g^*) = (140, 6), (160, 7), (120, 10), (100, 120, \text{ and } 160, 15)$). It was found that the flow regimes strongly depended on the separation ratio as well as the Reynolds number.
- (ii) The vortex shedding frequency strongly depended on the separation ratio. The secondary cylinder interaction frequencies also play a strong role for the chaotic flow regime. It is also found that the modulations in C_D and C_L for cylinders C_1 and C_2 in chaotic flow regime are significant. With increasing separation ratio, the primary vortex shedding frequency dominates the flow and remains nearly constant for the antiphase and in-phase synchronized vortex shedding flow regimes. In these flow regimes, the flow finds enough space between C_1 and C_2 to roll up in the form of shed vortices. We found the well-known von Karman vortex street behind each cylinder at larger separation ratio between the cylinders. In case of quasi-unsteady flow regime, we found the steady behavior of drag force of cylinder C_2 .
- (iii) The secondary cylinder interaction frequencies dominate the flow in case of critical flow regime. On the other hand, the primary vortex shedding frequency dominates the flow at larger separation ratios.
- (iv) It is found that the $C_{D_{mean3}}$ and $C_{D_{mean4}}$ decrease with the increase in g^* , except at $Re = 80$ and $g^* = 2$. This is due to the flow transition from single bluff-body flow regime to quasi-unsteady flow regime. However, the opposite trend is

observed for the $C_{D\text{mean}2}$; i.e., it decreases first to $g^* = 6, 5, 4, 4,$ and 3 for $\text{Re} = 80, 100, 120, 140,$ and $160,$ respectively; then starts to increase; and again decreases by increasing the values of g^* . The maximum average drag force can be observed at $g^* = 1$ for all Re values for $C_{D\text{mean}2}$. As the spacing ratio increases, the $C_{D\text{mean}3}$ and $C_{D\text{mean}4}$ values approach the SC value for all Reynolds numbers. The $C_{D\text{mean}2}$ value are mostly affected up to $g^* = 5$ due to critical flow regime observed at $2 \leq g^* \leq 5$. We found that the vortex shedding frequencies are slightly different for each individual cylinder by changing the value of g^* at fixed Re . Furthermore, we also found that the vortex shedding frequency considerably depends on the separation ratio, especially at $1 \leq g^* \leq 6$. For the antiphase and in-phase synchronized vortex shedding flow regimes, the vortex shedding frequency of cylinders is almost constant at $9 \leq g^* \leq 15,$ very close to that ($St = 0.1516, 0.1596, 0.1644, 0.1644,$ and 0.1644 for $\text{Re} = 80, 100, 120, 140,$ and $160,$ respectively) in the isolated cylinder case. In general, the $C_{D\text{rms}1}$ and $C_{L\text{rms}1}$ have larger values compared to the other cylinders, $C_2, C_3,$ and $C_4,$ for all chosen Re and g^* .

Nomenclature

$C_D = 2F_x/\rho u_{\text{max}}^2 D$:	Drag coefficient
$C_L = 2F_y/\rho u_{\text{max}}^2 D$:	Lift coefficient
$C_{D\text{mean}}$:	Mean drag coefficient
$C_{D\text{rms}}$:	Root-mean-square value of drag coefficient
$C_{L\text{rms}}$:	Root-mean-square value of lift coefficient
D :	Size of the cylinder (m)
e_i :	Discrete velocities
f_s :	Vortex shedding frequency
f :	Particle distribution function
$f^{(\text{eq})}$:	Maxwell–Boltzmann distribution function
F_x :	Drag force in the streamwise direction
F_y :	Lift force in the transverse direction
g^* :	Separation ratio
L_u :	Upstream distance from the inlet position
L_d :	Downstream distance up to the exit of the computational domain
L_x :	Computational length
L_y :	Computational height
Ma :	Mach number
p :	Pressure
$\text{Re} = u_{\text{max}} D/v$:	Reynolds number
S :	Surface-to-surface distance between the cylinders
$St = f_s D/u_{\text{max}}$:	Strouhal number
u_{max} :	Maximum inflow velocity
\mathbf{u} :	Flow speed (m/s)
w_i :	Weighting coefficients

β :	Blockage ratio
ρ :	Density of the fluid (kg/m^3)
ν :	Kinematic viscosity of the fluid (m^2/s)
τ :	Single-relaxation-time parameter
Ω :	Collision operator.

Data Availability

The data that support the main findings of this numerical study are available from the corresponding author upon request.

Conflicts of Interest

The authors declare that there are no conflicts of interest regarding the submission and publication of this manuscript.

Acknowledgments

The second author Dr. Shams-ul-Islam is especially grateful to Higher Education Commission (HEC), Pakistan, for providing funds under Project No. 9083/Federal/NRPU/R&D/HEC/2017 to buy the system for running the codes.

References

- [1] V. Kolar, D. A. Lyn, and W. Rodi, "Ensemble-averaged measurements in the turbulent near wake of two side-by-side square cylinders," *Journal of Fluid Mechanics*, vol. 346, pp. 201–237, 1997.
- [2] C. H. K. Williamson, "Evolution of a single wake behind a pair of bluff bodies," *Journal of Fluid Mechanics*, vol. 159, no. 1, pp. 1–18, 1985.
- [3] D. W. Guillaume and J. C. LaRue, "Investigation of the flopping regime with two-, three- and four-cylinder arrays," *Experiments in Fluids*, vol. 27, no. 2, pp. 145–156, 1999.
- [4] S. Kang, "Characteristics of flow over two circular cylinders in a side-by-side arrangement at low Reynolds numbers," *Physics of Fluids*, vol. 15, no. 9, pp. 2486–2498, 2003.
- [5] A. Agrawal, L. Djenidi, and R. A. Antonia, "Investigation of flow around a pair of side-by-side square cylinders using the lattice Boltzmann method," *Computers & Fluids*, vol. 35, no. 10, pp. 1093–1107, 2006.
- [6] M. M. Alam and Y. Zhou, "Intrinsic features of flow around two side-by-side square cylinders," *Physics of Fluids*, vol. 25, no. 8, p. 085106, 2013.
- [7] H. Ding, C. Shu, K. S. Yeo, and D. Xu, "Numerical simulation of flows around two circular cylinders by mesh-free least square-based finite difference methods," *International Journal for Numerical Methods in Fluids*, vol. 53, no. 2, pp. 305–332, 2007.
- [8] P. Burattini and A. Agrawal, "Wake interaction between two side-by-side square cylinders in channel flow," *Computers & Fluids*, vol. 77, pp. 134–142, 2013.
- [9] Z. Han, D. Zhou, J. Tu, C. Fang, and T. He, "Flow over two side-by-side square cylinders by CBS finite element scheme of Spalart-Allmaras model," *Ocean Engineering*, vol. 87, pp. 40–49, 2014.
- [10] S. U. Islam, H. Rahman, and C. Y. Zhou, "Effect of gap spacings on flow past row of rectangular cylinders with aspect ratio 1.5," *Ocean Engineering*, vol. 119, pp. 1–15, 2016.

- [11] M. M. Zdravkovich, "Flow induced oscillations of two interfering circular cylinders," *Journal of Sound and Vibration*, vol. 101, no. 4, pp. 511–521, 1985.
- [12] S. C. Yen, K. C. San, and T. H. Chuang, "Interactions of tandem square cylinders at low Reynolds numbers," *Experimental Thermal and Fluid Science*, vol. 32, no. 4, pp. 927–938, 2008.
- [13] A. Etminan, M. Moosavi, and N. Ghaedsharafi, "Determination of flow configurations and fluid forces acting on two tandem square cylinders in cross-flow and its wake patterns," *International Journal of Mechanical Sciences*, vol. 5, no. 2, pp. 63–74, 2011.
- [14] A. Sohankar, "A numerical investigation of the flow over a pair of identical square cylinders in a tandem arrangement," *International Journal for Numerical Methods in Fluids*, vol. 70, no. 10, pp. 1244–1257, 2012.
- [15] X. Zhao, D. Cheng, D. Zhang, and Z. Hu, "Numerical study of low-Reynolds-number flow past two tandem square cylinders with varying incident angles of the downstream one using a CIP-based model," *Ocean Engineering*, vol. 121, pp. 414–421, 2016.
- [16] A. T. Sayers, "Flow interference between four equispaced cylinders when subjected to a cross flow," *Journal of Wind Engineering and Industrial Aerodynamics*, vol. 31, no. 1, pp. 9–28, 1990.
- [17] K. Lam and S. C. Lo, "A visualization study of cross-flow around four cylinders in a square configuration," *Journal of Fluids and Structures*, vol. 6, no. 1, pp. 109–131, 1992.
- [18] T. Farrant, M. Tan, and W. G. Price, "A cell boundary element method applied to laminar vortex-shedding from arrays of cylinders in various arrangements," *Journal of Fluids and Structures*, vol. 14, no. 3, pp. 375–402, 2000.
- [19] Y. Song, R. Zhu, T. Simon, and G. Xie, "Computational fluid dynamics modeling patterns and force characteristics of flow over in-line four square cylinders," *Thermal Science*, vol. 21, no. 6 Part A, pp. 2553–2563, 2017.
- [20] K. Lam, W. Q. Gong, and R. M. C. So, "Numerical simulation of cross-flow around four cylinders in an in-line square configuration," *Journal of Fluids and Structures*, vol. 24, no. 1, pp. 34–57, 2008.
- [21] Z. Lin, L. Yu-feng, and L. Hong, "Flow patterns and fore characteristics of laminar flow past four cylinders in diamond arrangement," *Journal of Hydrodynamics*, vol. 23, no. 1, pp. 55–64, 2011.
- [22] W. S. Abbasi, S. U. Shams-Ul-Islam, S. C. Saha, Y. T. Gu, and Z. C. Ying, "Effect of Reynolds numbers on flow past four square cylinders in an in-line square configuration for different gap spacings," *Journal of Mechanical Science and Technology*, vol. 28, no. 2, pp. 539–552, 2014.
- [23] M. Liu, L. Xiao, and L. Yang, "Experimental investigation of flow characteristics around four square-cylinder arrays at subcritical Reynolds numbers," *International Journal of Naval Architecture and Ocean Engineering*, vol. 7, no. 5, pp. 906–919, 2015.
- [24] J. Zhang, H. Chen, B. Zhou, and X. Wang, "Flow around an array of four equispaced square cylinders," *Applied Ocean Research*, vol. 89, pp. 237–250, 2019.
- [25] Y. Gao, K. Yang, B. Zhang, K. Cheng, and X. Chen, "Numerical investigation on vortex-induced vibrations of four circular cylinders in a square configuration," *Ocean Engineering*, vol. 175, pp. 223–240, 2019.
- [26] L. Zhang, M. M. Bhatti, A. Shahid, R. Ellahi, O. A. Beg, and S. M. Sait, "Nonlinear nanofluid fluid flow under the consequences of Lorentz forces and Arrhenius kinetics through a permeable surface: a robust spectral approach," *Journal of the Taiwan Institute of Chemical Engineers*, vol. 124, 2021.
- [27] P. K. Yadav, K. Sourav, D. Kumar, and S. Sen, "Flow around a diamond-section cylinder at low Reynolds numbers," *Physics of Fluids*, vol. 33, no. 5, p. 053611, 2021.
- [28] Y. Zhou and M. Mahbub Alam, "Wake of two interacting circular cylinders: a review," *International Journal of Heat and Fluid Flow*, vol. 62, pp. 510–537, 2016.
- [29] C. Ren, L. Cheng, F. Tong, C. Xiong, and T. Chen, "Oscillatory flow regimes around four cylinders in a diamond arrangement," *Journal of Fluid Mechanics*, vol. 877, pp. 955–1006, 2019.
- [30] F. Tong, L. Cheng, M. Zhao, and H. An, "Oscillatory flow regimes around four cylinders in a square arrangement under small and conditions," *Journal of Fluid Mechanics*, vol. 769, pp. 298–336, 2015.
- [31] S. Malekzadeh and A. Sohankar, "Reduction of fluid forces and heat transfer on a square cylinder in a laminar flow regime using a control plate," *International Journal of Heat and Fluid Flow*, vol. 34, pp. 15–27, 2012.
- [32] H. Huang, M. C. Sukop, and X. Y. Lu, *Multiphase Lattice Boltzmann Methods: Theory and Application*, John Wiley & Sons, Hoboken, NJ, USA, 2015.
- [33] A. A. Mohamad, *Lattice Boltzmann Method: Fundamentals and Engineering Applications with Computer Codes*, Springer, Berlin, Germany, Second edition, 2019.
- [34] L.-S. Luo, "Unified theory of lattice Boltzmann models for nonideal gases," *Physical Review Letters*, vol. 81, no. 8, pp. 1618–1621, 1998.
- [35] D. Wolf-Gladrow, *Lattice-Gas Cellular Automata and Lattice Boltzmann Models*, Springer, Berlin, Germany, 2000.
- [36] M. Sukop and D. Thorne, *Lattice Boltzmann Modeling: An Introduction for Geoscientist and Engineers*, Springer, Berlin, Germany, 2006.
- [37] S. Succi, *Lattice Boltzmann Method for Fluid Dynamics and beyond*, Oxford University Press, Oxford, UK, 2001.
- [38] Z. Guo and C. Shu, "Lattice Boltzmann method and its applications in engineering," *Advances in Computational Fluid Dynamics*, vol. 3, 2013.
- [39] T. Kruger, H. Kusumaatmaja, A. Kuzmin, O. Shardt, G. Silva, and E. M. Viggen, *The Lattice Boltzmann Method: Principles and Practice*, Springer, Berlin, Germany, 2017.
- [40] X. He and L.-S. Luo, "Theory of the lattice Boltzmann method: from the Boltzmann equation to the lattice Boltzmann equation," *Physical Review E*, vol. 56, no. 6, pp. 6811–6817, 1997.
- [41] Y. H. Qian, D. D'Humières, and P. Lallemand, "Lattice BGK models for Navier-Stokes equation," *Europhysics Letters (EPL)*, vol. 17, no. 6, pp. 479–484, 1992.
- [42] M. Breuer, J. Bernsdorf, T. Zeiser, and F. Durst, "Accurate computations of the laminar flow past a square cylinder based on two different methods: lattice-Boltzmann and finite-volume," *International Journal of Heat and Fluid Flow*, vol. 21, no. 2, pp. 186–196, 2000.
- [43] D. Yu, R. Mei, L.-S. Luo, and W. Shyy, "Viscous flow computations with the method of lattice Boltzmann equation," *Progress in Aerospace Sciences*, vol. 39, no. 5, pp. 329–367, 2003.
- [44] Z. Guo, B. Shi, and N. Wang, "Lattice BGK model for incompressible Navier-Stokes equation," *Journal of Computational Physics*, vol. 165, no. 1, pp. 288–306, 2000.
- [45] D. A. Perumal, G. V. S. Kumar, and A. K. Dass, "Numerical simulation of viscous flow over a square cylinder using lattice

- Boltzmann method,” *ISRN Mathematical Physics*, vol. 201216 pages, 2012.
- [46] S. Sen, S. Mittal, and G. Biswas, “Flow past a square cylinder at low Reynolds numbers,” *International Journal for Numerical Methods in Fluids*, vol. 67, no. 9, pp. 1160–1174, 2011.
- [47] Y. Zhou, Z. J. Wang, R. M. C. So, S. J. Xu, and W. Jin, “Free vibrations of two side-by-side cylinders in a cross-flow,” *Journal of Fluid Mechanics*, vol. 443, pp. 197–229, 2001.
- [48] S. R. Kumar, A. Sharma, and A. Agrawal, “Simulation of flow around a row of square cylinders,” *Journal of Fluid Mechanics*, vol. 606, pp. 369–397, 2008.